High Frequency Power Converters

Based on Energy Injection Control

for IPT Systems

Hao Leo Li

High Frequency Power Converters

Based on Energy Injection Control

for IPT Systems

By

Hao Leo Li

A thesis submitted in partial fulfillment of the requirements

for the degree of Doctor of Philosophy in Engineering

Department of Electrical and Computer Engineering
The University of Auckland

New Zealand
January 2011

Abstract

A contactless power transfer system has many advantages over conventional power transmission due to the elimination of direct electrical contacts. With the development of modern technologies, IPT (Inductive Power Transfer) has become a very attractive technology for achieving wireless/contactless power transfer over the past decade. IPT has been successfully employed in many applications for materials handling, lighting, transportation, bio-medical implants, etc.

To transfer power across an air gap, an IPT system employs a primary power converter to generate a high frequency alternating current in a track/coil which is then magnetically coupled to one or more power pick-ups. The design and implementation of the primary side power converter and controller are of great importance in an IPT system because they affect the whole system performance under both steady state and transient conditions. Therefore, any development and control improvement within the primary power converter are desirable.

This thesis focuses on the development of converters for IPT systems based on circuit resonance and energy injection control. A voltage fed DC-AC energy injection inverter is introduced. Basic characteristics and underlying principles of the inverter are studied. A variable frequency ZCS (Zero Current Switching) control strategy is developed for the switching operation. The new DC-AC inverter can achieve high frequency AC power generation using relatively low switching frequencies with predicable current ripple and transient behavior. Furthermore the soft switching operation ensures low switching losses and reduced EMI.

A detailed analytical method has been developed and extended to a system level by taking system bifurcation and power transfer capability into consideration. The critical boundaries of both the loading and coupling conditions are determined for designing energy injection inverters without frequency bifurcation. It has been found there is an optimal coupling coefficient which results in the maximum power transfer capability of the inverter. Using such a system level inverter design process, a primary track current

regulation method based on energy injection control has been proposed. Furthermore, as an example, a practical contactless slip ring system has been developed using the proposed control method.

A new type of direct AC-AC converter is also proposed. A control strategy is developed based on energy injection control for the AC-AC matrix converter to achieve a high frequency current generation with soft switching operation. The converter operation is analytically analyzed in detail, including the current ripple and sag caused by the alternating input voltage. The theoretical analysis is proven by simulation studies and practical experiments.

The energy injection concept is also applied to push pull resonant converters with a "dual" transformation in performance which leads to a boost operation. A mathematical model employing a stroboscopic mapping technique is developed for a push pull inverter to find the multiple ZVS operation points. It has been proven by both simulation and experimental studies that the power transfer capability of a traditional push pull inverter can be increased significantly by operating it at selected low ZVS frequencies without using any additional front-end boost circuits.

Acknowledgements

There are many people whom I would like to show my appreciation during my PhD study in the past four years. They have helped me in numerous ways in my journey of conducting this research.

First and foremost, I wish to thank Dr. Aiguo Patrick Hu for introducing me into the field of IPT (Inductive Power Transfer) and giving me valuable guidance throughout the course of my study. His guidance, advice and positive manner have always been helpful and encouraging.

Next, special thanks should go to Associate Professor Grant Covic for his tremendous help in many ways, particularly for his patience in reading my draft writings.

Thirdly, I would like to express my gratitude to PowerbyProxi Limited for offering me a PhD scholarship as well as technical and experimental assistance. Thanks also go to the Research Committee of The University of Auckland for providing me the funding to attend international conferences.

In addition, I wish to thank Mr. Howard Lu for his laboratory assistance. Also, I can never forget my schoolmates and friends including Dr. William Hsu, Dr. Ping Si, Mr. Chao Liu, Mr. Stephen Zhao, Mr. David Huang, Mr. Hunter Wu, and Mr. Bob Wang for their company, friendship, and various help.

Last but not least, I would like to express my gratitude to my parents. Sincere gratitude goes to my loving wife for her deep understanding and full support all the time.

<div align="right">

Hao Leo Li

1 January 2011 Auckland

</div>

Table of Contents

Nomenclature

<u>**Acronyms**</u>

AC	Alternating current
AGV	Automated guided vehicle
CCL	Capacitor- capacitor- inductor connection
CLC	Capacitor-inductor-capacitor connection
CPLD	Complex programmable logic device
CPS	Contactless power supply
CPT	Capacitive power transfer
DC	Direct current
EMC	Electro-magnetic compatibility
EMI	Electro-magnetic interference
ESR	Equivalent series resistance
FPGA	Field-programmable gate array
G1	Generation one (current-fed parallel resonant) IPT power supply
G2	Generation two (voltage-fed series resonant) IPT power supply
G3	Generation three (voltage-fed or current-fed) IPT power supplies
IGBT	Insulated gate bipolar transistor
IPT	Inductive power transfer
LC	Inductor–capacitor connection
LCD	Liquid crystal display
LCL	Inductor–capacitor-inductor connection
MOSFET	Metal oxide silicon field effect transistor
ms	Milliseconds
PLECS	Piecewise linear electrical circuit simulation
PLL	Phase locked loop
PWM	Pulse width modulation
Q	Quality factor
RF	Radio frequency
rms	Root mean square

VHDL	Very-high-speed-integrated circuit hardware description language
s	Seconds
SCR	Silicon controlled rectifier
TET	Transcutaneous energy transmission
WISA	Wireless interface to sensor and actuators
ZCS	Zero current switching
ZVS	Zero voltage switching

Symbols

ε_0	Permittivity
E_{in}	Injected energy (Joules)
E_{store}	Stored energy (Joules)
V_{DC}	DC voltage (Volts)
V_{in}	Input voltage (Volts)
V_p	Primary side input voltage (Volts)
I_{in}	Input current (Amperes)
I_{track}	Track current (Amperes)
I_{ref}	Reference current (Amperes)
C	Capacitor (Farads)
C_P	Primary Capacitor (Farads)
C_S	Primary Capacitor (Farads)
f	Frequency (Hz)
f_0	Undamped natural frequency (Hz)
f_1	Fundamental ZVS frequency (Hz)
f_s	Switching frequency
G_v	Voltage output gain
i	Instantaneous current (Amperes)
I	Current magnitude (Amperes)
j	Complex operator ($\sqrt{-1}$)
k	Magnetic coupling coefficient
k_0	Optimal magnetic coupling coefficient
L	Self-inductance (Henrys)

L_a	Splitting inductance (Henrys)
L_b	Splitting inductance (Henrys)
L_d	DC inductance (Henrys)
L_p	Primary inductance (Henrys)
L_s	Secondary inductance (Henrys)
L_{sp}	Splitting transformer
M	Mutual inductance (Henrys)
M_0	Optimal mutual inductance (Henrys)
N	The number of the pick-ups
P	Power (Watts)
R	Resistance (Ω)
R_p	Primary side equivalent series resistance (Ω)
R_s	Secondary side equivalent series resistance (Ω)
R_{DC}	DC Load (Ω)
R_L	Equivalent AC load (Ω)
t	Time (seconds)
T	Time constant (seconds)
T_{in}	Energy injection period (seconds)
V	Voltage magnitude (Volts)
v	Instantaneous voltage (Volts)
V_{RL}	Voltage over load resistor (Volts)
Vos	Pick up open circuit voltage (Volts)
Z_r	Reflected impedance (Ω)
Z_t	Total impedance from primary side (Ω)
Z_s	Secondary side impedance (Ω)
X_p	Primary side reactance (Ω)
X_m	Mutual reactance (Ω)
X_s	Secondary reactance (Ω)
ζ	Damping factor
ϕ	Phase angle
μ	Normalized frequency
θ	Phase angle

τ	Time constant (seconds)
ω	Actual angular frequency (radians/s)
ω_0	Nominal operation angular frequencies (radians/s)

Algebraic Notations

Φ	Control matrices of a discrete state space equation
d/dt	Differential operator
dP/dM	Differential operation to mutual inductance
Δ	Discriminant of a polynomial equation
I	Identity square matrix
Im	Imaginary part of a complex expression
Re	Real part of a complex expression

Subscripts

AC	AC value
DC (d)	DC value
in	Input
o	Output
max	Maximum value
min	Minimum value
p	Primary track
r	Referred back from the pick-up to the primary track
s	Secondary pick-ups

Superscripts

^	Peak value
·	Phasor value
′	Derivation

List of Figures

List of Tables

Chapter 1

Introduction

1.1 Background
1.2 Introduction to IPT Systems
1.3 Constraints and Challenges of IPT Power Converters
1.4 Objectives and Scope of the Thesis

1.1 Background

1.1.1 Need for contactless power transfer

Traditionally, electrical power is transferred via a wired circuit by direct cable connections. With the development of modern technologies, such a conventional power transfer technology is facing difficulties in many applications, such as AGVs (Automated Guide Vehicles), material handling systems, aerodrome beacons, clean LCD (Liquid Crystal Display) manufacturing plants, road lightings, battery charging systems, biomedical implants, etc.

Trailing cables, sliding contact systems are the traditional methods to supply power to moveable loads such as AVGs, electrical trams, assembly lines, etc. In these applications, to transfer power to a moving object, the trailing cable has to follow the movement of the object. The difficulty of retracting trailing cables limits the speed and range of the movement. In addition, long-term exposure to the weather increases the risk of system failure and electric shock. Compared to the trailing cable, a sliding bus bar can supply power to a fast moving object with less limitation. However, it has electrical isolation problems. The direct electrical contacts used mean that the sliding bus bar suffers from friction, spark and erosion problems, and thus reduces the system safety and reliability.

Therefore, these traditional power delivery solutions are unsuitable in many applications with moving objects.

For other applications, such as aerodrome beacons, rotating tanks, or radio telescopes, etc., a continuous 360° mechanical rotation is required on one side. To transfer power from a stationary base to a rotary side, an electric slip ring system is commonly used. The mechanical contacts of the sliding brushes inside the slip ring constrain the rotation speed and increase the friction. As a result, frequent maintenance is needed which increases the system operating cost. In addition, the sliding mechanical connection limits the relative displacement of the stationary and rotary parts.

Contactless power transfer is often needed in extremely clean or harsh environments, for example, a dust-free LCD (Liquid Crystal Display) manufacturing plant, or a tunnel lighting system in very wet or under water environments. Direct cable electrical power transfer is not feasible in such applications, and brushed systems produce carbon residues that may cause product failure in LCD manufactory. As a result, the manufacturing costs are further increased by requiring additional equipment to eliminate the friction residues. Similarly, power delivery in harsh environments increases the erosion of the cable and could cause an explosion in some applications where flammable gases exist. Consequently, the system may fail or cause an accident.

With the development of modern technologies, some new and expanding applications of contactless power transfer are becoming popular, such as portable electric devices, consumer gadgets, laptop computers, and electrical vehicles to overcome the traditional charging limitations. Currently batteries are the major solution to supply power to these devices. In most cases, the batteries of these devices need to be taken out for recharging, and a backup battery is replaced. As such, the extra battery increases the overall cost. Although cable connected online charging can be adopted individually, it is not convenient to carry many different adaptors when traveling. Consequently, there is a desire to produce equipment and devices which can be charged without any cable connections.

For some systems with special requirements, for example, biomedical TET (Transcutaneous Energy Transmission) systems, it is not suitable to use a direct contact power transfer, because it imposes high infection risks by having cables passing through

the skin. Presently, a battery is the major solution to power low-power biomedical devices, for example, pacemakers or sensors. Patients have to receive regular treatment for exchanging the batteries. This increases the sufferings of the patient and the medical risk. However, for those applications with a higher power requirement, powering by batteries is infeasible. Therefore, a contactless power transfer solution for power delivery or battery charging without direct electrical contact is preferred for these special applications.

1.1.2   Possible contactless power transfer solutions

Contactless power transfer has been known for a century since Nicola Tesla tested his coil in 1890 [1]. Although his experiment was terminated due to the lack of funding; it has drawn people's attention to contactless power transfer technologies. Theoretically, power can be wirelessly transferred through many different methods: laser [2-4], electromagnetic waves [5-7], static electric field [8-10], and static magnetic fields [11-13].

Laser is an optical method whereby power is transferred wirelessly. It has been found in applications such as opto-couplers. This method requires the electric power to be converted firstly to light for emission. The laser beam is then transferred back to electric power after being received. This method requires the laser transmitter and receiver to be perfectly aligned, meaning it is not ideal for transferring power to moving devices. In addition, the technology is very sensitive to the environment. The intensity of the laser beam decays quickly in air. All of these make constant energy flow across long distances using lasers very difficult.

Using electromagnetic waves to transfer power wirelessly over long distances is feasible [14]. It has been proven using microwaves. Experiments in the tens of kilowatts have been performed recently (1997) at Grand Bassin on Reunion Island [15]. The advantage of transferring high power over a long distance makes the technology attractive. However, the problems involved in the large size and the complexities of structure make this power transfer technology difficult for normal use. In addition, human and equipment safety concerns constrain its use in normal life.

CPT (Capacitive power transfer) is one of the contactless power solutions to movable objects via electric field coupling. It uses two plates to form a capacitor to allow power to jump across an air gap. Unlike a laser which requires a point to point optical transfer

channel, in a CPT system a distributed electric field serves as a power flow channel, although electric field intensity is a major concern. If air is the power transfer medium channel, CPT has the limitation of maximum electric field intensity 30kV/cm and a very low permittivity ε_0 (8.854×10^{-12}) [16]. The low power transfer ability in air makes CPT unsuitable for high power and large gap applications, unless very high permittivity dielectric materials are used as the medium between the two plates.

Magnetic rather than electric fields are a more feasible method of achieving wireless power transfer. An electrical transformer can be regarded as the simplest instance of contactless energy transfer. However, the non-existence of an air gap, due to the tightly coupled primary and secondary sides, means that it is not really contactless, and does not allow far movement. Meaningful inductive power transferring over larger gaps at higher power levels was introduced recently and termed IPT (Inductive Power Transfer) [17]. By comparing to the permeability in a CPT system (ε_0 (8.854×10^{-12})), the permeability μ_0 ($4\pi\times10^{-7}$) of air makes IPT technology easier to transfer power across a relatively long distance compared to CPT technology [8].

All these wireless power transfer technologies have advantages and constraints. However, generally, IPT technology is the most feasible method for normal use complied with advances in modern converter technologies. Many research groups and commercial companies have shown an interest in IPT technologies. After many years of development, IPT has gained successes in many commercial applications, and with improvements of magnetic materials, high frequency wire capacitors and switches, is now being considered as a cost effective alternative in more areas.

1.2 Introduction to IPT Systems

1.2.1 System structure and basic operation principle

An IPT system is a system which transfers power from one side to another side wirelessly via a magnetic field coupling. Figure 1-1 shows a typical configuration of an IPT system. As shown, such a system comprises two electrically isolated sections: a stationary primary side and a movable secondary side.
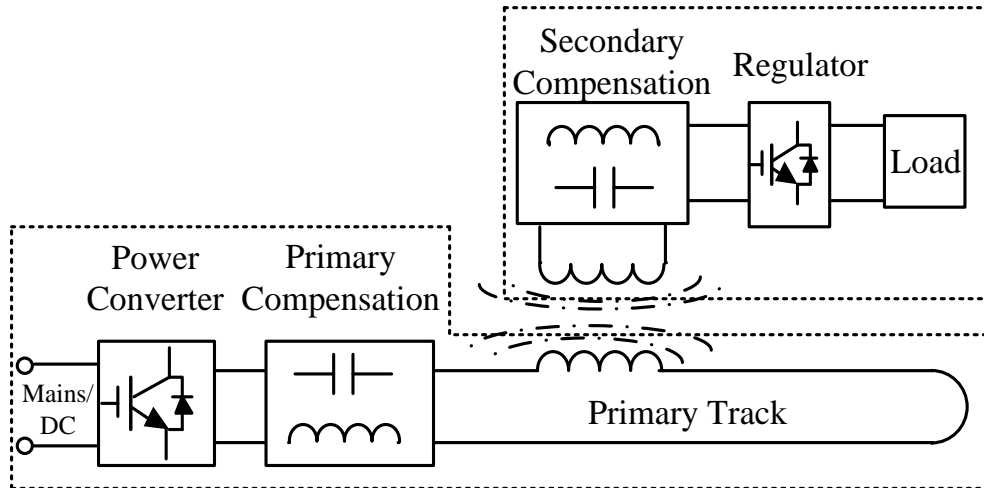
Figure 1-1: Typical configuration of a contactless power transfer system.

The stationary primary side is connected to a front-end low frequency power source, which is usually the electric utility at 50Hz or 60Hz, single-phase or three-phase. For some special applications, the power source can be a DC source or a battery. The primary side consists of a high frequency power converter which generates and maintains a constant high frequency AC current in a compensated conductive track loop/coil normally within the range from 10kHz-1MHz [18, 19]. The pickup coil of the secondary side is magnetically coupled to the primary track to collect energy. The reactance of the secondary side increases proportionally with an increase in operating frequency, and as such is normally compensated by other capacitors or inductors. In order to have a controlled output for different loads, usually a switch mode regulator is used on the secondary side to control the power flow and maintain the output voltage to be constant [20, 21].

1.2.2   General features

The IPT system is electrically isolated between the primary and secondary sides. It has many advantages over conventional conductive power transfer and other contactless power transfer technologies. Some of the major features of this IPT technology are listed below:

➢ **Mechanical flexibility**

Unlike an electrical transformer, an IPT system delivers power using a loose inductive coupling. A loose coupling is not ideal from the point view of power transfer capability; however the mechanical flexibility between the primary side and pickup allows the secondary side of the IPT system to move freely along the track or in the proximity to a coil on the primary side. This feature makes IPT systems very attractive for both movable and stationary applications.

➢ **Operation safety**

By getting rid of the direct electrical contacts between the primary and the secondary side of an IPT system, mechanical and electrical wear and tear caused by a traditional sliding contact power transfer system can be eradicated by an IPT system. The potential electrical shock under wet or harsh environments is eliminated. This feature greatly improves the operational safety of the electrical devices.

➢ **Environmentally friendly**

Apart from a high operation safety level, another great feature of an IPT system is that the system is environmentally friendly. Because of the elimination of electrical contacts between primary side and secondary side, an IPT system can supply power without affecting most environments, e.g. both in harsh and clear ultra clean environments. It can supply a carbon residue free power delivery. Since the magnetic field can pass through most nonmetallic materials, an IPT system can be used in many applications as described earlier. In addition, the operating frequencies of an IPT system are normally within a range from 10 kHz-1MHz; this frequency does not affect communication channels. The operating frequency of a typical IPT system is harmless for human body and its safety has been proved by many biomedical TET systems [22, 23].

➢ **Reliability**

Without the electrical connections, the manufacturing requirements of the primary and the secondary sides can be treated separately according to their local operating conditions. Separate primary and secondary side enclosures can overcome electrical shock or chemical erosion. As such, it increases the lifespan of the electric components and the overall system reliability as well.

1.2.3   Achievements of IPT technologies

Owing to the advantages of the IPT technology, it has made many remarkable achievements in both research areas and in commercial applications. However, it is also facing some technical challenges. In this section, the achievements and the technical challenges of the IPT technology are presented.

➢ **Research perspective**

There are presently many research groups that have been involved in the research of IPT technology around the world in the latter half of the 20th century, such as MIT (Massachusetts Institute of Technology), The University of Auckland, Tokyo University, Sojo University, Tohoku University, City University of Hong Kong, Chongqing University, Zhejiang University, etc.

The earlier IPT research by MIT can be dated back to 1966 [24]. A 2.5MW system over a 10mm air gap was reported. The system operates at 18 kHz with ferrites to increase the coupling between the primary side and the secondary side. The primary track current was almost 400A. Later in 2006, Professor Marin Soljacic showed their recent technology "WiTricity" based on IPT technologies to transfer power contactlessly. Their research was published in Science [25, 26]. A prototype system could achieve a 60W power transfer ability over more than 2m. Contactless power transfer capability over such a distance has drawn considerable public interest as a result.

The University of Auckland began work on IPT in the 1970's but increased its focus on this technology in the late 80's. Over the last two decades it has become the world leader in IPT research for industrial applications. The research interests of the IPT group are focused on basic IPT theory, system level designs, primary converter technologies, secondary power flow controls and magnetic coupling designs [27-32]. There are many research publications on IPT technologies which have attracted wide attention. The university holds tens of patents on IPT technologies. The power levels of the research group range from millwatts for biomedical applications to thousands of watts for electrical vehicle battery charging [33, 34]. Much of the research and patents have been applied practically in applications by many enterprises and corporations, such as Conductix-Wampfler in German, Daifuku in Japan, and Telementary Research, Halo IPT,

Powerbyproxi, Cabco industries, Dream solutions and 3I innovations in New Zealand [35].

In Japan, Tokyo University, Sojo University and Tohoku University have set up research groups on IPT technologies. Professor Takao Someya of Tokyo University and his research group presented their low-cost, low-power, large-area smart sheet, which can deliver power and offers communications among electric devices such as laptops, portable gadgets in December 2007 [36]. The smart sheet is a multilayer print sheet, in which each layer performs different functionality. Functionally, power layers are mainly for transfer power via inductive coils in the print sheet. The target object detection layer is to sense the location of the target electric devices, which needs to be charged, through a combination of organic transistors and plastic micro-electromechanical switches. The system can automatically detect and charge the devices. The Journal of Nature Material reported the smart sheet could transfer a 40W power to multiple electric devices [37]. Sojo University, Yokohama National University and Tohoku University have shown more interest in IPT applications that include electrical vehicle applications, biomedical devices and underwater devices. Their research mainly covers modeling of IPT systems and magnetic coupling improvements, etc. [38, 39]. Among them, multiple primary transmitters for powering electric vehicles show great promise for powering a moving object. Yokohama National University specifically focuses on inductive power transfer to high speed moving trains [40]. In their latest research, artificial biomedical devices powered outside of the human body shows great potential for new applications of IPT. They also have many researches from fundamental theories to practical applications of IPT technologies [41-43].

With the development of IPT technologies, more and more universities and research groups have joined this area. Professor Jürgen Meins in Brunswick University of Germany has put their efforts into IPT railway systems. Korean Kyungpook National University has focused their research on IPT technologies for rotary devices[44, 45]. Professor S.Y. Hui in Hong Kong has shown their research in battery charging based on coreless printed circuit board coreless transformer for low power devices, such as mobile phones, toothbrushes, etc. [46-49]. Zhejiang University, Nanjing Aeronautics, and Astronautics University and Chongqing University of China started their research in early 2000 [50-52].

They have been researching many aspects of IPT systems including magnetic modeling, converters, and controls [53-55].

In addition to the expanding list of universities interested in this research, many commercial research groups have become involved in the development of IPT systems.

➢ **Commercialization perspective**

With the development of new semiconductors, as well as theory, IPT technology has gradually become mature and has translated into production.

The earlier example of transferring the research to manufacture is the corporation between Daifuku, a Japanese material handling manufacture, and Uniservices, which is the technology commercial arm of The University of Auckland and focuses on the commercialization of university's intellectual property. Figure 1-2 shows some of IPT products by Daifuku Japan. The first commercialized IPT prototype was developed for an overhead monorail system in 1991 [17]. Later the "ramrum" material handling application was successfully manufactured and wildly used in many factories, such as storage and retrieval systems. Later this mature product was adapted for use in clean factory system, such as semiconductor and LCD manufacture. A series of CLEANWAY and CLEAN STOCKER products were successfully developed. AGV systems powered and guided by a 165A IPT track have also been used in car manufacture factories.

(a) "Ramrum" material handling system   (b) AVG powered by IPT system

Figure 1-2: Daifuku IPT applications

Conductix-Wampfler Germany is another company, which has been involved in developing IPT systems for a wide range of applications [56]. The world's first vehicle for people transport was successfully implemented in partnership between Conductix-Wampfler and Uniservices and has been in operation in Roturua New Zealand shown in Figure 1-3 since 1998 [57]. A series of products were developed further to meet modern industrial requirements. A spectrum of IPT based products was developed including IPT floor, IPT rail, IPT charger for different applications and environments in the last few years. Their IPT system was firstly installed in BMW plant in Germany and later adopted by other car manufactures-Daimler, GM, and Ferrari. More IPT solutions are designed and applied, such as vehicles on the water ride in Walibi World (Holland) and Legoland (USA), and have been used in elevators, etc.

Figure 1-3: IPT vehicle for people mover in Rotorua New Zealand [58]

Another German company VAHLE specializes their products for inductive power transfer system in large size applications, such as crane systems, elevators, traffic systems, floor systems, etc. [59]. In 1999, their CPS (Contactless Power Supply) system was introduced to conveyor technology. The CPS system has also been successfully used in the Tower Automotive monorail system in USA.

Recently, many more well-known companies have begun IPT product development for different applications. Seiko-Epson in Japan firstly announced their commercialized product of a general purpose wireless power transfer module, which has separate coils to achieve 2.5W power transfer ability with a 0.8mm coil [60, 61]. As shown in Figure 1-4,

the smaller size and output power range make it is a common module adopted by many small electric applications to achieve contactless power charging.
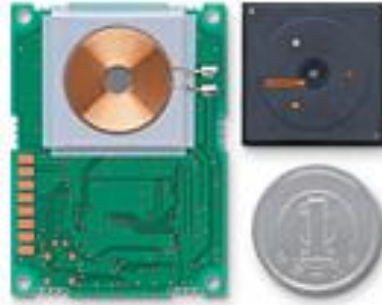
Figure 1-4: Commercialized commonly used wireless power transfer module [61]

In 2003, ABB developed their WISA system (Wireless Interface to Sensor and Actuators) shown in Figure 1-5. This system is also based on IPT technology and can supply power to many wireless sensors. Meanwhile, it has wireless communication channels to collect sensor data [62].
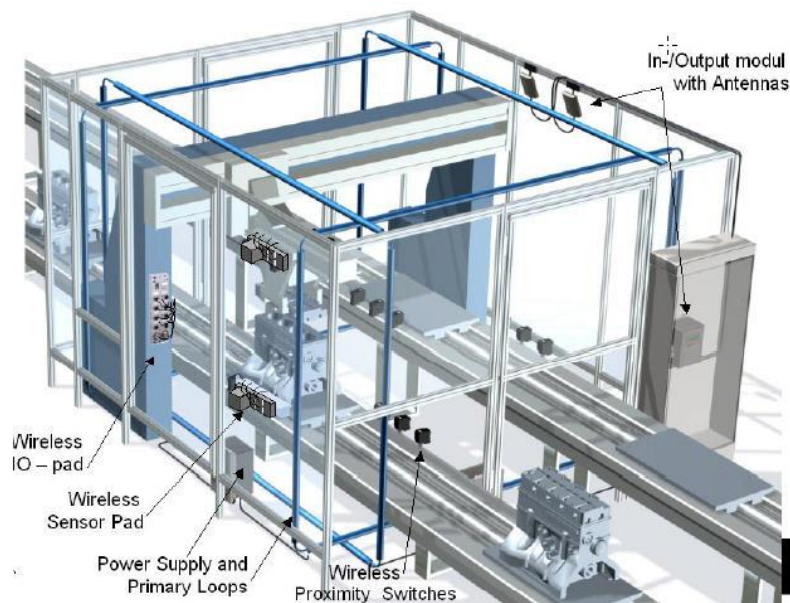
Figure 1-5: ABB WISA system based on IPT technology [63]

Energizer [64] recently starts to sell their Energizer-pad product to supply power to mobile phones and other portable gadgets shown in Figure 1-6. This product intends to offer a general solution for small electric devices to get rid of the charger adaptors. Such a

product gives a guide to commercialize the IPT chargers for home applications. Witricity [65], SpikeCharger [66], Powercast [67], Wipower [68] have developed similar products to charge small portable gadgets, medical devices, toys, and electric tools.

Figure 1-6: Energizer-pad for charging small portable devices [64]

3I-Innovation Ltd. in New Zealand has been selling their products of wireless roadway/tunnel lighting systems and equipment, one application is shown in Figure 1-7 since the mid 90's. PowerbyProxi Ltd. recently has developed contactless slip rings for many world class companies; one example application is for forest harvest machines for John Deere [69]. Their new rotary IPT system for wind turbine pitch control is under development.

Figure 1-7: IPT powered roadway lighting system of 3i Innovations Ltd. [70]

In addition, Telemetry Research Ltd. is one of the companies commercializing IPT products in biomedical TET areas. It provides wireless power transfer supplies to drive left

ventricular heart assist devices, implantable stimulators, motors and pumps, and sensors for freely moving animals [71].

With the vigorous development of IPT technology, a wireless power consortium has been recently established. It has further drawn the public's attention to contactless power transfer technology and aims to supply a better platform for the development of low power charging applications of general appliances. The new "Qi" low power standard, delivering up to 5 Watt into wireless power pickups, has been established for wireless IPT technology [72]. It is being recognized by many consumer electronics companies.

1.3 Constraints and Challenges of IPT Power Converters

In the past decade, IPT systems have advanced significantly, and have gained many remarkable achievements in different fields. As the majority of applications are magnetic fields generated from primary side to couple to pickups, the design and development of the primary power supply has become a critical factor in the IPT system. IPT power converter technologies have been improved over the past decade, but also face some difficulties and challenges ahead as power and frequency are increased, such as challenges include dynamic response, overshoot control, simplicity of control and practical implementation, economic considerations, etc.

As IPT technology relies on the power converter technology, the development of the conversion and control technique contributes to the IPT systems. Currently, in order to generate a high frequency current in the primary track, the operation of inverters has to be equal to the actual frequency of the current. As a result, the circuit transient process involved in those power converters, such as the overshoot and dynamic response speed during the startup or load variation, is normally complex. The design and implementation of the associated controller could be a challenge.

To date, most IPT primary power supplies are directly connected to the mains. The existence of an AC-DC conversion stage and a front-end DC-DC inverter is required to obtain a suitable DC input power for IPT inverters. The extra components and circuitry reduce the overall efficiency of the primary converter. Having an IPT power supply without energy storage is an intrinsically safe approach for applications and is desirable. In

addition, a power supply with high efficiency and less cost would be perfect for applications. However, reducing the power supply cost while maintaining its reliability could be a challenge.

The power supply can take a large space in many applications because of the relatively complicated structure. However, for some applications the installation space is very limited, so that a large sized power supply may not be suitable and may unnecessarily increase cost. Design structurally simple and compact power supplies with high performance are desirable and could be a challenge.

As an IPT system has one or more pickups, the loading and coupling conditions of the secondary side will affect the power transfer ability and system performance. It is always important to have a stable system in practice. The understanding of the effect of pickups is desired, and designing a stable IPT system with high performance could be a challenge for variable frequency controlled power converters.

Practically, it is normally impossible to have one converter to meet all the requirements of all IPT applications at the same time. Therefore, trade-offs are often needed, and understanding the requirements and constraints would be the first step in designing better IPT power converters.

1.4 Objective and Scope of the Thesis

The objective of this research is to propose and develop new converters taking into account the challenges and constraints of present IPT power converters. The thesis focuses on the development of new converters based on energy injection control to achieve a better system performance with reduced system cost, size and power losses. Different converter topologies and control strategies are investigated for both DC and AC power sources.

The following thesis chapters are arranged as follows.

Chapter 2 presents an overview of the converter technology of IPT systems, starting from a fundamental theory of IPT power converters. Basic conversion topologies and switching

strategies and control methods are presented. Some currently existing power converters will be discussed in general according to their types and generation classifications.

Chapter 3 presents a new conversion method based on energy injection and free oscillation control. The basic properties of the DC-AC energy injection converters are studied. The comparison of both a full-bridge and a half-bridge is undertaken. A soft switching strategy is developed to implement the energy injection control. The simulation studies and experiment is implemented to verify a full bridge DC-AC example under both dynamic and steady state conditions.

Chapter 4 discusses the stability and power transfer capability of the proposed power converter power at a system level. To design IPT system without bifurcation, the proposed energy injection inverter is analyzed against loading conditions for IPT systems with single pickup and multiple pickups. Analysis of the effects of mutual inductance on frequency stability and maximum power transfer capability is also undertaken. Then the effect of the component variations on frequency sensitivity is investigated.

Chapter 5 proposes a power flow control method on the primary side based on energy injection control with secondary feedback. The analysis of the operation and the design considerations are presented. Simulation study is conducted for the verification under both the steady state and load variation conditions. A practical contactless slip ring system is designed and implemented to verify the primary power flow control method.

Chapter 6 proposes a novel direct AC-AC converter to generate high frequency AC currents without any DC energy storage elements based on free oscillation and energy injection control. It covers the development of topology and control method. A mathematical modeling and performance analyses including the current ripple and sag are undertaken. Simulation and experiments are carried out to verify the direct AC-AC converter.

Chapter 7 investigates a push pull inverter for IPT system with boost mode operations at different ZVS frequencies. The operation principle is presented. Accurately soft switching operation period are discussed with the analysis of the effects on the resonant voltage and track current at different ZVS frequencies. The existence condition of the multiple ZVS

operation frequencies is analyzed. Simulation study and experiment are conducted to verify the boost mode operation.

Chapter 8 summarizes the conclusions reached in this thesis. The contributions of the thesis are outlined and directions for future work are suggested.

Chapter 2

Overview of High Frequency Converters for IPT Systems

2.1 Introduction
2.2 Fundamental of IPT Power Converters
2.3 DC-AC High Frequency Inverters
2.4 AC-AC Conversion Technologies
2.5 Summary
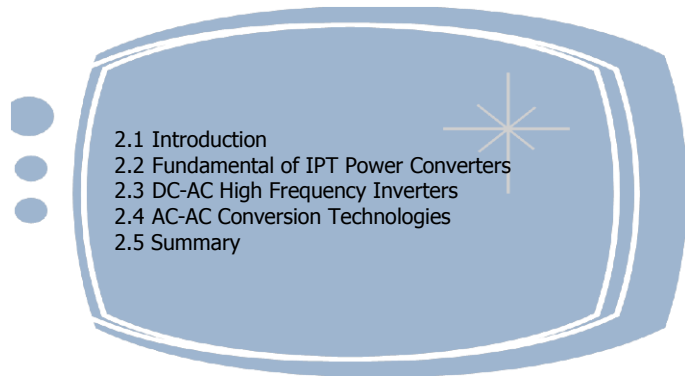
2.1 Introduction

IPT systems have recently become practicable due to technical advances in ferrites, Litz wire, semiconductor switches and switching control technologies. In order to achieve power transfer contactlessly from a primary platform to a secondary power pickup circuit via magnetic field coupling, the key factor lies in the generation of a high frequency current on a primary track/coil. High frequency power converters are often designed to achieve such a task. Different types of power converter and associated controllers have been developed depending on the design considerations and requirements in the cost, size, power rating, power transfer capability, system stability, EMI, etc. [73].

In order to have a better understanding of the high frequency power converter operations and their state of the art, this chapter provides a general overview of the popular converter technologies used for high frequency applications. Basic power conversion topologies, switching methods, and controllers involved in IPT applications will be presented first. The chapter then outlines the existing DC-AC high frequency converters, followed by a description of the basic conversion concepts and the relevant switching control methods. Finally, a review of the concept and control methods of possible high frequency AC-AC

converters will be presented. This chapter will, therefore, present the reader with sufficient knowledge to comprehend the high frequency converters discussed later in this thesis.

2.2 Fundamentals of IPT Power Converters

2.2.1 *Conversion types*

Converters are commonly used to generate a high frequency current on the primary side of a contactless power transfer system. Practically, there are two approaches to achieve high frequency current generation: linear amplifiers or switch mode power converters [74-77]. In the former case, the semiconductor devices are operated in a linear region. Even though the development of different classes of linear electronics amplifiers provides various improvements, the nature of high power loss in linear region limits a linear amplifier to low power applications, where power efficient is not so important. Comparing to linear amplifiers, switch mode power converters can achieve high efficiency by fully on/off control [16]. Therefore switch mode power converters are widely used to generate high frequency track currents for medium or large IPT applications, where the power efficiency is one of the major concerns [40, 78, 79].

Numerous switch mode power converters are currently being deployed to generate high frequency track currents for IPT systems. The input power source for a switch mode high frequency power converter can be either a DC or directly from AC mains [29, 51, 80]. Thus, the switch mode power converter for an IPT system can be commonly classified further into two categories according to the type of their input sources. They are DC-AC inverters and direct AC-AC converters.

Practically, because a direct DC source is not ubiquitous for accessing to generate high frequency currents, at present most of the power converters used for IPT systems are two-stage AC-DC-AC converters. To obtain a constant DC power source, a front-end AC-DC rectifier is needed. In addition, energy storage elements are necessary to link the rectification circuits and the DC-AC inverter to buffer the difference between the instantaneous input and output power within a two-stage converter. In order to meet the requirements of international standards and improve efficiency, many methods are applied to the AC-DC conversion stage, such as synchronous rectifiers, filters, power factor

correction circuits, etc. Once a stable DC power is obtained, a second stage DC-AC inverter is required for the high frequency track current generation. A considerable amount of research has been carried out in the area of DC-AC inverters for IPT systems. Several topologies and switching control methods have been developed. All of them have various advantages, disadvantages or limitations in terms of switching stress, power efficiency, implementation, and EMI for high frequency applications. A brief review of the commonly used high frequency DC-AC inverters will be presented in the following section.

Theoretically, an AC-AC converter can also be used to convert an AC power source such as the mains supply to another AC power source, where the output frequency can be set arbitrarily. Conventional phase controlled AC-AC choppers, PWM controlled AC choppers and cyclo-converters cannot achieve a high frequency conversion. However, a hybrid matrix converter using multiple bidirectional switches and local resonance offers a possibility to generate a high frequency power from a low frequency power by its matrix conversion structure. The complexity of the structure and the associated switching control makes a normal matrix converter difficult to directly fulfill the high frequency generation task for IPT applications. A new matrix AC-AC converter based on the concept of energy injection control and circuit resonance is proposed in Chapter 6 to provide a high frequency current generation approach for IPT applications.

2.2.2   *Basic switching techniques*

A PWM hard switching technology is commonly used in the design of power converters. Using such a switching technique, the on and off transients of the switches may take place at non zero voltage or current instants leading to a hard switching operation [81, 82]. In addition, during the on and off switching transients, the semiconductors have to withstand high voltage and current simultaneously resulting in high switching losses and stress.

Although passive inductive or capacitive components can be used as snubbers of semiconductor switches to reduce the switching *dv/dt* and *di/dt*, these extra components limit the freedom of the PWM switching control [83, 84]. For example, a voltage fed converter described in [16], parallel capacitors are employed and designed for a certain residue voltage. Any variation of the dead time caused by the switching control will cause

an incomplete charging/discharging of the snubber capacitors. As a result, the residue voltage will be shorted, which may cause devices to fail.

Soft switching techniques, which combine conventional PWM technology with resonant concepts, offer another switching technique for IPT converters. Such soft switched converters have similar switching waveforms to those of conventional PWM converters except that the rising and falling edges of the waveforms are 'smoothed' without transient spikes. Soft switched converters usually utilize the resonance in a controlled manner. Resonance is allowed to occur just before and during the turn on and turn off processes so as to create ZVS and ZCS conditions [30, 85]. Apart from this, they behave just like conventional PWM converters. With simple modifications, many customized and integrated control circuits designed for conventional converters can be employed for soft switched converters. Because the switching losses and stress have been reduced, a soft switched converter can be operated at the very high frequency up to a few MHz level. They also provide an effective solution to suppress EMI and have been applied within AC-AC, AC-DC and DC-AC converters. Because of the characteristics of the inductively coupled contactless power transfer technology, the track or the coil can be treated as an individual inductor. With a suitable compensation for the reactance of the inherit track inductor, a full resonance can be constructed. For such a reason, a series of load resonant converters have been developed and implemented over the past two decades for IPT applications.

2.2.3   *Track tuning method*

Although the output of the converter can drive a track or coil directly, it is difficult for a power converter to drive a long track, or a large coil. This is because, at a high frequency of operation, the track reactance may become too large for the power supply to generate a high magnitude track current, unless the output rating of the power supply is very high. High power ratings require high power V/I rated semiconductors, consequently this increases the operational difficulty of the converter and its cost. However, with appropriate tuning, the track reactance can be partially compensated [86].

Apart from the above reactive compensation, another important feature of track tuning is to construct resonant tanks to obtain soft switching operation for the converter design.

This track tuning also acts as a harmonic filter to improve the quality of the current and voltage waveforms, thereby reducing the EMI of IPT systems [87].

A track can be tuned with reactive components placed either in series, parallel, or in a hybrid form as shown in Figure 2-1 (a)-(c). As will be discussed later, different tuning configurations may lead to different resonant power converters with quite different properties, such as reactive power flow, power factor, track current sensitivity, stability, and efficiency.

| (a) series tuning | (b) parallel tuning | (c) hybrid tuning |
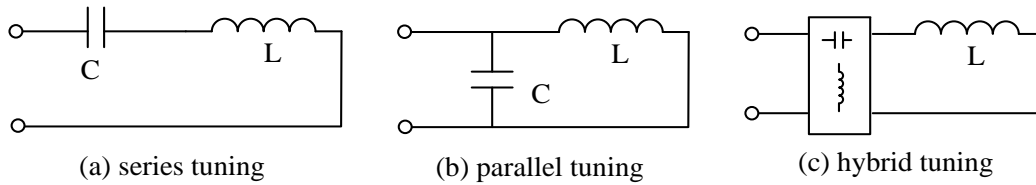
Figure 2-1: Track tuning methods

For Figure 2-1 (a) and (b), the compensation capacitor (*C*) is usually designed to fully tune the track inductance (*L*) at a predefined operating frequency *f* which is normally the nominal operating frequency of the system. Therefore the value of the capacitor normally can be expressed as:

$$C = \frac{1}{4\pi^2 f^2 L} \qquad (2\text{-}1)$$

However such a design methodology for series or parallel compensation cannot simply be applied to a hybrid compensation network as in Figure 2-1 (c), because the hybrid tuning configuration may be different based on the design purposes and converter topologies [51, 88, 89].

2.2.4 *Track current controls*

As discussed previously, the purpose of the primary side of an IPT converter is to generate a high frequency current in a track/coil. There are many different control objectives involved in the design of the primary power converter. Although the IPT converter types may vary based on applications, the controllers for the power converters are generally

classified into one of three different categories according to their control mechanisms: variable /fixed frequency control, magnitude controller, and frequency stability controller.

● **Variable/fixed frequency control**

In order to generate a high frequency current within a track/coil, there are two major control strategies, namely, fixed frequency control and variable frequency control. Fixed frequency control is used to turn on and off the switches at a predetermined frequency. The fixed frequency control is independent of the loads, or circuit parameters. Therefore, the fixed frequency controller is easy to implement, but the associated switching stress, switching losses and EMI are high. In contrast, variable frequency control is another control approach which controls the switches on and off with some extent of frequency variation. By varying switching frequency, soft switching at zero voltage or zero current instances can be achieved. The advantage of the variable frequency control strategy includes the low switching stress, low switching losses and reduced EMI, etc. The disadvantage of variable frequency control is that the operation frequency may drift away from the nominal operation frequency. In the extreme conditions, the operation frequency will bifurcate, which causes frequency stability and power transfer capability problems [90, 91].

● **Magnitude control**

The current magnitude control is one of the major tasks of the primary power converters. To keep the track current constant, a feedback control loop is normally required. Generally, track current magnitude control can be achieved from the input side by varying the input voltage or current. To increase or decrease input value, a front-end buck or boost converter is normally required [33, 92]. Such a solution is very simple in structure and suitable for all of current fed or voltage fed converters. But the drawbacks are also obvious. For example, if a buck converter is used to regulate the input DC voltage, more components are required. Those extra components may contribute to additional power losses, EMI, size and cost. In addition, the dynamic response can be very different to analyse and control.

An alternative solution is to regulate the high frequency inverter voltage or current by controlling the on/off shift angles [93-95]. Because no extra components are required,

converter size and weight are not compromised. There are many different methods, which can be used to implement the magnitude control of different converter topologies [93, 96]. For example, as described in [96], an LCL inverter operated at discontinues current mode is different to a normal series tuned inverter. The control method requires a special consideration on phase angles to ensure the inverter current fully drops to zero. Consequently, the effects on control, implementation, or other perspectives will be different depending on topologies, which will be briefly discussed in a later section of this chapter.

- **Frequency stability control**

Frequency stability is another major concern when controlling the primary current. As described that variations in loading conditions or system parameters may lead to frequency drift. Although a fixed frequency switching control strategy can control the switches at predefined frequency, the frequency drift may lead to a phase variation between the input voltage and the input current. As a result, switching losses may increase, and then system reactive power may increase.

Adding passive stabilization circuits is one solution, which increases the system Q. This method can help to reduce the frequency drift caused by load variation. But it cannot eliminate the frequency variation caused by loads and other system parameter variations. Actively switching a capacitor or an inductor and using a saturable inductor are commonly used methods to change the equivalent tack inductance or tuning capacitance. As a result, the new tuning frequency will be varied against the frequency drifts to stabilize the system at or near the desired frequency [20, 33, 97].

2.3 DC-AC High Frequency Inverters

A block diagram of a typical DC-AC power inverter for IPT applications is shown in Figure 2-2. Here high frequency inverter is used to invert the DC power into a high frequency power to drive the resonant tank. Depending on the type of input source, DC-AC inverters can be categorized into two groups: voltage fed DC-AC inverters or current fed DC-AC inverters. There are three IPT power inverters that have been designed and implemented at The University of Auckland. These are described as: G1 (generation 1),

G2 and G3, although there are a few associated derivatives, which will be briefly discussed here.
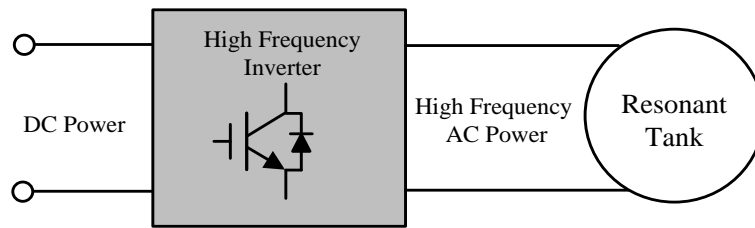
Figure 2-2: A block diagram of a high frequency DC-AC converter

2.3.1 *Current fed G1 power inverter*

Strictly speaking current fed inverters should employ a current source as the input power. An ideal current source should output a constant current independent of the voltage across it. It has two fundamental characteristics:

- ➢ It supplies a constant current, and
- ➢ Its voltage can vary freely.

Practically because a current source cannot stand alone like a voltage source unless superconductors are used, a commonly used economic solution to construct a current source is to use a series connected DC inductor with DC voltage source. Such a configuration provides a quasi voltage-controlled current source with a nearly constant current at a high frequency steady state operation.

Current fed inverters have two typical inverting configurations: the full bridge topology and the push-pull topology as shown in Figure 2-3. It can be seen that in addition to the DC inductor, the full bridge current fed topology consists of four switches. However, instead of the upper two switches, the current fed push pull configuration employs a splitting transformer to form a continuous path for the current flowing. Both full bridge topology and the push pull topology have to keep at least one side of the switch(es) on at all times to maintain the current flow.

(a) Full bridge   (b) Push-pull
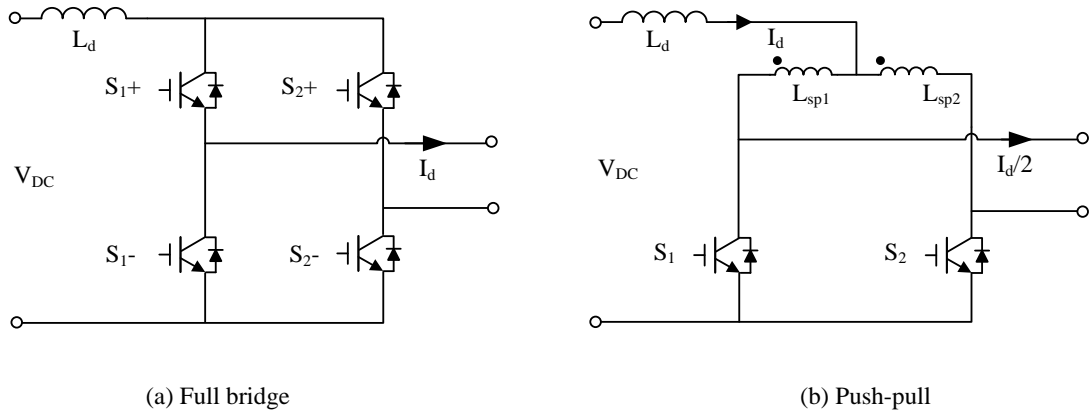
Figure 2-3: Current fed switching network topologies

It should be noted that two current sources should not be connected arbitrarily to avoid over-voltage generation. A current fed inverting network cannot be directly connected to a track/coil within an IPT system. As such, a parallel tuned resonant tank or other derivative resonant structure with a voltage source property are needed for a current fed inverter [16].

A typical full bridge current resonant inverter is shown in Figure 2-4. The switching network is connected to the track via a simple parallel tuned capacitor branch. The switches S_1+, S_1- and S_2+, S_2- are controlled to turn on and off to generate a high frequency inverting current in the resonant tank.
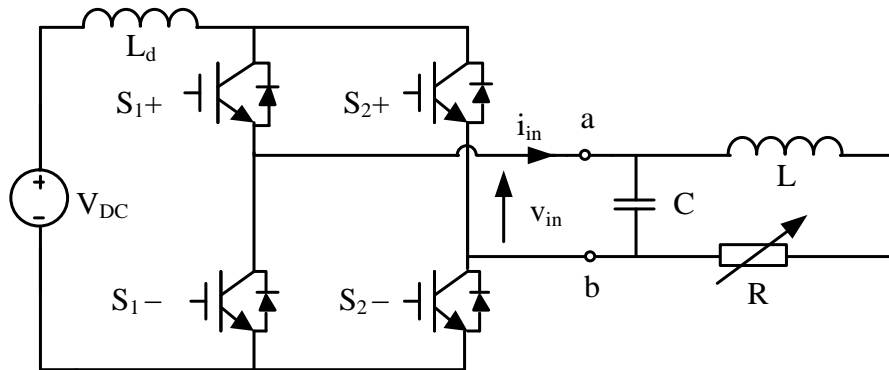
Figure 2-4: A typical full bridge current fed inverter for an IPT system

A symmetrical fixed frequency switching strategy offers the simplest solution to control a current fed converter. The diagonal switch pairs are forced to turn on and off symmetrically, i.e. when S_1+ and S_2- are on, then S_2+ and S_1- are off. With such a switching strategy, the full bridge current fed inverter has three different switching states

under fixed frequency operation as shown in Figure 2-5 (a)-(c). The switches operate with non ZVS condition for the leading or lagging states as shown in Figure 2-5 (a) and (b). Therefore, the voltage and current ratings of the inverter are high, unless the switching instants occur at ideal ZVS conditions as shown in Figure 2-5 (c).

(a)i_{in} leading v_{in}

(b)i_{in} lagging v_{in}

(c)i_{in} and v_{in} in phase
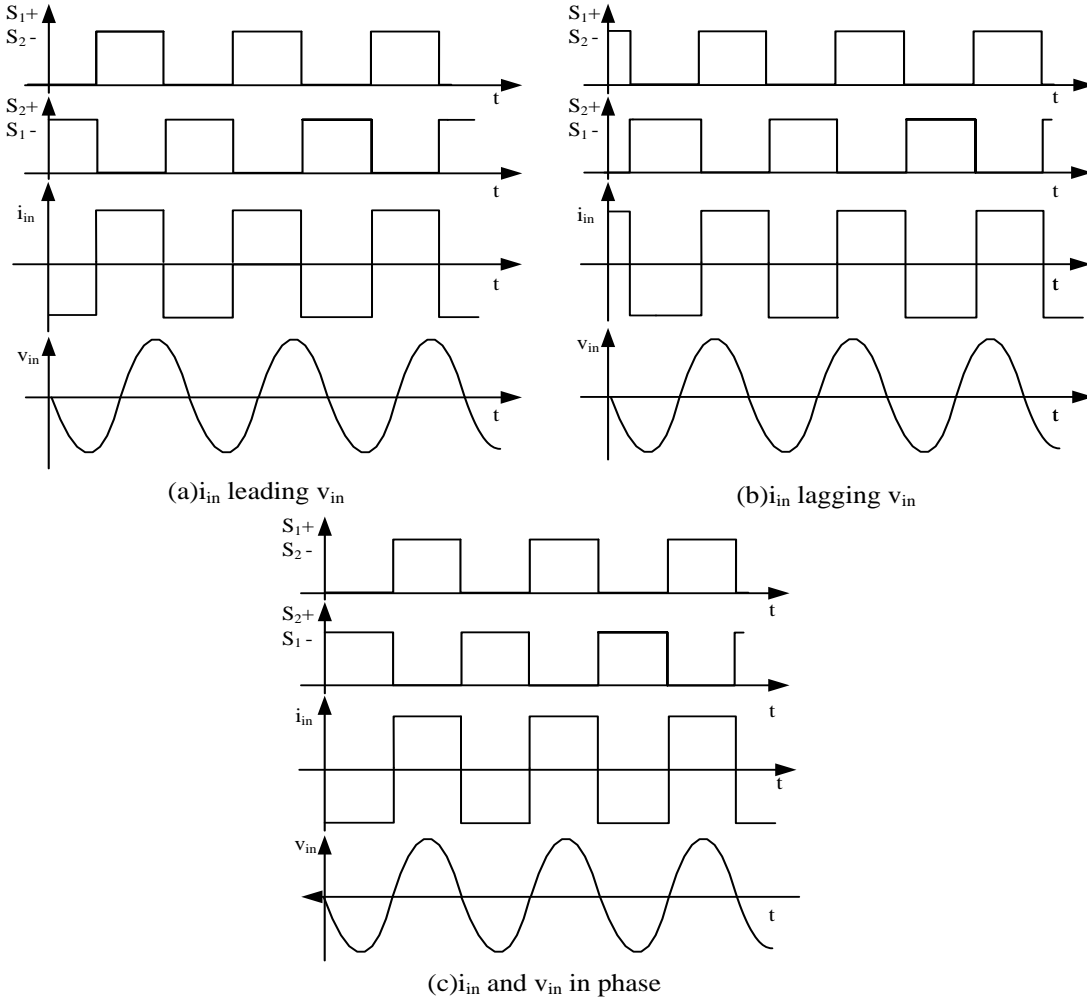
Figure 2-5: Operational states of the full bridge current fed inverter

The advantage of a fixed frequency switching control strategy is that the control method is simple and easy to implement. The switching frequency is normally designed to be equal to the nominal circuit resonant frequency. Therefore, it is not necessary to consider the system bifurcation. But such a fixed switching operation may result in a high reactive power when the inverter works under leading or lagging switching conditions. The forced switching operation therefore can impose a high voltage and/or current stress and high

EMI. In addition, the fixed frequency control strategy cannot achieve direct output track current regulation without a front-end DC power regulator.

The PWM phase shift switching strategy is also a fixed frequency switching strategy but with phase control. The phase switching operation can be used to control the magnitude of current from a full bridge current fed inverting network, and then to regulate the track current of the IPT system. To regulate the output current from the inverting network, the on and off overlap period of the switches is controlled. A typical operation of the phase shift control is shown in Figure 2-6. It can be seen that the switches are controlled to have a phase shift angle, so that the inverter current is regulated. As a result the resonant voltage is controlled. Such a phase shift control results in the top two switches having turn on losses but no turn off losses, while the bottom two switches have turn off losses but no turn on losses.
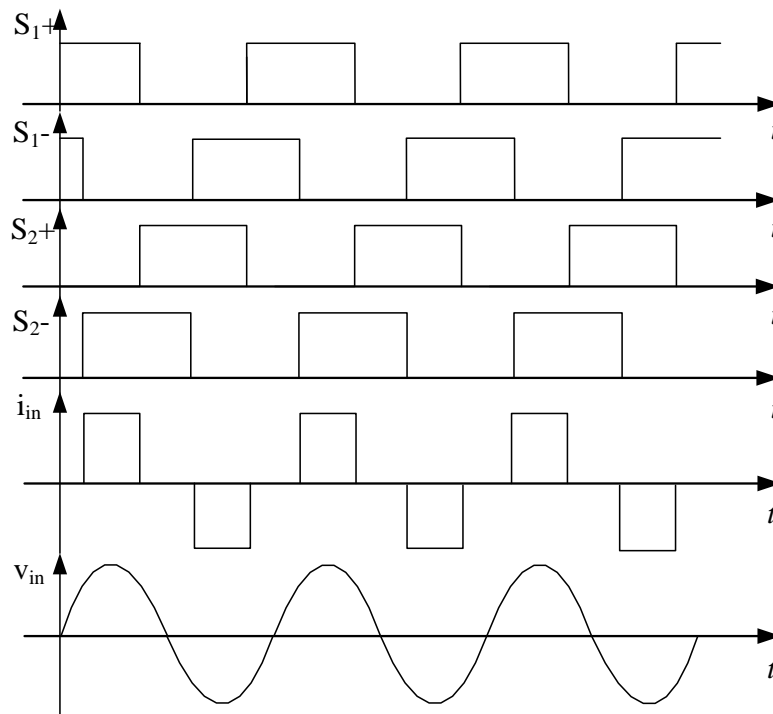
Figure 2-6: PWM phase shift operation of a full bridge current fed inverter

Apart from the fixed frequency control strategy, a variable frequency control strategy enables soft switching conditions for all the switches of a current fed inverter during operation. It allows the switches to follow the system resonance to ensure the input voltage

and current to the resonant frequency is in phase. Here the zero voltage switching frequency can be approximately expressed as [98]:

$$f = \frac{1}{2\pi\sqrt{LC}}\sqrt{1 - \frac{1}{Q^2}} \qquad\qquad (2\text{-}2)$$

where Q is the quality factor. A special attention for a current fed inverter is that at least one of the switches has to be conducted to maintain the current flow. The switch transitions have to be at the zero voltage switching frequency. Failing to achieve ZVS operation will result in shorting of the resonant capacitor and the occurrence of a large over-current.

In comparison, the push pull configuration has a similar performance to the full bridge configuration, except for the splitting transformer. It has a very good feature for IPT applications because its resonant voltage is twice that of the full bridge owing to the action of the splitting transformer. This enables the push pull inverter to drive a longer track or a larger coil. Another good feature of the push pull topology is that no isolated or high/low side gate drive is needed because the two switches used have a common ground. The phase splitting transformer basically divides the DC current in two halves, and the peak output voltage from inverting network can be expressed as [57]:

$$\hat{V}_{in} = \pi V_{DC} \qquad\qquad (2\text{-}3)$$

This means the resonant voltage is proportional to the DC input with the variable frequency control. By controlling the DC input voltage using a DC-DC buck converter, the output resonant voltage, and consequently the track current can be controlled.

In addition to a traditional push pull inverter, many new inverter structures have been developed. Figure 2-7 shows a self-sustained push pull inverter without using an external controller to drive the switches.
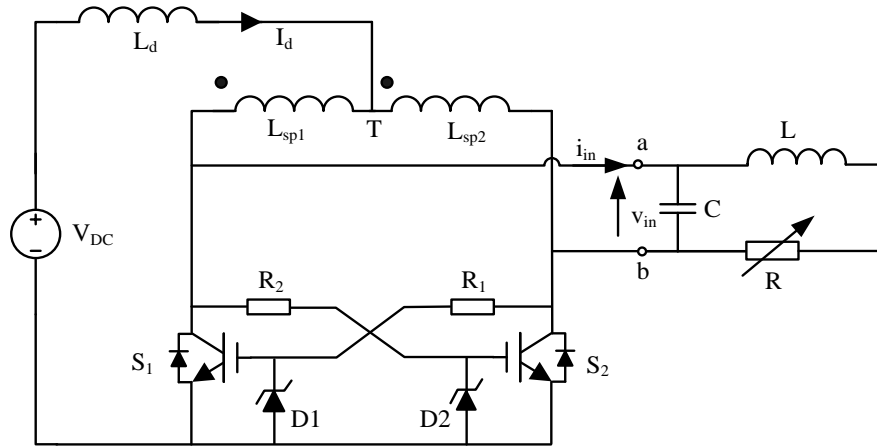
Figure 2-7: Self-sustained push pull resonant inverter without external controller

As shown, only two Zenar diodes and two resistors are connected to drive the switches. No extra detection and control circuit is needed. This inverter is essentially an autonomous system. However, if high resonant current is required, the high voltage over the resonant capacitor causes the voltage drop at the resistors to be high, resulting in high losses. Therefore such a drawback limits the self-sustained inverter to low power applications. Moreover, because no power control can be achieved by the switching network of the self-sustained inverter, an extra power control stage may be required if power flow control is needed. System bifurcation problems associated to parallel tuned inverters also exist for such a self-sustained inverter. In addition, a special startup circuit with ramping input voltage may be needed to reduce the current overshoot at start up [99].

2.3.2   *Voltage fed G2 power inverter*

Figure 2-8 shows both voltage fed full bridge and half-bridge topologies. The full bridge configuration consists of four semiconductor switches. However, the half-bridge topology employs two capacitors on each leg instead of the switches. It is simpler, but needs more passive components compared to the full bridge topology. Because the half bridge can only supply $\pm V_{DC}/2$ (half of the input voltage), the power capability is lower compared to the full bridge configuration.
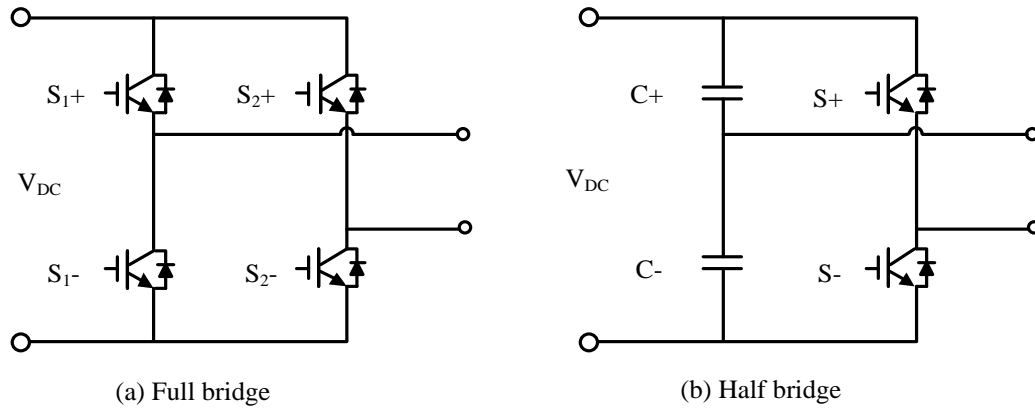
Figure 2-8: Voltage fed switching network topologies

In practice, the output high frequency inverting voltage cannot be arbitrarily connected to a voltage source type load, and therefore the load type of the voltage fed inverter has to be purely resistive or have a current sourced property, e.g. a series tuned resonant tank. A typical voltage fed power supply for high frequency IPT applications is shown in Figure 2-9. It comprises a DC voltage source, full bridge inverting network, track, and its tuning capacitors.
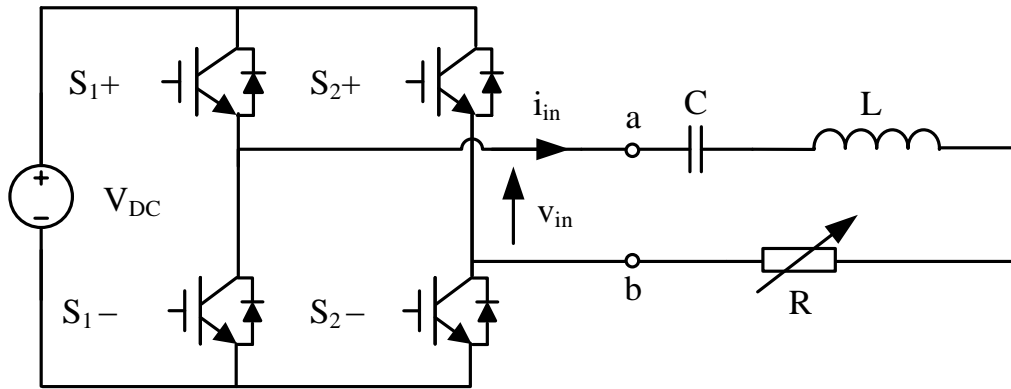
Figure 2-9: A typical voltage fed high frequency inverter

In order to generate a high frequency current in the track, fixed frequency operation is commonly used in this voltage fed G2 power inverter to force the switches to operate at a predefined frequency of the resonant tank [100]. Similar to a current fed G1 power converter, the fixed frequency operation of the semiconductor devices for the voltage fed G2 inverters will also lead to three different operating states in terms of the inverting voltage and resonant current as shown in Figure 2-10. Ideally, if the switches operate

exactly at the zero current crossing points as shown in Figure 2-10 (a), the inverter voltage and the current are in phase; and there should be no switching losses.

However, practically such ZCS operation conditions are difficult to achieve by the simple fixing frequency switching strategy. This is because the actual resonant frequency of track current may drift due to variations in one or more of the circuit parameters. Therefore, a leading or lagging angle between the square wave inverter voltage and the output current will exist as shown in Figure 2-10 (b) and (c).

(a)v_{in} and i_{in} in phase

(b)v_{in} leading i_{in}

(c)v_{in} lagging i_{in}

(d)Phase shift
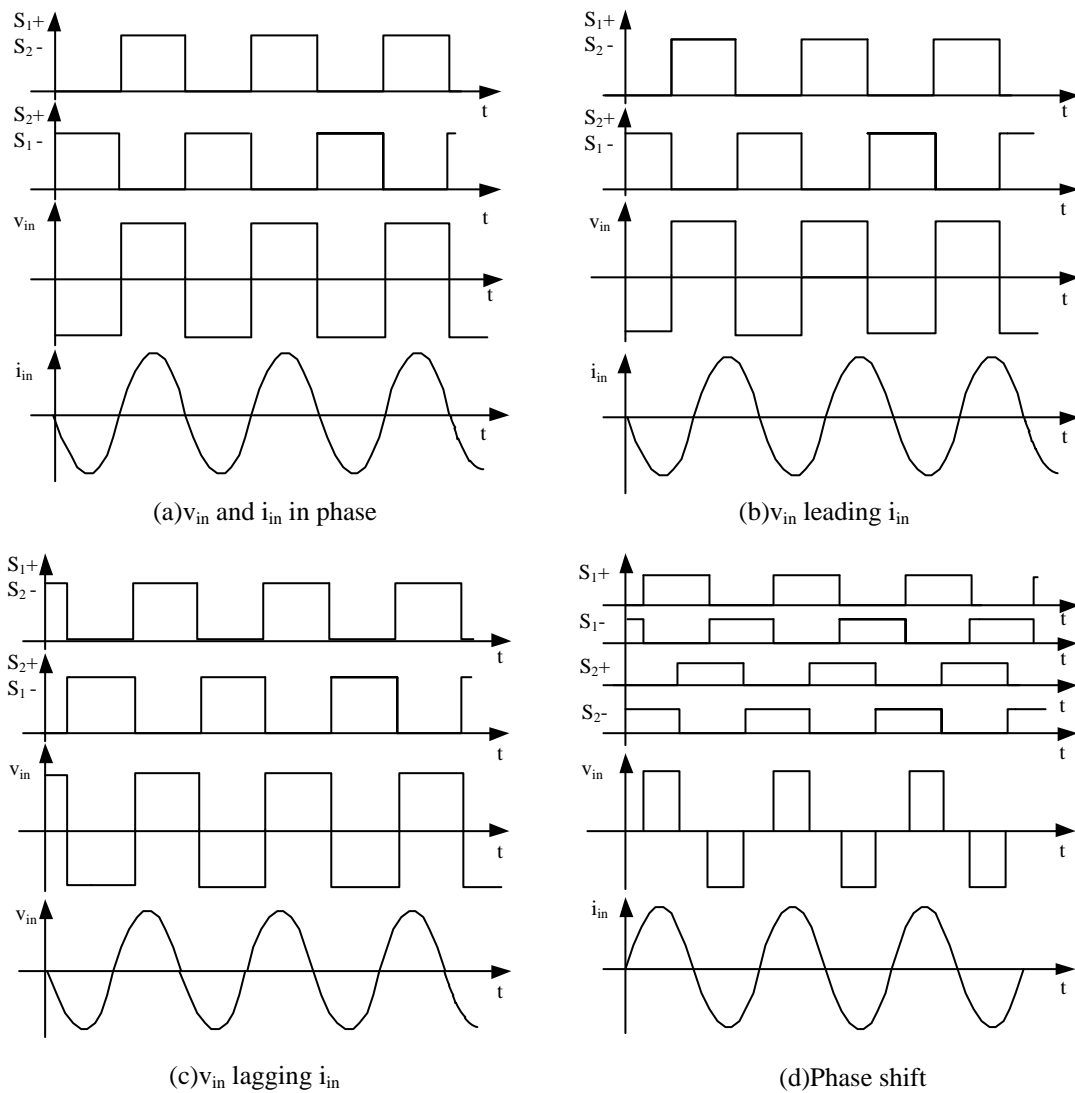
Figure 2-10: Switching state of fixed frequency switching operation

Although the fixed frequency control strategy is very simple and easy to implement, operation under hard switching results in high switch losses and EMI. In addition, the

fixed frequency operation has additional difficulties in accomplishing the magnitude control of the output current, unless phase shift control strategy is applied.

In order to realize the current magnitude control under a fixed frequency operation, the phase shift control is also commonly used for voltage fed inverters [101]. The phase shift control strategy developed for the voltage fed G2 inverters is different from that of the current fed G1 inverter. Here, G2 inverter controls the phase angle of either the two upper or the two lower switches. A typical switching operation of a series tuned full bridge inverter under the phase shift control is shown in Figure 2-10 (d). It can be seen that by controlling the phase shift angle ϕ of the switches, the square wave inverter voltage v_{in} on the track can be regulated.

If the switches pairs S_1+ and S_2+ are completely out of phase, the phase shift angle is 180 degrees, and the output voltage will reach their maximum value to obtain the maximum track current. Opposite to this, if both the upper switch pairs S_1+ and S_2+ are totally in phase (S_1- and S_2- are also in phase as well), the phase angle is zero degree. There is no output voltage applied to the resonant track, and the track current will eventually become zero as well. In consequence, continuous phase shift control method is able to regulate the output magnitude of the current. The relationship between the input voltage and the output voltage can be expressed as:

$$V = \frac{4}{\pi\sqrt{2}} V_{DC} \sin\left(\frac{\phi}{2}\right) \tag{2-4}$$

As S_1+ and S_1- are switched on after the zero crossing point of the current, while S_2+ and S_2- are switched off before the zero crossing of the current, then there are no turn-off losses on S_1+ and S_1-, and no turn-on losses on S_2+ and S_2-. Therefore, soft switching operation is not fully achieved by such a control method. To achieve soft switching for these switch pairs, a small parallel soft switching capacitor is normally employed [16]. Due to the charging and discharging of the soft switching capacitors, the switching operation occurs at either zero voltage or zero current instants so that the switching losses are eliminated. However, due to the additional components added, the final system becomes complicated to design and control.

Full resonant G2 inverters with variable frequency control have been investigated to achieve soft switching. With such variable frequency operation, the switching frequency is allowed to follow the natural resonance. Consequently, a full ZCS soft switching operation can be achieved.

While a front-end inverter could be used to regulate the input voltage and then the track current, in practice an alternative approach is a quantum inverter that uses an integral cycle control method to control the magnitude of the high frequency current by generating a series of voltage pulses in or out of phase with the resonant current on a half cycle basis [102]. Apart from this, by switching the system to hop among its multiple soft switching operating points, current magnitude regulation can be also achieved. The advantage of using variable frequency control is that soft switching condition can be achieved and the efficiency can be improved. But the variable frequency control methods of a full resonant G2 power supply cannot cope with system frequency variation unless a frequency stabilization approach is applied.

2.3.3 *Voltage fed G3 power inverter*

A voltage fed LCL resonant G3 inverter is one of the widely used topologies in IPT systems, especially for high power applications [96, 103, 104]. The voltage fed LCL power inverter improves the performance of the G2 inverter discussed earlier by adding an LC filter into the track. A typical voltage fed G3 power inverter is shown in Figure 2-11.
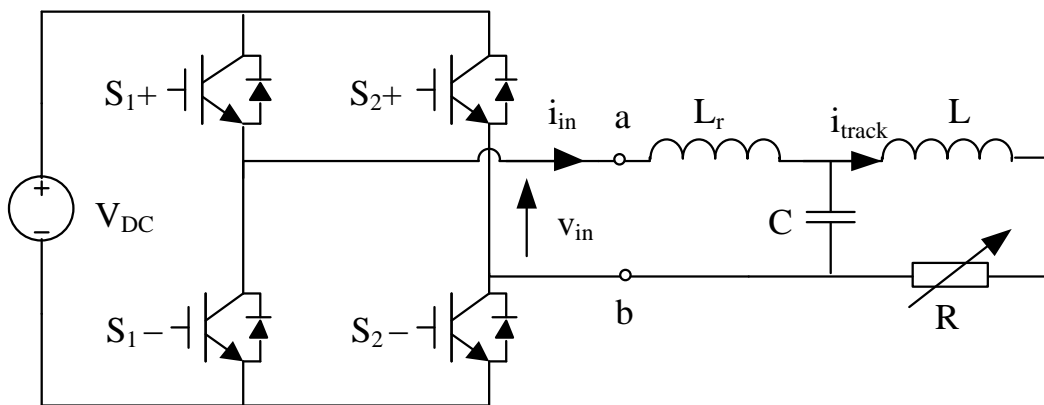
Figure 2-11: A typical structure of a voltage fed LCL inverter

Fixed frequency control can also be used for this power inverter. The typical fixed frequency operation of an LCL power inverter is shown in Figure 2-12.
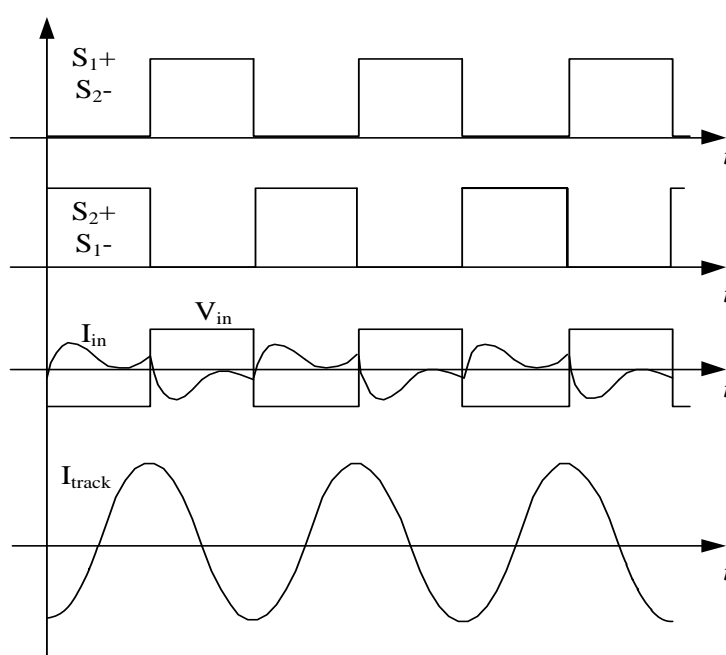
Figure 2-12: Typical operation waveforms of LCL resonant inverter

One of the good features of the voltage fed G3 is that the track current does not flow through the semiconductor switches as only the real power is supplied by the inverting network. In addition, there is no bifurcation problem associated with this inverter under fixed frequency switching control. In consequence, switching losses are low compared to the voltage fed G2 inverter at light load. However, as shown in Figure 2-12, the disadvantage is that the fixed frequency hard switching operations make the input current of the LCL inverter very poor. As a result the switching stress and power losses can be high.

A similar phase shift control method used in a series tuned G2 voltage fed power inverter can be adapted to regulate the output current for an LCL resonant inverter [105]. The phase shift control is also used here to control the inverter voltage and current under hard switching conditions. An improved switching method is proposed in [96]. It operates the inverter current in a discontinuous mode, by which the inverter is switched so that the inverter current drops to zero and stays there for a finite period during each half cycle. A partially variable frequency switching control method to achieve ZCS is proposed as well in [96]. Here the switches are controlled to ensure that the inverter voltage always has the same polarity as the input resonant current. By controlling the phase shift angle of

individual switches in the inverting network, it is possible to control the magnitude of the inverter input current and consequently the track current. This discontinuous mode control philosophy was shown to reduce the required VA rating of the power supply as well as the turn-on losses, but required a complex design procedure.

If the switches are controlled to maintain the resonance of the input current to the LCL network, the G3 inverter can also operate under continuous current mode at another operating frequency [51, 106]. Using such a switching strategy, the switching losses are virtually non-existent due to the soft switching. As a consequence, the system performance will be different. A large inverter current occurs because the low impedance in a natural resonant frequency of the whole LCL tuning configuration.

2.3.4   Current fed G3 power inverter

The current fed G3 power inverter is based on modification of G1 power supply. The current fed G3 converter also requires a parallel capacitor first in order to avoid voltage overshoots caused by sudden changes in the direction of the inverting current [16]. Following such a principle, a CCL current fed inverter can be developed, where a capacitor is in parallel with a series tuned LC circuit. It is the dual of the voltage fed LCL inverter. In addition, if another LC tuning circuit is added to form a tuning π network as shown in Figure 2-13 below and proposed in [16], the inverter performs even better for IPT systems. Advantages of using the π network compensation is that unity power factor can be obtained under fixed frequency operation. In addition, this π network also functions as a band-pass filter to ensure low distortion in the track current. Similar to normal current fed inverters, variable frequency operation can be used, but the ZCS operation frequency may drift away from the nominal resonant frequency. Therefore, a more complicated performance due to the high order nature of the circuit increases the design process complexity, and can lead to unpredictable results, if care is not taken in design and operation.
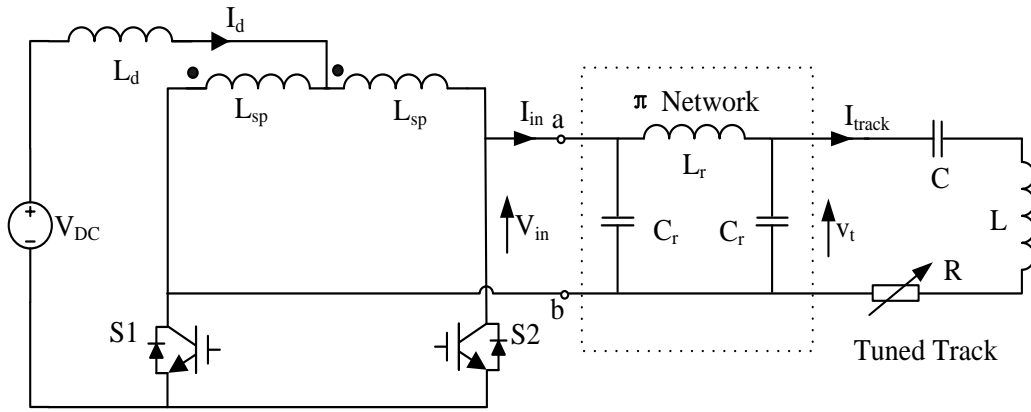
Figure 2-13: Basic structure of current fed G3 power inverter

2.3.5   *Single switch Class-E inverter*

The class-E inverter topology with a single switch offers an alternative to generate high frequency current for IPT applications. A typical structure of the class E converter is shown in Figure 2-1.
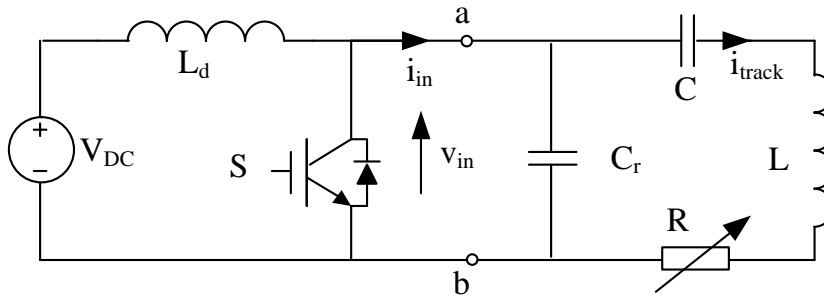
Figure 2-14: A typical structure of Class-E converter

A class E topology employs only one switch, a DC inductor L_d, capacitor C and a series tuned track. The DC inductor here can be considered to form a current source supplying constant current during circuit operation. The class E inverter has to operate at a fixed frequency for L_d to form a nearly constant current source [107]. The circuit can operate at zero voltage switching over a limited range of load and the voltage stress of the switch can be as high as 3.5 times of the input DC voltage [108]. Therefore, the class E inverter is not suitable for high power IPT applications. In addition, special consideration is required in designing the controller to match the resonant frequency, because of the two different resonant frequencies by a tuned L_d and C_r or a tuned L and C [109]. An advantage of such

a class E structure is that the switching control strategy is simple because of the fixed frequency operation and control of only one switch. Consequently the controller design can be very simple. Fewer component counts, light weight, compact size, and high frequency operation make it a popular choice for low power applications [110, 111].

2.4 AC-AC Conversion Technologies

In the above section it has been shown that most practical IPT systems rely on a two stage AC-DC-AC converter, where the AC-DC rectifier and the DC-AC inverter are decoupled by an energy storage element. Theoretically, this two stage conversion process can be reduced to one single conversion stage (direct AC-AC) through the use of a matrix converter. This type of converter uses bi-directional switches to conduct and block the current flow in two directions as required. Figure 2-15 shows a basic structure of an AC-AC matrix converter with an arbitrary number of inputs and outputs.
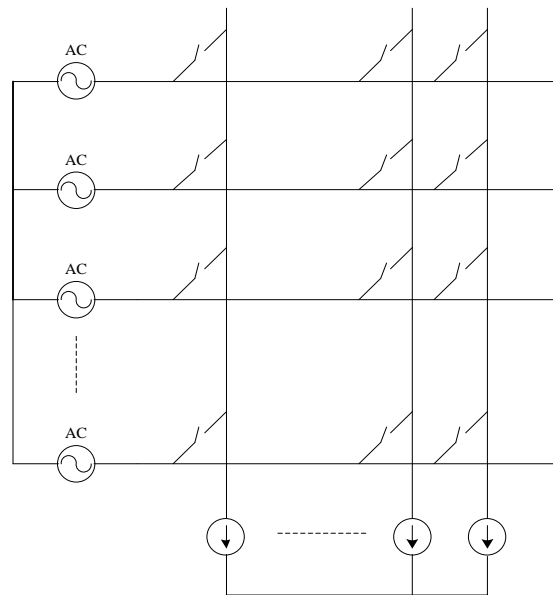
Figure 2-15: A basic structure of an AC-AC matrix converter [112]

Due to the lack of power storage components within the matrix converter, the output power must be equal to the input power at all times, assuming the switches have zero loss. The frequency at the input side and the output side are however independent. The restriction on the converter operation is that if each input appears as a voltage source, then each output must be in the form of a current source, or vice versa. The circuit is arranged

such that any output line of the converter can be connected to any input line. To illustrate the basic AC-AC conversion concept, a simplest single phase AC-AC matrix converter is shown in Figure 2-16.
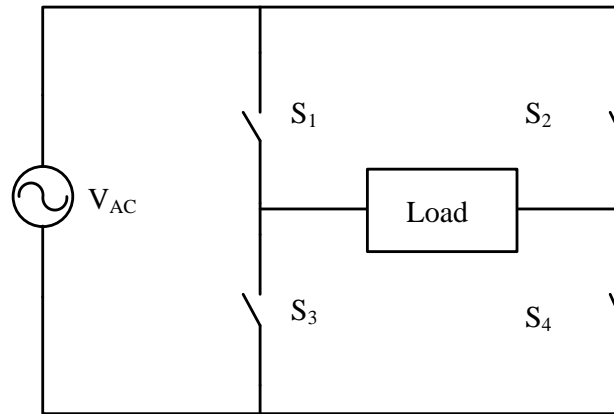
Figure 2-16: A simple single phase AC-AC matrix converter

2.4.1   AC switches

Switches S_1 to S_4 in Figure 2-16 are bi-directionally controllable and conductible semiconductor switches. To date, fast AC switches have not been commercially available. Figure 2-17 shows three common methods of forming ideal AC switches using available DC semiconductor switches. The first configuration (Figure 2-17 (a)) combines four fast diodes in a full bridge configuration and an active switch; the second configuration (Figure 2-17 (b)) employs two fast diodes and two active switches in a parallel connection; the third configuration (Figure 2-17 (c)) utilizes two switches in a series connection.

Each of these configurations has advantages and disadvantages. For instance, the gate controller is simple for the first one, because only one semiconductor switch is required to be driven. The second and the third options have the advantage of allowing the individual control of each switch. The voltage drop for all these combined switches is however high, compared to a single switch. In addition the resultant conduction losses are high. Overall, trade-offs are needed in selecting power switches between the application requirements and the properties of the actual switching devices.

(a)   (b)   (c)
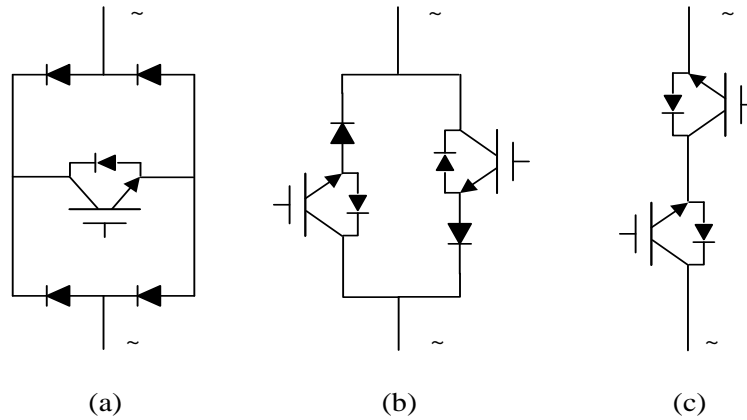
Figure 2-17: Combined bi-directional controllable ac switches

2.4.2 Control methods

In order to generate power at high frequency and transfer it to the load, the driver circuit associated to switches can be different, but generally it is simply required to generate the required high frequency gate signals for the switches. In the configuration shown in Figure 2-16, if only the two diagonal switches are on and off at any time and the AC output and the AC input are synchronized, as the switching frequency increases, the frequency of the output will also increase.

Figure 2-18 illustrates the conducting states of the switches of the single phase matrix converter with different input voltage polarities. The relationship between the AC input and the high frequency output is shown in Figure 2-19, where the output frequency that doubles and triples the input frequency is illustrated as an example. In order to generate a high frequency AC current or voltage, the switches need to operate in such a way that they operate at a high frequency to synchronize the AC source cycles and output cycles for different load types all the time.

(a) Input in the positive cycle   (b) Input in the negative cycle
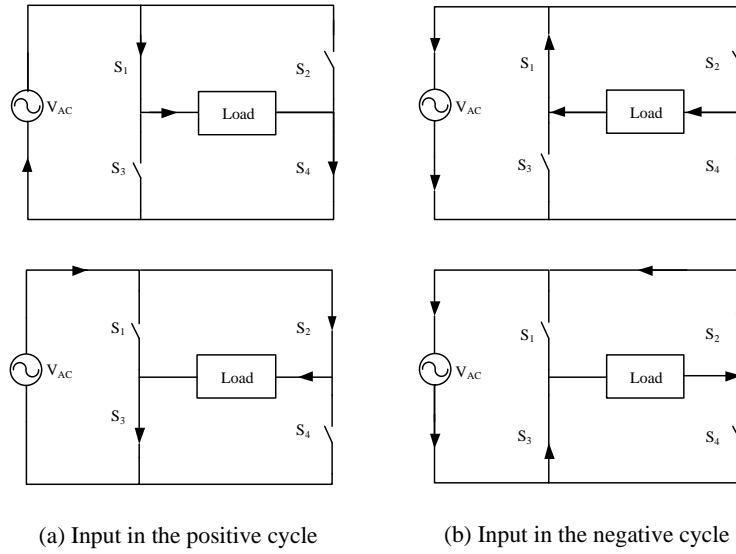
Figure 2-18: The state of the switches at different input polarities
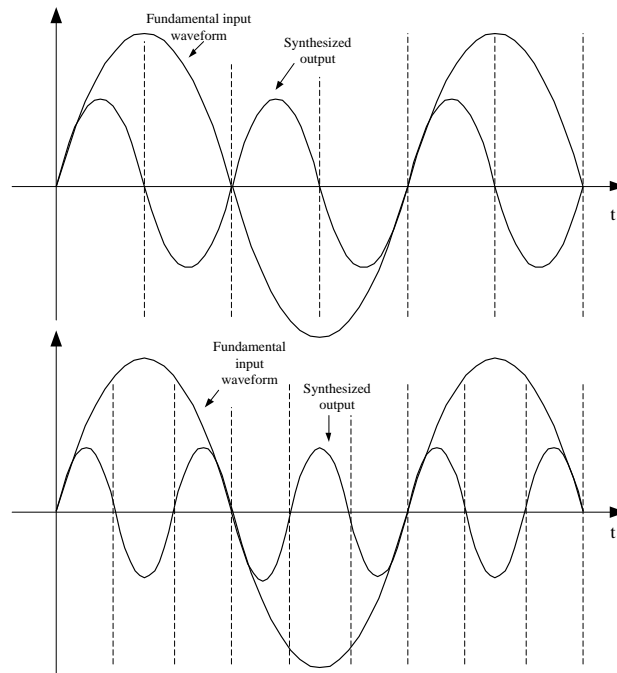
Figure 2-19: The relationship of the input waveform and the output waveform

Based on such a method, a fixed frequency PWM switching strategy with switching commutation has been reported that drives a three phase to single phase matrix converter for induction heating applications [113]. However, the converter configuration is very complicated. The generated PWM switching sequences are very complex at high

frequency to commutate the switches during zero crossing. In order to implement the switching commutation, the compromise of the fixed frequency operation leads to a hard switching operation. Moreover, the magnitude of the current was found to be uncontrollable, unless a more complicated control is applied.

In general, the circuit transient process involved in a high frequency matrix converter is normally complex. The switching control and commutation are very complicated. Therefore, the complicacy of the control and the switch configuration makes a direct AC-AC conversion difficult to be directly used in practical IPT applications, unless special structure and control is applied. To overcome the problems, in this thesis, a simple matrix converter suitable for IPT systems using circuit oscillation and energy injection control will be investigated.

2.5 Summary

A general overview of the technologies applied in high frequency power converters for IPT systems was presented in this chapter. Several types of commonly used high frequency converter topologies and the control strategies were reviewed.

DC-AC inverters are the most widely used for a range of applications. Various developments labeled generations 1, 2 and 3 have been developed. G1 and G2 are based on typical current fed and voltage fed topologies respectively. G3 topologies are improved versions, which use LCL T network in voltage fed configuration or π network in the typical current fed switching network. In addition, a class E structure was discussed, which is common in low power applications. Each topology and control strategy has its own advantages and disadvantages. Fixed frequency often results in high switching losses. Soft switching is good for achieving high power efficiencies and low EMI. But the circuit transient process involved in these types of power supplies is normally very complex and difficult to analyze.

A matrix converter can be developed to provide a direct AC-AC conversion without a DC link. But synchronizing the operation of the switches between the instantaneous input and output can be very difficult, and the output waveform quality is usually poor due to the complicated switching combinations required to shape the waveforms. Furthermore, the

circuit transient process involved in matrix converters is normally complex. The difficulties involved in the switching synchronization and the magnitude regulation of the high frequency output make such matrix converters difficult to use in practical IPT applications.

In conclusion, although DC-AC inverters and AC-AC matrix converters are available for high frequency applications, they have different drawbacks in generating high frequency currents for IPT systems, such as difficulties in implementation, poor output waveforms, or high switching losses, etc. Therefore research and development of new types of high frequency converters is still necessary. The following chapters discuss a range of converters based on circuit free oscillation and energy injection concept suitable for IPT systems.

Chapter 3

High Frequency DC-AC Inverters Based on Energy Injection Control

3.1 Introduction
3.2 Fundamentals of Energy Injection and
    Free Oscillation
3.3 A Full Bridge Energy Injection Inverter
3.4 Summary
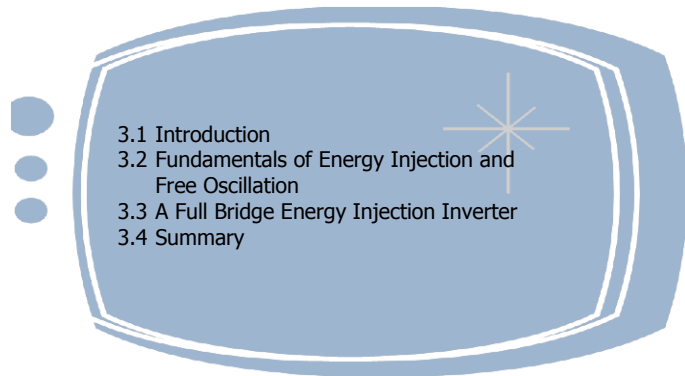
3.1 Introduction

In Chapter 2, the basic conversion concepts and existing high frequency power converters currently used in IPT systems have been presented. Each of them has clear advantages and drawbacks in terms of the topology and control strategy. Most of the resonant converters are operated in a forced switching manner [80, 85, 94]. As such, the switching frequency has to be equal to the fixed frequency.

In this chapter, a new concept of energy injection and free oscillation is introduced. According to this concept, a new conversion method is proposed based on high frequency circuit resonance. Some possible topologies and their related control methods are developed to generate high frequency track currents using low switching frequency for IPT applications.

3.2 Fundamentals of Energy Injection and Free Oscillation

Most of the existing converters for IPT applications are resonant converters, where the track is tuned with one or more reactive components in series, parallel or hybrid connection. Regardless of the tuning method, if a resonant tank is oscillatory, even without

excitation, a resonant current will oscillate freely provided some energy is stored initially in the resonant tank. A simple free oscillation path can be naturally formed by connecting a capacitor to a track inductor. This can be achieved in many ways using a switching network. However, special attention is required in designing such a network to achieve energy injection when the power source is taken into consideration. As stated in Chapter 2, if the input source is a voltage type, it can only inject energy into a resonant network in a current format. The switching network only allows an energy injection when the capacitor and the track inductor are in series connection. Figure 3-1 (a) shows a basic configuration of a voltage sourced energy injection and free oscillation inverter. It comprises a power supply, a switching network and a resonant tank consisting of a track inductor L, a capacitor C and a resistor R.
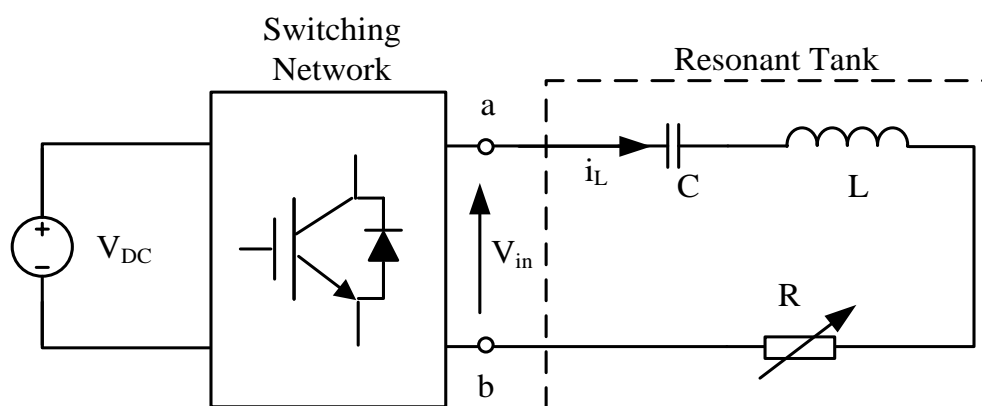
Figure 3-1: Principle diagram of injection method of voltage source.

The inverter has two operating modes: energy injection and free oscillation. When terminals a and b are connected to the power source by the switching network during a suitable period, energy can be injected into the resonant tank. However, when the terminals a and b are shorted by the switching network, the track inductor L, its tuning capacitor C and the resistor R form a free oscillation network, which is decoupled from the power supply. The stored energy in the closed path of a resonant tank will oscillate in the form of an electric field in the capacitor and a magnetic field in the inductor, and finally will be consumed by the equivalent resistance, which represents the load and the ESR. To maintain the required energy level in the resonant tank for sustained oscillation and energy transfer to any attached loads, more energy is required to pump into the tank by reconfiguring the switch network to connect to the power source. From an energy balance

point of view, such an operation based on discrete energy injection and free oscillation control is very different from normal voltage or current fed inverters. Therefore, the controller design and performance of the inverters based on this approach are very different from other traditional controllers as well.

3.2.1   Structure and operation

Figure 3-2 shows a simple primary power inverter based on the proposed free oscillation and energy injection concept for IPT systems. The overall primary inverter simply comprises two semiconductor switches, which can be MOSFETs or IGBTs with anti-parallel body diodes, and a series resonant circuit consisting of an equivalent track inductor L, a capacitor C, and an equivalent resistor R.
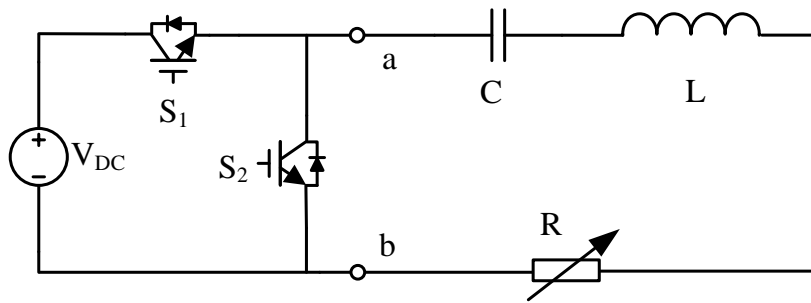
Figure 3-2: A two switches energy injection inverter

The basic operation of the inverter is shown in Figure 3-3. Initially, switch S_1 and S_2 are all in their off state; there is no electric and magnetic energy stored in the tuned track loop/coil. The voltage across C and the current in the track loop/coil are all zero. When S_1 is controlled on, the source voltage (V_{DC}) is applied to the resonant track. Consequently, new energy is injected into the track. If S_1 is turned off and S_2 is turned on, the current freely oscillates in the track loop/coil and the energy transfers indefinitely between C and L assuming there is no load to damp the oscillation. In practice however, damping does exist in the form of the load or the circuit loss elements (such as the ESR of the track); causing the energy in track loop/coil to eventually be consumed. If new energy is injected into the resonant tank periodically to replenish the energy consumed, the resonant current in the track loop/coil can be maintained.

(a) Energy injection state

(b) Free oscillation state
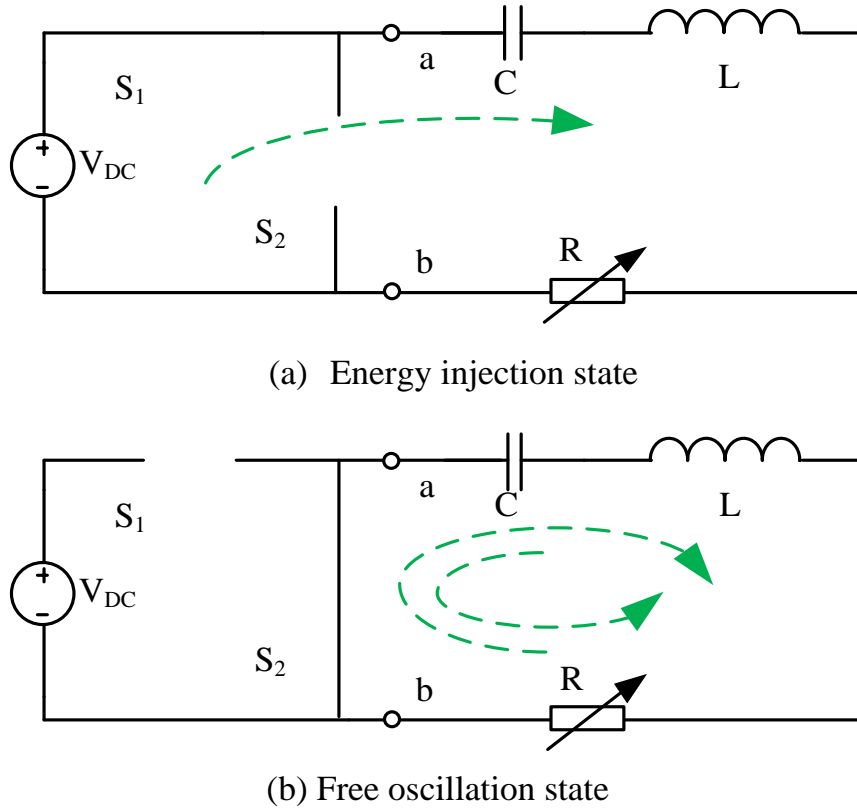
Figure 3-3: Basic operating states of the half bridge inverter

3.2.2   Steady state analysis

The input voltage to the resonant tank can be defined as:

$$\begin{cases} V_{DC} & Injection \\ 0 & Oscillation \end{cases} \tag{3-1}$$

There are two individual operating conditions during the control of the proposed inverter: free oscillation and energy injection. According to Kirchhoff's voltage law (KVL), second order differential equations can be obtained for the free oscillation states as:

$$\begin{cases} L\dfrac{di_L}{dt} + Ri_L + v_C = 0 \\ i_L = C\dfrac{dv_C}{dt} \end{cases} \tag{3-2}$$

Similarly, second order differential equations can also be obtained for the energy injection states as:

$$\begin{cases} L\dfrac{di_L}{dt} + Ri_L + v_C = V_{DC} \\ i_L = C\dfrac{dv_C}{dt} \end{cases} \tag{3-3}$$

Irrespective of the state of the circuit (free oscillation or energy injection), the differential equation in terms of the track current can be rewritten as:

$$LC\frac{d^2 i_L}{dt^2} + RC\frac{di_L}{dt} + i_L = 0 \tag{3-4}$$

The full solution to the track current during the energy injection states can be obtained as:

$$i_L(t) = \frac{V_{DC} - v_C(0)}{\omega L_L} e^{-\frac{t}{\tau}} \sin \omega t + i_L(0)\frac{\omega_0}{\omega} e^{-\frac{t}{\tau}} \cos(\omega t + \theta) \tag{3-5}$$

During the circuit free oscillation states, because the resonant tank is decoupled from the power supply, the solution of the track current therefore can be expressed without the input voltage term as:

$$i_L(t) = \frac{-v_C(0)}{\omega L} e^{-\frac{t}{\tau}} \sin \omega t + i_L(0)\frac{\omega_0}{\omega} e^{-\frac{t}{\tau}} \cos(\omega t + \theta) \tag{3-6}$$

where $v_C(0)$ and $i_L(0)$ are the initial voltage of the tuning capacitor and the initial current of track inductor. $\tau = 2L/R$ is the decay time constant, ω (the zero phase angle frequency of the resonant current) is determined by the circuit parameters, which can be further expressed by the following equation [16]:

$$\omega = \omega_0 \sqrt{1 - \zeta^2} = \omega_0 \sqrt{1 - \frac{1}{4Q^2}} \tag{3-7}$$

where ω_0 is the undamped natural frequency ($\omega_0 = 1/\sqrt{LC}$), which is determined by the inductance and capacitance of the resonant loop/coil, but it is independent of the load and ESR. ζ is the damping factor of the network, which can be expressed as:

$\zeta = R/2\sqrt{L/C} = 1/2Q$,while Q is the equivalent quality factor which can be defined as $Q = \omega_0 L/R = 1/2\zeta$, and the phase shift angle θ in equation (3-5) and equation (3-6) can be expressed as:

$$\theta = \arctan\left(\frac{1}{\omega\tau}\right) = \arctan\left(\frac{1}{2Q}\right) = \arctan(\zeta) \tag{3-8}$$

From equation (3-7) it can be seen that in order to make network oscillation occur, the damping factor ζ should be less than 1. Therefore, the quality factor Q must be greater than 0.5, otherwise the circuit will be over damped. It is easy to understand that a high Q will help the circuit to generate a high quality track current with lower distortion. In addition, a high Q primary track helps to store more energy at the resonant frequency, so a lower switching frequency can be designed to maintain the high resonant frequency.

If the switching transitions are controlled to occur at the zero current crossing points, so that zero current switching (ZCS) is achieved, then the initial current $i_L(0)$ is zero. The corresponding initial voltage of the tuning capacitor $v_C(0)$ will be around its peak value if the circuit Q is high. Under such a condition, the second term of equation (3-6) becomes zero, resulting in a simple current equation given by:

$$i_L(t) = \frac{-v_C(0)}{\omega L} e^{-\frac{t}{\tau}} \sin \omega t \tag{3-9}$$

And during energy injection, the track current can be expressed as:

$$i_L(t) = \frac{V_{DC} - v_C(0)}{\omega L} e^{-\frac{t}{\tau}} \sin \omega t \tag{3-10}$$

The amount of injected energy in each half cycle is determined by the magnitude of the input DC voltage, the track current, and the injection period [112]. Therefore it can be expressed as:

$$E_{in} = \int_0^{T_{in}} V_{DC} i_L(t) dt \tag{3-11}$$

where T_{in} is the energy injection period. If switch S_1 is on and S_2 is off during every positive half cycle of the track current, the maximum injection time period is achieved, and the fundamental voltage magnitude (in rms) can be given as:

$$V_{rms} = \frac{2}{\pi\sqrt{2}} V_{DC} \tag{3-12}$$

Consequently, the maximum current that can be achieved in the track with this maximum energy injection can be expressed as:

$$I_{rms} = \frac{\sqrt{2}V_{DC}}{\pi R} \tag{3-13}$$

where R is the total equivalent resistance of the primary circuit. Therefore the controllable range of the reference of the current for the half bridge topology is from zero to the maximum current described by equation (3-13), which corresponds to no energy injection and maximum possible energy injection respectively. Ignoring the harmonics, the maximum power that can be supplied by a given DC voltage source for the simplest half bridge structure can be obtained by I^2R and expressed as:

$$P_{max} = 0.2\frac{V_{DC}^2}{R} \tag{3-14}$$

3.3 A Full Bridge Energy Injection Inverter

3.3.1 *Inverter structure*

According to the above analysis, it can be seen that energy injection by a half bridge structure is only possible in one direction of the resonant current. Although the half bridge topology is simple and easy to control, dual side energy injection control would be better to allow energy to be injected to the resonant tank faster. Figure 3-4 shows such an improved inverter structure, which can achieve energy injection from both directions of the resonant current. Here S_1 and S_4 control the positive energy injection, and the negative energy injection control is achieved by S_2 and S_3 together. S_2 together with S_4 or S_1 together with S_3 can form a path for the current free oscillation. Actually there are many

different combinations of semiconductor switches to construct a switching network to achieve both the free oscillation and the energy injection control.
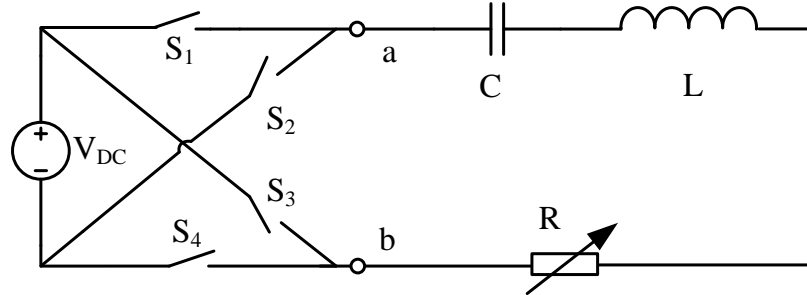
Figure 3-4: Bidirectional energy injection inverter structure

By utilizing the inherent anti-parallel body diodes of some MOSFETs or IGBTs, a full bridge switching network can be used to achieve the current free oscillation and bidirectional energy injection as shown in Figure 3-5.
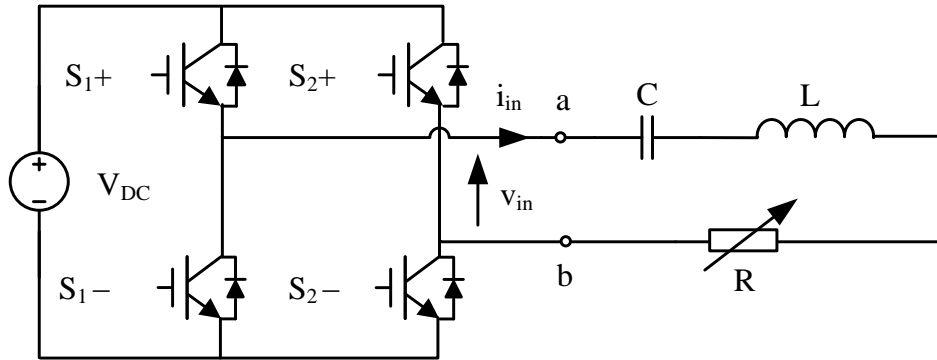
Figure 3-5: An energy injection inverter with full bridge topology

Although the structure of the proposed energy injection inverter is not much different to a conventional full bridge voltage fed resonant inverter, the control strategy of the proposed inverter is very different. Here, the switching network can be designed to control the energy injection in either one or both directions of the resonant current. The unique feature of the inversion method lies in the control of the resonant current to ensure proper energy

injection into the network if required. The inverters can be hard or soft switched, and the basic principle of controlling a full bridge inverter is similar to a half bridge inverter as discussed in the previous section. The energy injection is required to compensate for the power losses promptly and smoothly without significantly affecting the frequency and magnitude of the track current within the circuit.

3.3.2   *Operating principle of the full bridge topology*

As stated, the operation of the switches of the full bridge inverter is simply to maintain a constant energy in the primary track. Initially, the four semiconductor switches S_1+, S_1-, S_2+ and S_2- are all in their off state, there is no electric and magnetic energy stored in the resonant tank. As such, the voltage across C and the current in the track inductor L are all zero. The operation of the inverter can be divided into three states according to the outcome of their switching operation, being positive energy injection, negative energy injection and free oscillation.

➢ **Free oscillation**

The switch operation of free oscillation is to construct a close loop to allow current flowing freely. Due to the structure of a full bridge topology, there are two different methods that can form such a path.

If only the two upper switches S_1+ and S_2+ are turned off, while the two lower S_1- and S_2- are turned on, switches S_1-, S_2-, and their anti-parallel body diodes form a oscillation path to allow current freely flow as show in Figure 3-6(a).

(a) S_1-, S_2- on
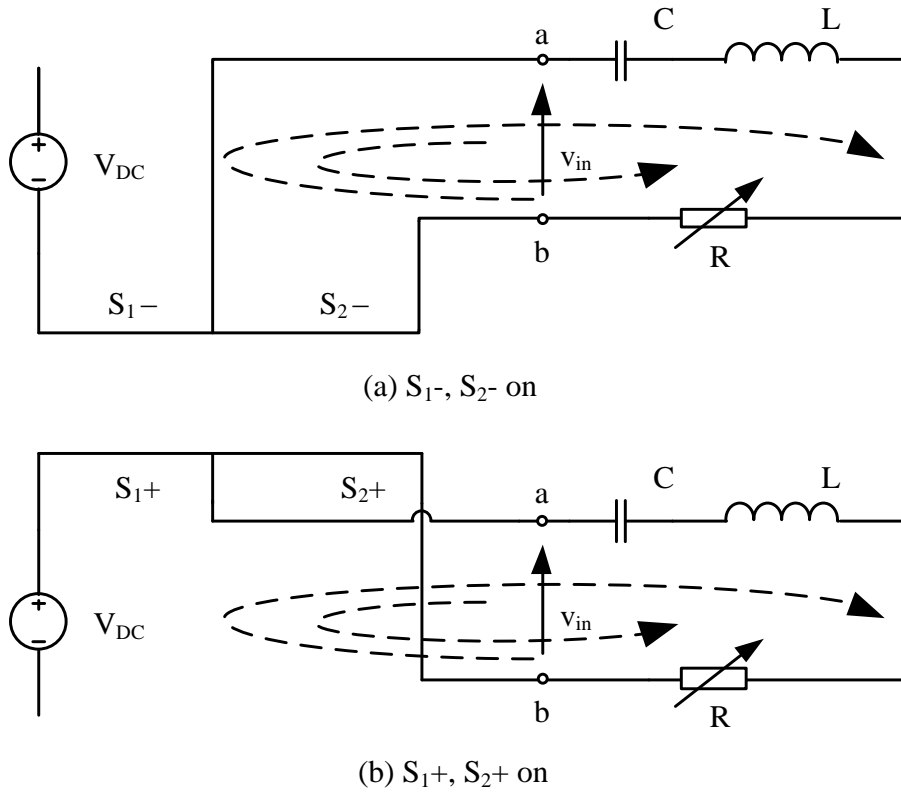
(b) S_1+, S_2+ on

Figure 3-6: Basic free oscillation operating states of the inverter

An energy injection path can also be formed by keeping switches S_1+and S_2+ on, and S_1- and S_2- off as shown in Figure 3-6(b). S_1-, S_2- and their anti-parallel body diodes construct a close loop.

During the circuit free oscillation, because the resonant tank is decoupled from the power supply, the solution of the track current therefore can be expressed without the input voltage term. It is same as that for a half bridge topology as described in equation (3-9).

➢ **Energy injection**

To inject energy in both directions, S_1+, S_2- is controlled to be on (S_2+, S_1- off) in positive cycle of the resonant current; or S_2+, S_1- is on (S_2+, S_1- off) in the negative cycle of the resonant current as shown in Figure 3-7(a) and (b) respectively.
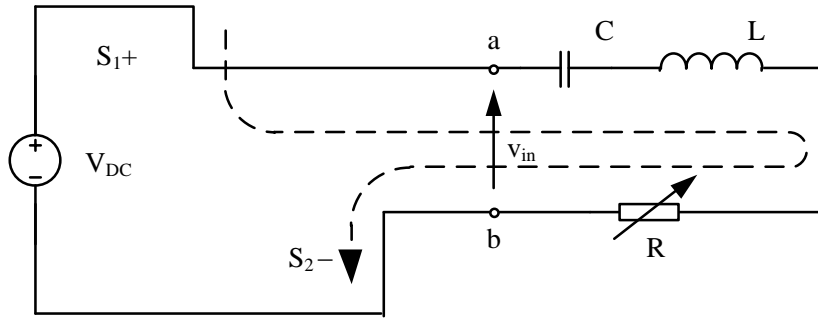
(a)   Energy injection state in positive cycle of
resonant current
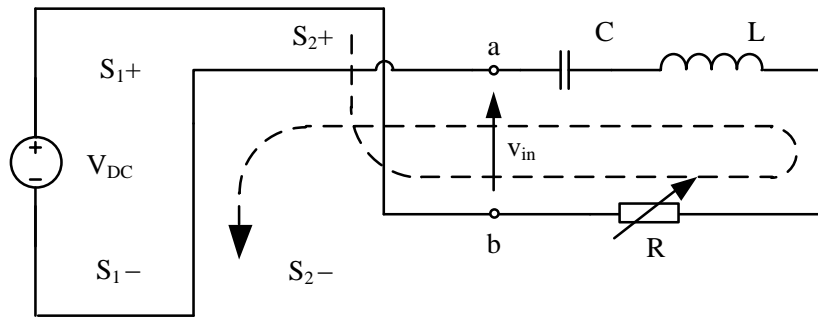
(a)   Energy injection state in negitive cycle of
resonant current

Figure 3-7: Basic energy injection operating states of the inverter

In fact, the operation of an inverter with a full bridge topology is similar to the half bridge topology. During the energy injection period the resonant circuit is connected to the power source V_{DC} with the current flowing in the same direction, so that the energy is brought into the network. Therefore, the voltage over the tuned track can either be positive or negative as:

$$v_{in}(t) = \begin{cases} V_{DC} & (\textit{Positive Energy Injection}) \\ -V_{DC} & (\textit{Negative Energy Injection}) \end{cases} \tag{3-15}$$

In the positive energy injection stages, if the switching transient is at the zero crossing points, the solution of the current can be expressed as:

$$i_L(t) = \frac{V_{DC} - v_C(0)}{\omega L} e^{-\frac{t}{\tau}} \sin \omega t \tag{3-16}$$

Similarly, if the energy injection happens when the input voltage is added to the track, and the track current is in negative direction, the solution of the current can be expressed as:

$$i_L(t) = \frac{-V_{DC} - v_C(0)}{\omega L} e^{-\frac{t}{\tau}} \sin \omega t \tag{3-17}$$

Note $v_C(0)$ is the instantaneous initial voltage. It is negative at positive zero current crossing transient (from low to high). It is positive at negative zero current crossing transient (from high to low). If energy is brought into the resonant tank in a fast and efficient manner to replenish the consumed energy, the resonant current in the track will be maintained at the free oscillation frequency. Therefore, the total electromagnetic energy of the resonant tank can be maintained and controlled., If energy is injected in each positive and negative cycle, the maximum power that can be supplied by a DC voltage source is achieved and can be expressed as:

$$P_{max} = \frac{8}{\pi^2} \frac{V_{DC}^2}{R} \tag{3-18}$$

Compared to equation (3-14), the full bridge inverter can supply four times more power than the half bridge with maximum energy injection. It is simply because a full bridge inverter can inject energy in both directions of the track current, while the half bridge topology can only inject energy in the positive direction. Therefore, the power range that can be controlled by a full bridge topology doubles that of a half bridge topology. Furthermore, the full bridge topology enables a faster dynamic response during startup or load variations because of the bidirectional injection.

3.3.3 Variable frequency ZCS control

A control strategy is developed in this section for the full bridge inverter. For the intended IPT application a high frequency primary track current is often required. Because the only major difference between the half and full bridge topologies is the control of the energy injection in either one or both directions of the track current respectively, the control strategy developed for a full bridge topology can be easily applied to a half bridge topology. Due to the features of resonance and discrete energy injection, the operating

period of the switches S_1+ and S_2+ is constrained by the direction of the track current and the requirement of the energy level in the resonant tank.

There are many switching technologies that can be applied to achieve a necessary control. The options include hard switching, soft switching, and combined hard/soft switching. Because full soft switching operation can generate good waveforms with reduced switching losses and EMI, this research focuses on soft switching control realized by ZCS operation, which is described in [94]. In the full bridge inverter shown in Figure 3-5, the actual ZCS frequency is not necessarily equal to the nominal natural resonant frequency of the oscillation circuit. Therefore, a fixed switching frequency controller is unable to follow the actual resonant frequency variation during operation, consequently the switches can experience high voltage/current stress, as well as high power losses and EMI when the load varies or the circuit parameters drift. To achieve a full soft switching operation, a variable frequency control method is proposed and developed in this research to allow the frequency variation, thus the actual circuit resonance is ensured and a reasonably good quality track current can be generated. From controller design point of view, allowance of variable frequency operation makes zero current switching easy to achieve during both energy injection and free oscillation states. Furthermore, such a control scheme helps to reduce the system cost, size and power efficiency due to maximum power factor operation resulting from the frequency variation. In practice, if the IPT system is properly designed with a large equivalent primary circuit quality factor Q (with the reflected components from secondary side taken into consideration), the actual frequency variation is very small during operation [73].

➢ **Soft-switched startup**

Owing to the circuit resonance, the startup of the inverter can also follow the resonance of the track current. Figure 3-8 shows the soft-switched startup process of the proposed inverter. Initially, all switches are in their off state, there is not electric and magnetic energy stored in the track loop/coil. The voltage across C and the current in the track loop/coil are all zero. When S_1+, S_2- are controlled on; and S_2+, S_1- are controlled off, the source voltage (V_{DC}) is applied to the resonant loop/coil and energy is injected into the track in the positive half cycle. After C is fully charged, a free oscillation path for the current can be formed, if S_1+,S_2+ are controlled off and S_2-,S_1- are turned on.
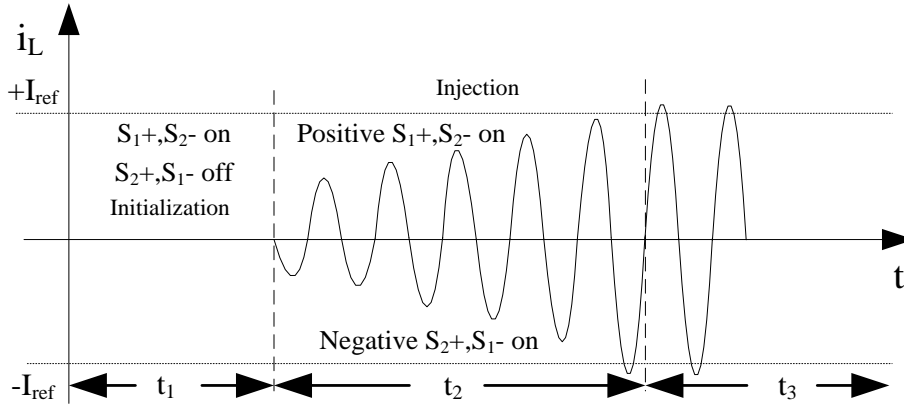
Figure 3-8: Soft switched startup process

➢ **Steady-state operation**

A control strategy that uses the current as the control variable to achieve ZCS operation in both the energy injection and free oscillation states is proposed. If the peak value of the track current in previous half cycle is always smaller than a predefined reference, energy injection will be controlled to occur in next half cycle. Otherwise, if the peak current in the previous half cycle is larger than the predefined reference, the free oscillation of the resonant circuit will be maintained. When this basic principle is applied to the full bridge inverter topology, the control strategy with reference to the track current is illustrated in Figure 3-9.
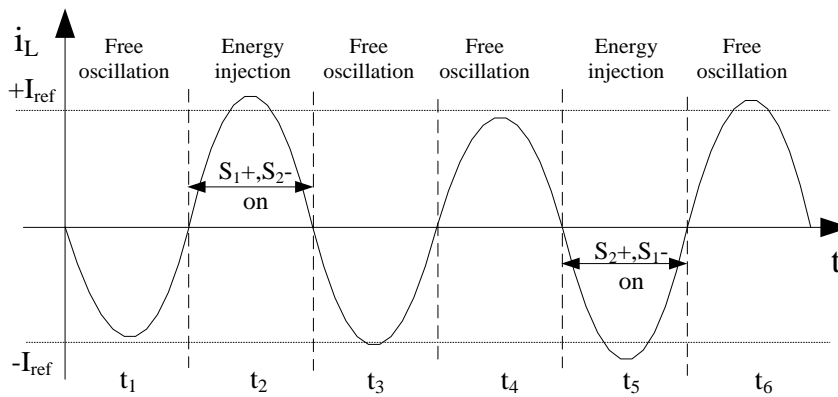
Figure 3-9: Steady state ZCS energy injection control strategy

Switches S_1+, S_2- are turned on at the zero crossing point when the track current in the network is positive and its peak value in the previous half cycle (t_1) is smaller than a

predefined threshold reference. The on state will be held until the current finishes its positive half cycle (t_2) and goes back to zero. Similarly S_2+, S_1- can be controlled on to allow energy injection in the negative cycles (t_5) of the track current. If the detected peak value of the track current is larger than the reference in a previous half cycle, S_1- and S_2- (or S_1+ and S_2+) will be kept on to maintain free oscillation. All the switches operate at either zero current crossings, so ZCS conditions are ensured. The detailed control of the inverter switches is shown in Table I. The flow chart of the control algorithm is shown in Figure 3-10.
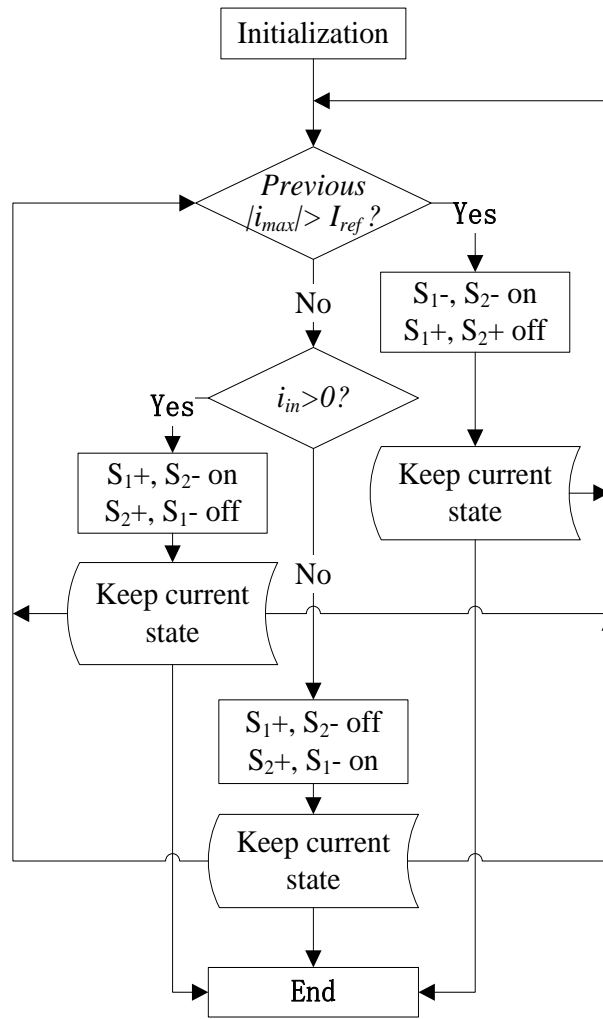
Figure 3-10: Flow chart of the control algorithm

Table 3-1: Basic control states of a full bridge inverter

Energy injection							
$i_L(t) > 0, \hat{i}_L/pre\frac{T}{2} < +I_{ref}$				$i_L(t) < 0, \hat{i}_L/pre\frac{T}{2} < -I_{ref}$			
S_1+	S_1-	S_2+	S_2-	S_1+	S_1-	S_2+	S_2-
on	off	on	off	on	off	on	off
Free oscillation							
$i_L(t) > 0, \hat{i}_L/pre\frac{T}{2} > +I_{ref}$				$i_L(t) < 0, \hat{i}_L/pre\frac{T}{2} > -I_{ref}$			
S_1+	S_1-	S_2+	S_2-	S_1+	S_1-	S_2+	S_2-
off	on	off	on	off	on	off	on

3.3.4 Current ripple analysis and discussion

As can be seen from the previous analysis, the energy injection and free oscillation control approach will introduce current ripples in the track. For analysis and design purposes, it is important to quantify the magnitude of the current ripple. Because the extent of the current ripple is load dependent, and it varies with the energy injection instants and different inverter topologies, it is very difficult to conduct accurate ripple analysis under all the operating conditions. However, a worst case analysis is possible to find the maximum and minimum currents, which quantify the worst ripple that an inverter can have.

As discussed, the control of the energy injection is based on the preset current reference. This reference is within the range from zero to the maximum current. Ideally, the maximum current of a proposed full bridge topology inverter is related to the parameters of the inverter and the input voltage, and it is achieved by full energy injection. The output voltage of a full bridge topology when added to the track, reaches its maximum value with the fundamental magnitude given by:

$$\hat{V}_{in} = \frac{4}{\pi} V_{DC} \qquad (3-19)$$

Therefore the maximum current reference that can be requested of the full bridge inverter can be calculated as:

$$I_{ref\_max} = \frac{4V_{DC}}{\pi R} \tag{3-20}$$

With a given reference lower than the value defined by equation (3-20), the current ripple occurs around the reference. Among different operation conditions, the maximum peak current i_{L_max} occurs under the condition when there is no load, and the current peak in the previous half cycle is slightly smaller than or just equal to the reference value I_{ref}, so that the energy is injected into the resonant network in the next half cycle. The current waveform under such a worst case condition is shown in Figure 3-11. It can be seen that the maximum current i_{L_max} appears in the following half cycle after the energy injection.
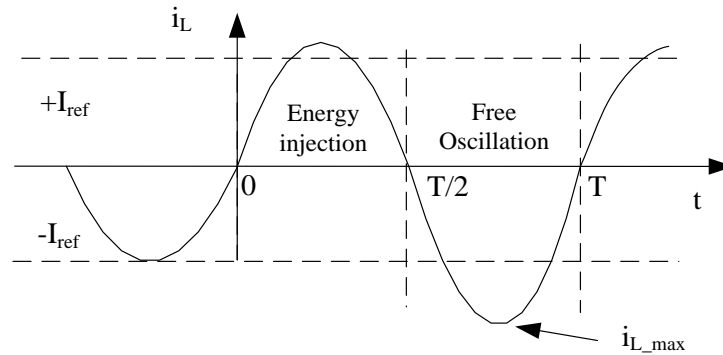
Figure 3-11: Maximum track current under worst case condition

Because there is no load, the capacitor voltage is zero when the track current is at its peak. As such, the total energy stored in the resonant circuit before the energy injection can be expressed as:

$$E_{store} = \frac{1}{2}LI_{ref}^{2} \tag{3-21}$$

After the half period energy injection, the total energy storage in the circuit becomes:

$$\frac{1}{2}L\hat{i}_{L\_max}^{2} = \frac{1}{2}LI_{ref}^{2} + E_{in} \tag{3-22}$$

The amount of injected energy is determined by the magnitude of the input DC voltage and the track current governed by equation (3-11), where (assuming ZCS operation is required) the period of the energy injection is half of the resonant period of the track current. According to equation (3-10), the maximum current during energy injection can be expressed as:

$$\overset{\wedge}{i_L} = \frac{V_{DC} - v_C(0)}{\omega L} e^{\frac{-T}{4\tau}} \tag{3-23}$$

where $v_C(0)$ is the initial value of the capacitor voltage at t=0, which can be determined by:

$$v_C(0) = \sqrt{\frac{L}{C}} I_{ref} \tag{3-24}$$

From equations (3-23) and (3-24), the injected energy in a half period can be expressed as:

$$E_{in} = V_{DC} \int_0^{\frac{T}{2}} i_L(t) dt = \frac{TV_{DC}(V_{DC} + \sqrt{\frac{L}{C}} I_{ref})}{\sqrt{\frac{L}{C}} \pi} \tag{3-25}$$

Substituting equation (3-25) into (3-22), the maximum current can be obtained and expressed as:

$$\overset{\wedge}{i_{L\_max}} = \sqrt{I_{ref}^2 + \frac{2TV_{DC}}{\pi} + \sqrt{\frac{C}{L}} \frac{2TV_{DC}^2}{\pi I_{ref}}} \tag{3-26}$$

Equation (3-26) shows that the worst case track current overshoot (above its reference value) is determined by the input voltage, the track current oscillation frequency, and the circuit parameters.

While the maximum current is caused by the energy injection at no load, the minimum current i_{L_min} is caused by circuit damping. The worst case scenario arises when the load is at its maximum, and the peak current is slightly larger than the reference value, so there is no injection in the next half cycle causing the current to decay. Starting from $i_L(0) = -I_{ref}$ and $v_C(0) = 0$, equation (3-6) can be further expressed as:

$$i_L(t) = -I_{ref} \frac{\omega_0}{\omega} e^{-\frac{t}{\tau}} \cos(\omega t + \theta) \tag{3-27}$$

Note that strictly speaking when the current is at its peak, the capacitor voltage is not exactly zero due to the existence of the load. But for inductive power transfer applications, the primary circuit Q is very high so the error caused by assuming it is zero will be very small.

For a full bridge topology, the current reaches the minimum value after a half period from the previous peak value, so i_{L_min} can be expressed as:

$$\hat{i}_{L\_min} = I_{ref} \frac{\omega_0}{\omega} e^{-\frac{RT}{4L}} \tag{3-28}$$

For a half bridge topology, the minimum current is worse, because energy can only be injected in positive half cycles. Even the current becomes smaller than I_{ref} in the first positive half cycle, the current damping will continue for another negative half cycle. In general, the worst case minimum track current (below than the reference current) is mainly determined by the load, the resonant frequency, and the circuit parameters.

3.3.5   *Simulation study*

To evaluate and investigate the proposed energy injection control strategy and the theoretical analysis, simulation studies were undertaken for the proposed full bridge inverter during startup, steady state and load variations using the PLECS toolbox in a MATLAB/Simulink environment. The simulation system circuit configuration and the schematic diagram are shown in Figure 3-12 (a) and (b) respectively. The parameters of the components are listed in Table 3-2.
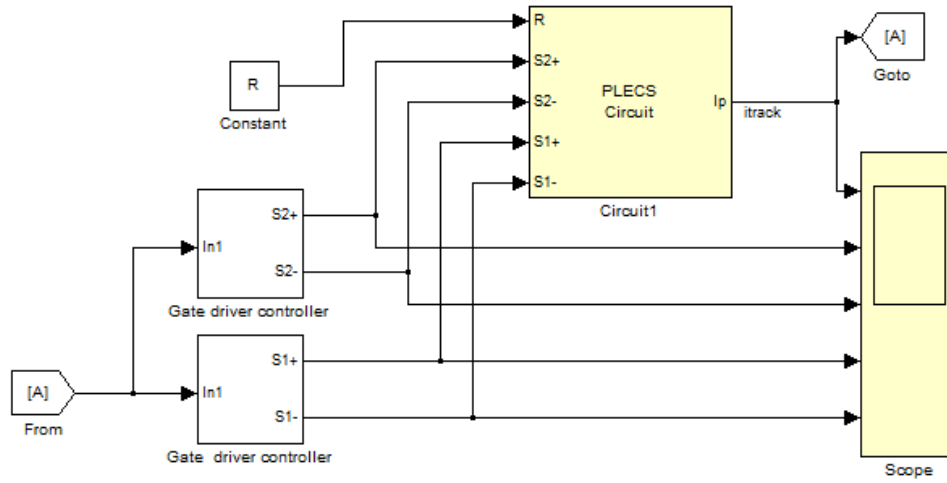
(a) simulation model of full bridge with energy injection control
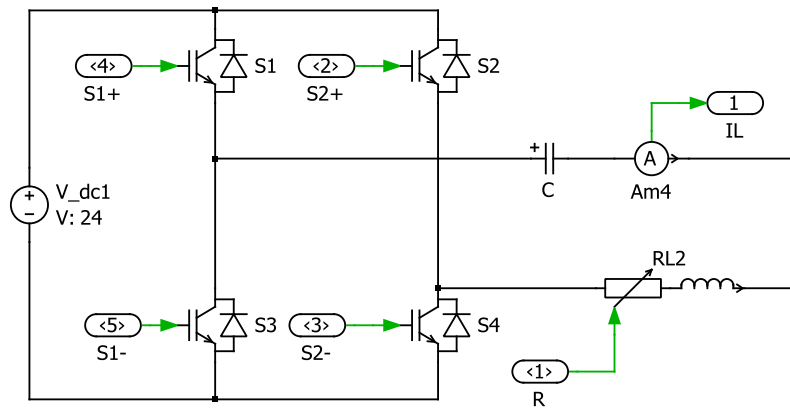
(b) PLECS circuit model

Figure 3-12: System configuration for simulation

In order to investigate the proposed conversion method, the control and the switching strategy, a simulation study was carried out focusing in particular on the startup transient. Figure 3-13 shows the simulation result of the track current and the switches gate driver signals under the proposed energy injection control without load (only ESR is present).

From Figure 3-13 it can be seen that S_1+ and S_2- are controlled on at the initial stage resulting in the series capacitor becoming fully charged and equal to the source voltage. After this, the upper two switches S_1+ and S_2+ are switched off, while switches S_1- and S_2- are turned on, thus a free oscillation path is formed with the track current flowing in the

negative direction. Once the first oscillation cycle is complete, the current increases gradually and reaches the reference after only a few cycles. In addition, there is an invisible overshoot during the startup phase. The maximum overshoot current is well limited by the last half cycle energy injection, where the previous maximum current is less than the reference. The maximum current overshoot in the half period energy injection can be quantified using the previous theoretical analysis for analyzing maximum current overshoot.

Table 3-2: Circuit components parameters

Notes	Symbol	Value
Input DC voltage	V_{DC}	24 V
Primary track/coil inductance	L	67.81 µH
Primary tuning capacitance	C	0.88 µF
ESR	R_{ESR}	0.2 Ω
Maximum equivalent Load	R	0.5 Ω
Nominal system frequency	f	20 kHz
Reference peak current	I_{ref}	15 A

It can be seen that the startup transient is a fully soft switched process, where all the switches are switched on and off at ZCS condition, therefore the switch losses should be reduced during the startup.
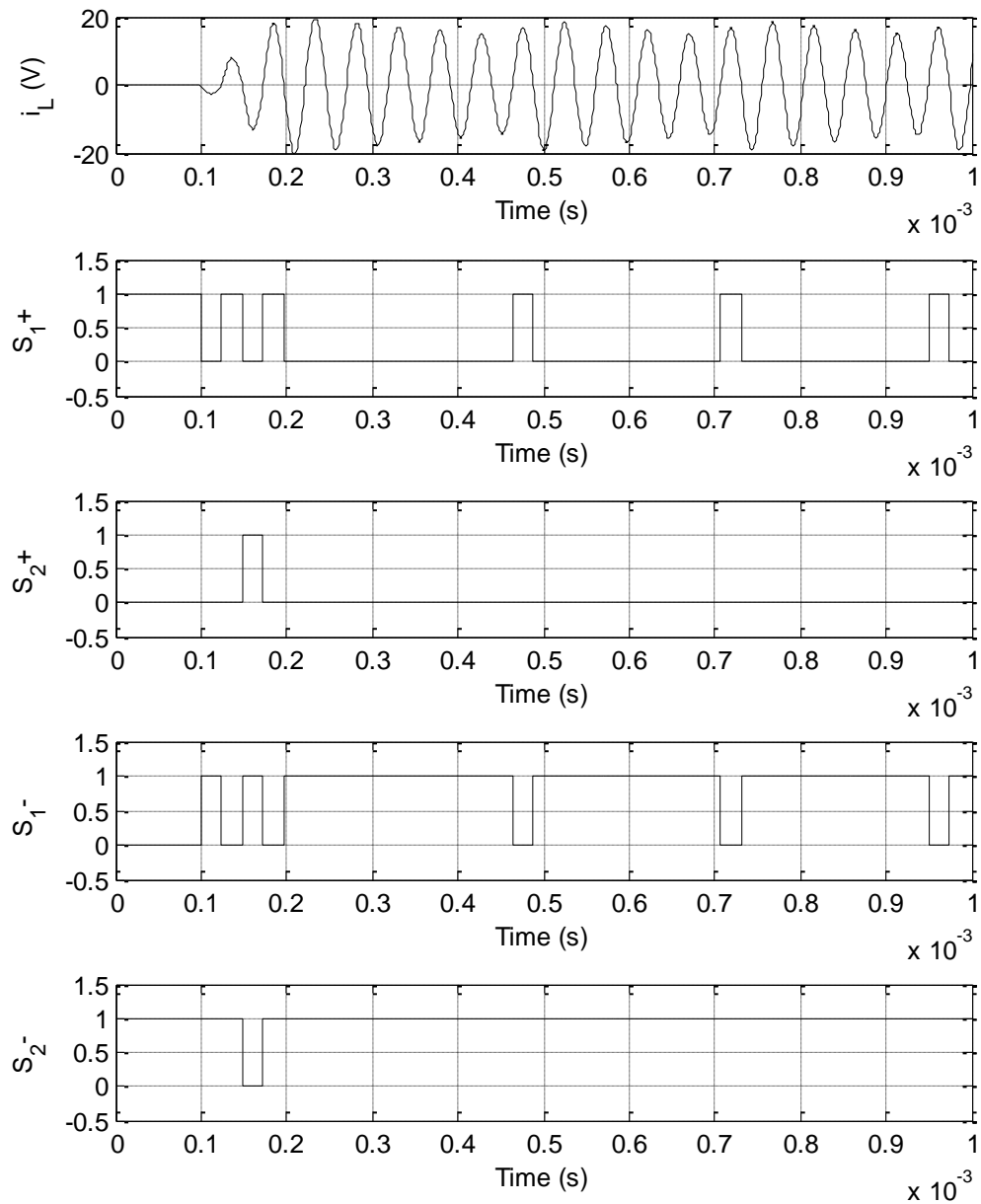
Figure 3-13: Simulation results of startup

In addition to the startup transient, Figure 3-14 shows the operation of the inverter under steady state. It can be seen that the energy is injected using S_1+ in its positive direction or S_2+ in its negative direction. However, when the both S_1- and S_2- are on, there is no energy being injected. As shown, the resonant track current is maintained around the predefined reference value of 15A, but with an asymmetrical operation. In fact, the switch operation of such an inverter is determined by the input voltage, the load, the ESR of the track and the predefined reference. Any small perturbation will change the operation

condition, thus inverter operation is discrete and almost unpredictable due to the nonlinearities of the circuit operation.
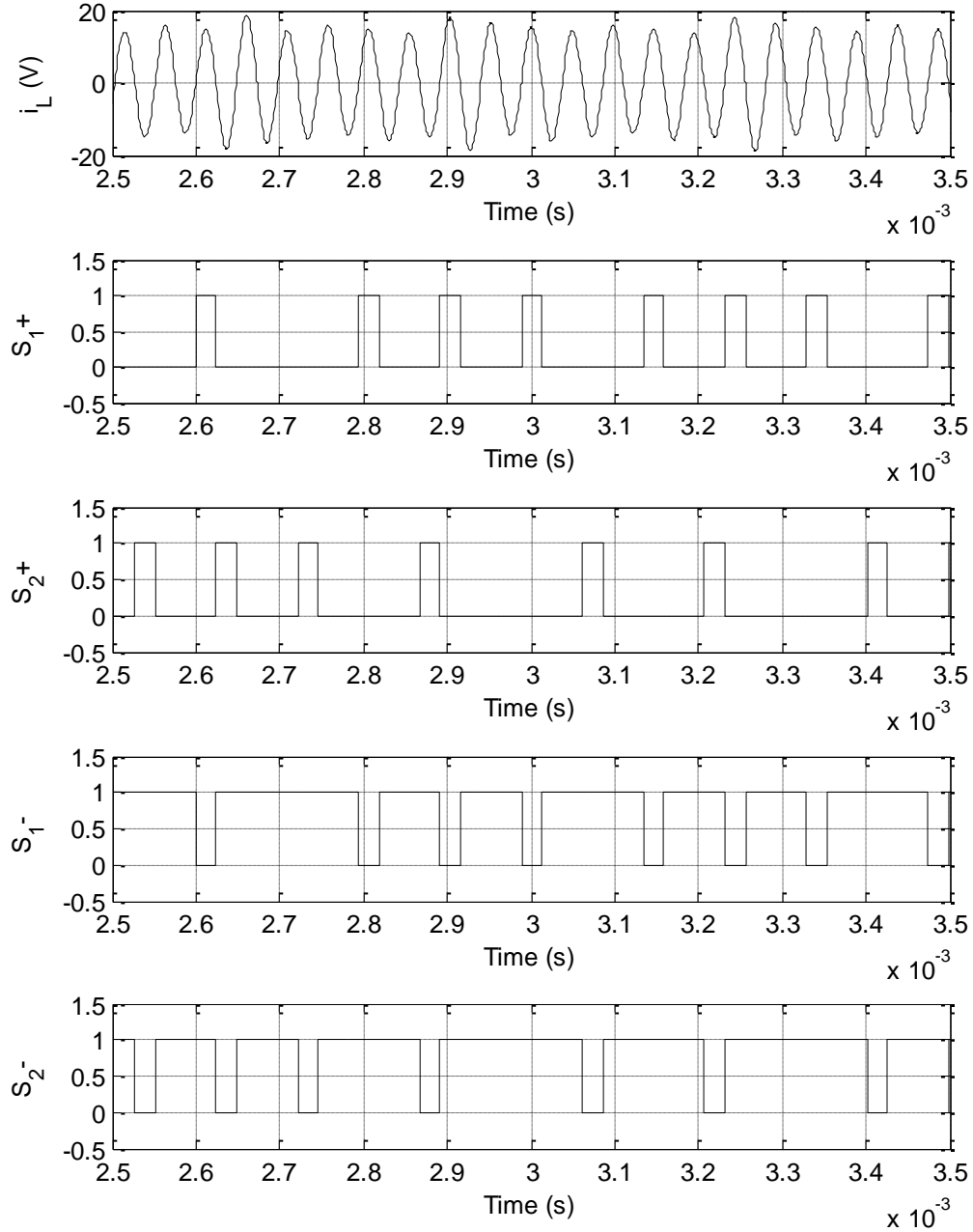
Figure 3-14: Simulation results of steady states operation

In order to investigate the proposed control and switching strategy under different loading conditions, a simulation was undertaken by varying the load from no load condition (with only ESR present) to full load condition. It can be achieved by varying the value of the

simulation model RL2 in Figure 3-12 (b). The simulation results obtained are shown in Figure 3-15.
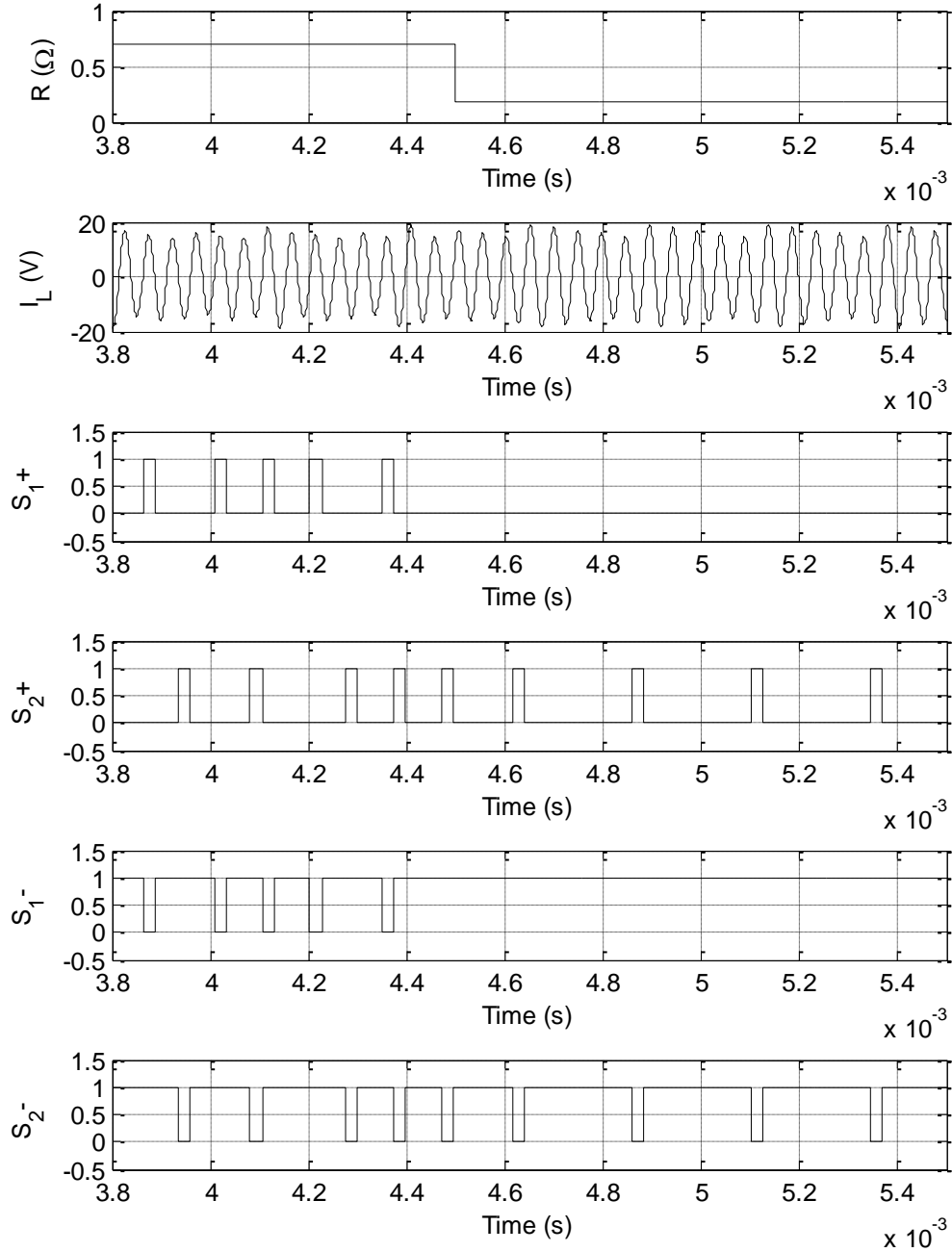
Figure 3-15: Simulation results of load variation transient

The load variation occurs around 4.5ms as indicated in Figure 3-15. Notably, the switching operation is different from steady state operation shown in Figure 3-14. The switching pattern has changed when the loading condition varies. Here S_1+ fully stops

injection of energy if the load is removed. For the majority of the time, the converter operates in a free oscillation state. S_2+ operates at a very low switching frequency to inject energy to compensate the energy consumed by the ESR and the load. It can be seen that such energy injection control has a very fast response against load variations.

3.3.6 *Experimental implementation and results*

The same circuit parameters for the simulation study are used to build an experimental system. To realize the proposed control strategy with fast sampling and minimal delay, a FPGA controller was designed and implemented to achieve ZCS operation. The circuit control system and the associated gate driver circuit are shown in Figure 3-16.
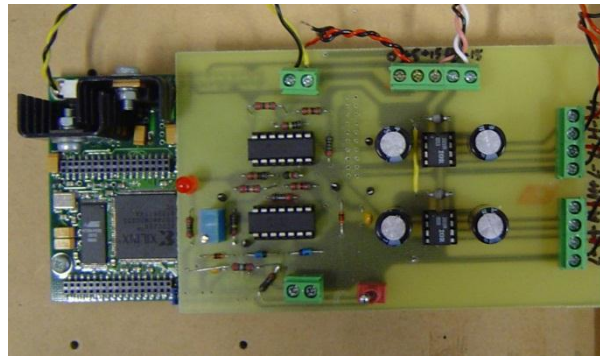
Figure 3-16: FPGA based controller and gate driver

Figure 3-17 shows the experimental results of the startup transient response of the proposed inverter. The gate drive signals of S_1+ and S_2+ are displayed together with the resonant track current (i_L). It can be seen that at the beginning S_1+ is kept on for a short period (S_2- is also on but is not shown). Once the voltage of the capacitor equals the input voltage, S_1+ and $S_2 +$ are both turned off (S_2- and S_1- are turned on), and an oscillation path is formed so that the current oscillates freely in the track. After the initial forced energy injection and the first half cycle oscillation, S_1+ turns on in each positive half cycle and S_2+ turns on in each negative half cycle to ensure the maximum energy injection to boost the current to the reference 15A as fast as possible. Once the peak track current reaches a predefined reference, the switching frequency decreases to reduce the energy injection and maintain the track current relatively constant. The duration of the startup transient to steady state takes only a few cycles from the experiment. The waveform is very similar to the simulation result shown in Figure 3-13. The current overshoot during startup is well controlled. The maximum peak current at the startup transient is about 18A,

which is close to the simulated value 19.6A shown (only ESR). Both of them are within the range of the theoretical worst case value 20.47A, which is under no load condition and can be predicted by equation (3-26).
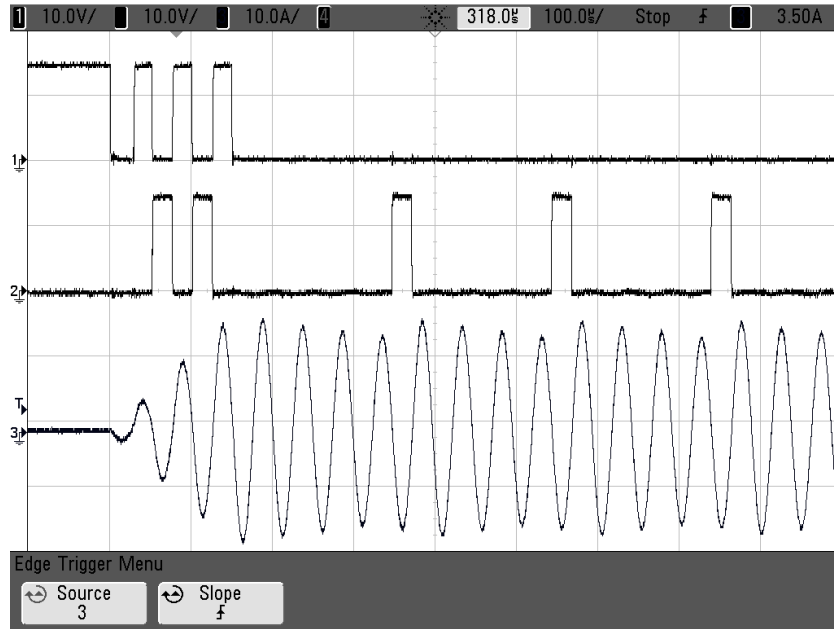
Figure 3-17: The transient response of the proposed inverter on startup

In order to investigate the inverter operation with load, a practical pickup is added to couple to the primary track having a mutual inductance $M=7.66\times10^{-6}$ μH. Under such coupling conditions, the pickup is tuned at the primary operation frequency of 20 kHz and presents a reflected load $Z_r=0.5\Omega$ to the track. The steady state operation is shown in the early part of Figure 3-18.

From top to bottom, the waveforms are voltage over the load on the pickup (V_{R_L}), the primary track current (i_L), S_2+ and S_1+. Here the track current frequency is operating close to the nominal resonant frequency which the pickup is tuned to operate at. By the control strategy the inverter has a good dynamic response. A high frequency track current is generated, and its magnitude is maintained around the reference level despite the low switching operation.
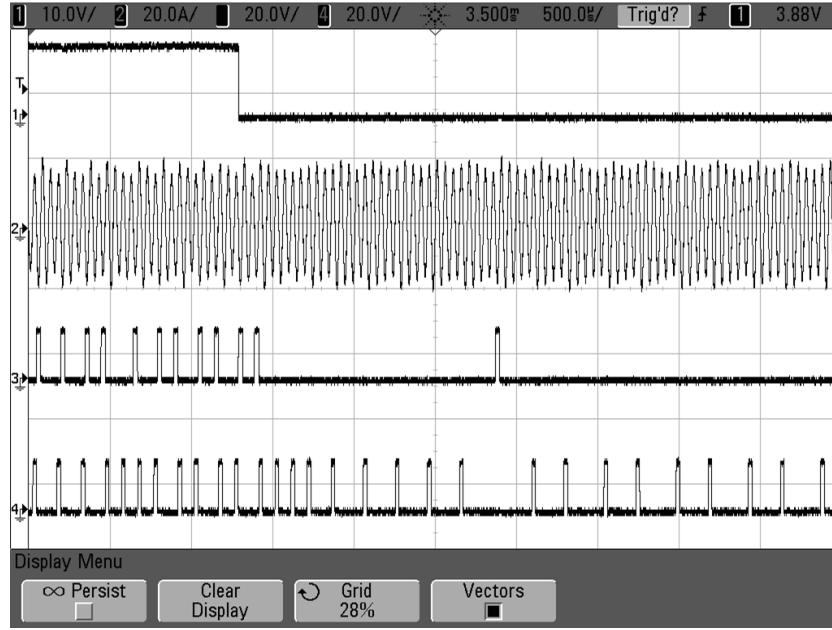
Figure 3-18: The response from full load to no load

In order to investigate the proposed control method for the applications under load variation conditions, an experiment is undertaken with same specification shown in Table 3-2, but the load on the pickup was suddenly removed. The experimental waveform of the track current and the gate driver signals are shown in the later part of Figure 3-18. In the beginning the system operates at steady state. Around 10ms, the load is removed (indicating no energy is desired by pickup) in order to evaluate the response of the inverter. At this point the voltage over the load V_{R_L} of the load resistor of the pickup is shown to drop to zero Figure 3-18 (trace1). The inverter now only operates to overcome the track losses and maintain the current on the primary resonant circuit. Furthermore, the transient overshoot of the primary current which exists as a result of the energy injection is naturally limited, which is close to the simulation result shown in Figure 3-15, and can be well predicted as discussed in the ripple analysis. In addition, all switches operate at low switching frequencies and the switching pattern is different from the full load condition. It also can be observed that only S_1+ is operating, $S_2 +$ is standing by under this "no load" condition. As discussed in previous simulation study, the switching pattern is related to the reference value of the track current and the loading condition, which is difficult to predict.

It can be seen from Figure 3-18 that small fluctuations in current arise under both full load and no load conditions, because of the fast energy consumption of the load during the free

oscillation period, and a slight over energy injection during the half period of energy injection, which is limited by the half period energy injection if the ZCS condition is maintained. Figure 3-18 shows that the practical experimental value of the maximum current is about 19A, which is smaller than the theoretical worst case value of 20.47A. The practical minimal current obtained is about 14A, which is also within theoretical limit of the calculated value of 13.74A. In fact, such a waveform is sufficiently good for an IPT system, where the major task is to transfer the average rather than the instantaneous power. If necessary, these fluctuations can be minimized or eliminated by controlling the energy injection using a hard switching strategy, or a combined hard/soft switching approach, but in either case full ZCS will be compromised.

3.4 Summary

In this chapter, a high frequency inversion and control method was proposed for IPT applications based on free oscillation and energy injection control principles. The inversion topologies of the simple half bridge and the improved full bridge configurations were discussed.

Theoretical modeling and analysis were conducted to understand the operation of the proposed method. An analysis was taken to predict the about the current fluctuation under the worst case conditions. A ZCS strategy was proposed to control the full bridge inverter, which was verified by simulation and experimental studies to evaluate variations under startup, steady state, and load variations. A FPGA based controller was developed as the core control unit to implement the control strategy so as to achieve a fast and accurate ZCS operation. Both simulation and experimental results have demonstrated that the proposed inversion method is able to generate a high frequency output current at a low switching frequency. The inverter operates at full ZCS conditions and has very good startup and steady state properties. Furthermore, track current fluctuations that arise during operation, but they are well controlled even under load transients.

Chapter 4

Frequency Bifurcation and Sensitivity Analysis

4.1 Introduction
4.2 Bifurcation Phenomenon
4.3 System Load Model
4.4 Effect of Loading Condition
4.5 Effect of Coupling Condition
4.6 Components Sensitivity Analysis
4.7 Summary
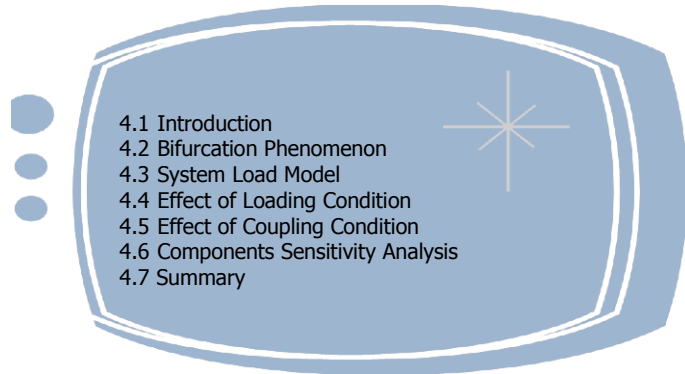
4.1 Introduction

In the previous chapter, DC-AC inverters for IPT systems based on energy injection control were proposed and discussed. However, the previous study mainly focused on the primary inverters by assuming that the reflected load was purely resistive. Practically, IPT systems are designed to deliver power from a stationary primary side to one or multiple movable secondary loads via magnetic coupling. Therefore, the behavior of the primary inverter is affected by the pickup circuit(s), and it is mathematically complex and highly sensitive to variations in system parameters such as self-inductances, tuning capacitances of primary side and secondary sides, loading conditions, and the mutual magnetic coupling conditions, etc. For an IPT system with a variable frequency power supply, system parameter variations may result in a system frequency variation and affect the power transfer capability; in consequence the system performance can be very different.

In this chapter, in order to have a better design for the proposed primary energy injection inverter at a system level, the influences of the secondary pickups on the behavior of the proposed inverter including the phenomenon of system frequency bifurcation, the sensitivity of various key components and the power transfer capability will be analyzed.

4.2 Bifurcation Phenomenon

In order to have a better current waveform and reduce the switching losses, the proposed energy injection controller uses a variable frequency control. The inverter is operated in such a manner that is to follow the system resonance for achieving soft switching operation. The switches of the inverter are operated under ZCS conditions with theoretically no switching losses. Despite the advantages of using a variable frequency control scheme, the proposed inverters can face frequency stability problems which are mainly caused by heavy loads and/or tight coupling of one or more power pickups. For such a high order system, if any of the system operating conditions varies, for instance, the loading or coupling condition, the system may bifurcate and result in more than one stable operational frequency [91, 114].

In order to understand the system bifurcation phenomenon, the proposed inverter is studied together with coupled pickups. Figure 4-1 shows the IPT system, which have a primary energy injection inverter with a series tuned pickup.
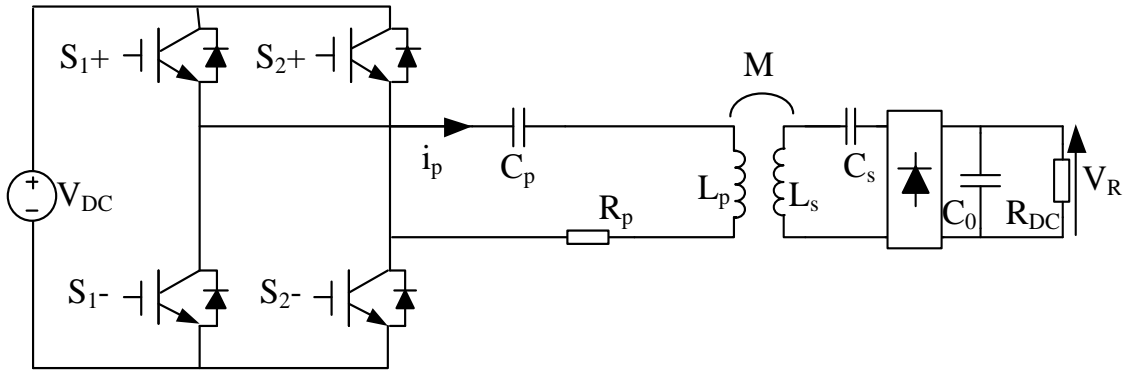
Figure 4-1: A primary energy injection inverter with a series-tuned pickup

Figure 4-2 shows a typical surface plot of the imaginary part of the total impedance of the resonant network (when the pickup load is treated as linear) by sweeping the system operation frequency with one of the system operation conditions varying according to the given system parameters listed in Table 4-1. Figure 4-2 (a) shows the imaginary part of the total impedance seeing from the primary side with the load variations on the secondary side. It can be seen that if the secondary side has a light load, there is only one frequency corresponding to $Im(Z_t)=0$. However, with the load increasing, there are more than one

zero phase angle frequency appearing.
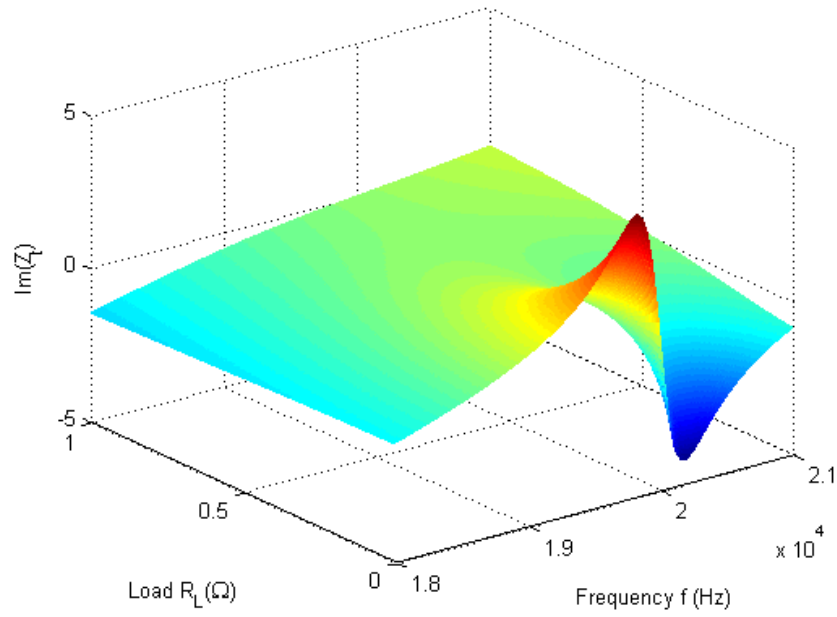
(a) Pickup loading condition variation
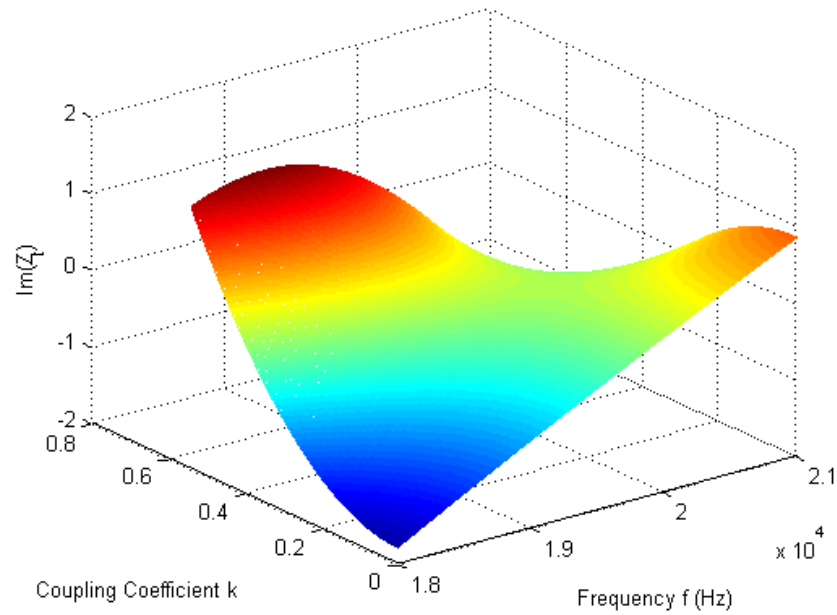
(b) Mutual coupling condition variation

Figure 4-2: Imaginary part from the primary with operation conditions variations

Table 4-1: IPT system parameters

Notes	Symbol	Value
Input dc voltage	V_{DC}	25 V
Primary coil inductance	L_p	67.81 µH
Secondary coil inductance	L_s	45.16 µH
Primary tuning capacitance	C_p	0.905 µF
Secondary tuning capacitance	C_s	1.360 µF
Mutual inductance	M	7.66×10^{-6} µH
Primary coil ESR	R_p	0.150 Ω
Secondary coil ESR	R_s	0.095 Ω
DC Load resistance	R_{DC}	0-2 Ω
Angular nominal operating frequency	ω_0	1.276×10^5 rad/s

Similarly, Figure 4-2 (b) shows the imaginary part of the system with mutual coupling variations. It can also be seen that the system will have more than one zero phase angle frequency under tight coupling conditions.

The system bifurcation phenomenon is directly related to system operation conditions, and it can affect the power transfer capability of the system [115]. If the operation frequency drifts, the pickup will also be detuned from the designed frequency. As a result, the primary power inverter may have a lower power transfer capability. Under the worst case scenario, if the frequency suddenly jumps from the nominal frequency to either the lowest or highest frequency, it is possible that the transient frequency variations may cause the controller difficult to response. As such, frequency stability problem will need to be investigated for the proposed variable frequency energy injection primary inverter with one or multiple secondary pickups. The results obtained can be very useful for designing an energy injection inverter.

4.3 System Load Model

In order to analyze the proposed energy injection inverter at a system level, a power pickup is included in the IPT system. A typical series tuned pick is shown here in Figure 4-3.
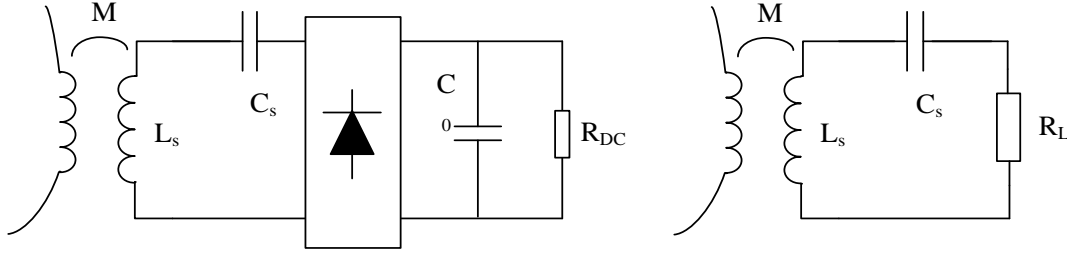
Figure 4-3: Series resonant pickup resonant structures with equivalent load

Here, the pickup is designed to have a resonant frequency at ω_0, which is given by:

$$\omega_0 = \frac{1}{\sqrt{L_s C_s}} \qquad (4\text{-}1)$$

The load here is a DC load, which is connected to the pickups with the filtering and rectification circuitry.

It has been shown [28] that under the assumption that the rectifier is in continuous conduction, the ideal equivalent AC load (R_L) can be presented by:

$$R_L = \frac{8}{\pi^2} R_{DC} \qquad (4\text{-}2)$$

This implies that the equivalent AC load R_L, which is used in the following analysis, is linearly proportional to the actual DC load. In order to simplify the analysis, all the switches of the primary inverter are assumed to be ideal. There are no delays from energy injection operation to free oscillation operation and vice versa. With these assumptions, the circuit shown in Figure 4-1 can be modeled as two separate series tuned circuits that

are coupled to each other with a mutual inductance (*M*), and each of them has a self ESR. The equivalent circuit model of the proposed system is shown in Figure 4-4.
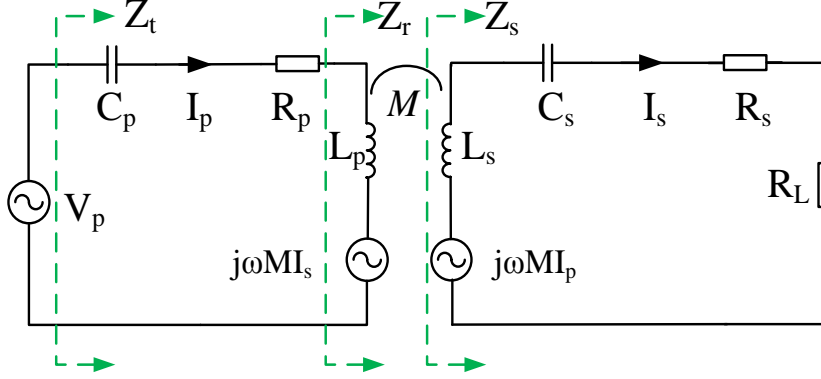
Figure 4-4: System coupling model

The equivalent impedance of the secondary pickup can be modeled as in [116] by:

$$Z_s = j\omega L_s + \frac{1}{j\omega C_s} + R_s + R_L \tag{4-3}$$

Looking at the primary side, the reflected impedance from the secondary side can be calculated as:

$$Z_r = \frac{\omega^2 M^2}{Z_s} \tag{4-4}$$

Accordingly, the total input impedance of the primary inverter can be expressed by:

$$Z_t = j\omega L_p + \frac{1}{j\omega C_p} + R_p + Z_r \tag{4-5}$$

By substituting equations (4-3) and (4-4) to equation (4-5), the total impedance of the IPT system can be expressed as:

$$Z_t = j\omega L_p + \frac{1}{j\omega C_p} + R_p + \frac{\omega^2 M^2}{j\omega L_s + \frac{1}{j\omega C_s} + R_s + R_L} \tag{4-6}$$

After rearranging equation (4-6), the resistive and reactive components of the total impedance from the primary side can be expressed by a real part and an imaginary part respectively as follows:

$$\mathrm{Re}\left(Z_t\right) = R_p + \frac{\left(R_s + R_L\right)\omega^2 M^2}{\left(R_s + R_L\right)^2 + \left(\omega L_s - 1/\omega C_s\right)^2} \tag{4-7}$$

$$\mathrm{Im}\left(Z_t\right) = \omega L_p - \frac{1}{\omega C_p} - \frac{\omega^2 M^2 \left(\omega L_s - 1/\omega C_s\right)}{\left(R_s + R_L\right)^2 + \left(\omega L_s - 1/\omega C_s\right)^2} \tag{4-8}$$

4.4 Effect of Loading Condition

4.4.1 Single pickup system

Because the proposed inverter is designed to operate at a variable frequency, when switching harmonics are ignored, the imaginary part of the system total impedance $\mathrm{Im}(Z_t)$ from the above load model has to be equal to zero, which can be expressed as:

$$\omega L_p - \frac{1}{\omega C_p} = \frac{\omega^2 M^2 \left(\omega L_s - 1/\omega C_s\right)}{\left(R_s + R_L\right)^2 + \left(\omega L_s - 1/\omega C_s\right)^2} \tag{4-9}$$

As can be seen, it is very complicated to analyze the operation angular frequency of the inverter because of the high order of the system. The angular frequencies (ω) here are determined by circuit parameters, and the loading condition on the secondary side (R_L). As such, it is worth to understand how the loading condition affects the operation frequency of the primary inverter, and it is necessary to determine a valid load range to design a proper primary inverter without bifurcation.

In order to simplify the analysis along with the frequency spectrum of the IPT system, a normalized frequency is introduced based on the designed frequency ω_0, and it is defined as:

$$\mu = \frac{\omega}{\omega_0} \tag{4-10}$$

Note that if the operation frequency is higher than the designed frequency ω_0, the normalized frequency is larger than 1, for example, μ is equal to 1.1 if the operating

frequency is +10% higher than ω_0. In addition, both the primary and secondary circuits of an IPT system are normally tuned to the nominal undamped resonant frequency [27]:

$$\omega_0 = \frac{1}{\sqrt{L_p C_p}} = \frac{1}{\sqrt{L_s C_s}} \tag{4-11}$$

According to equation (4-9), all the solutions to the frequency ω are the possible frequencies for achieving ZCS operations. Naturally the nominal frequency ω_0 is one of the theoretical operating frequencies for the series-series tuned configuration as shown in Figure 4-4. If $\omega=\omega_0$ according to equation (4-11), the term $(\omega L_p - \frac{1}{\omega C_p})$ and $(\omega L_s - \frac{1}{\omega C_s})$ in the equation can be cancelled. As such, the order of the system is reduced, and equation (4-9) therefore can be simplified as follows:

$$\left(1 - \omega^2 L_s C_s\right)^2 + \omega^2 C_s^{\,2}\left(R_s + R_L\right)^2 - \omega^4 M^2 C_p C_s = 0 \tag{4-12}$$

Substituting equation (4-10) into (4-12), the equation (4-12) can be rewritten as a function of the normalized frequency μ as:

$$\mu^4\left(1 - \omega_0^{\,4} C_s C_p M^2\right) + \mu^2\left(\omega_0^{\,2} C_s^{\,2}\left(R_s + R_L\right)^2 - 2\right) + 1 = 0 \tag{4-13}$$

As stated earlier, all of the obtained solutions result in possible ZCS operating frequencies. By solving the equation, theoretically, there are four possible normalized solutions as listed below:

$$\mu_1 = \sqrt{\frac{-\left(\omega_0^{\,2} C_s^{\,2}\left(R_s + R_L\right)^2 - 2\right) + \sqrt{\left(\omega_0^{\,2} C_s^{\,2}\left(R_s + R_L\right)^2 - 2\right)^2 - 4\left(1 - \omega_0^{\,4} C_s C_p M^2\right)}}{2\left(1 - \omega_0^{\,4} C_s C_p M^2\right)}} \tag{4-14}$$

$$\mu_2 = \sqrt{\frac{-\left(\omega_0^{\,2} C_s^{\,2}\left(R_s + R_L\right)^2 - 2\right) - \sqrt{\left(\omega_0^{\,2} C_s^{\,2}\left(R_s + R_L\right)^2 - 2\right)^2 - 4\left(1 - \omega_0^{\,4} C_s C_p M^2\right)}}{2\left(1 - \omega_0^{\,4} C_s C_p M^2\right)}} \tag{4-15}$$

$$\mu_3 = -\sqrt{\frac{-\left(\omega_0^2 C_s^2 (R_s + R_L)^2 - 2\right) + \sqrt{\left(\omega_0^2 C_s^2 (R_s + R_L)^2 - 2\right)^2 - 4\left(1 - \omega_0^4 C_s C_p M^2\right)}}{2\left(1 - \omega_0^4 C_s C_p M^2\right)}} \quad (4\text{-}16)$$

$$\mu_4 = -\sqrt{\frac{-\left(\omega_0^2 C_s^2 (R_s + R_L)^2 - 2\right) - \sqrt{\left(\omega_0^2 C_s^2 (R_s + R_L)^2 - 2\right)^2 - 4\left(1 - \omega_0^4 C_s C_p M^2\right)}}{2\left(1 - \omega_0^4 C_s C_p M^2\right)}} \quad (4\text{-}17)$$

Even though the analytical solutions of μ_3 and μ_4 are the theoretical angular frequencies, they are meaningless in practice. This is because they are negative, and it is impossible to have negative frequencies in a practical system. For such a reason, μ_3 and μ_4 are neglected, and only μ_1 and μ_2 will be considered.

In order to keep a real solution for equation (4-13), the term $\left(\omega_0^2 C_s^2 (R_s + R_L)^2 - 2\right)^2 - 4\left(1 - \omega_0^4 C_s C_p M^2\right)$ has to be larger than zero in both equation (4-14) and (4-15). Therefore, the equivalent maximum loading condition has to satisfy the following boundary condition as:

$$R_L \geq \frac{\sqrt{-2\sqrt{(C_s^2 L_s^2 - C_p C_s M^2)} + 2L_s C_s}}{C_s} - R_s \quad (4\text{-}18)$$

To clearly see the two bifurcation frequencies and the boundary loading conditions, according to Table 4-1 with other parameters being assumed to be constant, the calculated results of the two possible frequencies μ_1 and μ_2 are plotted and shown in Figure 4-5. In addition, for comparison purposes, the nominal frequency μ_0 is also plotted here.
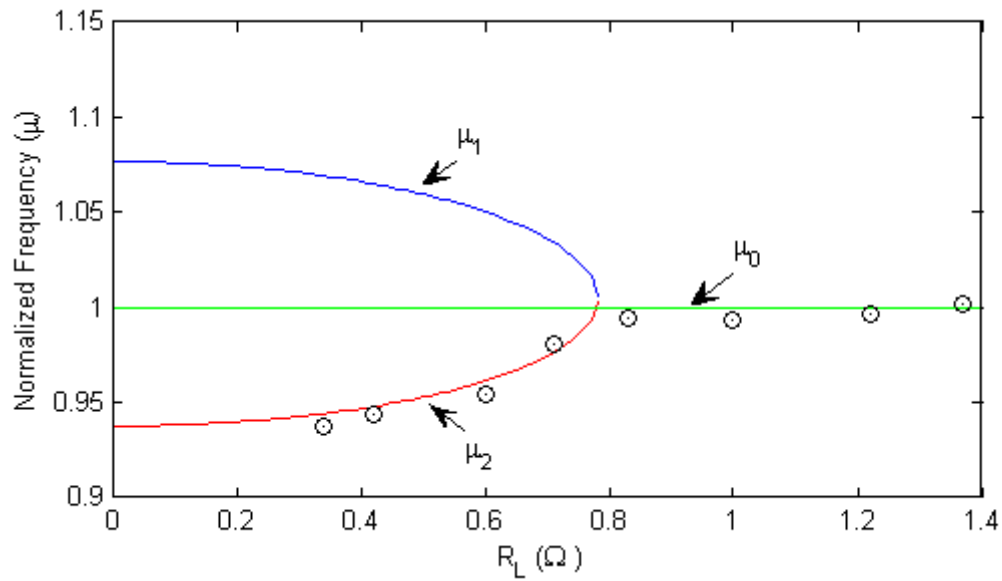
Figure 4-5: Normalized zero phase angle frequency with load range

From Figure 4-5, it can be seen that if the secondary load resistance is high (representing a light load), the system will have only one normalized angular frequency μ_0. However, when the secondary load resistance decreases (load resistance) beyond the critical value R_L=0.781(calculated from equation (4-18)), the system frequency bifurcates resulting in two separate resonant frequencies which are either higher or lower than the nominal frequency. Increasing in the load (decreases of the R_L) will cause the bifurcated frequency to drift away from the nominal frequency.

To verify the theoretical analysis, a practical experiment was carried out with the same system parameters listed in Table 4-1. In order to clearly compare with the theoretical frequencies, all the measured practical operation frequencies under different load conditions are also plotted in Figure 4-5. Notably, under light load, the practical operation frequency is very close to the system designed frequency ω_0, being almost constant. However, as the load increases beyond the bifurcation free range, the system operation frequency starts to bifurcate. Theoretically, the system may end up operating at either of the two frequencies, but it is difficult to predict which one will be the actual frequency.

According to the observation from the experiment, when the load is heavier than the critical load, all the practical operation frequencies are smaller than the normalized frequency. This proves that the critical load condition obtained from the theoretical

analysis is valid. The obtained result is very important for designing an inverter without frequency bifurcation.

4.4.2 *Multiple pickups system*

In addition to an IPT application with a single pickup, some IPT applications have multiple pickups for distributed loads. Figure 4-6 shows a typical IPT system with multiple pickups, where the primary inverter is an energy injection inverter with a series tuned track. Each pickup also has a series tuned configuration.
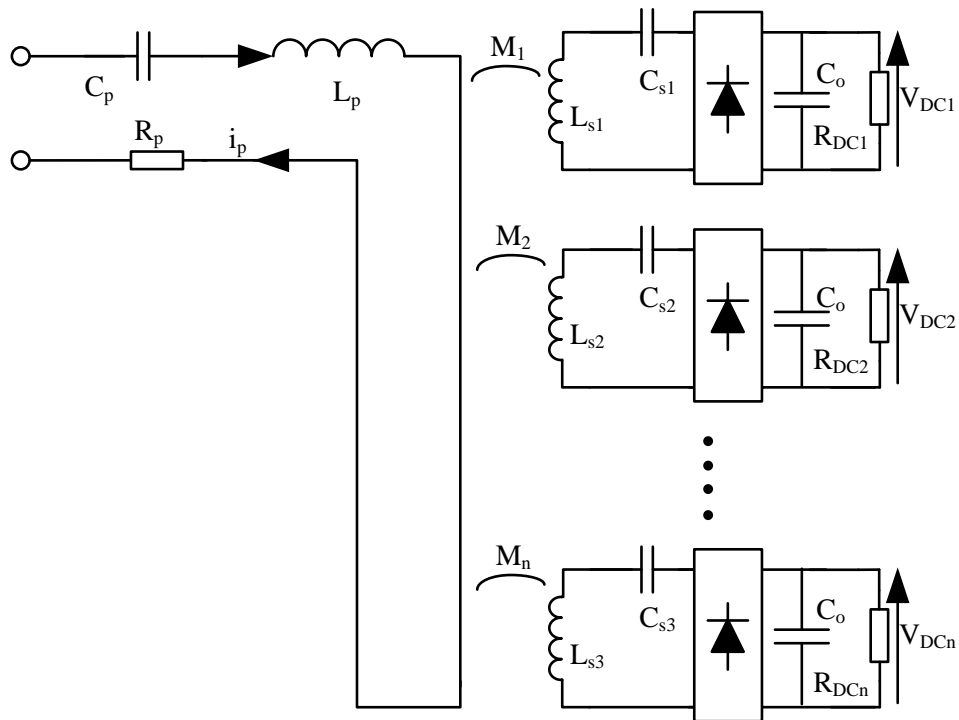
Figure 4-6: Load modeling of multiple tuned pickups

Similar to a single pickup IPT system, if multiple pickups are coupled to the primary track with different loading and coupling conditions, the accumulated total impedance on the primary side can be calculated as:

$$Z_{total} = Z_p + \sum_{n=1}^{k} \frac{\omega^2 M_n{}^2}{j\omega L_{sn} + \dfrac{1}{j\omega C_{sn}} + R_{sn} + R_{Ln}} \qquad (4\text{-}19)$$

where k is the total number of the pickups, M_n is the mutual inductance between the primary track/coil and the nth pickup. R_{sn} is the ESR of the nth pickup. R_{Ln} is the equivalent AC load resistance which can be obtained from equation (4-2) under the assumption that the rectifier on the secondary side is in continuous conduction when delivering power to the load. To simplify the analysis by assuming all the pickups to be identical under identical coupling and loading conditions, equation (4-19) can be simplified to:

$$Z_{total} = j\omega L_p + \frac{1}{j\omega C_p} + R_p + \frac{n\omega^2 M^2}{j\omega L_s + \dfrac{1}{j\omega C_s} + R_s + R_L} \qquad (4\text{-}20)$$

Theoretically, if there are no coupled pickups or no load on all coupled pickups, the ZCS operational frequency of the primary inverter would be equal to the zero phase angle frequency when only the fundamental is considered. If more pickups are coupled to the primary side, additional zero phase angle frequencies may exist. Figure 4-7 shows a plot of the relationship between the zero phase angle frequencies and the pickups numbers, using the system circuit parameters of Table 4-1.
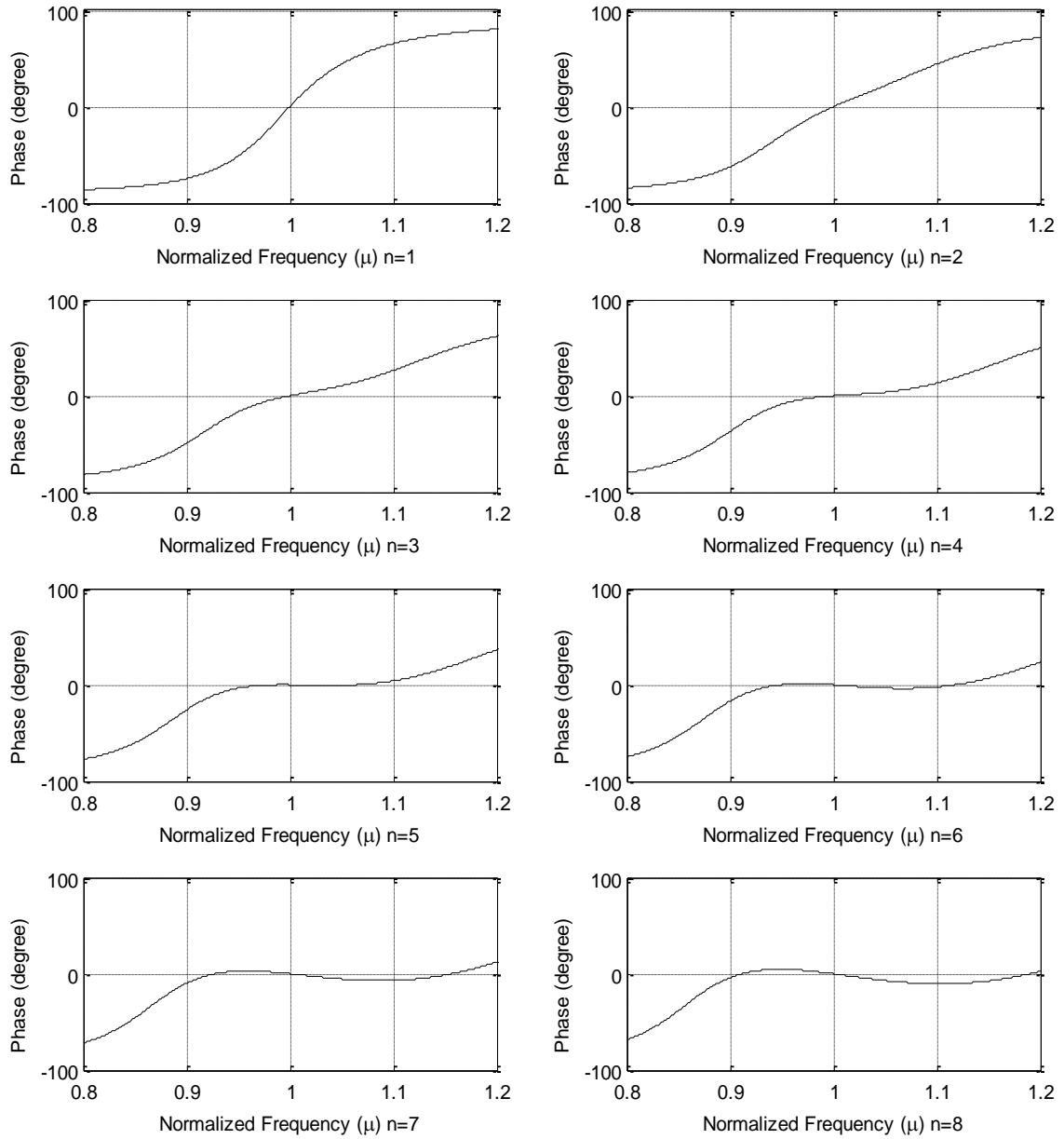
Figure 4-7: Relationship of the phase angles and the number of the pickups

It can be seen that with the increase of the total number of the distributed pickups, the number of the zero phase angle frequencies increases from one to three. This frequency bifurcation phenomenon of the primary inverter with multiple pickups is similar to the system with a single pickup, but the total load range over which the circuit bifurcation occurs can be very different. Figure 4-8 shows the comparison of the phase angle of the total primary impedance seen from the input of the inverter. Trace 1 presents the phase

angle of the IPT system with a single pickup which has a load R_L=1.62Ω. Trace 2 presents the phase angle of the IPT system with three pickups, and each of them has a load R_L=1.62Ω. For comparison purpose, trace 3 presents the phase angle of the IPT system with a single pickup. The single pickup has some configuration and coupling is the same as that for trace 1 except that the load resistance is R_L=0.54Ω that is the same load condition for trace 3. It can be seen that, the frequency bifurcation occurs for the single pickup system under heavy load as shown in trace3. However there is no bifurcation for the multiple pickups system which has the same equivalent load in total as shown in trace2. This is because the multiple pickups equivalently increase the total mutual inductance and transfer more power to the distributed loads. This feature makes the proposed inverter very suitable for an IPT system with multiple distributed pickups.
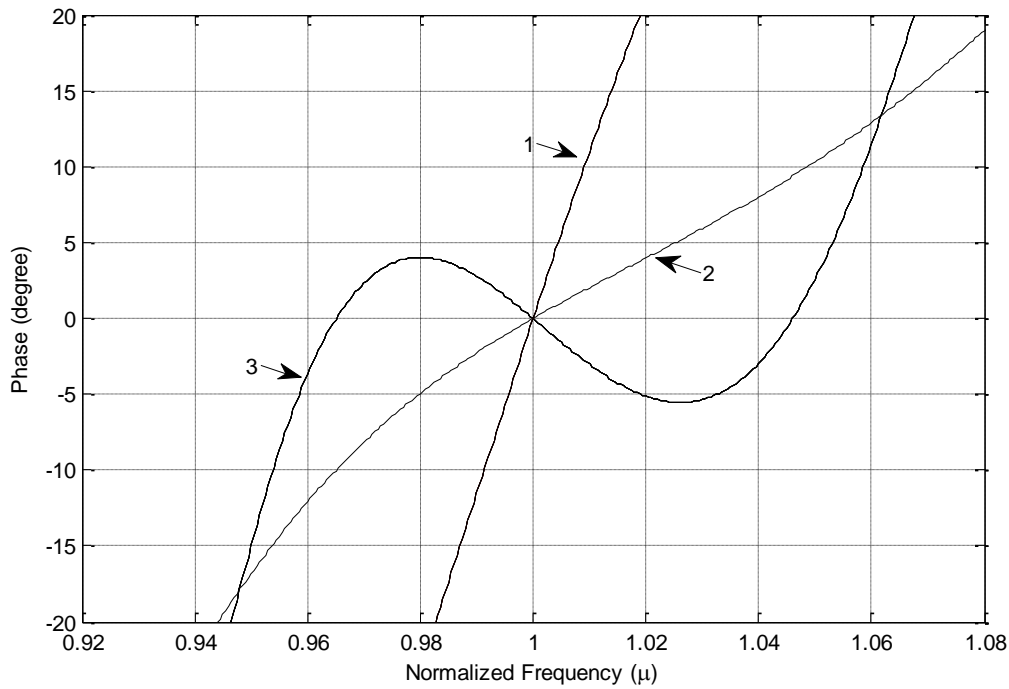
Figure 4-8: Phase angel of the system

1) single pickup with nominal load, 2) three nominal load pickups, 3) single pickup with same load as three nominal pickups.

In order to design the proposed inverter with multiple pickups without frequency bifurcation, it is desirable to determine the maximum pickup numbers. Similar to the analysis conducted for a single pickup system, theoretically the pickup numbers can be

obtained by solving equation $\text{Im}(Z_t)=0$. The imaginary part of the system with multiple pickups can be obtained from equation (4-20). The normalized zero phase angle frequency of the IPT system with multiple pickups can be expressed as:

$$\mu^4\left(1-n\omega_0^4 C_s C_p M^2\right)+\mu^2\left(\omega_0^2 C_s^2(R_S+R_L)^2-2\right)+1=0 \qquad (4\text{-}21)$$

Given the nominal frequency ω_0, there are two other possible zero phase angle frequencies that can be obtained by:

$$\mu_{1,2}=\sqrt{\dfrac{-\left(\omega_0^2 C_s^2(R_S+R_L)^2-2\right)\pm\sqrt{\Delta}}{2\left(1-n\omega_0^4 C_s C_p M^2\right)}} \qquad (4\text{-}22)$$

where the Δ is expressed by:

$$\Delta=\left(\omega_0^2 C_s^2(R_S+R_L)^2-2\right)^2-4\left(1-n\omega_0^4 C_s C_p M^2\right) \qquad (4\text{-}23)$$

To obtain a valid analytical solution for the equation (4-22); the maximum theoretical number of the identical pickups can be obtained as flows:

$$n=\dfrac{4L_s L_p C_s(R_S+R_L)^2-L_p C_s^2(R_S+R_L)^4}{4L_s M^2} \qquad (4\text{-}24)$$

The relationship between the normalized frequencies and the number of pickups is shown in Figure 4-9. It can be seen that for the given nominal load on each pickup, when there are more than five pickups coupled to the primary side, the system will bifurcate. The possible bifurcation frequencies have two solutions and can be calculated by equation (4-22). Conversely if multiple pickups are designed to have more power and no bifurcation, the total number of pickups has to be reduced to meet the requirements of equation (4-24).
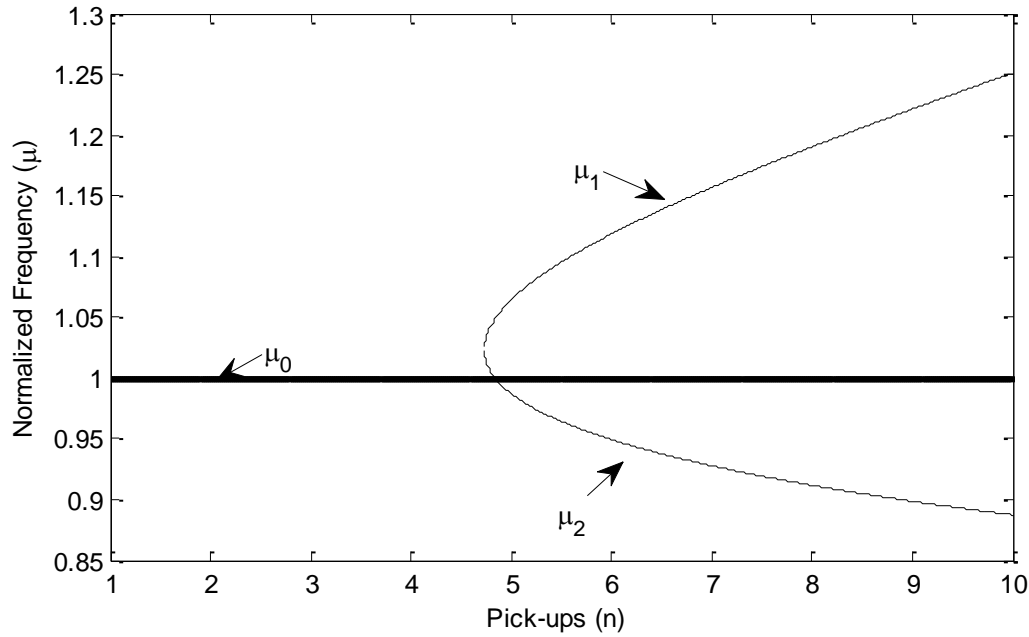
Figure 4-9: Bifurcation frequencies and the pickup numbers

4.5 Effect of the Coupling Condition

4.5.1 Coupling conditions to system frequency

The investigation of the loading effect on system frequency is very important when designing an IPT system to avoid bifurcation using the proposed energy injection power inverter. However, in addition to the impact of load variation, understanding of the impact of coupling is often required. From the coupling model of the system shown in Figure 4-4, the variation of the coupling between the pickup and the primary track will affect the system operation frequency and may cause frequency bifurcation phenomenon. Ideally, if the secondary side does not couple to the primary track, the zero phase angular frequency of the proposed inverter will be at ω_0. However, if the secondary side is close to the primary side, the mutual inductance increases. A tighter coupling will cause a higher reflected load as the reflected impedance of the secondary side is proportional to the square of the mutual inductance. Consequently, the operating frequency of the primary side will vary. Similar to the frequency bifurcation caused by increasing the load, the increase of the mutual inductance will cause the system frequency to have stability

problem as well. In order to understand how the mutual inductance affects the system frequency, the operation frequency of the proposed inverter will be analysed.

From the above load model of equation (4-9), it can be seen that the possible zero phase angle frequencies are not only determined by the loading conditions of secondary side, but also the mutual inductance (or the coupling coefficient). By introducing the coupling coefficient:

$$k = \frac{M}{\sqrt{L_p L_s}} \tag{4-25}$$

Equation (4-9) can be re-expressed as:

$$\frac{k^2 \omega^4 L_p C_p L_s C_s \left(\omega^2 L_s C_s - 1 \right)}{\omega^4 C_s^3 (\omega^2 L_p C_p - 1)(R_s + R_L)^2 + \omega C_s (\omega^2 L_p C_p - 1)(\omega^2 L_s C_s - 1)^2} - 1 = 0 \tag{4-26}$$

It can be further expressed as a function of the normalized frequency μ and simplified as:

$$\mu^4 \left(1 - k^2\right) + \mu^2 \left(\omega_0^2 C_s^2 \left(R_s + R_L\right)^2 - 2 \right) + 1 = 0 \tag{4-27}$$

It can be seen from equation (4-27), there are four possible solutions of the normalized frequency μ. Ignoring the invalid negative frequencies, the possible bifurcation frequencies are the function of the coupling coefficient and can be expressed as:

$$\mu_1 = \sqrt{\frac{-\left(\omega_0^2 C_s^2 \left(R_s + R_L\right)^2 - 2\right) + \sqrt{\left(\omega_0^2 C_s^2 \left(R_s + R_L\right)^2 - 2\right)^2 - 4\left(1 - k^2\right)}}{2\left(1 - k^2\right)}} \tag{4-28}$$

$$\mu_2 = \sqrt{\frac{-\left(\omega_0^2 C_s^2 \left(R_s + R_L\right)^2 - 2\right) - \sqrt{\left(\omega_0^2 C_s^2 \left(R_s + R_L\right)^2 - 2\right)^2 - 4\left(1 - k^2\right)}}{2\left(1 - k^2\right)}} \tag{4-29}$$

Figure 4-10 shows the calculated values of the normalized frequencies with different coupling coefficient. It can be seen that except for the nominal frequency μ_0 (ω_0), there are

two possible bifurcation frequencies μ_1 and μ_2 shown in the figure, if the coupling coefficient is larger than 0.36.
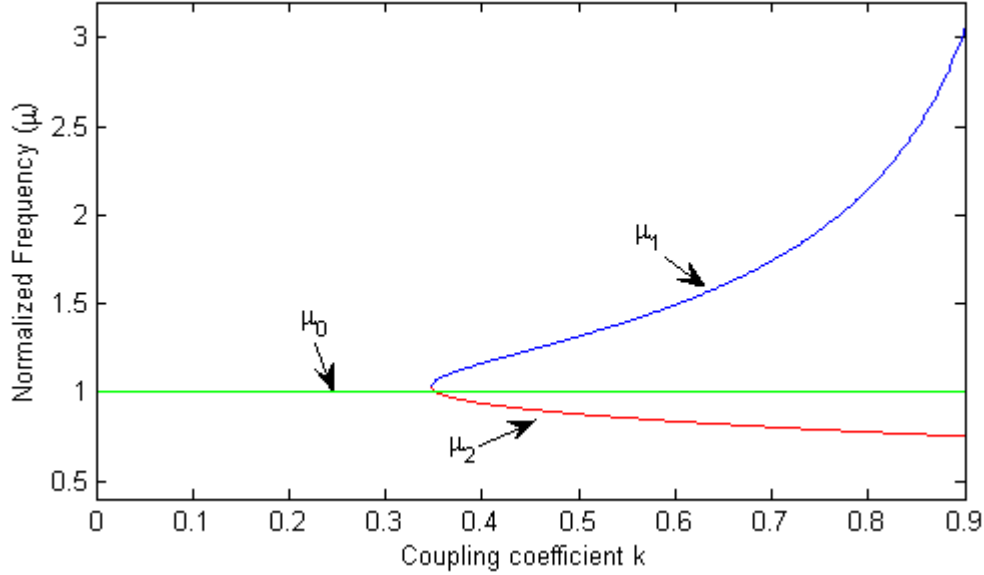
Figure 4-10: Normalized frequency with different coupling coefficients

From equations (4-28) and (4-29), it can be seen that these bifurcation frequencies are mainly determined by the secondary side components (L_s, R_s, C_s), load R_L and the coupling coefficient k. In order to obtain the possible frequency solutions, equation (4-27) should satisfy the following inequality condition:

$$\left(\omega_0^2 C_s^2 \left(R_s + R_L\right)^2 - 2\right)^2 - 4\left(1 - k^2\right) \geq 0 \tag{4-30}$$

To have an analytical result for the boundary coupling coefficient, all the parameters of the system are assumed to be constant. The boundary condition of the coupling coefficient which ensures the system to have a singular frequency can therefore be expressed by:

$$k \leq \sqrt{\frac{1}{4L_s^2}\left(4C_s L_s \left(R_s + R_L\right)^2 - C_s^2 \left(R_s + R_L\right)^4\right)} \tag{4-31}$$

4.5.2 Coupling condition for power transfer capability

Power transfer capability is another important aspect when designing an IPT system. In addition to design an IPT system without bifurcation, it is preferable to have higher power transfer ability. Generally, to obtain a higher power transfer to the secondary pickup, a higher open circuit voltage on the secondary side is required. A higher open circuit voltage can be achieved when the secondary side works at the same operating frequency as the primary side, where other system parameters are assumed to be constant [117]. Therefore, it is preferable to design the secondary side to be fully tuned to the primary operating frequency.

In addition, as can be seen from the mutual coupling model in Figure 4-4, a high open circuit voltage can be also obtained if the mutual coupling increases between the pickup coil and the primary track. Therefore, a common understanding is that a tight coupling will lead to a higher open circuit voltage because of the increased mutual coupling. However, when the interaction of system tuning and coupling of both, primary and secondary side together, with the loading conditions is considered, such an assumption may not be valid anymore. This is because a high coupling coefficient may cause an increased current drop within the proposed inverter under high reflected load. If maximum energy injection is allowed by the primary inverter, the primary power inverter may not supply a constant track current on the track. As a result, the power transfer capability of the primary side drops. In this section, a thorough analysis of the primary power transfer capability is undertaken at a system level.

➢ **Analytical solution**

From the coupling model of the IPT system with the proposed primary inverter, the open circuit voltage of the secondary pickup coil can be expressed by:

$$V_{os} = -j\omega M I_p \qquad (4\text{-}32)$$

This equation shows that in order to have a higher open circuit voltage on the secondary side, it requires a higher coupling or a higher primary track current, assuming the system frequency is constant.

By considering the primary side impedance and the reflected impedance from the secondary side, the primary side track current I_p can be expressed as:

$$I_p = \frac{V_{in}}{j\omega L_p + \dfrac{1}{j\omega C_p} + R_p + \dfrac{\omega^2 M^2}{j\omega L_s + \dfrac{1}{j\omega C_s} + R_s + R_L}} \tag{4-33}$$

From equations (4-32) and (4-33), it can be seen that the open circuit voltage of the secondary is determined by the primary side input voltage and the real part of the total impedance presented on the primary side. By considering the primary current and the induced open circuit voltage on the secondary pickup coil, the current on the secondary side can be obtained as:

$$I_s = \frac{-j\omega M V_{in}}{\left(j\omega L_p + \dfrac{1}{j\omega C_p} + R_p \right)\left(j\omega L_s + \dfrac{1}{j\omega C_s} + R_s + R_L \right) + \omega^2 M^2} \tag{4-34}$$

The secondary side current is determined by all the circuit parameters. When the circuit components on both the primary and the secondary side are fixed, the secondary side output current is proportional to the mutual inductance. Figure 4-11 shows the relationship of the output current of the secondary side with different mutual inductances.
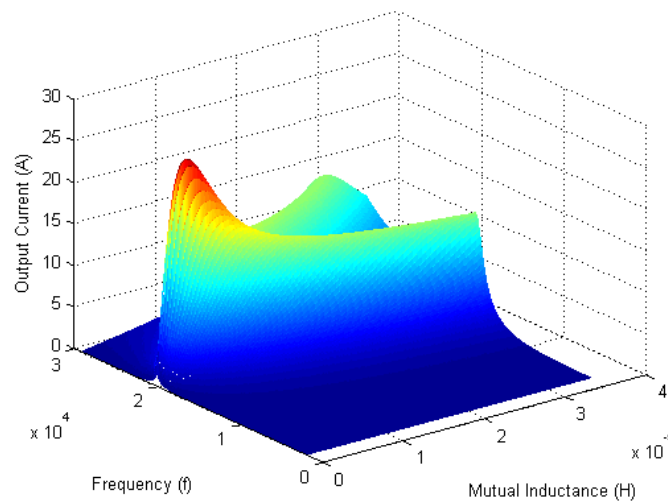
Figure 4-11: Pickup current with different mutual inductances and frequencies

It can be seen that the output current of the pickup varies with different operation frequencies and mutual inductances. The maximum current happens around the nominal frequency of 20 kHz. With an increase in mutual inductance within the critical bifurcation free region, the secondary side current can reach a maximum value at the given input voltage. Figure 4-12 shows the relationship of the maximum current and the mutual inductance at the nominal frequency without bifurcation. The boundary *M* indicates the critical coupling condition without bifurcation.
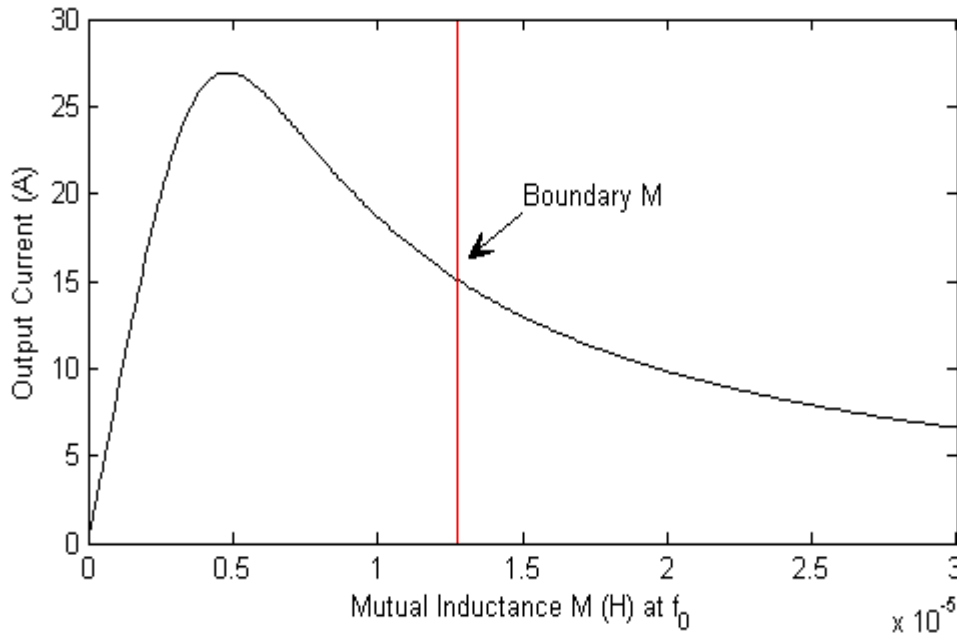
Figure 4-12: Relationship of the maximum current and the mutual inductance without bifurcation

If the system operates at the nominal angular frequency ω_0, and both the primary and the secondary circuits are tuned to this frequency, the magnitude of the secondary current I_s in rms can be simplified as:

$$I_s\Big|_{\omega=\omega_0} = \frac{\omega_0 M V_{in}}{R_p\left(R_s + R_L\right) + \omega_0^2 M^2} \qquad (4\text{-}35)$$

The maximum voltage over the load therefore can be expressed as：

$$V_{R_L}\Big|_{\omega=\omega_0} = \frac{\omega_0 M R_L V_{in}}{R_p\left(R_L + R_s\right) + \omega_0^2 M^2} \qquad (4\text{-}36)$$

According to equations (4-35) and (4-36), the output power to the load can be represented by:

$$P = \frac{R_L \omega_0^2 M^2 V_{in}^2}{\left[R_p (R_s + R_L) + \omega_0^2 M^2 \right]^2} \tag{4-37}$$

It can be seen that the power transfer capability is determined by the mutual inductance if other circuit parameters are known. The following expression enables the optimal mutual inductance for the maximum power on the load to be calculated:

$$\frac{dP}{dM} = 0 \tag{4-38}$$

To have the maximum power, according to equation (4-38), the mutual inductance has to satisfy the follow equation：

$$M = M_0 = \frac{\sqrt{R_p (R_s + R_L)}}{\omega_0} \tag{4-39}$$

The maximum power which can be transferred to the load can therefore be expressed as:

$$P_{max} = \frac{R_L V_{in}^2}{4 R_p (R_s + R_L)} \tag{4-40}$$

The optimal coupling condition for the maximum power transfer capability determined by equation (4-40) can be further expressed using the coupling coefficient k_0 as:

$$k_0 = \frac{1}{\sqrt{Q_p Q_s}} \tag{4-41}$$

where $Q_p = \omega_0 L_p / R_p$ and $Q_s = \omega_0 L_s / (R_s + R_L)$ are the quality factors of the primary coil and secondary circuit respectively.

➢ Discussion on power efficiency

Besides pursuing a higher power capability, the power efficiency associated to the mutual coupling condition is also very important when designing the IPT system with proposed

inverter tuning structure. From the above analysis, it can be seen that by varying the mutual coupling, the power capability can be very different. To achieve the maximum power transfer ability, the associated primary track current must be high, which can lead to high power losses due to the ESR of the circuit as well.

According to equation (4-33), when the system operates at the nominal frequency, the input of the power can be expressed by:

$$P_{in} = \frac{(R_s + R_L)V_{in}^{2}}{R_p(R_s + R_L) + \omega_0^{2}M^{2}} \tag{4-42}$$

The power efficiency can therefore be expressed as:

$$\eta = \frac{R_L\omega_0^{2}M^{2}}{R_p\left(R_s + R_L\right)^{2} + \omega_0^{2}M^{2}\left(R_s + R_L\right)} \tag{4-43}$$

The power efficiency is related to the mutual inductance. A higher mutual inductance may result in a higher efficiency but lower power transfer capability. Therefore, at the optimal coupling coefficient that achieves the maximum power transfer, the power efficiency would be low. Figure 4-13 shows the relationship between the efficiency and the output power. It can be seen that under the optimal mutual inductance, the power efficiency is about 65% for the selected system.
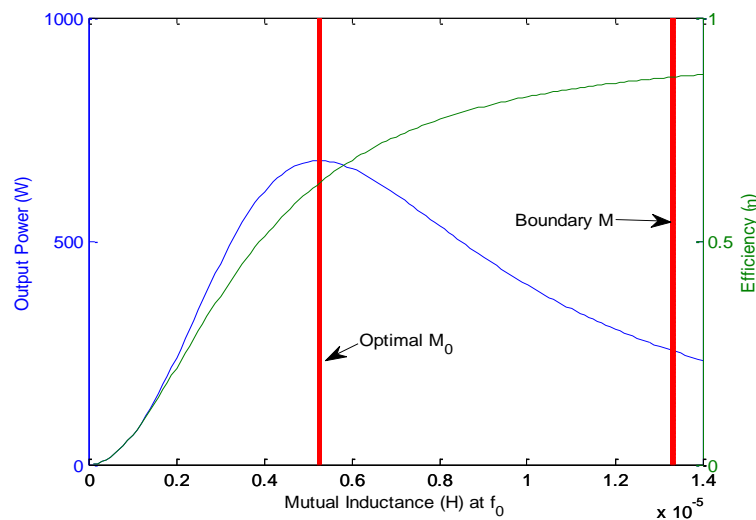
Figure 4-13: The efficiency and output power vs. mutual inductance

The characteristic shows that the optimal coupling is very useful for the system which requires the maximum power transfer with less care of power efficiency, such as a biomedical implant system, or systems that requires short periods of high power capability.

➢ Practical verification

An experiment circuit shown in Figure 4-1 has been set up to verify the theoretical analysis based on the circuit parameters listed in the Table 5-3 with the exception of the input voltage. This is because to verify the maximum power transfer capability, the primary side is required to handle a large current. If the input voltage is too high, then the primary current will also be dramatically increased under the fully tuned and loose coupling conditions. To simplify the experiment setup and have a safe operation, the input voltage (V_{DC}) of the system was chosen to be 4.5V in this experiment study.

For the given circuit, to have a variable coupling, the primary side is fixed and the pickup is moved to be close to or be away from the primary side. The output power is measured practically against the coupling variation. Experimental results are plotted in Figure 4-14.
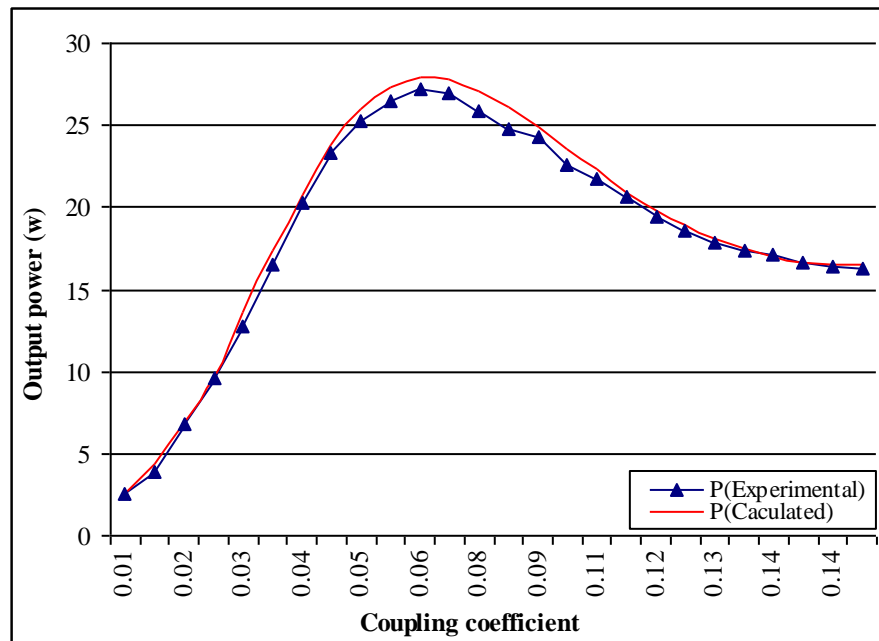
Figure 4-14: Experimental results of the output power under different coupling coefficients

For comparison purposes, the calculated results of output power from equation (4-37) are also plotted in the same diagram. As shown in Figure 4-14, the maximum power from the

experiment is about 26W when the coupling coefficient is 0.06. The calculated maximum power is 27.9W using equation (4-39), and an optimal coupling coefficient of 0.064 is obtained from equation (4-40). The experiment and theoretical results are in good agreement. Both, theoretical analysis and experimental results, have verified that an optimal coupling condition corresponds to the maximum power transfer of an IPT system

4.6 Components Sensitivity Analysis

The above analysis with the selected pickup was based on ideal components, the value of which are assumed to be constant during operation. However, practically, the components will have losses, parasitic, tolerances and operational variations. Consequently, these characteristics will influence the system frequency and the performance. Therefore the analysis of the effect on the system performance caused by the variation of the components is necessary. In this section, a sensitivity analysis is performed to help define the design parameters for an IPT system with the proposed energy injection inverter.

As stated before, the variable frequency operation of the proposed inverter enables the inverter to operate at the zero phase angle frequency of the load impedance. The system operational frequency and the power transfer capability depend on all system parameters.

Except for the coupling coefficient k and the load R_L, which are the major impact factors on the system frequency, variations in other components and parameters will also influence the frequency and the related power transfer capability. In particular, the variation of the tuning capacitors during operation will shift the operation frequency and result in a reduced power transfer capability.

Figure 4-15 shows an equivalent T shape network model which can be used to analyze the proposed IPT system . The ESRs of the reactive components are considered and the detailed parameter values can be found in Table 4-1. In order to avoid system bifurcation, the load and the mutual inductance are selected to be larger than the calculated values using equations (4-18) and (4-31). The equivalent AC load resistance of R_L is selected to be 1.66Ω as the fully loaded condition in this analysis.
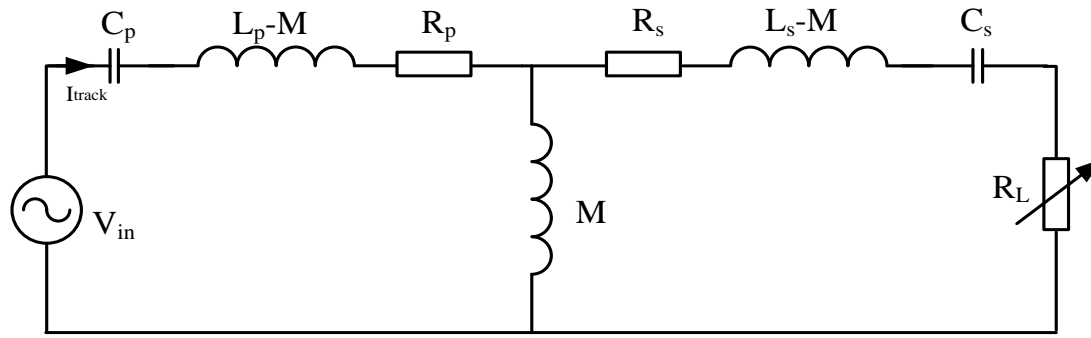
Figure 4-15: A T network model of proposed IPT system

Normal sensitivity and worst case analysis have been carried out to evaluate both the increases and decreases of the zero phase angle frequency of the input current where the voltage and resonant current are in phase. Table 4-2 shows the frequency shift under the normal sensitivity test, where the components are increased and decreased by 1%.

Table 4-2: Sensitivity analysis results of the frequency shifting around 20 kHz

Variables	Δ**f**	*Variables*	Δ**f**
$L_p\sim$ *+1%*	-133Hz (-0.653%)	$C_p\sim$ *+1%*	-133Hz (-0.654%)
$L_p\sim$ *-1%*	+136Hz (-0.668%)	$C_p\sim$ *-1%*	+136Hz (-0.668%)
$L_s\sim$ *+1%*	33Hz (-0.163%)	$C_s\sim$ *+1%*	33Hz (-0.163%)
$L_s\sim$ *-1%*	-32Hz (-0.160%)	$C_s\sim$ *-1%*	-32Hz (-0.160%)
$R_p\sim$ *+1%*	$\approx$0Hz (-7.07E-7%)	$R_s\sim$ *+1%*	$\approx$0Hz (-7.07E-7%)
$R_p\sim$ *-1%*	$\approx$0Hz (-7.07E-7%)	$R_s\sim$ *-1%*	$\approx$0Hz (-7.07E-7%)

It can be seen from Table 4-2 that the frequency shift is more sensitive to component variations on the primary side. The frequency decreases when the component values of the primary side increase. However, the trend is different for component variations on the secondary side. The frequency increases with increasing of the components values of secondary side, but the sensitivity is low. To clearly see the results, the primary track

current and the current phase shift with the variation of +1% in the circuit parameters is shown in Figure 4-16.
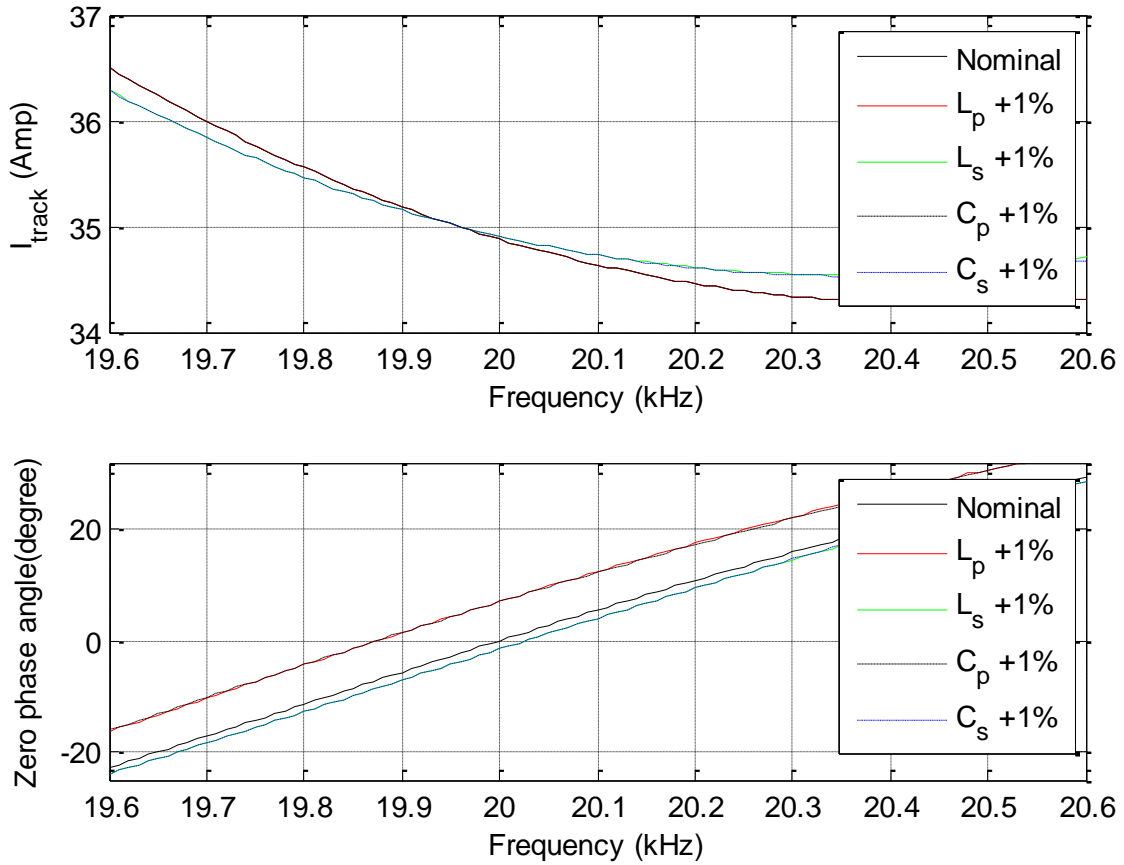
Figure 4-16: Frequency shifting caused by 1% increase of the circuit components

It can be seen that the zero phase angle frequency of the primary inverter varies accordingly with variations on the components. Figure 4-16 further shows that the phase angle of track current is clearly related to all components and is more sensitive to the primary components. Therefore, it implies that the most sensitivity components to the frequency are on the primary side. Increases of both primary inductance and capacitance will cause the frequency to decrease. But the magnitude of the maximum achievable track current is irrelevant to variations on the primary side components. Conversely variations of secondary side components will affect in both the frequency and the magnitude of track current on the primary side.

To observe the results more clearly, the sensitivities are analyzed under the worst case condition of the variation, which is a ±5% change in parameter variation. The variation in

the track current magnitude and the track network input current phase angle around the nominal frequency of 20 kHz are shown in Figure 4-17 and Figure 4-18 for variations in both the primary side components and the secondary side components respectively.
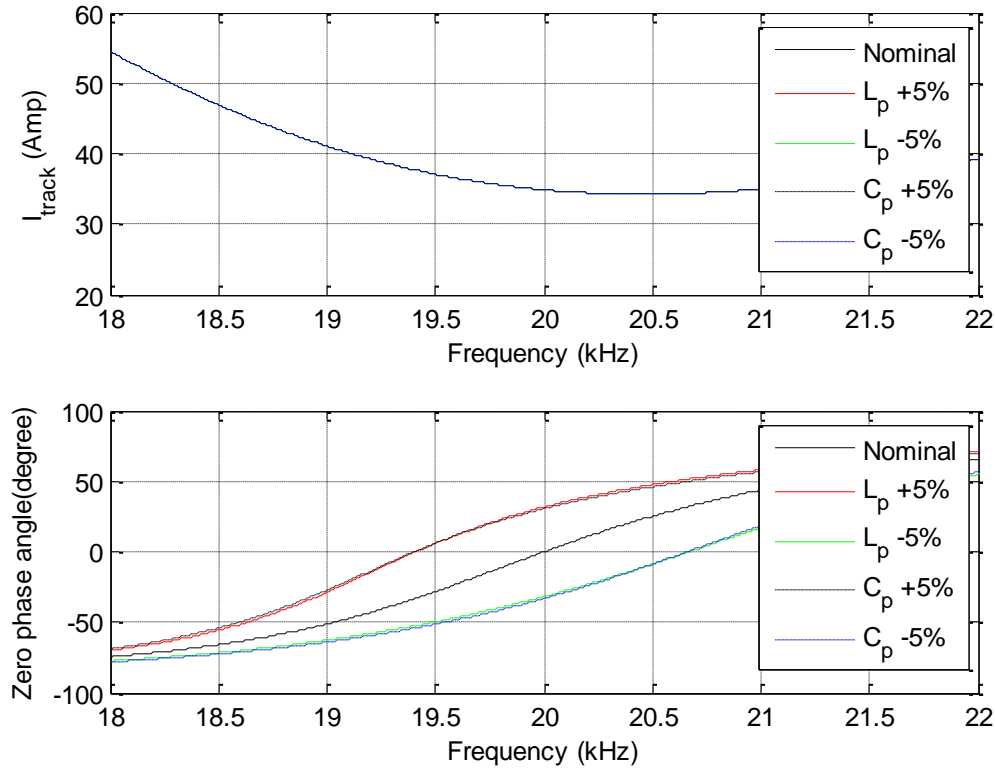
Figure 4-17: Worst case frequency shift with ±5% variation on the primary side components
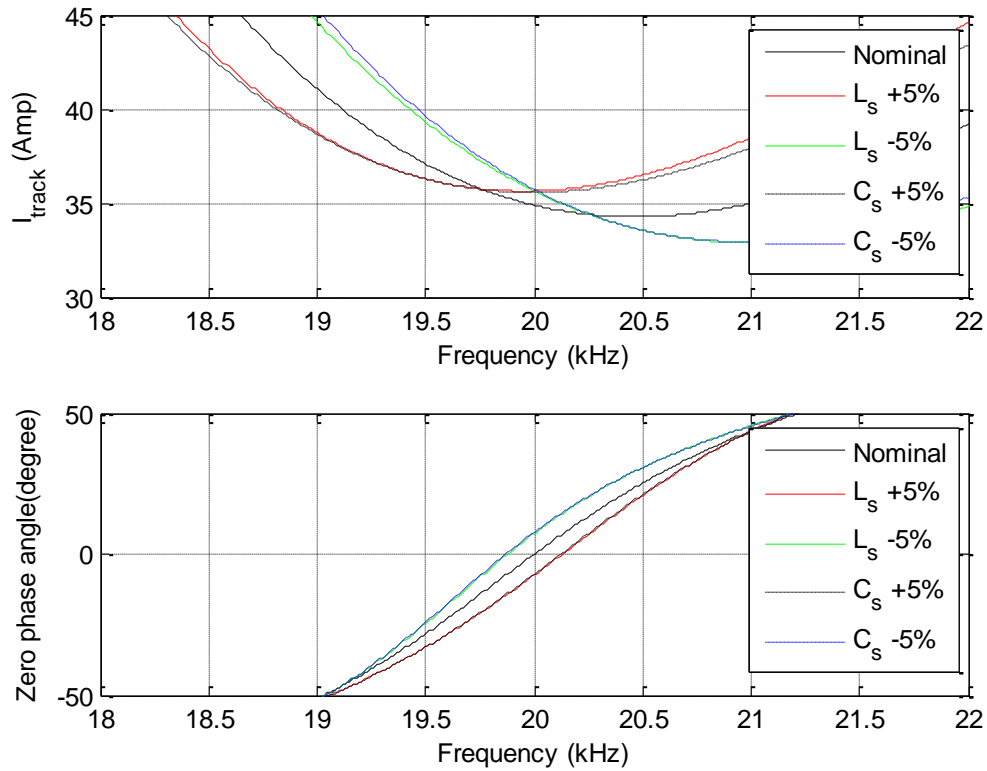
Figure 4-18: Worst case frequency shift with ±5% variation on the secondary side components

As shown, when the maximum tolerance of the primary side components is set to ±5%, the shift in maximum frequency is up to about ±3.0% from the original. A +5% and -5% variation on primary components causes the -5% or +5% variation on the primary current respectively. The frequency shift is about +1% with a -5% variation, and +1% with a -5% variation in the secondary components. The magnitude of the primary current varies about +5% with ±5% variations on components of the secondary side. This means that any variations of components on the secondary side may cause the track current of the proposed inverter to increase.

4.7 Summary

This chapter has discussed the behavior and properties of the proposed inverter with the considerations of the system bifurcation, power transfer capability, and frequency sensitivity at a system level, which has one or more secondary pickup included.

System bifurcation phenomenon was discussed using a full system model. The effect of the loading condition of a single pickup has been discussed. It was found that under variable frequency operation, the primary inverter with energy injection control may have more than one operational frequency when the load on the pickup increases to certain level. A theoretical analysis was undertaken and an analytical critical maximum loading condition was found. In addition, the frequency stability problem was analyzed for a system with multiple pickups. It was found that the proposed inverter can achieve a better power transfer when operating with multiple distributed pickups. To avoid the system bifurcation, the maximum boundary condition of the number of secondary pickups was determined.

The effect of coupling between the primary and the secondary pickups on the system frequency stability was also analyzed. The analytical solution of the boundary coupling condition was found to enable the design of a bifurcation free power inverter. An analysis was conducted to investigate the effect of system coupling condition on the output power. It was found that there is an optimal coupling condition corresponding to the maximum power transfer capability of the primary inverter. The experimental result has proven the validity of the theoretical analysis.

The component sensitivity analysis has been carried out finally with a bifurcation free system designed. Normal sensitivity and worst case analysis were applied. The trends in the frequency variation are different to the variation on the primary side and the secondary side components. It was shown that the frequency shift is more sensitive to the variation on primary side components.

Chapter 5

A Primary Power Flow Control Method Using Energy Injection with Secondary Feedback

5.1 Introduction
5.2 Structure of a Closed Loop System
5.3 Magnitude Regulated Power Flow Control
5.4 Controllable Output Range
5.5 Simulation Studies
5.6 Implementation and Experimental Verification
5.4 Summary
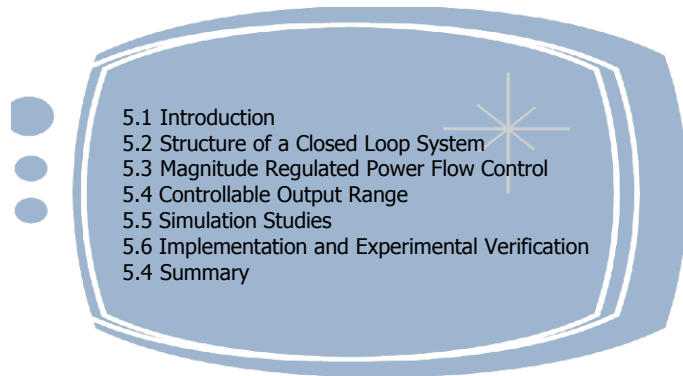
5.1 Introduction

Power flow control is of great importance when designing an IPT system. Due to the physical independency of the primary and secondary side, the power flow control can either be achieved on the primary power supply or the secondary power pickup of an IPT system. Both of them have gained success in different applications.

To date, power flow control on the secondary side is a popular solution and has been widely adopted by most IPT applications. Among the power flow control techniques on the secondary side, shorting control is the most well-known control technique and has gained great success due to the simplicity and effectiveness[118, 119]. By shorting the pickup coil, the induced power on the secondary side is decoupled from the load. As a result, the power flowing to the load is controlled. Apart from this shorting control method, the power flow to the load can also be controlled by tuning/detuning the secondary pickup, which can be achieved by varying the tuning inductance or capacitance [20, 95].

Because power regulation can be achieved individually on each pickup, power flow control on the secondary side is particularly suitable for multiple pickups systems, or a single pickup system with less limitation on weight, size, or heat, etc. However, practically, there are many applications where only one controllable pickup is coupled to a single primary power supply. The presence of extra controllers or switching circuits on the secondary can make the power pickup too large or too heavy to implement. Taking a biomedical TET application as an example, extra weight and size by extra circuitries could inflict severe pain on a patient. In addition, the heat generated by the additional controller in the pickup may cause tissue damage. Therefore it is preferable to control the power flow on the primary side for such applications where the size, weight, and heat generation are a major concern.

When the power flow is controlled from the primary side, feedback from the power pickup is needed. No matter what controller is used, fundamentally power flow control from the primary side is required to control the primary magnetic field. This can be achieved by either varying the magnitude of the primary current [33], or tuning/detuning the primary circuit [120]. To tune or detune the primary circuit, the effective tuning inductances or capacitances of the primary resonant converter can be changed by switching them in and out. Again, this involves extra components and circuitry. Consequently, it increases the power losses, the system cost and size, and control complication. To change the magnitude of the primary current, one popular method is to vary the input DC voltage, which can be achieved by using a buck or boost converter. This method is very simple, but it increases the cost, size and power losses of the primary converter. Another method is to shift the "on" and "off" switching phases so that the output voltage, and thus the track current is regulated. Such a method can be very complicated in control and difficult to achieve soft switching, thereby causing high power losses and EMI. Since auxiliary circuits need to be added to the main power circuits to realize soft-switching, the final system is often very complicated and costly.

This chapter proposes a power flow control method on the primary side using energy injection control to regulate the magnitude of the track current to supply power to a single power pickup. Compared to the quantum based open loop control for IPT applications [102], the proposed primary power flow control method can achieve power regulation

based on cycle control methods with wireless feedback from the secondary side. There are no extra switching components required to achieve the power regulation. In addition, all switches operate under ZCS conditions, and the output power flow is fully controllable from zero to rated maximum. A practical slip ring system is implemented to verify the proposed primary power flow control method.

5.2 Structure of a Closed Loop System

Figure 5-1 shows the basic structure of an IPT application for a contactless slip ring system with the proposed primary side track current magnitude control based on RF feedback from a secondary power pickup. The full bridge series tuned primary power converter is powered by a constant DC voltage source (V_{DC}). Unlike other magnitude control methods, which vary the input voltage by applying a DC-DC power converter such as a buck/boost converter, the proposed method only controls the semiconductor switches. The operation of the switches is controlled according to energy injection concepts determined by the output and the feedback from the secondary power pickup.
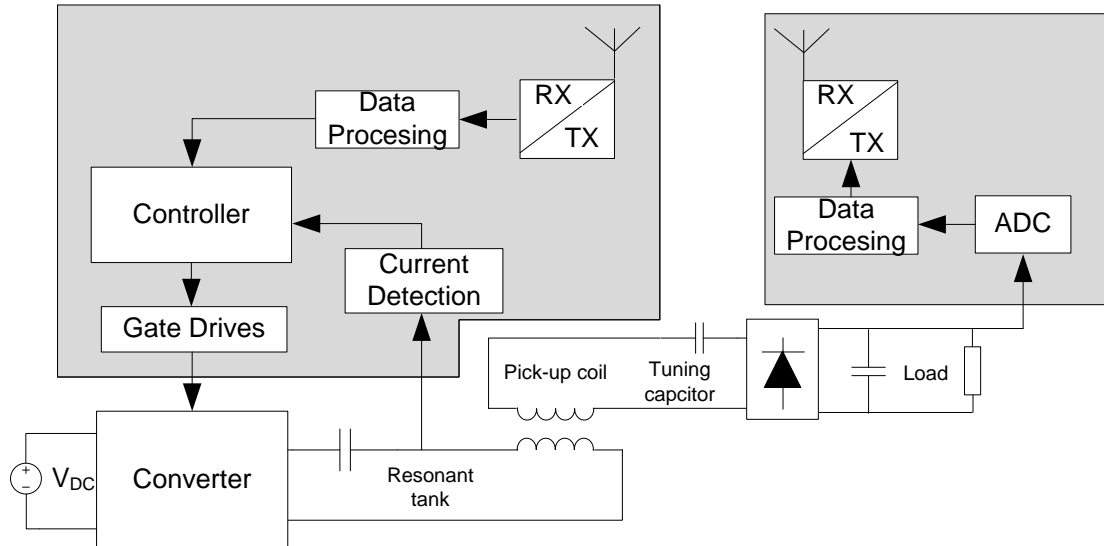
Figure 5-1: A magnitude controlled IPT system with a feedback

5.3 Magnitude Regulated Power Flow Control

To achieve the power flow control with soft switching operation on the primary side inverter, the resonant track current is detected to obtain the zero crossing points. The gate

drive control signal is generated according to the polarity of the track current and the output voltage. The output voltage of the pickup is detected on the secondary side. The value of V_o can be determined by the primary circuit through a radio communication channel. Through this closed-loop control means the power flow control can be achieved by controlling the magnitude of the primary side track current. As a result, the average value of the output voltage is maintained to be constant.

According to the primary side track current resonance, the detailed control method can be divided into three different modes as shown in Figure 5-2. Because of the mutual coupling of the primary track and the secondary pickup, the power flow control can be achieved by controlling the switches on and off on the primary side.

Mode I

Mode II

Mode III
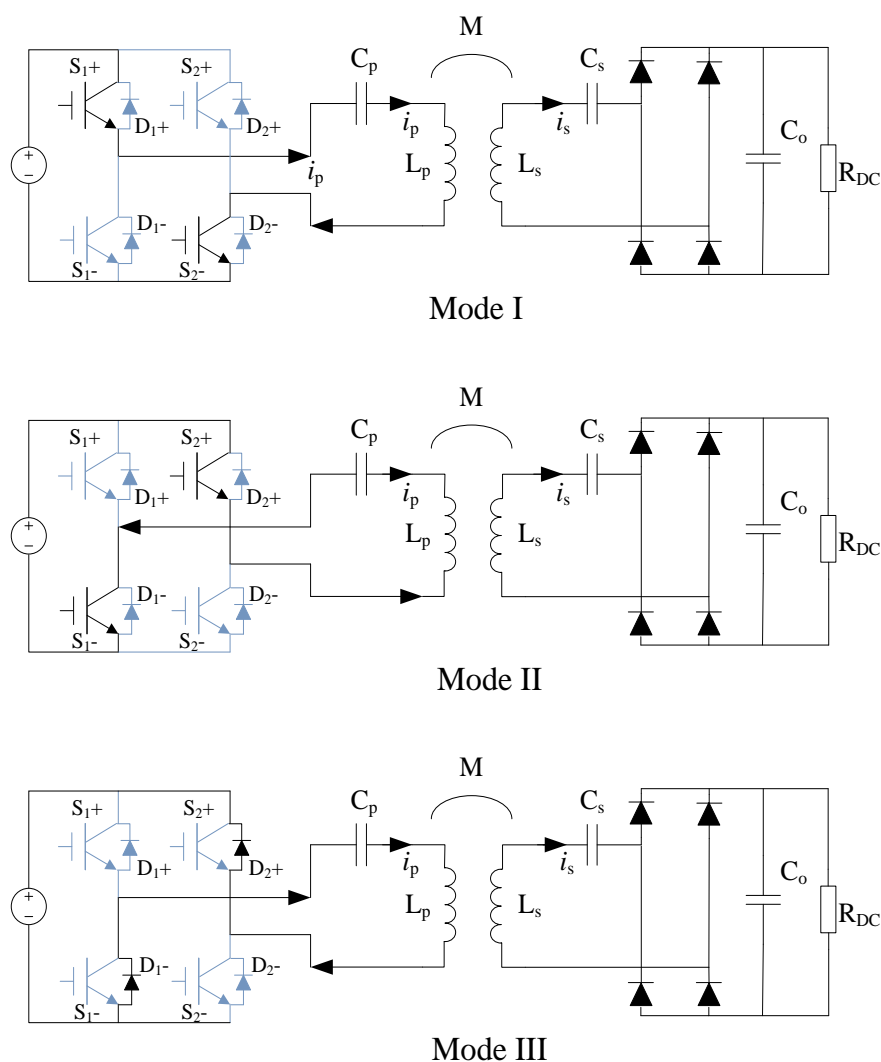
Figure 5-2: Operation modes of proposed method

It can be seen from Figure 5-2, in mode I, switches S_1+ and S_2- are controlled on when the resonant current is in the positive direction. The input voltage is added to the primary resonant tank and in phase with the primary resonant current which is in the positive direction. Under such a condition, new energy is injected into the primary resonant tank. The track current is then boosted and the induced power is transferred to the secondary side because of the mutual coupling. As a result, the voltage over the load increases.

In mode II, switch S_2+ and S_1- are controlled on, the input voltage is in phase with the current when it is in negative direction. New energy is then injected and transferred to the secondary if the required power on the secondary side appears to be insufficient. The primary power converter operates between these two operation modes I and II, until the output voltage on the secondary side reaches the demanded value, after which the operation changes to mode III.

In mode III, the resonant current is in the positive direction. All switches at this point are off having D_2+ and D_1- on to conduct the current until the resonant current falls back to zero. Therefore, no energy is injected during this operation. Instead, the stored redundant energy flows back to the power source.

Based on the possible operation modes, a detailed control strategy is developed to maintain the output voltage of the power pickup constant at some desired value. Soft switching operation of the primary converter is applied to reduce the voltage/current stress on the switches, the switching power losses, and to maintain the quality of the track current. To control the power flow on the primary side, the output voltage of the secondary is detected via the wireless feedback. The output voltage is compared to a predefined reference value to decide which switch pair to operate. In addition, the soft switching operation is achieved by detecting the polarity of the high frequency primary resonant AC current. When the output voltage is larger than the reference and the track current in the network is larger than zero, S_1+/S_2- are controlled to be on. This switching state is held until the current in the track loop finishes its positive half cycle and returns to zero. S_2+/S_1- are then turned on to keep the current flow until the output voltage is detected to be smaller than the reference.

Because of the existence of the rectification circuit on the secondary side, the resonant current of the secondary side may be discontinuous. This makes the system operation nonlinear. As such, the analysis becomes more complicated. To clearly understand all the operating conditions, the system is further examined with the consideration of the states of the secondary side current.

From Figure 5-2 it can be seen that, if the secondary side current is continuous, the equivalent circuit can be expressed as shown in Figure 5-3.
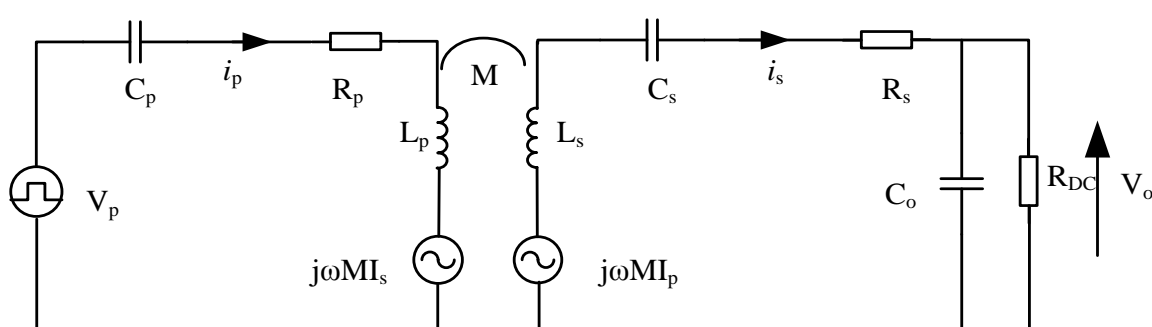
Figure 5-3: Equivalent circuit of the system under continuous current mode

Here V_p represents the input voltage of the resonant track, which can either be positive or negative as determined by the operation modes of the semiconductor switches. The possible operation modes of the system in terms of the directions of primary track current are presented in Figure 5-4. According to the conduction conditions of the semiconductor devices on both primary and secondary sides, the three circuit operating modes of the system can be further divided into eight different states according to the polarities of each current.
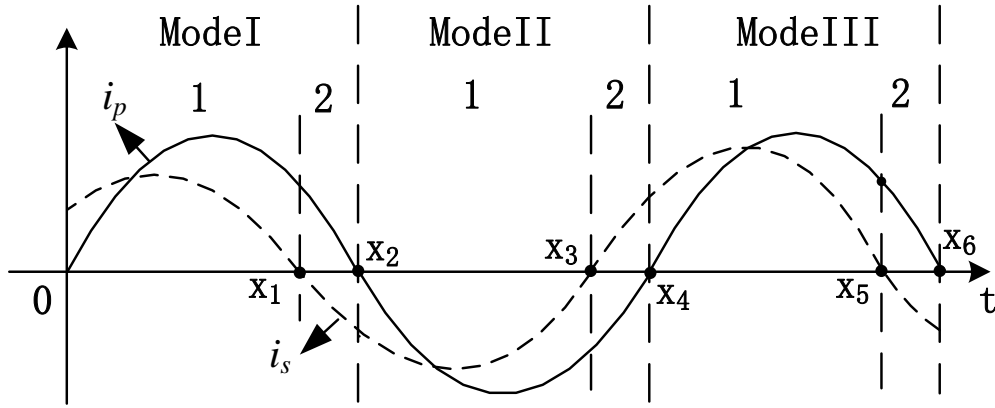
Figure 5-4: Basic operating states of the proposed converter under continuous mode

The detailed selection conditions of the operating modes, according to the output voltage and the conditions of the current are listed in Table 5-1.

Table 5-1: Circuit operation states with continuous secondary side current

$i_p>0$	$i_s>0$	$V_o<V_{ref}$	Mode I_1
$i_p>0$	$i_s<0$	$V_o<V_{ref}$	Mode I_2
$i_p<0$	$i_s<0$	$V_o<V_{ref}$	Mode II_1
$i_p<0$	$i_s>0$	$V_o<V_{ref}$	Mode II_2
$i_p<0$	$i_s<0$	$V_o>V_{ref}$	Mode II_3
$i_p<0$	$i_s>0$	$V_o>V_{ref}$	Mode II_4
$i_p>0$	$i_s>0$	$V_o>V_{ref}$	Mode III_1
$i_p>0$	$i_s<0$	$V_o>V_{ref}$	Mode III_2

Introducing two nonlinear state selection functions: the switching function S(t) and sign function $Sgn(x)$, which can be introduced as:

$$S(t) = \begin{cases} 1 & S_1+/S_2-, on \quad D_2+/D_1-, on \\ -1 & S_2+/S_1-, on \end{cases}$$
(5-1)

and

$$Sgn(x) = \begin{cases} 1 & x>0 \\ -1 & x<0 \end{cases}$$
(5-2)

according to Kirchhoff's voltage law, the differential equations for all the different operating conditions, when the secondary side current is continuous, can be expressed as:

$$
\begin{cases}
\dfrac{di_p}{dt} = \dfrac{L_s}{\Delta}(R_p i_p + V_{C_p} - V_p S(t)) + \dfrac{M}{\Delta}(R_s i_s + V_{C_s} + V_O) \\[2mm]
\dfrac{dv_{C_p}}{dt} = \dfrac{1}{C_p} i_p \\[2mm]
\dfrac{di_s}{dt} = \dfrac{L_p}{\Delta}(R_s i_s + V_{C_s} + V_O) + \dfrac{M}{\Delta}(R_p i_p + V_{C_p} - V_p S(t)) \\[2mm]
\dfrac{dv_{C_s}}{dt} = \dfrac{1}{C_s} i_s \\[2mm]
\dfrac{dv_O}{dt} = \dfrac{1}{C_o}\mathrm{sgn}(i_s) - \dfrac{V_O}{C_o R_{DC}}
\end{cases}
\qquad (5\text{-}3)
$$

where $\Delta = M^2 - L_p L_s$. Writing equation (5-3) in vector format, the system can be expressed as:

$$
\dot{X} = AX + BV \qquad (5\text{-}4)
$$

where

$$
A =
\begin{bmatrix}
\dfrac{L_s R_p}{\Delta} & \dfrac{L_s}{\Delta} & \dfrac{MR_s}{\Delta} & \dfrac{M}{\Delta} & \dfrac{M}{\Delta} \\[3mm]
\dfrac{1}{C_p} & 0 & 0 & 0 & 0 \\[3mm]
\dfrac{MR_p}{\Delta} & \dfrac{M}{\Delta} & \dfrac{L_p R_s}{\Delta} & \dfrac{L_p}{\Delta} & \dfrac{V_o L_p}{\Delta} \\[3mm]
0 & \dfrac{1}{C_s} & 0 & 0 & 0 \\[3mm]
0 & \dfrac{1}{C_O}\mathrm{sgn}(i_s) & 0 & 0 & -\dfrac{V_o}{C_o R_{DC}}
\end{bmatrix}
\qquad (5\text{-}5)
$$

$$
B = \begin{bmatrix} \dfrac{-L_s S(t)}{\Delta} & 0 & \dfrac{-MS(t)}{\Delta} & 0 & 0 \end{bmatrix}^T
\qquad (5\text{-}6)
$$

If the output voltage is high enough, no energy is required to be injected into the system. As a result, the primary track current decreases rapidly in just few cycles. Consequently

the induced power on the secondary side drops and becomes insufficient to sustain a continuous current through the rectifier. Under this situation, the primary side and the load are naturally decoupled. The primary side and the secondary side work separately. The current on the primary side track circulates. However, the secondary side current is discontinuous. Only the stored energy in the DC capacitor supplies power to the load. The equivalent circuit on this situation can be shown in Figure 5-5.
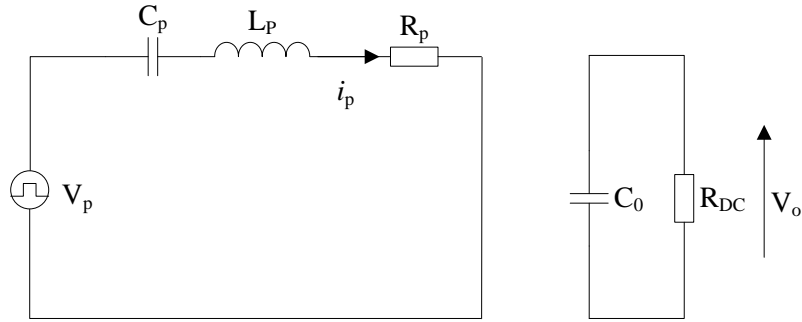
Figure 5-5: Equivalent circuit of the system under discontinuous mode

The mode of operation under such a situation becomes simple, as the secondary side current is zero, and is only determined by the conditions of the primary track current and the output voltage. The detailed selection conditions of the appropriate mode of operation according to the output voltage and the current are listed in Table 5-2.

Table 5-2: Circuit operation states with discontinuous secondary side current

$i_p>0$	$i_s=0$	$V_o<V_{ref}$	Mode I_3
$i_p>0$	$i_s=0$	$V_o<V_{ref}$	Mode I_4
$i_p<0$	$i_s=0$	$V_o<V_{ref}$	Mode II_5
$i_p<0$	$i_s=0$	$V_o>V_{ref}$	Mode II_6
$i_p>0$	$i_s=0$	$V_o>V_{ref}$	Mode III_3
$i_p>0$	$i_s=0$	$V_o>V_{ref}$	Mode III_4

The differential equations of the system under this situation, where the secondary side current is discontinuous, can be expressed as:

$$\begin{cases} \dfrac{di_p}{dt} = -\dfrac{1}{L_p}(R_p i_p + V_{C_p} - V_p S(t)) \\[2ex] \dfrac{dv_{C_p}}{dt} = \dfrac{1}{C_p} i_p \\[2ex] \dfrac{dv_O}{dt} = -\dfrac{V_O}{C_o R_{DC}} \end{cases} \tag{5-7}$$

Writing in a vector format as in equation (5-4), where

$$A = \begin{bmatrix} \dfrac{R_p}{L_p} & \dfrac{1}{L_p} & 0 & 0 & 0 \\[2ex] \dfrac{1}{C_p} & 0 & 0 & 0 & 0 \\[2ex] 0 & 0 & 0 & 0 & 0 \\[1ex] 0 & 0 & 0 & 0 & 0 \\[1ex] 0 & 0 & 0 & 0 & -\dfrac{V_o}{C_o R_{DC}} \end{bmatrix} \tag{5-8}$$

$$B = \begin{bmatrix} \dfrac{-S(t)}{L_p} & 0 & 0 & 0 & 0 \end{bmatrix}^T \tag{5-9}$$

As the differential equations are for the high order system, it is difficult to get an analytical solution. As such a discrete time mapping method can be applied to get the system numerical solutions, by taking the sampling period $T_s \ll T$ and get the discrete iterative equations as:

$$x(t) = \phi_i(T_s)x_n + \int_0^{T_s} \phi_i(T_s - \tau)B_i u\, d\tau \tag{5-10}$$

where $\phi_i(T_s) = e^{A_i T_s} = 1 + \sum\limits_{n=1}^{\infty} \dfrac{1}{n} A_i^n T_s^n$. The selection of each state is determined according to Table 5-1 and Table 5-2.

5.4 Controllable Output Range

The above modeling gives the general descriptions of the operation of the primary power converter. The result shows that the output voltage of the secondary is greatly related to

the operation of the primary converter. Power flow can be controlled within a range from zero to the rated maximum. Therefore, it is important to know the controllable region when designing the IPT system. This section analyzes and qualifies the maximum controllable output voltage on the secondary side of an IPT system.

According to the above analysis, in order to have a maximum output voltage, the primary side converter has to operate between mode I and mode II to have a continuous current. Therefore, the input voltage on the primary side has to be in phase with the resonant track current at all times. By neglecting the harmonics generated from the inverting network, the circuit in Figure 5-3 can be transformed into an equivalent T circuit shown in Figure 5-6 [121]. To simplify the analysis, only the fundamental part of the voltage is considered. The secondary side DC load can be expressed by an AC load R_L with an equivalent value $0.81R_{DC}$.
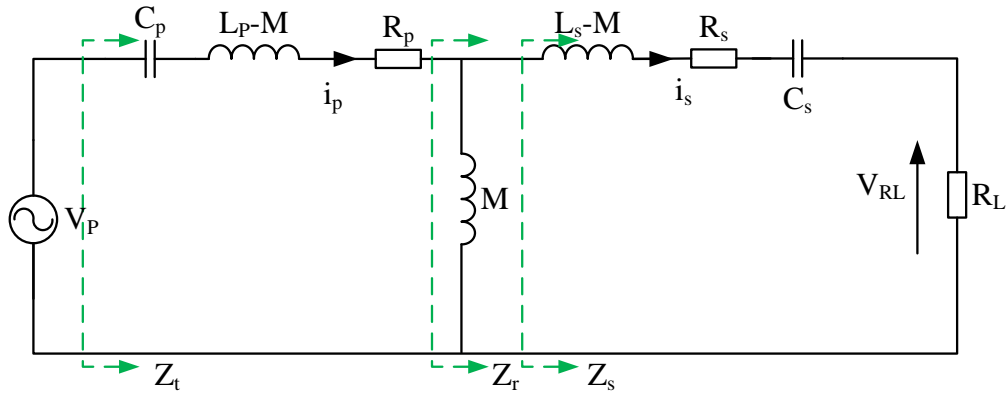
Figure 5-6: Equivalent circuit of a coupled IPT system

From Figure 5-6, it can be seen that the output voltage is related to the input voltage and the rest of the system components. The output voltage over the load can be expressed as:

$$V_0 = \left| \frac{Z_s R_L}{Z_t Z_r} V_p \right| \tag{5-11}$$

Here,

$$Z_s = X_s + R_s + R_L \tag{5-12}$$

$$Z_r = \frac{X_m Z_s}{X_m + Z_s} \tag{5-13}$$

$$Z_t = X_p + Z_r \tag{5-14}$$

$$X_p = \omega L_p - \omega M - 1/\omega C_p \tag{5-15}$$

$$X_s = \omega L_s - \omega M - 1/\omega C_s \tag{5-16}$$

$$X_m = \omega M \tag{5-17}$$

Substituting equations (5-12) -(5-17) into equation (5-11), the output voltage gain of the system can be obtained and expressed as:

$$G_v = \frac{\dfrac{R_L}{R_L + R_s}}{\sqrt{\left(1 + \dfrac{X_p}{X_m} + \dfrac{R_p}{R_L + R_2} + \dfrac{X_s R_p}{X_m (R_L + R_s)}\right)^2 + \left(\dfrac{X_p + X_s + \left(X_p X_s - R_p (R_L + R_s)\right)/X_m}{R_L + R_s}\right)^2}} \tag{5-18}$$

Based on this voltage gain equation, it can be seen that the output voltage is determined by selected coupling conditions and practical operation if the energy injection is taking place every half cycles. If the converter is designed to have both primary side and secondary side tuning at the same frequency:

$$\omega_0 = \frac{1}{\sqrt{L_p C_p}} = \frac{1}{\sqrt{L_s C_s}} \tag{5-19}$$

By defining the $Q_m = R_L/\omega_0 M$, then the relationship between the normalized frequency and output voltage gain of the system can be presented in Figure 5-7.
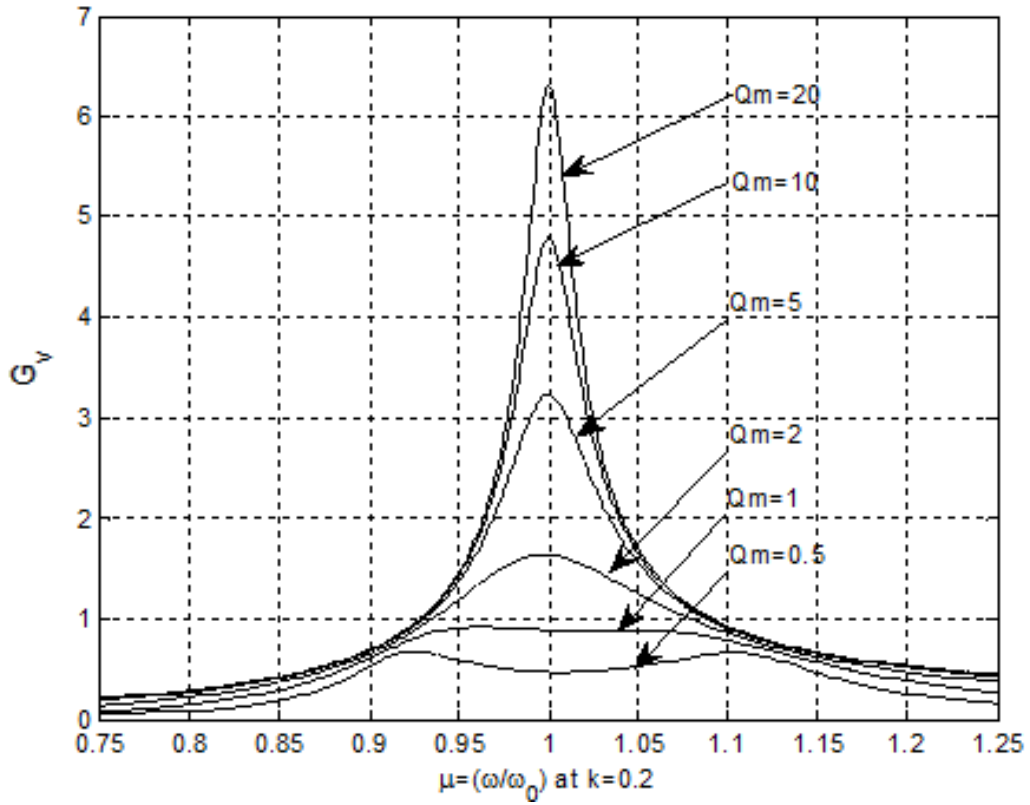
Figure 5-7: Relationship between G_V and Q_m

It can be seen from Figure 5-7 that different Q_m enables the output voltage to vary at different operation frequencies, but the output voltage gain reaches its maximum value if the system frequency is at the nominal tuned frequency. However, when Q_m is around or less than 1, the maximum output voltage gain is not at the nominal frequency, and higher output voltages occur at different frequencies. This is because a small Q_m represents a large loading condition for the IPT system. As a result, heavy loads cause system frequency bifurcation. This phenomenon has been discussed in Chapter 4. The maximum load has to be carefully selected to be within the load boundary as defined in Chapter 4.

If the system operates at the nominal angular frequency ω_0, by substituting equation (5-15) - (5-17) into equation (5-18), then the voltage gain from equation (5-18) can be simplified and expressed as:

$$G_v = \frac{R_L{}^2 Q_m}{R_L{}^2 + Q_m{}^2 \left(R_p\left(R_s + R_L\right)\right)} \tag{5-20}$$

The relationship between the output voltage gain and the Q_m under different system coupling conditions is shown in Figure 5-8.
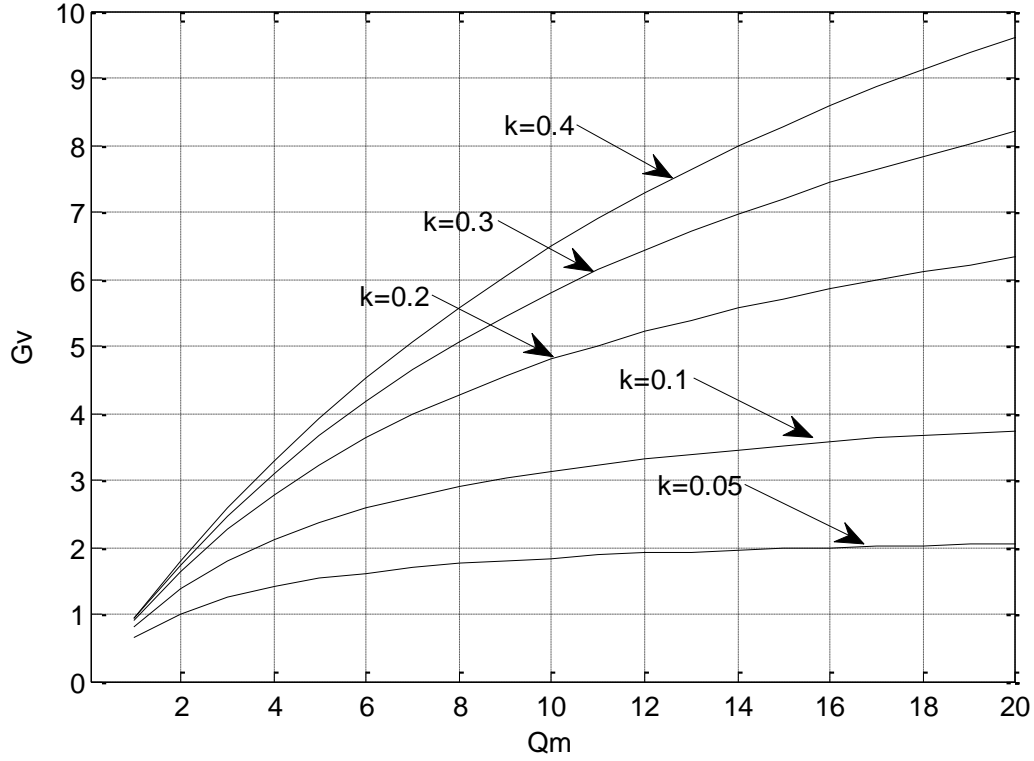
Figure 5-8: Relationship between G_V and the Q_m under different system coupling conditions

As can be seen from Figure 5-8, at the nominal operating frequency and typically for $Q_m>1$, the output voltage is higher if the system has good coupling. However, when the load R_L is fixed, the maximum output voltage can be obtained for certain loading condition, if the Q_m can satisfy the following condition:

$$Q_{m0} = R_L / \sqrt{R_p \left(R_s + R_L \right)} \tag{5-21}$$

By taking equation (5-21) into equation (5-20), the maximum output voltage gain under certain load can be obtained and expressed as:

$$G_v = \frac{R_L}{2\sqrt{R_p \left(R_L + R_s \right)}} \tag{5-22}$$

It can be seen that under the load condition of R_L=1.62Ω, the output voltage is different under different Q_m. It has been found that if Q_m is equal to Q_{m0}=3.19 from equation (5-21), then the best system coupling conditions can be obtained. For this load example condition, the coupling coefficient is calculated to be k=0.073, which is also plotted in Figure 5-9.
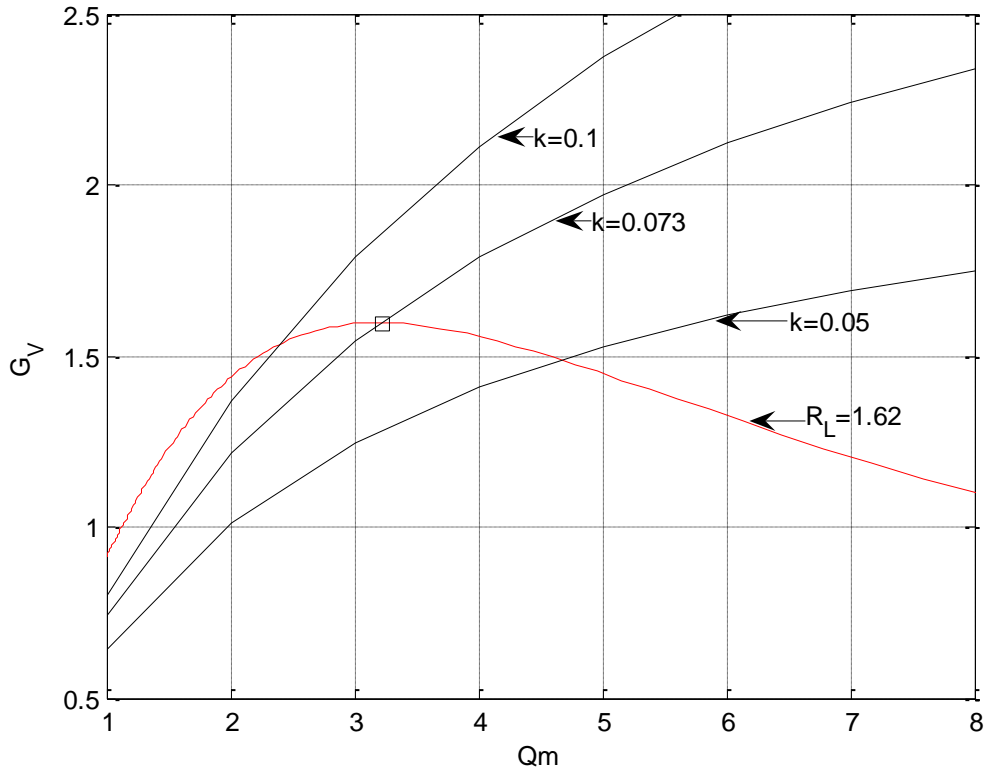
Figure 5-9: Relationship between the output voltage under fixed load with different coupling conditions

The crossing points represent the output voltage gain curves with different coupling conditions under a fixed load R_L=1.62Ω. This result means that under a given load condition, the controllable output voltage range of the IPT system from the primary side converter has to be within the maximum output gain obtained from equation (5-22).

5.5 Simulation Studies

A simulation study has been conducted to verify the proposed primary power regulation method based on the magnitude control of the primary current using the PLECS tool box

in Matlab. A flow chart of the control algorithm of the simulation study is shown in Figure 5-10.

Figure 5-10: Flow chart of the control algorithm

The simulation study is carried out to verify the proposed primary control under full load conditions. Detailed primary and secondary circuit parameters used for this simulation analysis are based on the parameters of a practical slip ring system and are listed in Table 5-3.

Table 5-3: Component parameters of the contactless slip ring system

Notes	Symbol	Value
Input dc voltage	V_{DC}	24 V
Primary coil inductance	L_p	67.81 µH
Secondary coil inductance	L_s	45.16 µH
Primary tuning capacitance	C_p	0.905 µF
Secondary tuning capacitance	C_s	1.360 µF
Mutual inductance	M	7.66×10^{-6} µH
Primary coil ESR	R_p	0.150 Ω
Secondary coil ESR	R_s	0.095 Ω
Output voltage	Vo	15 V
DC load resistance	R_{DC}	2 Ω
Output power	P	112W

5.5.1 System response in full load condition

From the given specifications, the output voltage on the secondary side of the IPT system is required to be at +15V at 112W for the practical slip ring application, which is within the maximum achievable range of the output voltage by equation (5-22). Figure 5-11 shows the simulation waveforms of primary side current i_p, secondary side current i_s, output voltage on the secondary side V_o and gate drive control signals of (S_1+/S_2-) from the startup transient to steady state.

It can be seen that the output voltage on the secondary side is controlled around the reference value of +15V. The resonance of the current is well maintained on the primary side by the switch operation with closed loop control. The control of the switches is based on the magnitude of the secondary side output voltage and the polarity of the primary current. When the voltage is lower than +15, the primary converter is working in Mode I (S_1+/S_2- on) and Mode II (S_2+/S_1- on). Energy is brought into the system continuously, and the current is rapidly boosted on the primary side with the maximum energy injection at the startup transient. As a result, the secondary side induced power and the output

voltage are boosted. Consequently the output voltage reaches its reference value in a very short amount of time because the maximum energy is being injected.
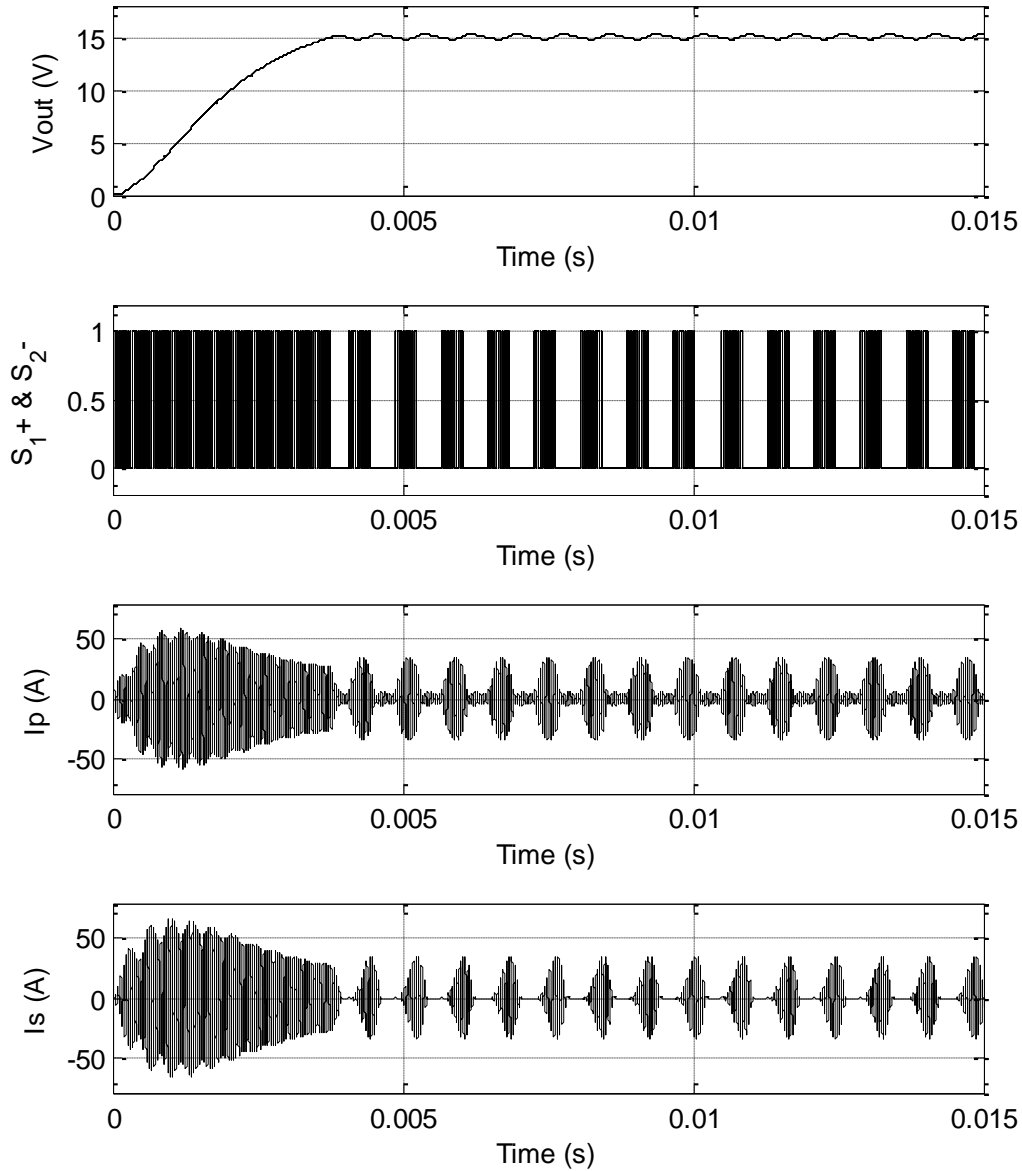
Figure 5-11: Simulation result of the track current with reference to output voltage and gate signals.

Figure 5-12 shows a clear switching operation during the circuit steady state. It can be seen under steady state, once the output voltage is larger than the reference V_{ref}, the switches operate at the ZCS points from Mode I and Mode II, having S_2+/S_1- on and S_1+/S_2- off. If the output voltage is lower than V_{ref}, the switch operation transfers to Mode II and Mode III. It can be seen that the resonant current is automatically maintained by the bidirectional conduction of S_2+, S_1-, D_2+, and D_1-. The magnitude of the track current on

the primary side rapidly reduces to a very low level. As a result, the output voltage decreases. Theoretically, the magnitude of primary current can be zero if the load is very low and stays low for a long period of time, but the output voltage can still be maintained around at the +15V.
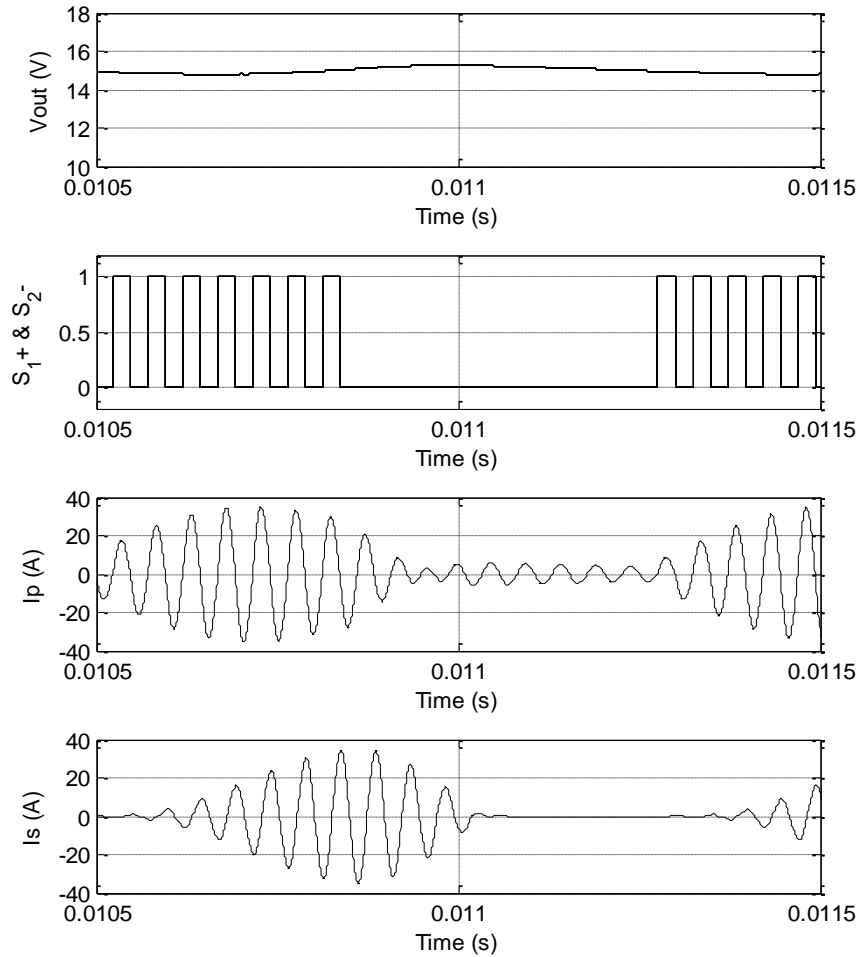
Figure 5-12: Simualtion waveforms of the gate signal and primary track current

5.5.2 *System response to loading variation*

A simulation study of the load variation is carried out to verify the performance of the primary power flow regulation method. According to practical requirements, the load on the system will be switched to half its value after 0.016s. The simulation result of this load variation is shown in Figure 5-13.
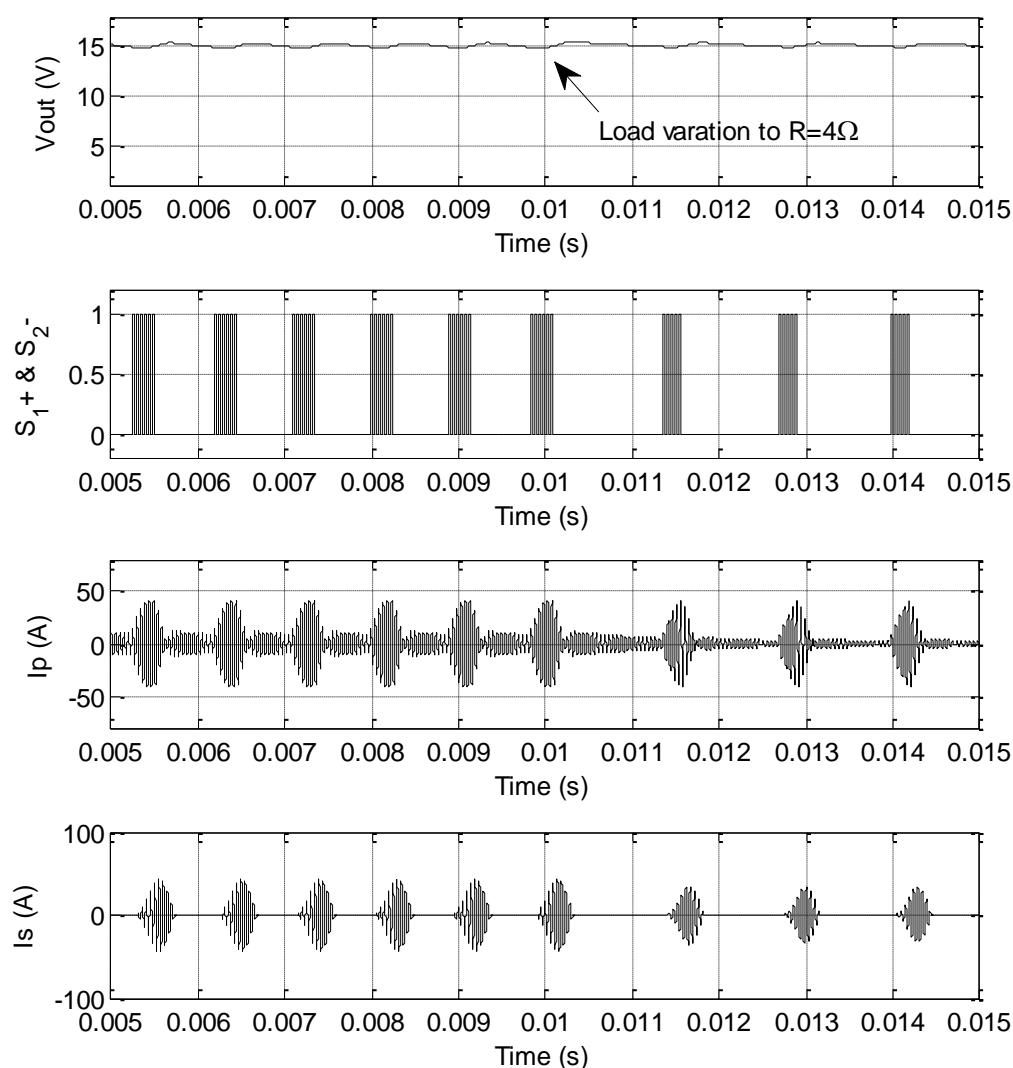
Figure 5-13: Simulation result of the track current with reference to output voltage and gate signals with load variation

It can be seen that the switching pattern of the converter changes promptly when the load varies from the nominal load condition to half its value. The primary track current under such a condition is promptly boosted with full energy injection even at different loading condition. In addition, because the proposed system controls the energy injection into the system or circulation back to the power source every half cycle, the speed of the response can be within one cycle period. The fast response speed is an advantage for the applications where the loading is not constant.

5.6 Implementation and Experimental verification

An overview of the prototype contactless slip ring system with the power flow control on the primary side and the implementation diagram are shown in Figure 5-14 and Figure 5-15 respectively.
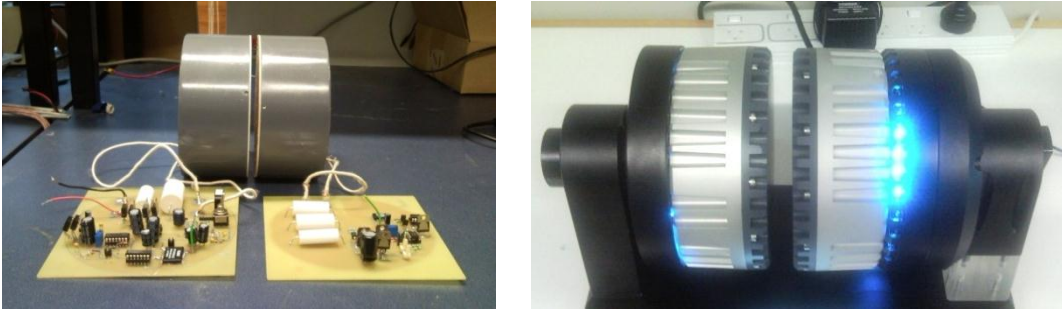
Figure 5-14: System overview of a slip ring with primary side power flow control (Courtesy of Powerbyproxi Ltd*)
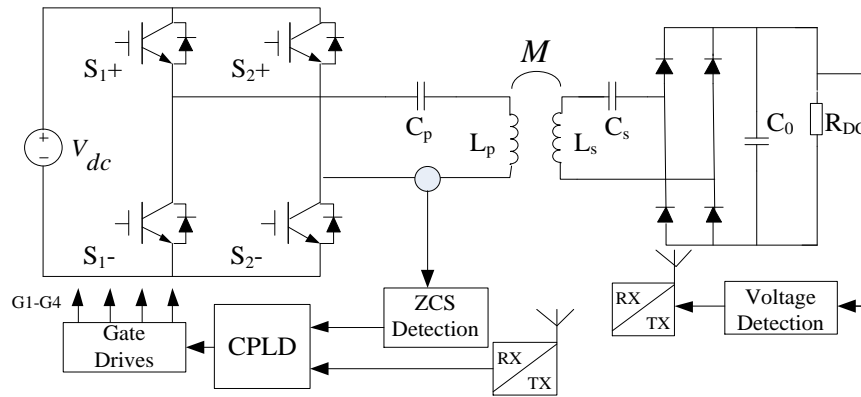
Figure 5-15: Experimental implementation diagram of slip ring with primary side power flow control

To obtain a fast and accurate ZCS operation and make the smaller size, a CPLD (Complex Programmable Logic Device) is used as the central controller, which contains programmable logic components and memory elements. In the design, a small CoolRunner-II CPLD VQ44 package chip in XC2C64A family was implemented in the real circuit. The LR series RF modules TXM-433-LR and RXM-433-LR have been chosen due to their low cost, small size, and ease of implementation. The track current signal is detected to obtain its zero crossing points. The output voltage at the secondary power pickup is detected and fed back to the primary side CPLD controller.

- 121 -

Based on the primary power flow control, the experimental results are shown from the Figure 5-16 to Figure 5-19. Figure 5-16 presents the operation of the primary converter under startup transient with a power requirement of 112W using the same circuit setup as in the simulation study. In Figure 5-16, the upper trace (trace 1) shows the output voltage of the secondary pickup, while the lower trace (trace 2) shows the primary track current. It can be seen that with the maximum energy injection (operating between Mode I and Mode II in Table 5-1), the output voltage is boosted to the reference value very quickly. The duration from startup to steady state takes less than 4ms, and the output voltage has almost no overshoot during the startup transient process with only minimal ripple at steady state observed. In practice, the response time of the startup depends on the source voltage and the load condition. A higher source voltage or a lighter load would make the process faster. Once the system operates at steady state, the switch pattern is stable if the load is stable.
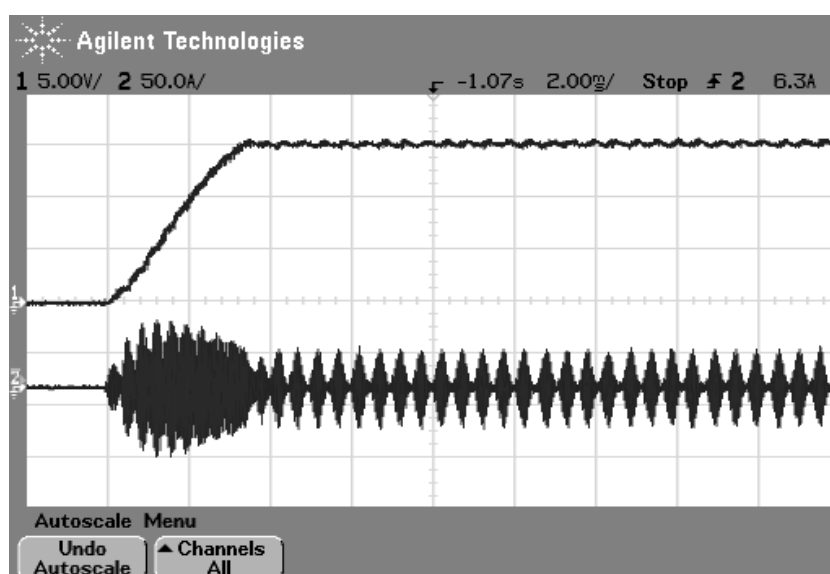
Figure 5-16: The transient response of the proposed converter during startup

Figure 5-17 presents the operation of the primary converter at steady state with the nominal load at 112W; the resonant track current waveforms (trace 2) and the gate signal of S_1+ (trace 1) are presented under the condition of a 15V output voltage.
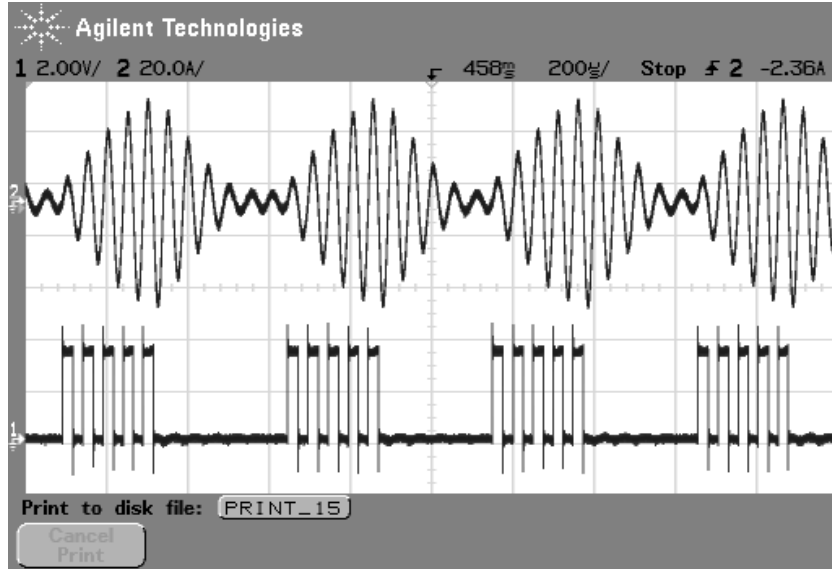
Figure 5-17: Track current and gate signal of S_1+ at 112w

As shown, the magnitude of the primary track current is controlled over a wide range according to the output voltage on the secondary side. S_1+/S_2- are controlled to follow the resonant current in positive direction, and the gate signals are in phase with the track current if the output voltage is lower than 15V. Because the primary switches operate randomly according to the energy requirements of the load, the transient process is short and the injected energy is fully controllable. In addition, it can be seen that the switches operate under ZCS conditions at each injection period.

In order to test the performance of the proposed primary current regulation method under different loading conditions, a sudden load variation was introduced. The contactless slip ring system was made to have a sudden load change from 112W to 56W. The experimental result of this load variation is shown in Figure 5-18 and can be compared with the simulation result shown in Figure 5-13.

Here a load step occurs in the middle of the captured waveform about 25ms in Figure 5-18. It can be seen by using the proposed magnitude control method, the output voltage (trace 1) is well maintained at 15V with nearly unnoticeable variation, but the primary track current (trace 2) is different. The average primary current becomes smaller in order to maintain a light load without losing the rapid boost ability.
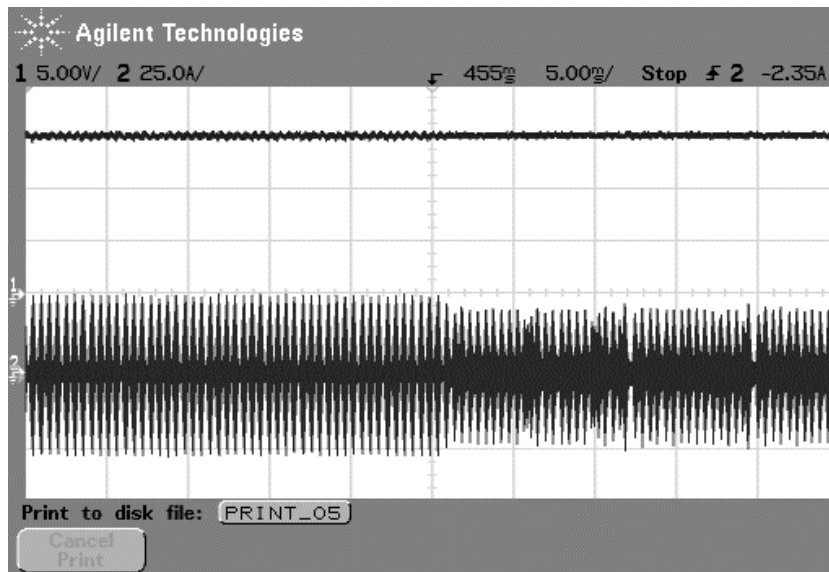
Figure 5-18: The transient process of load variations

To have a close observation for this lighter load condition 56W, a steady state track current (trace 2) and the gate signal of S_1+ (trace 1) is shown in Figure 5-19
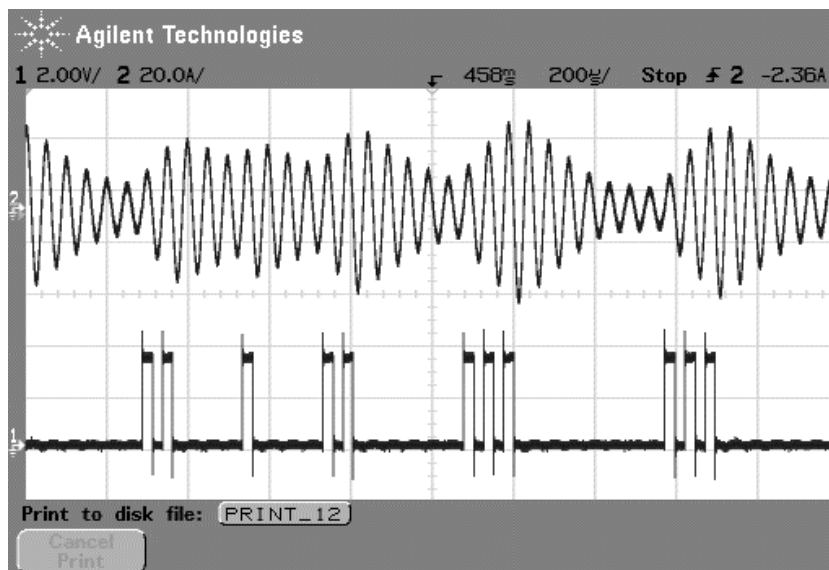
Figure 5-19: Track current and gate signal of S1+ at 56W

Compared to Figure 5-17, it can be seen that the switching pattern of the primary inverter changes with the load demand. The switching frequency becomes lower to allow a lower energy injection to maintain a small average current under a lighter load. A ZCS switching operation is still maintained. In addition, the fast dynamic response within half of a resonant cycle is also ensured.

5.7 Summary

In this chapter, a new power regulation method based on quantum energy injection control of the primary side was investigated for a single pickup IPT system.

The difference between the proposed control method and other power flow methods used in IPT systems was discussed. The detailed operation of the primary power flow control was then analyzed. The proposed method controls the power flow to the contactless power pickup by regulating the primary track current. An analysis was carried out to obtain the maximum output range which can be generated by the proposed control method.

Simulation studies were also conducted to verify the proposed power flow regulation method and performance of the proposed inverter under different operating conditions. The simulation results show that the proposed power flow control method has an excellent steady state and dynamic performance at startup and load variations.

Finally, a practical contactless slip ring system was designed and implemented to verify the power flow control. The experimental results show that the output voltage could be maintained constant by the primary side power flow control method using wireless feedback from the secondary side. In addition, these practical results also prove that the proposed methods can provide a ZCS operation and a fast dynamic response under both the startup and load variations.

Chapter 6

A Direct AC-AC Converter

6.1 Introduction
6.2 Elements and Structure
6.3 Operation Principle
6.4 Modeling and Analysis
6.5 PLECS Simulation Study
6.6 Experimental Results and Discussion
6.7 Summary
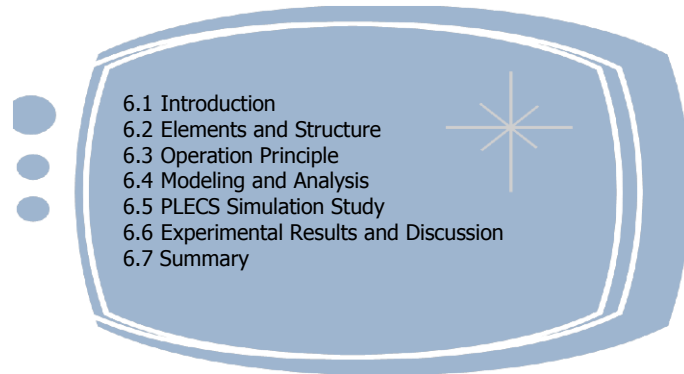
6.1 Introduction

At present, a DC-AC inverter is a common solution to generate a high frequency track current for an IPT system. Often a front-end low frequency mains power source is rectified into a DC power source, and then inverted to the required high frequency AC track current. Energy storage elements, such as DC capacitors, are used to link the rectifier and the inverter. These energy storage elements cause the AC-DC-AC converters to have some obvious drawbacks such as large size, increased system costs, and more complicated dynamic control requirements in practical applications.

Ideally an AC-AC converter would be a good alternative to obtain this high frequency power directly from the mains [122]. A matrix structure eliminates the need for the DC link, but the synchronization between the instantaneous input and output becomes very difficult, and the quality of the output waveform is usually poor due to complicated switching combinations involved [123]. Furthermore, the circuit transient process involved in the traditional forced switched matrix converters is normally complex and difficult to analyze. The control complications and synchronization limitations make traditional matrix converters unsuitable for IPT systems.

This chapter presents a direct AC-AC converter based on free circuit oscillation and energy injection control for IPT applications. A simple but unique AC-AC topology is

developed without a DC link. A variable frequency control and commutation technique is developed and discussed. The detailed circuit model and the converter performance are analyzed.

6.2 Elements and Structure

In chapter 3, based on energy injection control of a resonant network, a half bridge and a full bridge DC-AC inverter are developed for IPT systems. In principle, any power source may be used to generate high frequency currents apart from a DC source using free oscillation and energy injection control providing the converter topologies are properly designed. For such a reason, if the energy injection control and free oscillation is well coordinated, the energy storage components of an AC-DC-AC converter can be fully eliminated. Therefore, an AC power source can be directly used to generate a high frequency AC current for an IPT system. As a result, the cost, size and efficiency of an primary IPT converter can be significantly improved.

Eliminating the front-end AC-DC rectification and DC storage capacitors, a conceptual AC converter based on energy injection control can be created as shown in Figure 6-1.
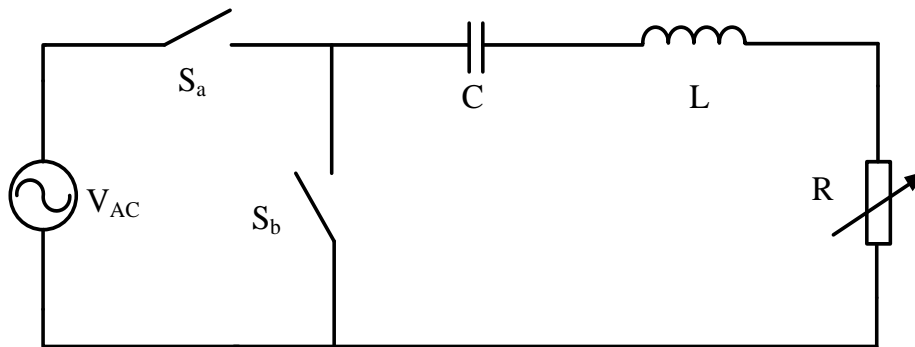
Figure 6-1: A conceptual direct AC-AC converter with energy injection control

It can be seen from Figure 6-1 that an AC source is directly connected to a resonant network by switches. The design of the switching topology could be very critical here to ensure the energy can be injected according to the load requirements, and to ensure that energy flowing back to the power source is prevented during circuit oscillation.

In practice, most semiconductor switches such as IGBTs and MOSFETs have anti-parallel body diodes. Such a structure ensures the switches can operate bi-directionally but with only one controllable direction. With a combination of the IGBTs or MOSFETs, an AC switch can be constructed to achieve bidirectional controllability [124]. As discussed in Chapter 2, any of the three constructed AC switches can be used to replace the ideal switches in Figure 6-1. After taking the practical consideration of implementation such as control simplicity, cost and efficiency, the proposed converter topology is developed as shown in Figure 6-2, which consists of minimum count of four semiconductors.
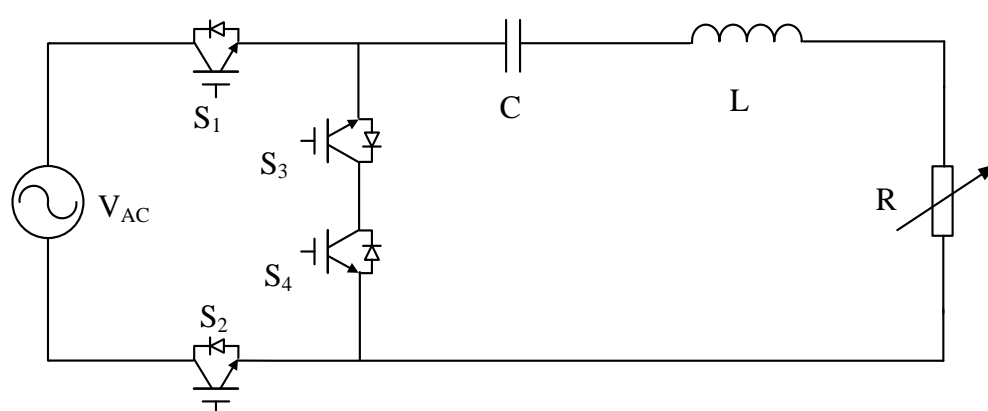
Figure 6-2: A typical configuration of a direct AC-AC converter

The ideal switch S_a in Figure 6-1 is presented by an AC switch S_1 and S_2 as shown in Figure 6-2. The ideal switch S_b is replaced by S_3 and S_4 to construct a free oscillation path for the current. By turning on/off the switches through a properly designed conduction combination, the energy injection and free oscillation can be maintained while the undesired energy circulation to the source can be prevented. The detailed control scheme for all those switches is discussed in the following section.

6.3 Operation Principle

6.3.1 *Normal switching operation*

The proposed AC-AC converter is based on a direct conversion topology without a middle DC link. Therefore, the commutation and synchronization of the source voltage and the resonant loop branch need to be considered. To determine the switch operation, it is necessary to identify the polarity of the input voltage and the resonant current. According

to the polarity of the low frequency input voltage and the resonant track current, the converter operation can be divided into four different modes as shown in Figure 6-3.
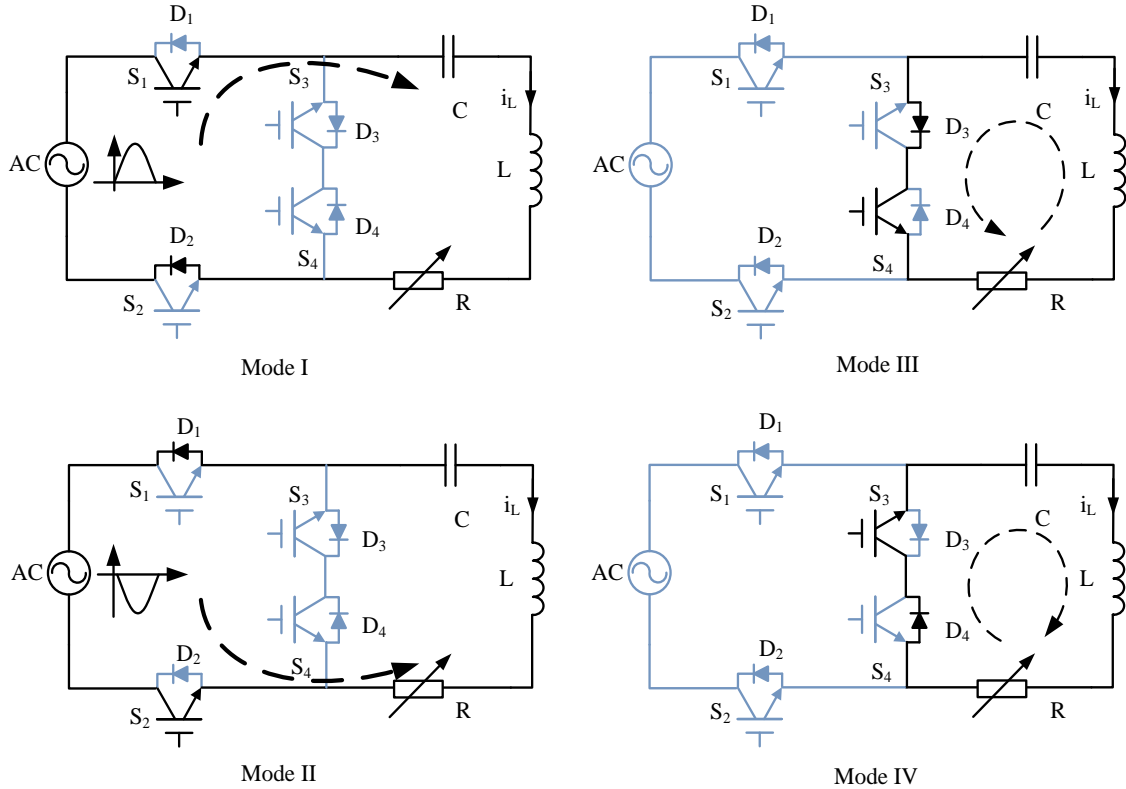
Figure 6-3: Switch operation of AC-AC converter

In Figure 6-3, Mode III and Mode IV present the current free oscillation in different directions. Mode I and Mode II are the states to control the energy injection based on the different polarities of the input voltage, which is also determined by the directions of the resonant current.

A typical current waveform of the converter and the associated switching signals when the input voltage is in the positive polarity are shown in Figure 6-4.
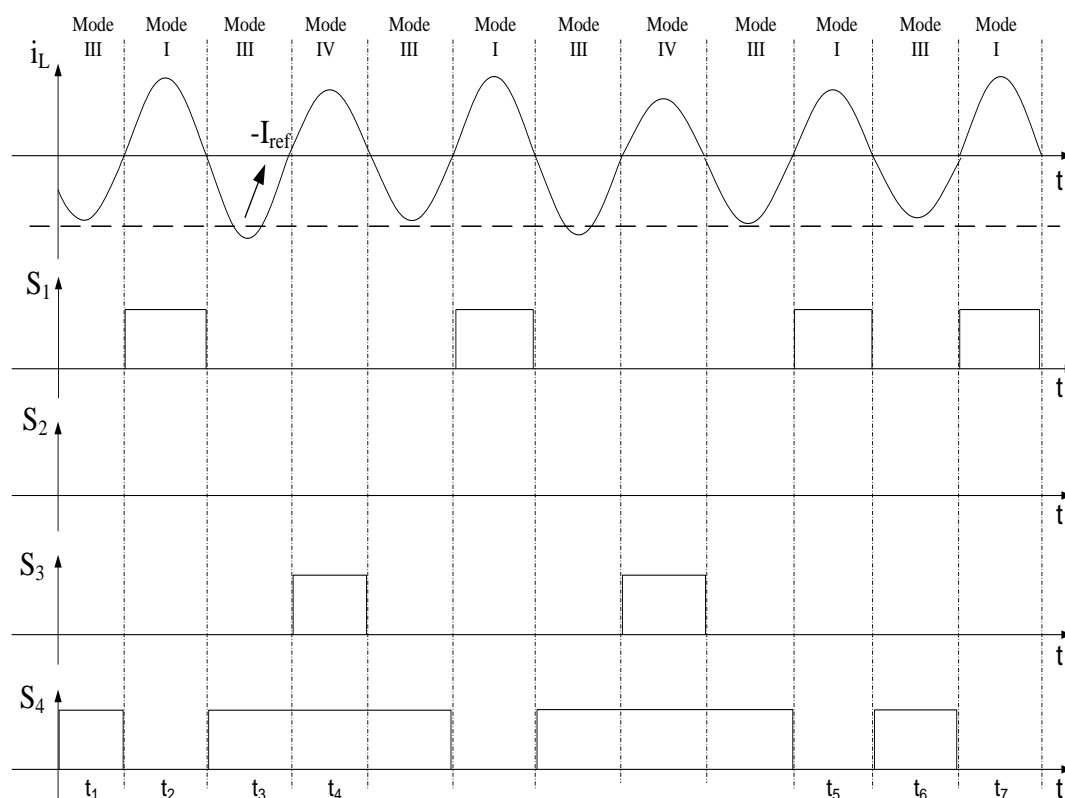
Figure 6-4: Converter operation when input voltage V_{AC}>0

In Figure 6-4, if the negative peak value of the resonant current is smaller than the designed reference value $-I_{ref}$ in t_1, switch S_1 is turned on in the following positive cycle when V_{AC}>0, while S_2, S_3 and S_4 remain off. As such, the instantaneous source voltage V_{AC} is added to the resonant tank. This operation results in a boost in the resonant current during t_2. Regardless of whether the peak current is smaller or greater than the reference value $-I_{ref}$, the operation of the converter in the next half cycle of t_3 would automatically be switched to Mode III, where switch S_3, S_4 are on and S_1, S_2 are turned off, such that the *L-C-R* forms a free oscillation circuit enabling the energy to circulate between the capacitor *C* and inductor *L*. However, if the peak current is larger than the reference $-I_{ref}$ at t_3, the converter operates in Mode IV at the next half cycle of t_4. If the negative peak current is still smaller than the reference $-I_{ref}$ after a positive energy injection (for example, peak current is still very small at t_6 even after the injection at t_5, and more energy is still needed in the next positive half cycle of t_7.), then, the converter will operate at Mode I at t_7, and continue to repeat the operation between Mode I and Mode III in the following half cycles until its peak magnitude larger than the predefined reference value.

The operation of the converter is similar to the situation when the input voltage $V_{AC}<0$. The only difference is that S_2 is used to control the negative input voltage which is applied to the resonant tank when the resonant current is negative. Additionally, the peak current would be compared to $+I_{ref}$ to determine if the converter is operated between Mode II/Mode IV, or Mode IV and Mode III. The selection of the mode during normal operation for both positive and negative input is summarized and shown in Figure 6-5.
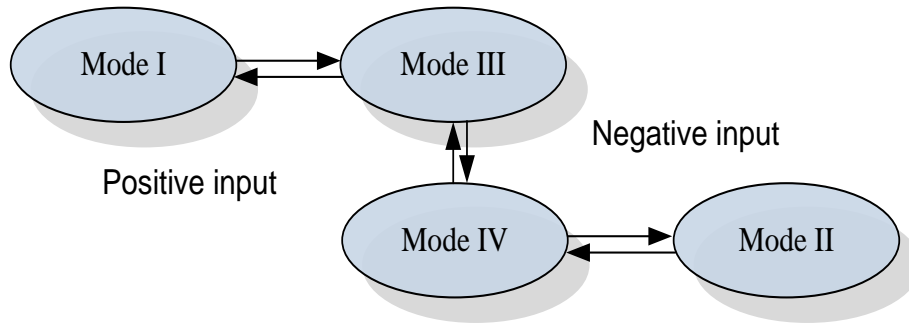
Figure 6-5: Mode selection diagram during normal operation

6.3.2 *Switching commutation*

The proposed converter inherits the simple matrix structure with less switching components and without commutation capacitors. By utilizing the body diodes of each switch, the circuit resonant current can be naturally maintained, even the switches operate at non ZCS condition. Like a DC-AC inverter, variable frequency control can also be employed in the AC-AC converter. Switches being operated under such a condition are switched at the zero crossing points to follow the resonance of the current so as to keep the magnitude of the current constant. Nevertheless, the variable frequency switching control also faces problems as a result of the frequency shift [31], which cause uncertainty in the direction of the resonant current when the input voltage is at its zero crossing points. This implies that the current completes an entire half cycle over the zero crossing point of input. The polarity change of the input voltage will make the modes of converter operation vary between energy injection states and free oscillation states. Therefore, it is necessary to consider the best switching commutation technique when a variable frequency control strategy is developed for the proposed AC-AC converter.

Theoretically, the track current may have four possible operating conditions around the zero crossing points of the source voltage according to the current directions and the variation tendency of the input voltage, as follows:

Condition A: The input voltage changes from positive to negative. The current stays positive over the zero crossing point as shown in Figure 6-6.

Here S_1 is on to maintain the current while S_3 is to be turned on to continue the current.

Condition B: The input voltage changes from positive to negative. The current stays negative over the zero crossing point as shown in Figure 6-6.

Here S_4 is on to maintain the current while S_2 is to be turned on to continue the current.

Condition A   Condition B
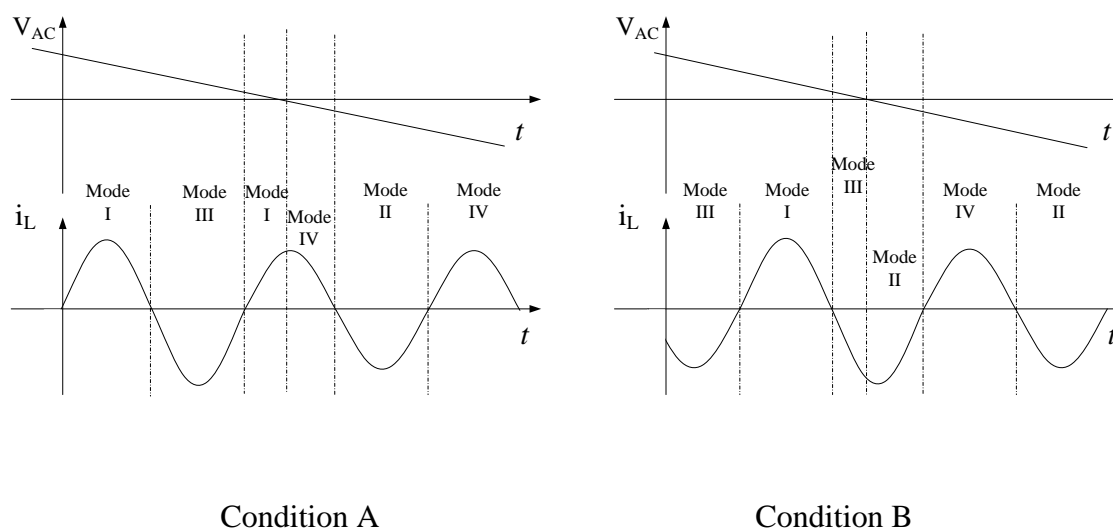
Figure 6-6: Operation transient when the input voltage from positive to negative

Condition C: The input voltage changes from negative to positive. The current stays positive over the zero crossing point as shown in Figure 6-7.

Here S_3 is on to maintain the current while S_1 is to be turned on to continue the current.

Condition D: The input voltage changes from negative to positive. The current stays negative over the zero crossing point as shown in Figure 6-7.

Here S_2 is on to maintain the current while S_4 is to be turned on to continue the current.
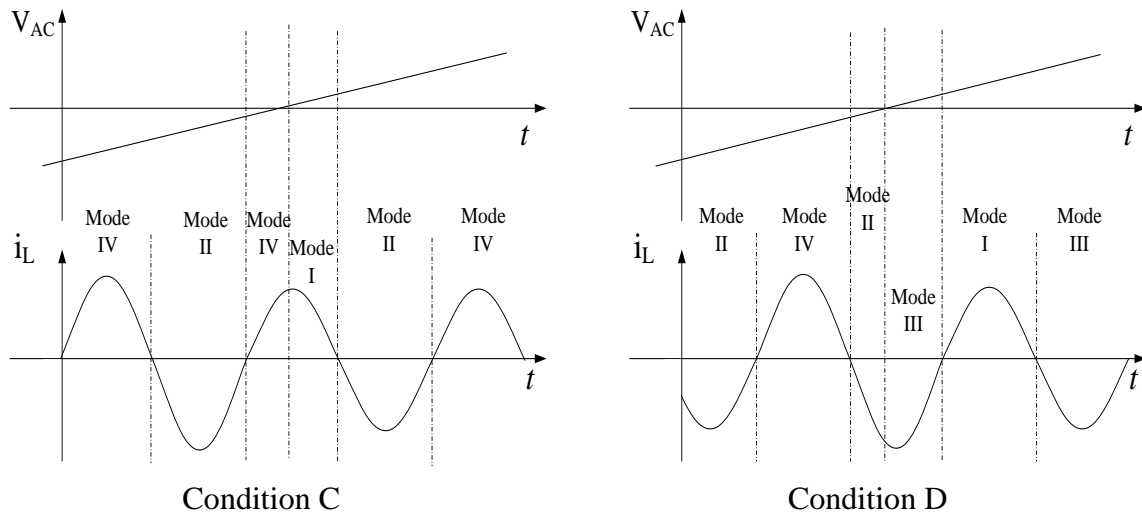
Figure 6-7: Operation transient when the input voltage from negative to positive

It can be seen that there are two additional conditions apart from the normal operation conditions. The operation mode around the zero crossing periods of the input voltage must change between Mode I and Mode IV, or Mode II and Mode III. In fact, the switching commutation between Mode I and Mode IV can be achieved if S_3 is always on when the input voltage is in the positive polarities. Similarly, the switching commutation between Mode II and Mode III also can be achieved by keeping S_4 on if the input voltage is negative. Such switch operations can maintain the oscillation without affecting the normal operation.

From the above discussion, the detailed operation of the AC-AC converter for all conditions is listed in Table 6-1, according to the input voltage, the resonant current and the predefined current reference. Typical waveforms of the converter with a smooth commutation using this variable frequency control strategy are illustrated in Figure 6-8.
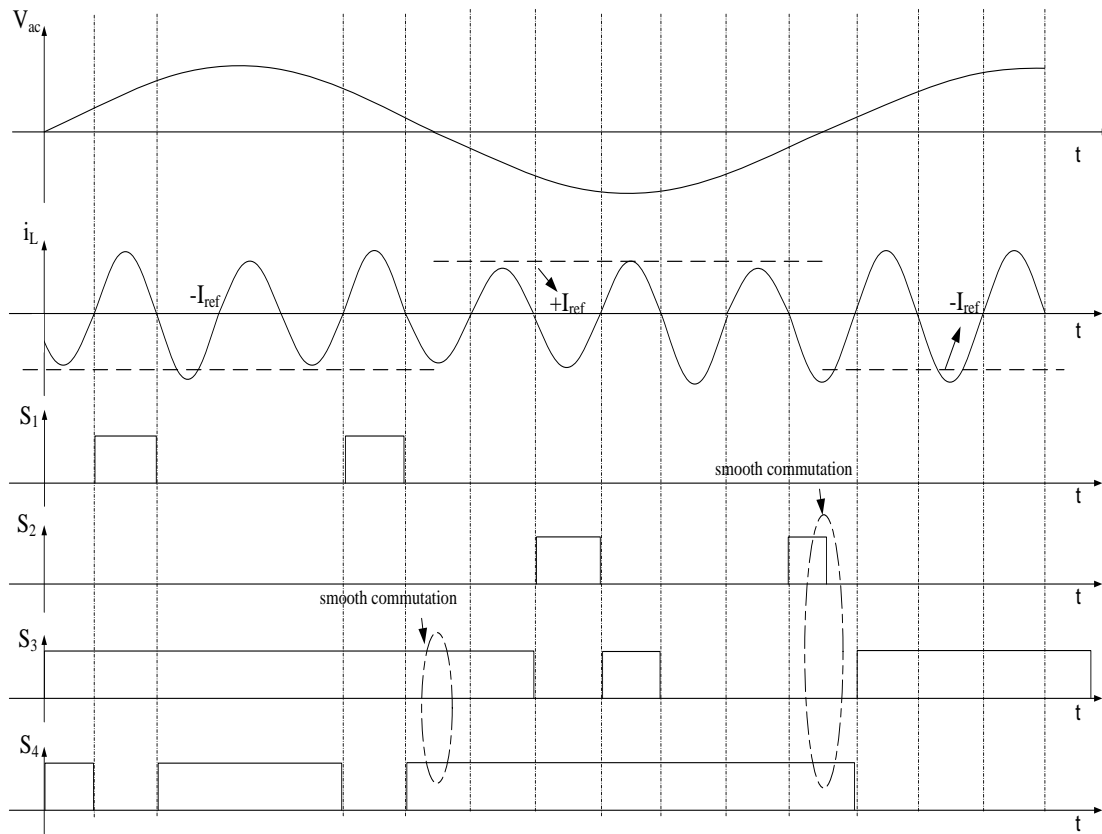
Figure 6-8: Waveforms of the converter with smooth commutation

The detailed shifting relationship between the operation modes during operation can be summarized in Table 6-1.

Table 6-1: Switching states of operation modes

Resonant Current	Input Voltage	SWITCHES/DIODES STATUS	Mode
$i_L>0$, and previous $\hat{i}_L > -I_{ref}$	$V_{AC}>0$	S_1/D_2on $S_2/S_3/S_4/D_1/D_3/D_4$off	Mode I
$i_L<0$, and previous $\hat{i}_L < +I_{ref}$	$V_{AC}<0$	S_2/D_1 on $S_1/S_3/S_4/D_1/D_3/D_4$off	Mode II
$i_L<0$	$V_{AC}>0$	S_4/D_3on $S_1/S_2/S_3/D_1/D_2/D_4$off	Mode III
Previous $\hat{i}_L > +I_{ref}$	$V_{AC}<0$		
$i_L<0$	$V_{AC}<0$	S_3/D_4on $S_1/S_2/S_3/D_1/D_2/D_3$off	Mode IV
Previous $\hat{i}_L < -I_{ref}$	$V_{AC}<0$		

6.4 Modeling and Analysis

The control strategy of the proposed converter is a discrete energy injection control based on the polarity of the input voltage and the resonant current. Since the energy injection occurs discretely, the input phase angle is different for each injection period. During the energy injection period while $V_{AC}>0$, the input voltage is in the same direction as the track current in its positive direction. However, the value of the input voltage during each injection varies according to the time instant of the injection. The situation is similar when $V_{AC}<0$; but the track current would be in the negative direction for energy injection. At each injection instant the input voltage over the track can be expressed by the instantaneous value of the AC source as:

$$v_{in}(t) = \hat{V}_{AC} \sin \beta \tag{6-1}$$

where $\hat{V}_{AC}$ is the peak value of the mains voltage, $\beta=\sin(\omega t)$ is the phase angle of the input AC voltage when energy injection occurs. Theoretically, the instantaneous input voltage during each injection period varies between the beginning and the end of the period. This variation in the input is very small if the resonant frequency is much higher than the mains frequency, as is normally the case for IPT systems. For such a reason, the input voltage applied in each half injection period can be assumed to be constant. The input voltage V_{in} can therefore be defined as:

$$V_{in} = \begin{cases} \hat{V}_{AC} \sin \beta \\ 0 \end{cases} \tag{6-2}$$

According to the control strategy of the converter, the differential equations of the equivalent circuit according to the Kirchhoff's voltage law of the circuit can be expressed as:

$$\begin{cases} \dfrac{di_L}{dt} = \dfrac{V_{in}}{L} - \dfrac{Ri_L}{L} - \dfrac{v_C}{L} \\ \dfrac{dv_C}{dt} = \dfrac{i_L}{C} \end{cases} \tag{6-3}$$

By solving these equations, the instantaneous value of the current during the energy injection and free oscillation periods can be expressed respectively as:

$$i_L = \frac{\hat{V}_{AC}\sin\beta + v_C(0)}{\omega L}\, e^{-\frac{t}{\tau}}\sin\omega t \tag{6-4}$$

$$i_L = \frac{v_C(0)}{\omega L}\, e^{-\frac{t}{\tau}}\sin\omega t \tag{6-5}$$

where $\tau=2L/R$, ω is the zero phase angle frequency. $v_C(0)$ is the initial voltage at the switching transient. It can be seen that the solution to the track current for a direct AC-AC converter is similar to that of the DC-AC energy injection inverters, but the input voltage is time dependent during different energy injection periods.

6.4.1 Current ripple during controlled periods

Under the discrete energy injection control strategy with variable frequency switching, the current resonance can be well maintained, but over energy injection will also occur especially when the AC input voltage reaches its peak. Figure 6-9 shows the typical waveform of the track current with a reference of the input voltage.
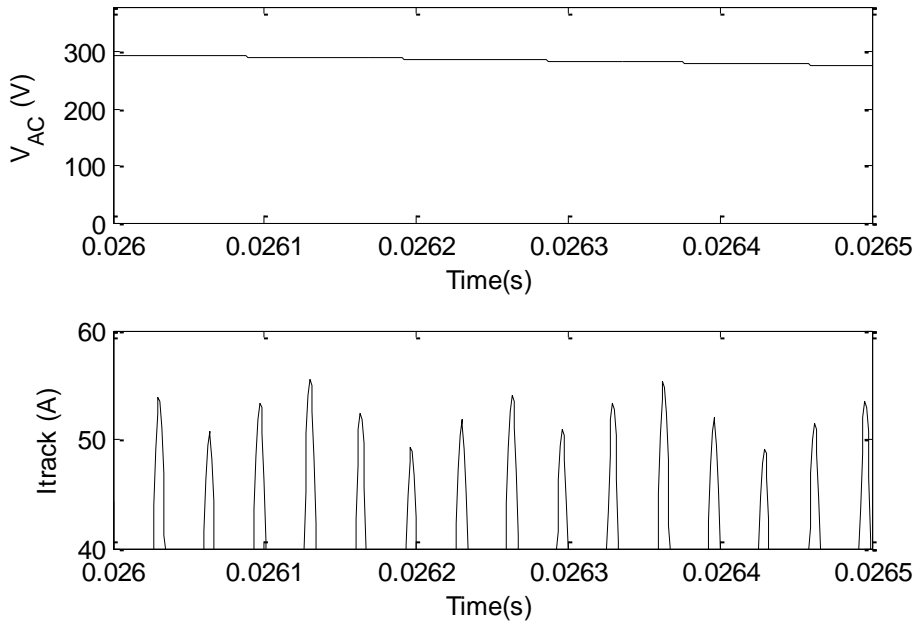
Figure 6-9: Current ripples during controlled period

It can be seen that the current presents a small ripple around the reference current during the controlled period at steady state. The amount of energy injected into the circuit at different phase angle of the mains voltage varies and can be more than what is required to maintain a constant track current. Any over injection of energy during each injection period results in a current overshoot. Similarly, any over consumption during the oscillation period contributes to the current ripple.

Similar to the analysis of a DC-AC converter in chapter 3, an approximated worst case method can be used to find the maximum and minimum peak current of the AC-AC converter caused by the magnitude variation of the AC input. In order to clearly understand the current ripple during the controlled period, a detailed waveform showing the track current under the worst case conditions is given in Figure 6-10.
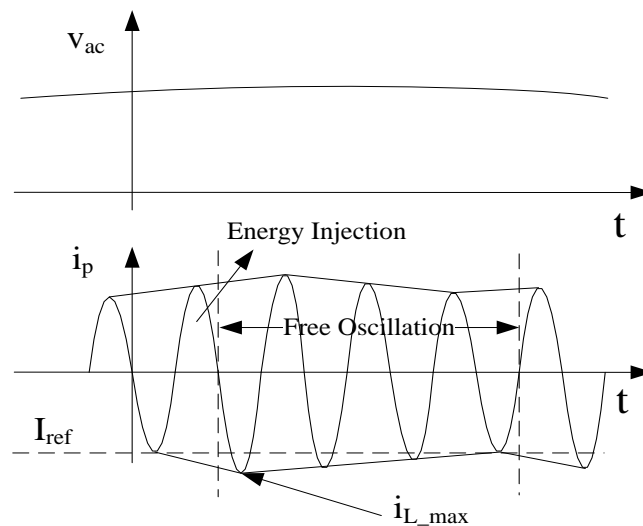
Figure 6-10: A detail current ripple waveform

It can be seen that during the control period, if the input voltage is at the positive cycle, the track current always enters the free oscillation state during its negative cycle. When the converter operates under free oscillation period, there is no energy injected. As a result, the track current is naturally damped by the load and ESR. If the peak current in the negative half cycle is slightly smaller than or equal to the reference value I_{ref}, energy will be injected by the controller into the resonant network in the next positive half cycle. With this energy injection, the current increases from zero to its peak during the positive cycle. Such a peak value will be larger than the previous negative peak value, but it is not the

maximum value. This is because the energy will be continually injected during the remaining time of the entire positive cycle and after this positive peak value. In fact, the real maximum peak current i_{L_max} appears in the following negative half cycle as shown in the figure after the half energy injection period is complete.

As stated, in the worst case scenario under the no load condition, the capacitor voltage will approximate to zero when the track current is at its peak. After the energy injection over half a period, the total energy storage in the circuit equals the stored energy, and the newly injected energy can be expressed as:

$$\frac{1}{2}L\hat{i}_{L\_max}^{\;2} = \frac{1}{2}LI_{ref}^{\;2} + \int_0^{\frac{T}{2}} v_{in}(t) \cdot i_L(t)dt \tag{6-6}$$

An energy balance principle can be applied to any energy injection period. But the worst case occurs when the current is just smaller than I_{ref} and energy is still being injected when the mains voltage is at its peak value as stated earlier.

As the frequency of the resonant current is much higher than the 50Hz input voltage, the voltage added to the resonant tank at the peak of 50 Hz can be approximately expressed as:

$$v_{in}(t) \approx \hat{V}_{AC} \tag{6-7}$$

Therefore the injected energy during the entire half period over the peak of the mains can be expressed by:

$$E_{in} = \int_0^{\frac{T}{2}} v_{in}(t) \cdot i_L(t)dt = \frac{\hat{V}_{AC}^{\;2} + 2\pi f \hat{V}_{AC} I_{ref} L}{2\pi^2 f^2 C} \tag{6-8}$$

From (6-6) and (6-8), the maximum track current can be obtained as:

$$\hat{i}_{L\_max} = \sqrt{I_{ref}^{\;2} + \frac{2T\hat{V}_{AC}\sqrt{LC}(I_{ref}\sqrt{\frac{L}{C}} + \hat{V}_{AC})}{\pi}} \tag{6-9}$$

It can be seen from equation (6-9) that the overshoot of the maximum track current is determined by the peak AC input voltage, the controlled reference current, the track current resonant frequency, and the circuit parameters.

Although the maximum peak current is caused by the energy injection, the minimum peak current i_{L_min} is caused by circuit damping. The worst case scenario arises when the load is at its maximum and the peak current is slightly larger than the reference value. Under such a condition there is no injection in the next half cycle. Strictly speaking when the current is at its peak, the capacitor voltage is not exactly zero due to the existence of the load resistance. But for inductive power transfer applications, the Q of the primary circuit is normally high so that the assumption of the initial conditions $i_L(0)= -I_{ref}$ and $v_C(0)=0$ does not cause any significant error. For the proposed AC-AC converter, if it is operated when the input voltage is in its positive cycle, the energy can only be injected in the following positive half cycle. The initial peak value under such a condition is equal to the reference value during negative cycles of the resonant current, and there is no energy injection in the following positive cycle of the current while the damping remains. Instead of damping in the positive half cycle, the damping of current would last for another negative half cycle. With such given initial conditions, the minimum peak current i_{L_min} can therefore be obtained as:

$$\hat{i}_{L\_min} = -I_{ref} \frac{\omega_0}{\omega} e^{-\frac{2\pi}{\omega\tau}} \tag{6-10}$$

According to the structure and control strategy of the AC-AC converter, the minimum current can only happen in the negative cycles. It can be seen from equation (6-10) that the worst minimum peak current is determined by the reference current and the circuit parameters. This is also similar to the DC-AC energy injection inverter with a half bridge topology.

6.4.2 Current envelope prediction

In addition to the current ripples caused by energy injection and energy consumption during the current controlled period, current sag occurs when the input voltage changes its polarity. Figure 6-11 shows the envelope of the typical current waveform when the input voltage changes from the positive half cycle to the negative half cycle. It can be seen that around the zero crossing point, the input voltage falls back to zero and the magnitude of voltage is very low. Consequently, there is not enough energy that can be injected to sustain the track current to be constant, even if the maximum possible energy is injected in every half cycle.
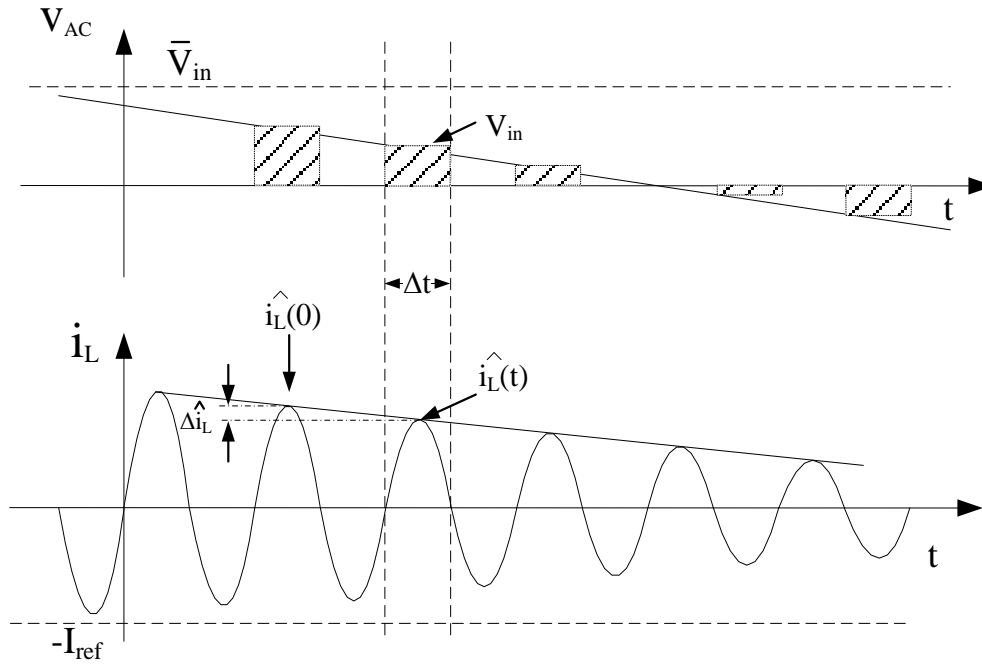
Figure 6-11: Current sags around zero crossing point of the input voltage

It can be seen that before the current sag occurs, the controlled current is around the reference value I_{ref} although small fluctuations exist due to the control. This means the input voltage is large enough to supply the energy to maintain a constant current around I_{ref}. However, over time, the input voltage drops to the boundary value, which is the minimum value to ensure the desired current without any control. This value can be obtained by:

$$\overline{V_{in}} = \frac{RI_{ref}\pi}{2} \tag{6-11}$$

Theoretically, if the input voltage is smaller than the boundary value, the newly injected energy will be too small to achieve the desired outcome and reaches zero when the input voltage is at the zero crossing point. During this period, the injected energy in each positive half cycle can be calculated by:

$$E_{in} = \int_0^{\Delta t} v_{in}(t)i_L(t)dt = \frac{V_{in}\cdot \hat{i}_L\cdot \Delta t}{\pi} \tag{6-12}$$

Apart from this newly injected energy in each half cycle, there will be some stored energy in the resonant network because of the energy storage components. As discussed before, because of the high Q characteristic on the primary track, the phase angle of the resonant current and the capacitor voltage is very small and can be ignored. Therefore, the stored energy on the capacitor can be treated as zero when the resonant current is at its peak value. This stored energy in the tank can be expressed in terms of the inductance. At each positive half cycle, the instantaneous stored energy in the resonant tank can be calculated and expressed as:

$$E_{store} = \frac{1}{2} L \hat{i}_L(t)^2 \qquad (6\text{-}13)$$

In order to identify the stored energy in different cycles, as shown in Figure 6-11, the stored energy during the previous energy injection cycle is equal to:

$$E_{store} = \frac{1}{2} L \hat{i}_L(0)^2 \qquad (6\text{-}14)$$

Since the difference in the peak current in two continuous positive half cycle is very small, the variation of the stored energy in one resonant period can be approximately expressed as:

$$\Delta E_{stored} = \frac{1}{2} L (\hat{i}_L(t)^2 - \hat{i}_L(0)^2) \approx L \cdot \Delta \hat{i}_L \cdot \hat{i}_L(t) \qquad (6\text{-}15)$$

In addition to the variation in stored energy variation and the injected energy during the zero crossing periods, the energy is consumed by the load during each half cycle. The consumed energy by the load during each resonant period can be expressed as:

$$E_{consumption} = \frac{\Delta t \cdot \hat{i}_L(t)^2 \cdot R}{2} \qquad (6\text{-}16)$$

According to the energy balance principle, the injected energy during each cycle should be equal to the stored and consumed energy when the input voltage is around its zero crossing point. Thus, the equation for expressing the total energy balance in the resonant tank can be obtained as:

$$E_{in} = \Delta E_{store} + E_{consumption} \qquad (6\text{-}17)$$

Substituting equation (6-12) to equation (6-17), the relationship between the minimum peak current and input voltage can be determined by:

$$\pi L \frac{\Delta \hat{i}_L}{\Delta t} + \frac{\pi}{2} R \hat{i}_L - V_{in} = 0 \qquad (6\text{-}18)$$

Because $\Delta \hat{i}_L$ and Δt are very small, equation (6-18) can be expressed in the format of a differential equation as:

$$L \frac{d \hat{i}_L}{dt} + \frac{R}{2} \hat{i}_L - \frac{1}{\pi} V_{in} = 0 \qquad (6\text{-}19)$$

It can be seen from this equation that the analysis of the peak current of the track is simplified to a first order differential equation with initial values. The envelope can be presented according to the calculated solutions in the time domain.

The input voltage during the current controlled operation period can be modeled as a constant voltage $\overline{V_{in}}$ which is used to maintain the reference current I_{ref}. Therefore, the initial value of the envelope peak current is the reference current, before the voltage drops to zero from the boundary value $\overline{V_{in}}$. Around the zero crossing point of the mains voltage, the input voltage shows a good agreement with a ramp signal shown in Figure 6-12. It can be seen that the first trace is the approximated ramp input. In comparison, this ramp signal is compared to a 50 Hz input in the second figure. The error between each other is almost imperceptible during the zero crossing point of the input voltage.
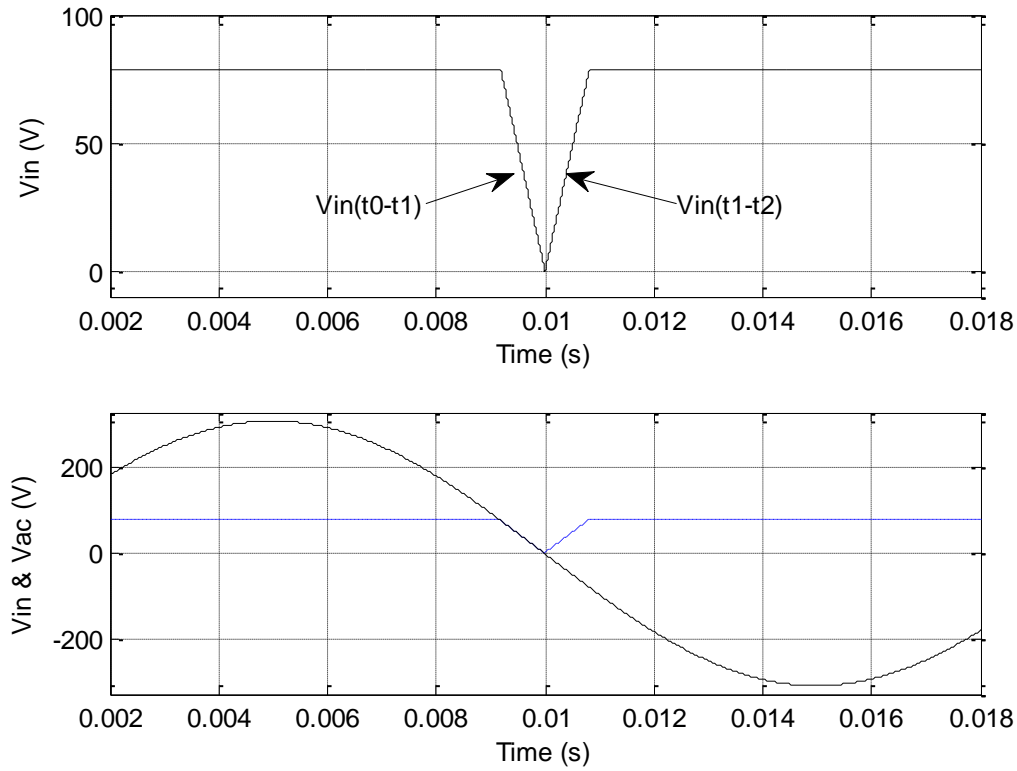
Figure 6-12: Piecewise ramp input voltage

As such, the input voltage of V_{in} around the zero crossing period can be approximated as a piecewise ramp input described by:

$$V_{in}(t_0 - t_1) = \frac{RI_{ref}\pi}{2}\left[1 - \frac{100\pi}{\arcsin(RI_{ref}\pi / 2\hat{V}_{AC})}t\right]$$ (6-20)

and

$$V_{in}(t_1 - t_2) = \frac{50RI_{ref}\pi^2}{\arcsin(RI_{ref}\pi / 2\hat{V}_{AC})}t$$ (6-21)

A figure of the response envelope current with the piecewise input voltage is shown in Figure 6-13. In order to clearly see the envelope current obtained by equation (6-19) under the defined voltage of equation (6-20) and (6-21), the simulation results of track current by PLECS during the zero crossing point of the mains voltage is also shown in the figure.
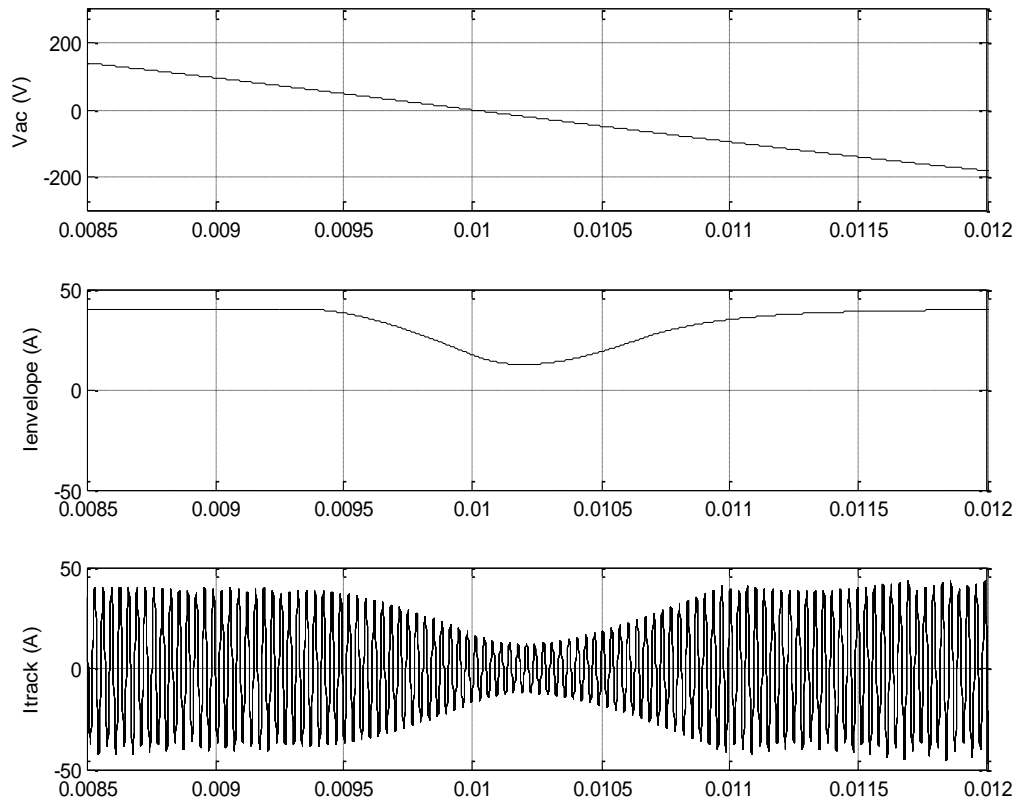
Figure 6-13: Current sag during zero voltage crossing of mains: a) Calculated track current envelope, b) Simulated track current

It can be seen that the envelope of the peak current described by equation (6-19) under the piecewise input voltage presents a good agreement with the envelope of the simulation track current. If the initial value of the peak current I_{ref} is known, the analytical solution of the minimum value of the current can be obtained by solving equation (6-19), with the two given piecewise input functions $(V_{in}(t_0 \text{-} t_1), V_{in}(t_1 \text{-} t_2))$.

By solving equation (6-19) for the function of the first piecewise input yields:

$$I(t_1) = Kt_1 + I_{ref} - K\tau(1 - e^{-\frac{t_1}{\tau}}) \tag{6-22}$$

where time $t_1 = \arcsin(RI_{ref}\pi / \hat{V}_{ac}) / 100\pi$. K is a constant which can be expressed by $K = -100\pi I_{ref} / \arcsin(RI_{ref}\pi / 2\hat{V}_{ac})$.

After obtaining the final value of the first damping ramp input, the final value of the first piecewise input will be the initial value for the next increasing ramp piecewise input voltage $V_{in}(t_1-t_2)$. The solution of the current envelope during this time period of t_1-t_2 can be expressed by:

$$I(t) = -Kt + K\tau + (I_{ref} + Kt_1 - 2K\tau + K\tau e^{-\frac{t_1}{\tau}})e^{-\frac{t}{\tau}} \quad (t_1 < t < t_2) \qquad (6\text{-}23)$$

It can be seen from Figure 6-12 that the second piecewise input voltage increases from zero to the reference value $\bar{V}_{in}$ during the time interval t_1-t_2, the current however reaches a minimum a short period after this. This is because initially the injected energy is very low and the consumed energy is larger than the injected energy. This means that the stored energy is needed to compensate for the over energy consumption. The total energy in the resonant tank would therefore decrease. With the voltage increasing, correspondingly the injected energy would increase. When the injected energy is larger than the energy consumption, the energy starts to increase. As a result the current envelope increases after reaching its minimum value. The exact time can be obtained during t_1-t_2 by taking:

$$I'(t) = 0 \qquad (6\text{-}24)$$

Therefore the time of the minimum of the current envelope can be obtained as:

$$t_{min} = -\tau \ln \frac{-K\tau}{K_2} \qquad (6\text{-}25)$$

where $\tau=2L/R$, $K_1 = K/L$ and $K_2 = 2K/R + I(t_1)$. After knowing the exact time at which the minimum peak current occurs, the minimum value can be obtained by substituting equation (6-25) into equation (6-23). The minimum sag current can then be expressed by:

$$\mathrm{I}_{min} = K\tau \left[\ln \frac{-K\tau}{K_2} + 1 - \frac{1}{K_2}(I_{ref} + Kt_1 - 2K\tau + K\tau e^{-\frac{t_1}{\tau}}) \right] \qquad (6\text{-}26)$$

The minimum value of the current sag of the converter is related to the circuit parameters. Ideally, if the consumption is very low and the stored energy is very large, the exponential

component has less effect. It requires a large primary Q to act as a filter for filtering off the low frequency components.

6.5 PLEC Simulation Study

The simulation study of the AC-AC converter was undertaken using Simulink/PLECS to investigate the operation and analysis of the converter. The PLECS model of the AC-AC converter is shown in Figure 6-14.
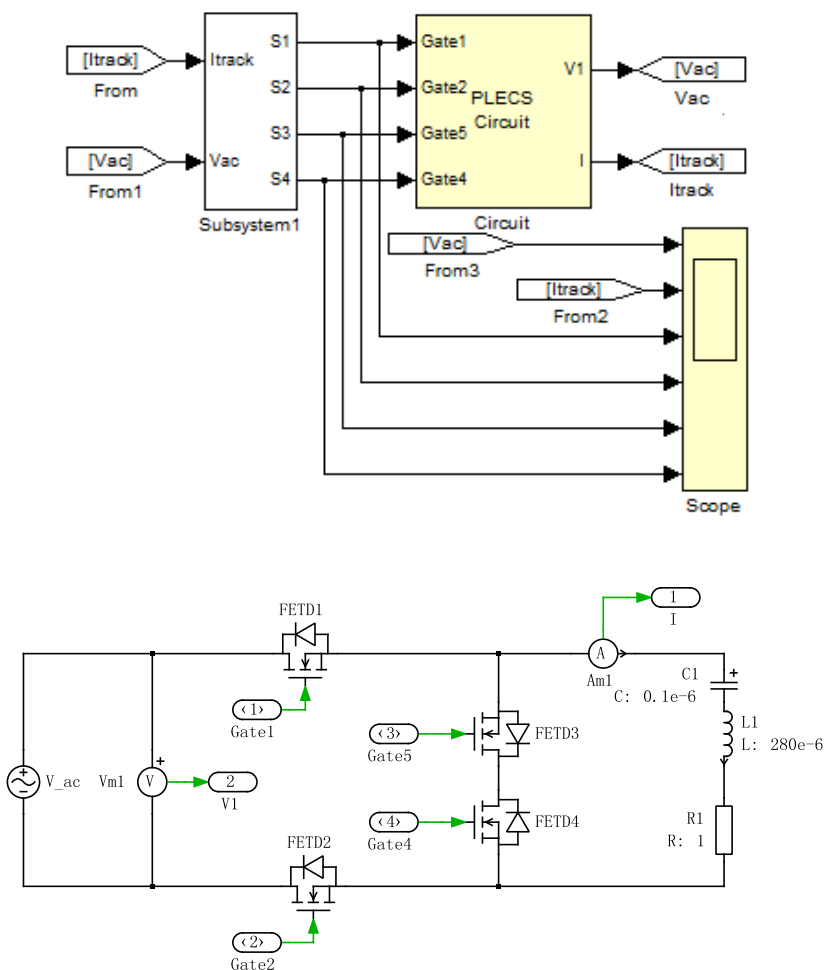
Figure 6-14: PLECS circuit model of direct AC-AC converter

It consists of four switches, an AC input source, and a tuning track. Gate control signals (gate1 to gate4) are fed in from the controller block. The input voltage and track current are measured and feed back to the controller. The converter is designed according to the parameters listed in Table 6-2.

Table 6-2: Converter circuit parameters of a direct AC-AC resonant converter

Symbol	Notes	Value
f_0	Operating frequency of the converter	30 kHz
V_{AC}	Input voltage in RMS	220 V
f_{AC}	Frequency of AC input	50 Hz
L	Track Inductance	280 μH
C	Tuning capacitors	0.1 μF
R	Equivalent total Load	1 Ω
I_{ref}	Track Current reference	40 A

Figure 6-15 shows the simulation results under variable frequency switching control, which include the waveforms of the input voltage V_{AC}, the track current (I_{track}), and the control signals of S_1-S_4.
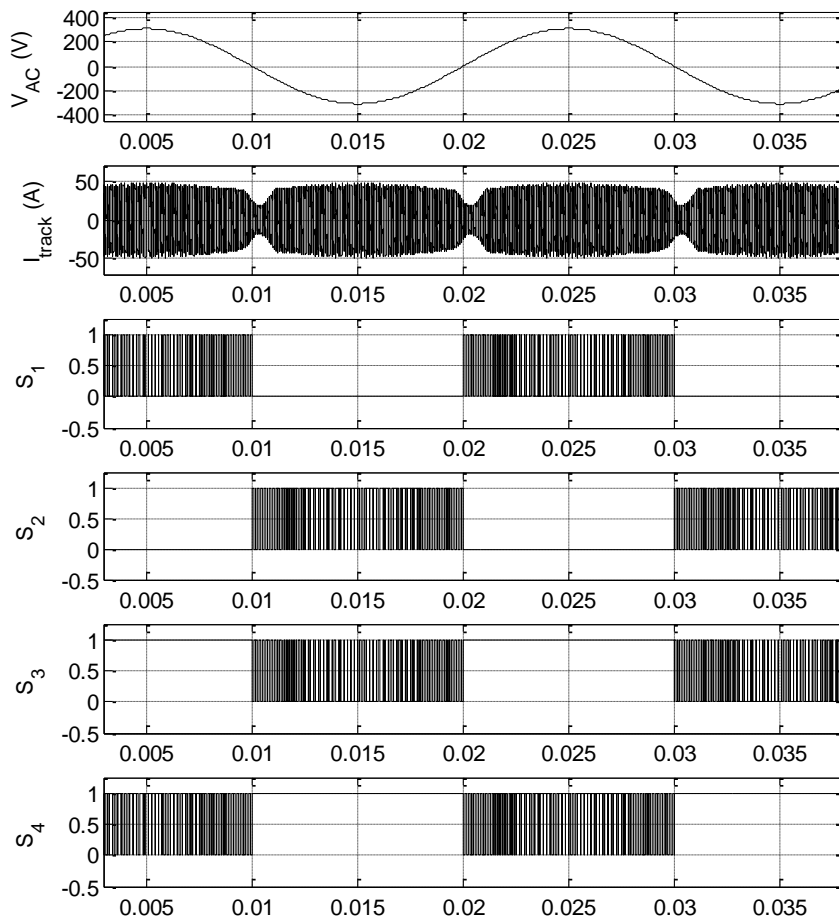
Figure 6-15: Simulation waveform of a typical energy injection AC-AC converter

It can be seen that a low frequency mains voltage can be used to generate a high frequency current for IPT applications under the proposed topology and operation of the AC-AC converter. From Figure 6-15, S_1 and S_4 control the energy injection and the current oscillation when the input is in the positive direction. S_2 and S3 control the energy injection and free oscillation during the negative direction of the input voltage. In addition, the switching commutation is achieved smoothly by the proposed switching control technique. The current waveform is controlled around the predefined reference some fluctuations including both the ripples during controlled period and the sages during zero crossing of the input voltage, which have been discussed and compared in the earlier analysis.

6.6 Experimental Results and Discussion

In order to verify the proposed switching control strategy and the theoretical analysis, an experiment was conducted using the circuit parameters as in the simulation study. In order to have a pure resistive load on the primary side, a series tuned pickup was coupled to the track and provides an effective 1Ω load on the primary side. In addition, to enable an easy implementation and a safe operation, the input voltage and reference current were scaled to 1/10 of the simulation study. The system control strategy implementation diagram is shown in Figure 6-16.
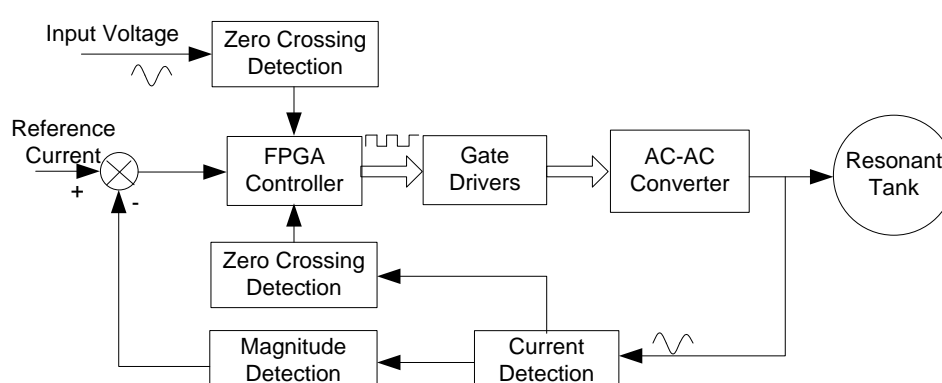
Figure 6-16: Controller block setup diagram

Figure 6-17 shows the experimental results of the converter with ZCS operation, with the input voltage, track current and gate driver signals of the switches S_1 and S_2 (as defined in

Figure 6-2). It can be seen that the AC-AC converter can generate a high frequency track current for IPT applications directly from a 50Hz low frequency input. S_1 and S_2 are used to control the energy injection when the input voltage is positive or negative respectively. The current sags have been demonstrated when the input voltage changes its polarity. The waveform of the track current is flat but has a small ripple during the controlled period which agrees with the simulation results. In addition, it can be seen that the maximum current ripple occurs at around the peak of the input voltage which can be clearly observed in Figure 6-18 and be in a good agreement with the previous analysis.
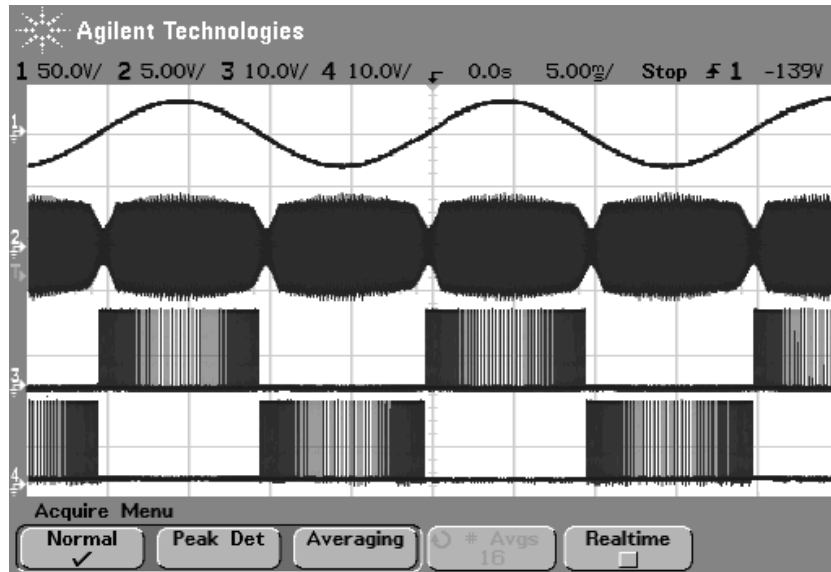
Figure 6-17: Experimental results of the proposed direct AC-AC converter

Figure 6-18 illustrates the experimental waveforms of the input voltage around a zero crossing point. It can be seen that the input voltage (trace1) is captured as it varies from the positive peak to the negative peak. The energy injection is controlled to provide a regulated 4A peak current in the primary track (trace 2) when the 50Hz input voltage is high enough regardless of being in the positive or negative cycles. It can be seen that in order to keep the track current constant, the switching frequency of S_1 (trace 3) and S_2 (trace 4) is much lower (about 1/10 of the resonant frequency) when the input voltage is near its peak. However, as the magnitude of the input voltage decreases, the operating frequency of S_1 increases and reaches half of the resonant current frequency to achieve full injection if the threshold voltage is lower than V_{in} in equation (6-11). Finally, switch S_1 stops conducting when the input voltage drops to zero in order to change into the negative direction, while the energy level in the resonant tank drops. The switch S_2 then starts to

inject energy from the zero crossing point. S_2 works at half the resonant frequency to obtain a full energy injection from the zero crossing point to the threshold value of the input voltage.
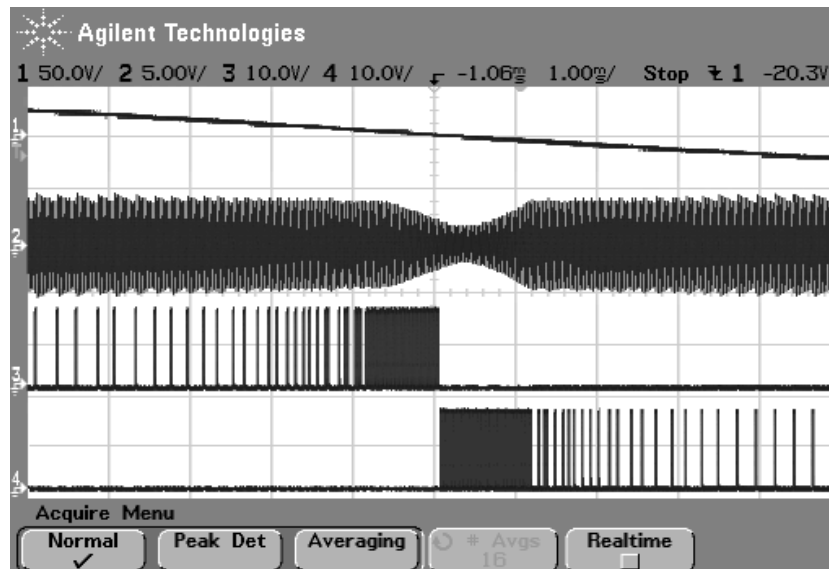
Figure 6-18: Current sag at zero crossing point

Current fluctuations can also be seen in the track current waveform (trace2) during operation. This shows the maximum track current when the input voltage is at its peak value, while the track current sag occurs around the zero voltage crossing point of the input AC voltage at a fixed load. Because the system quality factor is very high at a high frequency, the current damping is low. As expected, that the current ripple approximates a saw tooth waveform during the current controlled period. The result shows the maximum ripple occurs around the peak of the input voltage during the controlled period, which is caused by over injection and overconsumption. As a result, the maximum and the minimum current ripple during the controlled period are around 5.1A and 3.8A respectively. This is close and within the calculated values of the maximum value of 5.17A and the minimum value 3.78A, which can be obtained from equation (6-9) and (6-10) respectively.

In addition to this fluctuation during the controlled period, the track current (trace2) also shows that there is an obvious current sag around the zero crossing point of the input voltage. It can be seen that the envelope of track current from the experiment shows a good agreement with the circuit level simulation result using PLECS (trace2 in Figure

6-13) and the calculated result (trace 3 in Figure 6-13). The measured current sag of the experimental result is 1.78A, which is close to calculated value 1.81A using equation (6-26)

Figure 6-19 shows the transient of the switch commutation at the zero crossing point of the input voltage. It can be seen that the low frequency input voltage (trace 1) is changes from negative to positive. The variation of the magnitude of the input is nearly unnoticeable compared to the 30 kHz resonant current (trace 2). The magnitude of the track current decreases, even the input voltage starts to increase in the positive polarity. This further confirms the theoretical analysis. Trace 3 shows the gate drive signal of S_2, which controls the energy injection when the input voltage has a negative polarity. Trace 4 is the gate driving signal for S_4.
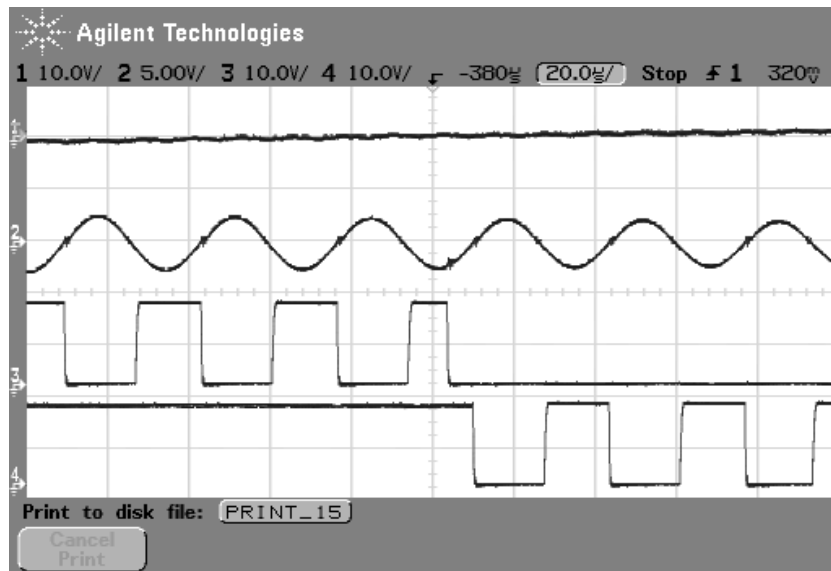
Figure 6-19: Switch commutation at Zero crossing point of input voltage

It can be seen that the negative input voltage is controlled by S_2 which has been applied to the resonant track when the track current is negative. The direction of the resonant current is the same as the direction of the input voltage. The converter will operate from Mode II to Mode III as stated in condition D and is shown in the illustration of Figure 6-7. In fact, the converter may operate at condition C from Mode IV to Mode I, when the input voltage changes from a negative to a positive polarity. As discussed before, the variable frequency is closely related to the circuit components and the practical operating conditions. Any

uncertainty of the variation in the resonant frequency or the input voltage frequency variation leads to a different operation, which is very difficult to predict.

Here, in Figure 6-19, when the input voltage is at the exact zero crossing point around the middle of the figure, according to the control strategy, S_2 is scheduled to turn off. Such a switch operation is also considered as soft switched ZVS; even though the resonant current is not at a zero crossing point. It also can be seen that S_4 is on when the input voltage is negative. However, the switch remains in its conduction state until the resonant current fully completes its half cycle even after the input voltage has already changed to be positive. The resonant current naturally flows through S_4 after S_2 turns off and a smooth commutation is therefore achieved.

6.7 Summary

In this chapter, a direct AC-AC IPT converter has been proposed. The converter has been shown to have a simpler structure compared to a traditional AC-DC-AC converter. This chapter focused on the analysis of the AC-AC converter in relation to the control strategy.

While there are a number of possible topologies for the direct AC-AC converters based on energy injection and free oscillation technique as discussed, only one selected example converter topology is described here. The operation principle and a detailed switching control sequence with reference to the current waveforms were analyzed. System modeling and theoretical analysis on the performance of the direct AC-AC converter were also conducted; in particular, the current ripple analysis including the current fluctuation during normal operation was undertaken. In addition, the current sag around zero crossing points of the input voltage was analyzed using energy balance principles. In the analysis, the approximate current envelope has also been derived to show the current sag.

The validity of both the theoretical analysis and the control method has been verified by simulation and experimental results.

Chapter 7

Investigation of a Push Pull Inverter Operating in Boost Mode

7.1 Introduction
7.2 Boost Mode Operation
7.3 System Modeling and Analysis
7.4 Multiple Operation Points Conditions
7.5 Simulation and Experimental Results
7.6 Summary
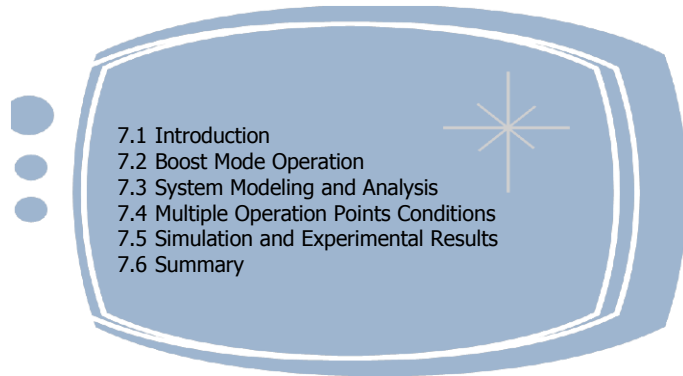
7.1 Introduction

Among different resonant configurations, the current fed push pull resonant inverter is one of the most popular primary power supplies for low to medium IPT applications due to its simplicity and high power efficiency [87]. To transfer power to one or more loosely coupled pickups, the input voltage of the push pull inverter is normally required to be high to obtain a high resonant voltage over the parallel tuned resonant tank. Since a parallel tuning configuration is the dual of a series one, a low frequency switching operation by the energy injection control, which reduces the current of the voltage fed inverters, thereby leads to a voltage boost up for a push pull (current fed) converter. As such, a boost in resonant voltage can help to extend the power transfer capability of the traditional push pull inverter.

This chapter investigates the boost operation of a push pull inverter. To ensure soft switching during the boost operation, multiple ZVS operation points will be determined by using a stroboscopic mapping model. Simulation and experimental analysis will be carried out to verify the boost operation of this push pull inverter at different ZVS operation points.

7.2 Boost Mode Operation

A typical push pull inverter for IPT applications is shown in Figure 7-1. It consists of a DC inductor, a phase splitting transformer, a parallel tuned track, and two semiconductor switches. A blocking diode in series with each switch is optional to prevent shorting the resonant capacitor if a full ZVS cannot be achieved.
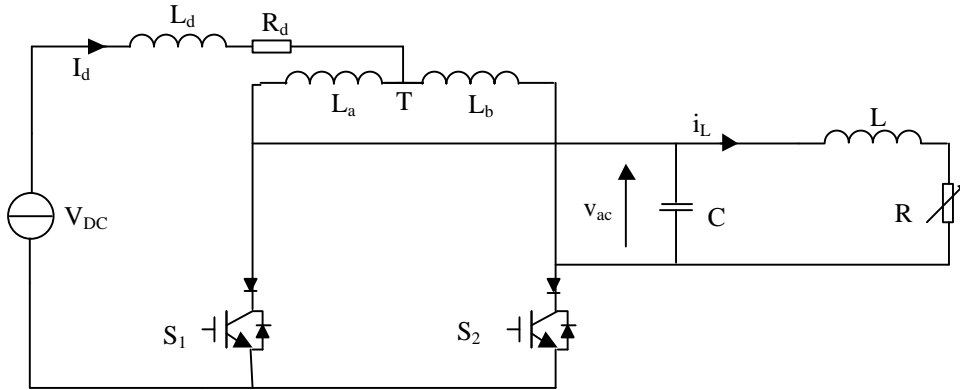
Figure 7-1: Typical Push pull inverter with series blocking diode

The push pull inverter normally operates at the ZVS frequency [125], where S_1 and S_2 are switched on and off at the zero voltage crossings of V_{AC} to drive the resonant tank. Therefore, the switches are essentially switched at 50% duty cycle. Under such an operation, the push pull resonant inverter produces nearly sinusoidal voltage and current in the resonant tank. Thus the switching losses are essentially eliminated, and a better waveform with low EMI is achieved.

Due to the high frequency operation, a push pull topology act as a quasi-current source inverter by alternating the conduction of the switch pairs. If each switch operates for a longer period than the resonant frequency, the current into the parallel resonant tank will be increased. For such a reason, if two switches are operated at a lower variable switching frequency than the fundamental ZVS resonant voltage, the output voltage can be boosted by following the relationship:

$$f_s < f_1 \tag{7-1}$$

Here f_s is the actual switching frequency; and f_1 is the fundamental ZVS frequency (given in [16]). Under such operation the resonant voltage will become higher. To have a better

understanding, Figure 7-2 illustrates the waveforms of the push pull converter when the actual switching frequency is about 1/3 of the fundamental ZVS frequency. For comparison purposes, the corresponding waveform of the push pull operated at the normal mode (operating at fundamental frequency f_1) is also illustrated in the same figure.

(a) $f_s = f_1$ (b) $f_s = f_1/3$
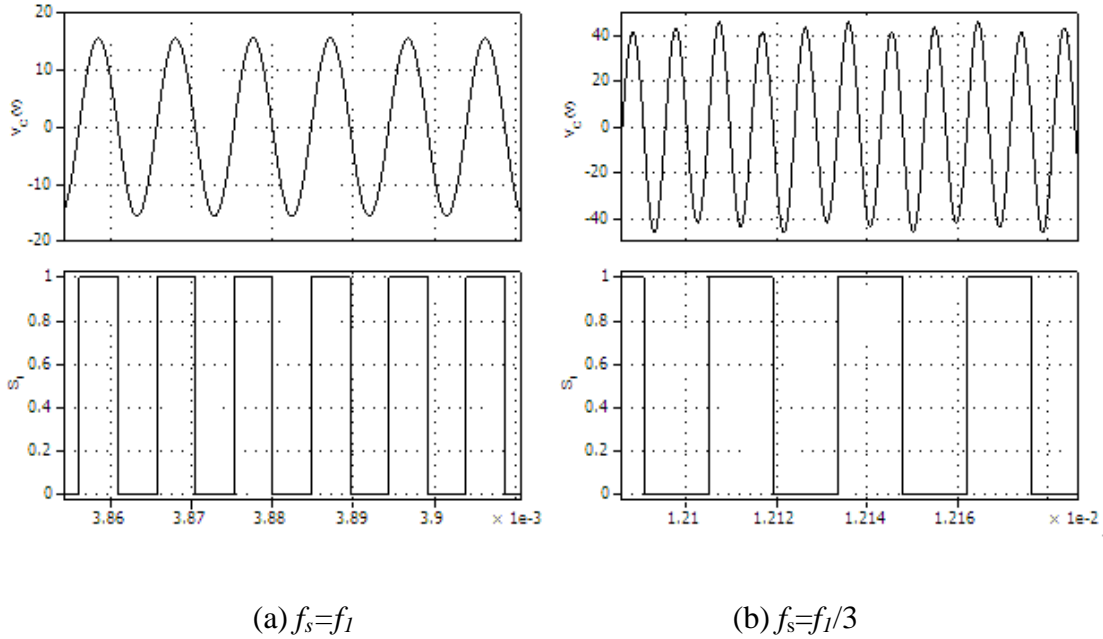
Figure 7-2: Switch operation of the inverter in boost mode

It can be seen that if the conduction frequency of each switches is lower than the fundamental ZVS frequency f_1, which is about 1/3 of f_1 in the example figure, the resonant voltage is increased by about three times. In fact, in addition to the fundamental ZVS frequency f_1, there may be multiple ZVS frequencies existing which can lead to different boosting features. Using this principle, a push pull inverter can be designed to have a higher power transfer capability by operating at lower ZVS frequencies. To understand whether more ZVS frequencies exist and where they are, as well as how the ZVS frequencies affect the inverter performance, a detailed analysis is undertaken in the following section.

7.3 System Modeling and Analysis

As discussed, running a push pull inverter at a lower switching frequency than the fundamental ZVS frequency can boost the resonant voltage. In addition, enabling a better performance and a reduction in the switching losses and EMI, it is desirable to operate the

push pull inverter at these low frequency ZVS points. However, even when multiple ZVS frequencies may exist for a high order push pull inverter, it does not mean all the ZVS frequency points are suitable for a boost operation without affecting the overall performance. In order to understand the exact ZVS operating frequencies and how this operation affects the output performance, a stroboscope mapping model method is used to analyse the ZVS frequencies of a push pull inverter. Unlike the traditional AC impedance analysis method, which is more suitable for a sinusoidal linear circuit, the stroboscopic mapping method is a numerical method for an accurate nonlinear switching circuit analysis [55]. It treats the switching period as a variable and can be used to find all possible steady state ZVS frequencies of a switch-mode converter.

7.3.1 Stroboscopic mapping model

In order to ensure soft switching operation of a push pull inverter shown in boost mode, switches S_1 and S_2 must operate alternately at the zero instants of the resonant voltage of the tuning capacitor. Each of the switches operates during half of the overall period of T_s under steady state condition. The equivalent circuit model of each operational state of the push pull inverter, where either (S_1 on/S_2 off) or (S_2 on/S_1 off), is shown in Figure 7-3 and Figure 7-4 respectively. Here the split windings of the transformer are modeled as uncoupled inductors. Selecting the currents and capacitor voltages in each equivalent circuit as state variables, the state space equations of the system can be obtained for each operation.
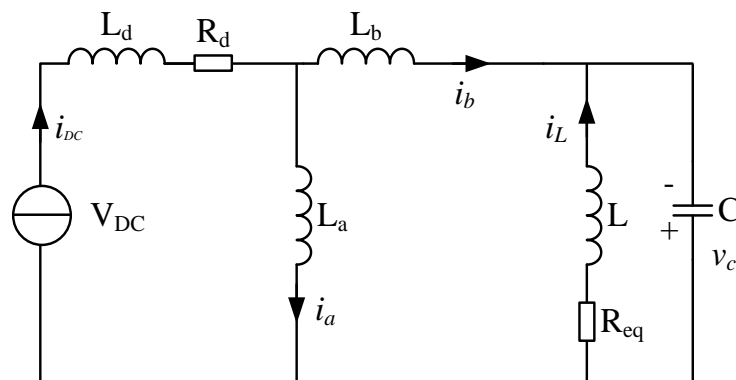
Figure 7-3: Equivalent circuit when S_1 is on, S_2 is off

From the equivalent model above, when S_1 is on, S_2 is off, the differential equation can be expressed as:

$$
\begin{cases}
\dfrac{di_a}{dt} = \dfrac{L_b V_{DC} - R_d L_b i_a - R_d L_b i_b - L_d v_c}{L_b(L_d + L_a) + L_a L_d} \\[3mm]
\dfrac{di_b}{dt} = \dfrac{L_a V_{DC} - R_d L_a i_a - R_d L_a i_b + (L_d + L_a)v_c}{L_b(L_d + L_a) + L_a L_d} \\[3mm]
\dfrac{dv_c}{dt} = -\dfrac{1}{C}(i_b + i_L) \\[3mm]
\dfrac{di_L}{dt} = -\dfrac{1}{L}(v_c - R_{eq} i_L)
\end{cases}
\tag{7-2}
$$
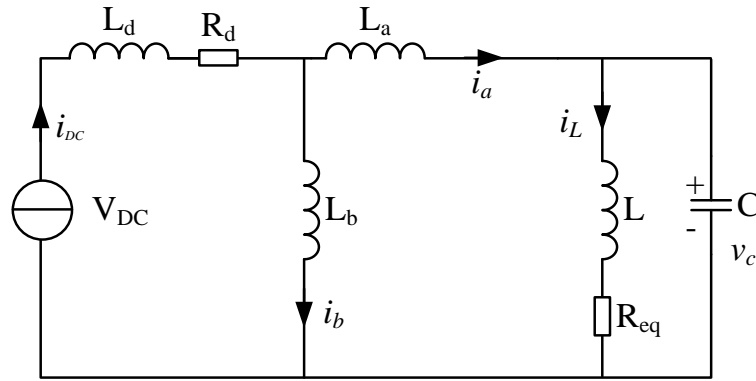
Figure 7-4: Equivalent circuit when S_2 is on, S_1 is off

Similarly, when S_2 is on, S_1 is off, the differential equation can be expressed as:

$$
\begin{cases}
\dfrac{di_a}{dt} = \dfrac{L_b V_{DC} - R_d L_b i_a - R_d L_b i_b - (L_d + L_b)v_c}{L_a(L_d + L_b) + L_b L_d} \\[3mm]
\dfrac{di_b}{dt} = \dfrac{L_a V_{DC} - R_d L_a i_a - R_d L_a i_b + L_d v_c}{L_a(L_d + L_b) + L_b L_d} \\[3mm]
\dfrac{dv_c}{dt} = \dfrac{1}{C}(i_a - i_L) \\[3mm]
\dfrac{di_L}{dt} = -\dfrac{1}{L}(v_c - R_{eq} i_L)
\end{cases}
\tag{7-3}
$$

Let $x = [i_a, i_b, v_c, i_p]^T$ and $v = [V_{DC}]$ be the state vector and the input vector respectively. The system can be described by the following state space model.

$$\dot{x} = Ax + Bv \qquad\qquad (7\text{-}4)$$

$A=A_1$, if S_1 is on and S_2 off.

$$A = A_1 = \begin{bmatrix} -\dfrac{R_d L_b}{\Delta_a} & -\dfrac{R_d L_b}{\Delta_a} & -\dfrac{L_d}{\Delta_a} & 0 \\[2mm] -\dfrac{R_d L_a}{\Delta_a} & -\dfrac{R_d L_a}{\Delta_a} & \dfrac{(L_d + L_b)}{\Delta_a} & 0 \\[2mm] 0 & -\dfrac{1}{C} & 0 & -\dfrac{1}{C} \\[2mm] 0 & 0 & -\dfrac{1}{L} & -\dfrac{R_{eq}}{L} \end{bmatrix}, \qquad B = B_1 = \begin{bmatrix} \dfrac{L_b}{\Delta_a} \\[2mm] \dfrac{L_a}{\Delta_a} \\[2mm] 0 \\[2mm] 0 \end{bmatrix}$$

$$\Delta_a = L_b(L_{DC} + L_a) + L_a L_{DC}$$

$A=A_2$, if S_2 is on, and S_1 off.

$$A = A_2 = \begin{bmatrix} -\dfrac{R_d L_b}{\Delta_b} & -\dfrac{R_d L_b}{\Delta_b} & -\dfrac{(L_d + L_b)}{\Delta_b} & 0 \\[2mm] -\dfrac{R_d L_a}{\Delta_b} & -\dfrac{R_d L_a}{\Delta_b} & \dfrac{L_d}{\Delta_b} & 0 \\[2mm] \dfrac{1}{C} & 0 & 0 & -\dfrac{1}{C} \\[2mm] 0 & 0 & -\dfrac{1}{L_p} & \dfrac{R_{eq}}{L_p} \end{bmatrix}, \qquad B = B_2 = \begin{bmatrix} \dfrac{L_b}{\Delta_b} \\[2mm] \dfrac{L_a}{\Delta_b} \\[2mm] 0 \\[2mm] 0 \end{bmatrix}$$

$$\Delta_b = L_a(L_{DC} + L_b) + L_b L_{DC}$$

Since the system matrix (A) is invertible, and the input voltage V_{DC} is a constant in each half operation period, the solution for each operation state can therefore be described as follows.

$$x(t) = e^{At} x_0 + \left(e^{At} - I\right) A^{-1} Bv \qquad\qquad (7\text{-}5)$$

Here x_0 is the initial value, and the identity matrix (I) is of the same size as the system matrix (A). Due to the alternating switching conduction repeating at steady state, x_n could be defined as the initial value of the current state of the nth switching period T, which is

also the final value of the last state. Similarly, x_{n+1} could to be defined as the final value of the current state, which is also the initial value at the next period. As such, the iteration equation of the states of $(n+1)^{th}$ period, therefore, can be expressed generally as:

$$x_{n+1} = e^{AT} x_n + \left(e^{A\frac{T}{2}} - I \right) A^{-1} B V_{dc} \tag{7-6}$$

Because the actual waveforms of each operation repeat at steady state, the state vector repeats periodically, which leads to a fixed point $x^* = x_{n+1} = x_n$. By the definition of $e^{A\frac{T}{2}} = \Phi(\frac{T}{2})$, then according to equation (7-6), all of the fixed operation points of the system can be obtained by:

$$x^* = \left(I - \Phi_2\left(\frac{T}{2}\right)\Phi_1\left(\frac{T}{2}\right) \right)^{-1} \left(\begin{array}{c} \left(\Phi_2\left(\frac{T}{2}\right)\left(\Phi_1\left(\frac{T}{2}\right) - I \right) A_1^{-1} B_1 V_{dc} \right) \\ + \left(\Phi_1\left(\frac{T}{2}\right) - I \right) A_2^{-1} B_2 V_{dc} \end{array} \right) \tag{7-7}$$

The resonant voltage and the track current at all the possible switching instants can be described as follows.

$$f_{v_C}(T) = Y x^* \tag{7-8}$$

$$f_{i_L}(T) = Z x^* \tag{7-9}$$

where $Y = [0 \ 0 \ 1 \ 0]$ and $Z = [0 \ 0 \ 0 \ 1]$ are the selection matrices of the capacitor voltage $v_c(t)$ and the track current $i_L(t)$ respectively. In order to obtain the ZVS points, the resonant voltage must be zero at the switching instants. This means that the resonant voltage of the model at fixed operating periods has to satisfy the boundary condition as following:

where for the first half cycle:

$$H_1\left(\frac{T}{2}, x^*\right) = Y\left(\Phi_1\left(\frac{T}{2}\right)x^* + \left(\Phi_1\left(\frac{T}{2}\right) - I \right) A_1^{-1} B_1 V_{dc} \right) = 0 \tag{7-10}$$

And for the second half cycle;

$$H_2\left(\frac{T}{2},\frac{T}{2},x*\right)=Yx*=0 \tag{7-11}$$

7.3.2 Determination of multiple ZVS periods

From the above stroboscopic mapping method, once the capacitor voltage reaches the boundary condition, it means that the switches are operating under a zero crossing condition. Accordingly, all of the obtained values of T_S are the possible ZVS periods of the push pull inverter. Based on such a mapping method, the voltage and the associated current at the different switching instants can also be obtained. Figure 7-5 shows the capacitor voltage and the track current of the stroboscopic mapping model of a given push pull inverter at different operation periods which are calculated by equations (7-8) and (7-9). The detailed parameters of the push pull inverter are listed in Table 7-1. The Matlab code for the calculation of the ZVS periods can be found in the Appendices. As can be seen from the figure, the ZVS periods are the points where the capacitor voltage is equal to zero. It has been found that there are more than one ZVS points for the push pull inverter. If the push pull inverter is operated at these ZVS periods, the inverter will be fully soft switched and leads to different voltages and track currents.

Table 7-1: Component parameters of push pull inverter

Notes	Parameters	Values
Input DC voltage	V_{DC}	10 V
DC inductor	L_d	1 mH
Splitting transformer	L_a	1 mH
Splitting transformer	L_b	1 mH
Primary resonant capacitor	C	0.67 μF
Primary resonant inductor	L	3.45 μH
ESR of track	R_{ESR}	0.012 Ω
Total Equivalent load	R	0.06 Ω
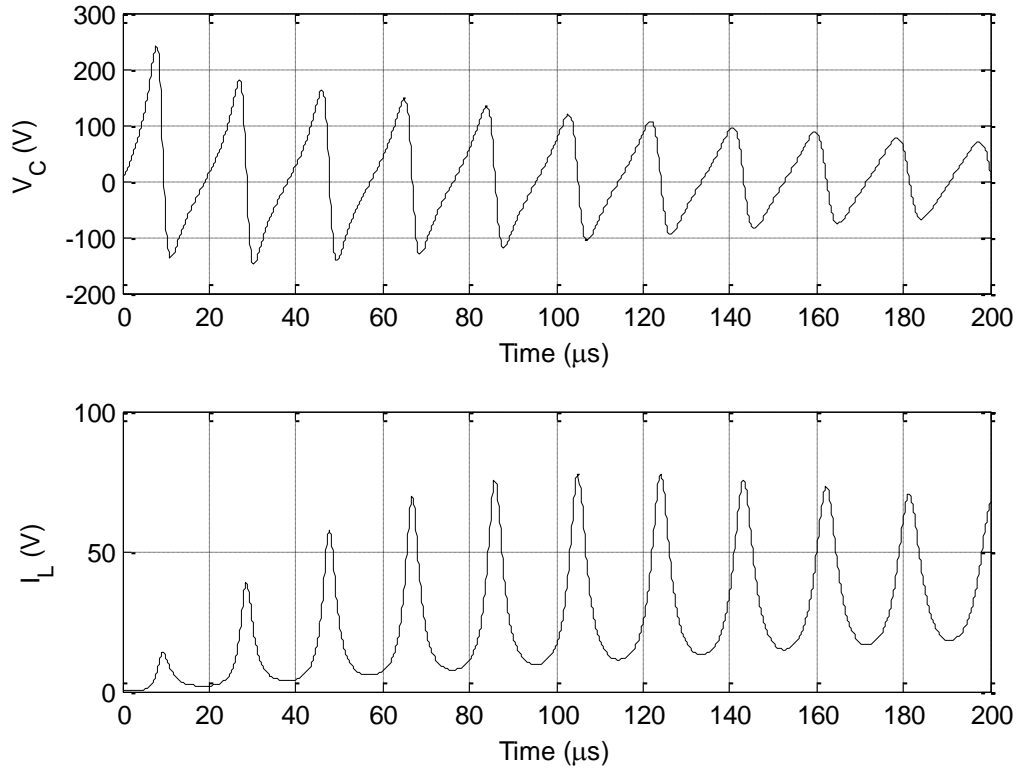
Figure 7-5: Voltage and current waveforms of ZVS points of the stroboscopic map

To clearly find these ZVS points and their relationship, the first nine of the ZVS periods and frequencies are listed in Table 7-2.

Table 7-2: Calculated value of first nine ZVS operation points

ZVS Points	1	2	3	4	5	6	7	8	9
T_z (μs)	9.60	19.1	28.7	38.2	47.8	57.3	66.9	76.4	86.0
f_z (kHz)	104.17	52.36	34.84	26.18	20.92	17.45	14.95	13.09	11.63

The first ZVS point is at 9.60μs, which is close to the free oscillation period 9.55μs. As can be seen in Figure 7-5, the track current at the first ZVS point is nearly located at the

first peak. This implies that if the resonant voltage of the capacitor is equal to zero, the resonant track current is nearly at its resonant peak due to the approximate 90 degrees phase angle delay. However, at the second ZVS point, which is about 19.1μs in Figure 7-5, it can be observed that the voltage is at zero but the corresponding track current at this instant is lower. It is difficult to determine the relationship between the resonant voltage and the track current at the 2nd and other even number operation points.

7.3.3 Waveforms

As shown in Table 7-2, the operation frequencies are nearly an integral multiple of the fundamental frequencies. After given the exact ZVS operation points, the steady state waveforms of the inverter output voltage and current can be obtained to understand how these ZVS operation points affect the resonant voltage and the resultant track current.

Due to the symmetrical operation of two switches, once the ZVS points are calculated by equation (7-7), the waveforms obtained during half period operation can be obtained. The resonant voltage waveform is identical for both half cycles at steady state. Therefore, the waveform obtained before reaching the first boundary condition defined by equation (7-10) can present the actual current at steady state. The resonant voltage and the track current can be expressed respectively as:

$$V_{C\_H_1}(t) = Y\left(\Phi_1\left(\frac{t}{2}\right)x* + \left(\Phi_1\left(\frac{t}{2}\right) - I\right)A_1^{-1}B_1V_{dc}\right) \qquad (7\text{-}12)$$

$$i_{L\_H_1}(t) = Z\left(\Phi_1\left(\frac{t}{2}\right)x* + \left(\Phi_1\left(\frac{t}{2}\right) - I\right)A_1^{-1}B_1V_{dc}\right) \qquad (7\text{-}13)$$

Figure 7-6 (a) – Figure 7-9 (a) show the half period waveform of the mapping model from equation (7-12) and (7-13), which are the first four operation points including both odd and even ZVS points. In fact, here the time span doubles for easy comparison with the zero crossings of $f_{V_C}(t)$. This means the magnitude of the actual voltage and current waveforms could decay by half over this time. The waveforms of the second half period repeat in the opposite direction.

To understand the relationship between the half period and full period waveforms easily, a steady state waveform also can be obtained by numerical calculation once the operation frequencies are obtained in Table 7-2. Figure 7-6 (b) – Figure 7-9 (b) show the voltage and track current using numerical calculations at steady state over an entire operating period.

(a)   (b)
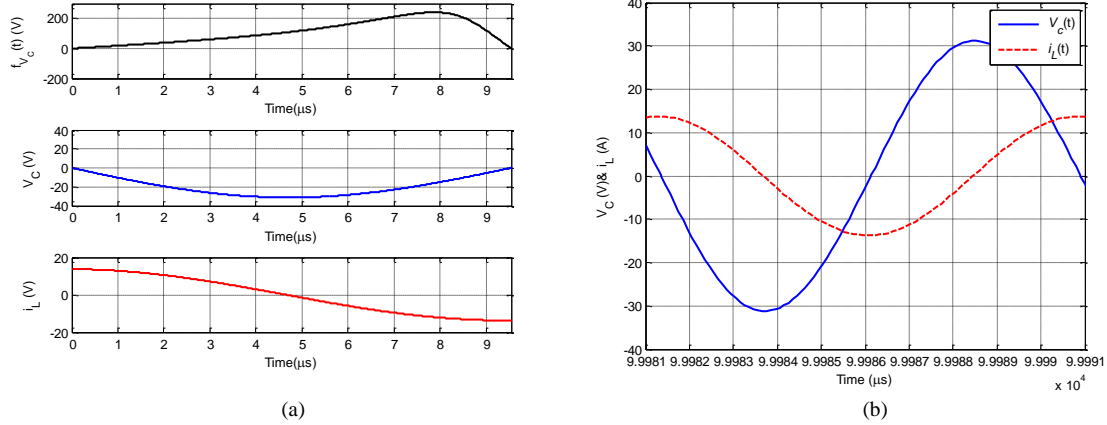
Figure 7-6: Voltage and current waveforms of at 1st ZVS point

(a)   (b)
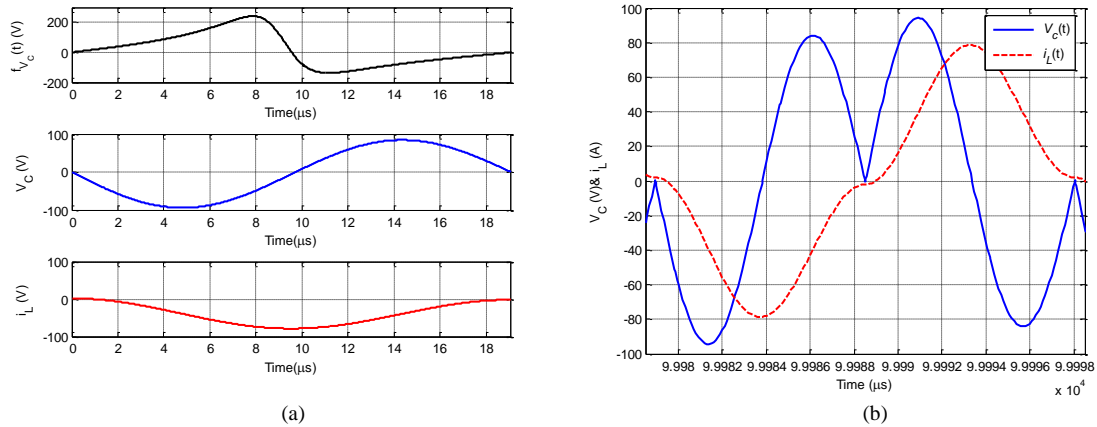
Figure 7-7: Voltage and current waveforms of at the 2nd ZVS point
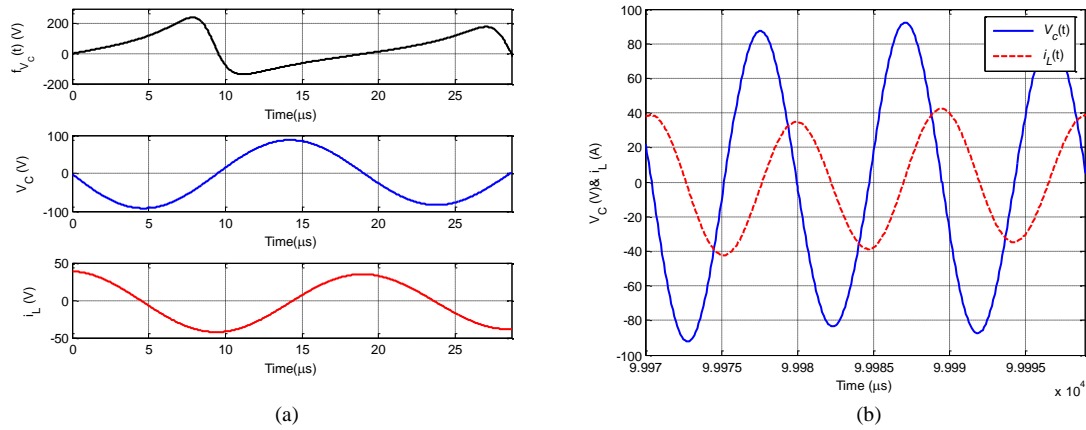
Figure 7-8: Voltage and current waveforms of at 3rd ZVS point
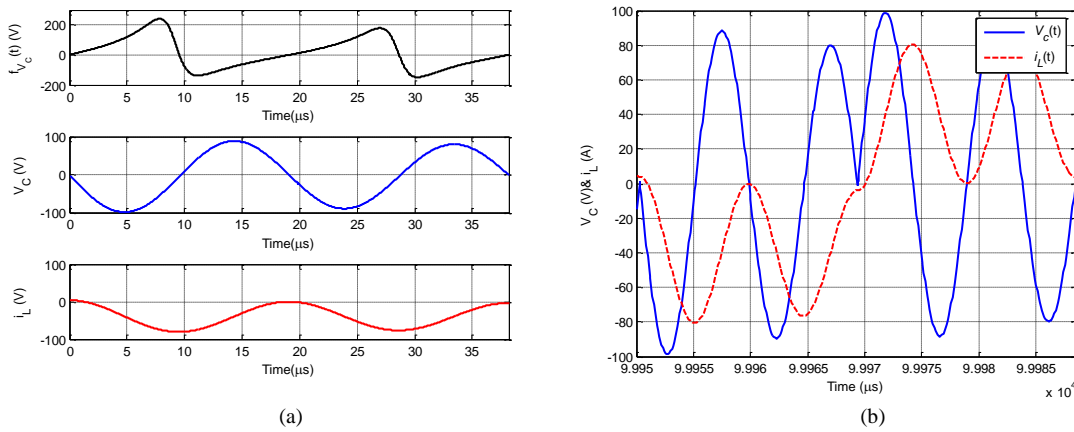
Figure 7-9: Voltage and current waveforms of at the 4th ZVS point

It can be seen from Figure 7-6 (a) that the voltage waveform is nearly a half sine wave from equation (7-12), if the inverter is operated at the fundamental ZVS point. After repeating this operation over the second half of the waveform as shown Figure 7-6 (b), it can be clearly seen that the voltage waveform is nearly completely sinusoidal. The track current waveform is also nearly sinusoidal with about 90 degrees phase delay. At the 2nd ZVS operation point shown in Figure 7-7 (a), it can be seen that, the peak value of the resonant voltage is boosted to about 100V which is nearly three times that of the first ZVS point. The resonant voltage over the half period is nearly sine wave but it is heavily distorted over a full period, resulting in a poor current waveform. The current at the secondary ZVS operation point is also boosted to around 80A. The waveform of an entire period in Figure 7-7 (b) however is not smooth. There are two continuous half positive or negative cycles in the voltage waveform at steady state. In addition, the current waveform is not sinusoidal at all and includes obvious harmonic distortion. When the push pull

inverter works at the 3rd ZVS operation point, the voltage draws a smooth and nearly sinusoidal waveform again as shown in Figure 7-8 (b), The current waveform also becomes much better compared to the 2nd ZVS point. Although the magnitude of the capacitor voltage and the track current at the third operation point drops compared with the 2nd operation point, both of them are almost boosted by almost three times over normal operation compared to the fundamental ZVS point. But it also can be observed from Figure 7-8, that a small fluctuation arises in both the voltage and current when working at this 3rd operation point. Figure 7-9 shows that if the inverter is operated at the 4th operation point, the operation frequency at this ZVS point is about 1/4 of the ZVS switching frequency of the fundamental ZVS point. As expected from the earlier results, two parallel positive or negative half cycle appear on both the voltage and current waveforms. The quality of the waveforms under this 4th operation point is very poor and not acceptable.

Further investigation shows that the resonant voltage waveforms of all even ZVS operation points are heavily distorted. In contrast, the resonant voltage waveforms of all odd ZVS operation points are smooth with less distortion. The amplitude of the voltage increases with the decrease of ZVS frequency. Good current waveforms are also obtained at odd ZVS operation points because the energy injection direction is consistent with the trend of the voltage oscillation. Such a phenomenon offers a good basis for designing a push pull inverter with a high power transfer capability without an additional boost stage to increase the DC input voltage.

Each of the odd operation points can be accurately obtained by the numerical solutions of the stroboscopic mapping method. But for a system with a high Q, the operation frequency can be approximated as follows:

$$f_S \approx \frac{1}{2n+1} f_1 \quad n_= 1, 2, 3 \tag{7-14}$$

Here f_1 is the first ZVS frequency, which is nearly equal to $f_1 = 1/2\pi\sqrt{LC}$ if Q is high.

7.4 Multiple ZVS Operation Points Conditions

According to the above stroboscopic mapping model, the numerical solutions of the multiple ZVS operation points can be obtained for a given push pull inverter. The

drawback of the stroboscopic model is that the numerical solution does not predict the conditions which can ensure a proper ZVS points for boost operation. In fact, the existence of the multiple ZVS points is determined by the circuit parameters, e.g. the quality factor of the resonant circuit. By looking at the structure of the push pull inverter in Figure 7-1, the DC inductor and the phase splitting transformer are mainly required to form a quasi-current source by alternating the switching operation of S_1 and S_2. In practice, they are normally designed to be much larger than the track resonant inductance [126, 127]. The large DC inductance and high frequency operation make the input current almost constant, so a fifth order push pull inverter could be simplified to a parallel tuned circuit excited by a current source.

Because the switches conduct alternately, the end of a particular switching period can be treated as the initial condition for the start of the next switching period. In addition, these conditions must last for an entire half switching period. The input of the push pull resonant inverter can be regarded as a step-input current source at each switching period. Figure 7-10 shows a model of the inverter exited by a step current injection at the switching instant of the ZVS points. Based on such a model, an approximated analysis can be conducted to find a general condition for the existence of multiple resonant frequencies.
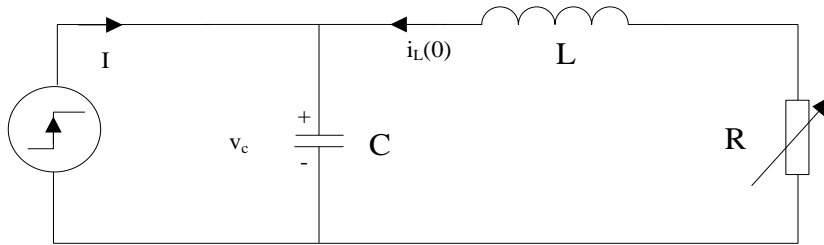
Figure 7-10: Step current injection model at ZVS points

For this step current injection model, the following equation can be obtained:

$$\begin{cases} \dfrac{di_L}{dt} = -\dfrac{R}{L}i_L - \dfrac{1}{L}v_C \\[2mm] \dfrac{dv_C}{dt} = \dfrac{1}{C}I + \dfrac{1}{C}i_L \end{cases} \qquad (7\text{-}15)$$

If the resonant voltage v_C is considered, a second order ordinary differential equation can be obtained as:

$$LC\frac{d^2 v_C}{dt^2} + RC\frac{dv_C}{dt} + v_C = IR \tag{7-16}$$

With the initial condition $v_C(0)=0$, $i_L(0)=C\dfrac{dv_C}{dt}-I$ the complete solution to the capacitor voltage can be easily obtained and expressed as:

$$v_c(t) = \frac{IR}{\sin\theta}e^{-\frac{t}{\tau}}\sin(\omega_f t - \theta) + IR \tag{7-17}$$

where $\omega_f = 2\pi f$ is the free ringing angular frequency, $\tau = 2L/R$ is the time constant, and θ is an initial phase angle which can be expressed as:

$$\theta = \arctan\left(\frac{\omega_f IRC}{i_L(0) + I(1 - RC/T)}\right) \tag{7-18}$$

It can be seen that the voltage equation consists of a forced DC offset component and a natural resonance with decay component. The competition between the DC offset and the decay will determine if the voltage has multiple ZVS points.

The ZVS period is determined by the circuit parameters L, C, R, the injection current and the initial track current. At each ZVS switching instant, the track current is lagging behind the capacitor voltage. The lagging current will offset the DC effect of the step injection current and contribute to more ZVS points. However, the initial current cannot be given arbitrarily, which is determined by operation conditions, e.g. input voltage and Q. A low input voltage with will cause a low current. At the switching transient, although the track current is around the negative peak, it can be close to zero if the input voltage is very small. Under such a condition, if assuming the initial current in equation (7-17) is zero, the critical ZVS condition obtained for the circuit will be valid for different inputs, which will cause a higher negative initial value which partly offsets the DC effect of the step injection current. According to this, if assuming the initial track current $i_L(0)=0$, a minimum critical value of Q obtained is which ensures the existence condition of the ZVS points. Under such a condition, by considering the complete solution from equation (7-17), the minimum value of the resonant voltage can be obtained if its derivate is equal to zero as expressed by:

$$v_C'(t) = 0 \tag{7-19}$$

It can be derived that the time corresponding to the minimum and maximum voltage is:

$$t = \frac{1}{\omega_f}\left(\arctan(\omega_f) + \pi + \theta\right) \tag{7-20}$$

A meaningful "t" corresponds to a minimal resonant voltage, and there may be more than one of these points. Substituting equation (7-20) into the equation (7-17), all the minimum or the maximum voltages can be expressed as:

$$v_C = -IRQ\,\mathrm{e}^{-\frac{t}{\tau}} + IR \tag{7-21}$$

The minimum or the maximum resonant voltage is related to the quality factor of the tuning circuit, the injection current, and the total equivalent load resistance. For the existence of the nth zero voltage crossing, the corresponding $v_{C\min}$ in the next negative half cycle will have to be smaller than or equal to zero and should meet the following condition:

$$Q\,\mathrm{e}^{-\frac{t_{\min}}{\tau}} \geq 1 \tag{7-22}$$

Here t_{min} varies for different zero points. It occurs at approximately at $((4n\text{-}1)\pi/2\omega_0)$, where n is integer. For example, it is $3\pi/2\omega_0$ for the 1st operation point and $7\pi/2\omega_0$ for the 3rd operation point. Because $\tau = 2Q/\omega_0$, equation (7-22) therefore can be solved for each operation point. The critical Q can be obtained to ensure the existence of ZVS points. Equation (7-22) therefore can be expressed for different operation points as:

$$Q\ln Q \geq \frac{(4n-1)}{4}\pi \tag{7-23}$$

It is easy to get the numerical solution to different ZVS operation points. For example, if the inverter is to operate at the 3rd ZVS point, the circuit has to be designed to have $Q>3.98$ to ensure resonance. Similarly, if it operates at the 5th ZVS point, Q should be larger than 5.23.

7.5 Simulation and Experimental Results

To investigate the operation of the push pull inverter in the proposed boost mode operation, a simulation study is undertaken using Simulink/PLECS. The PLECS model of the push pull inverter is shown in Figure 6-14 (a). The gate drive signal is generated according to the different ZVS periods which were obtained using the stroboscopic mapping method discussed earlier. The diagram of the push pull inverter is shown in Figure 6-14 (b). It consists of two MOSFETs and two blocking diodes in series connection to prevent possible shorting of the resonant capacitor by reversing conduction of the two MOSFETs. The detailed circuit parameters are listed in Table 7-1.
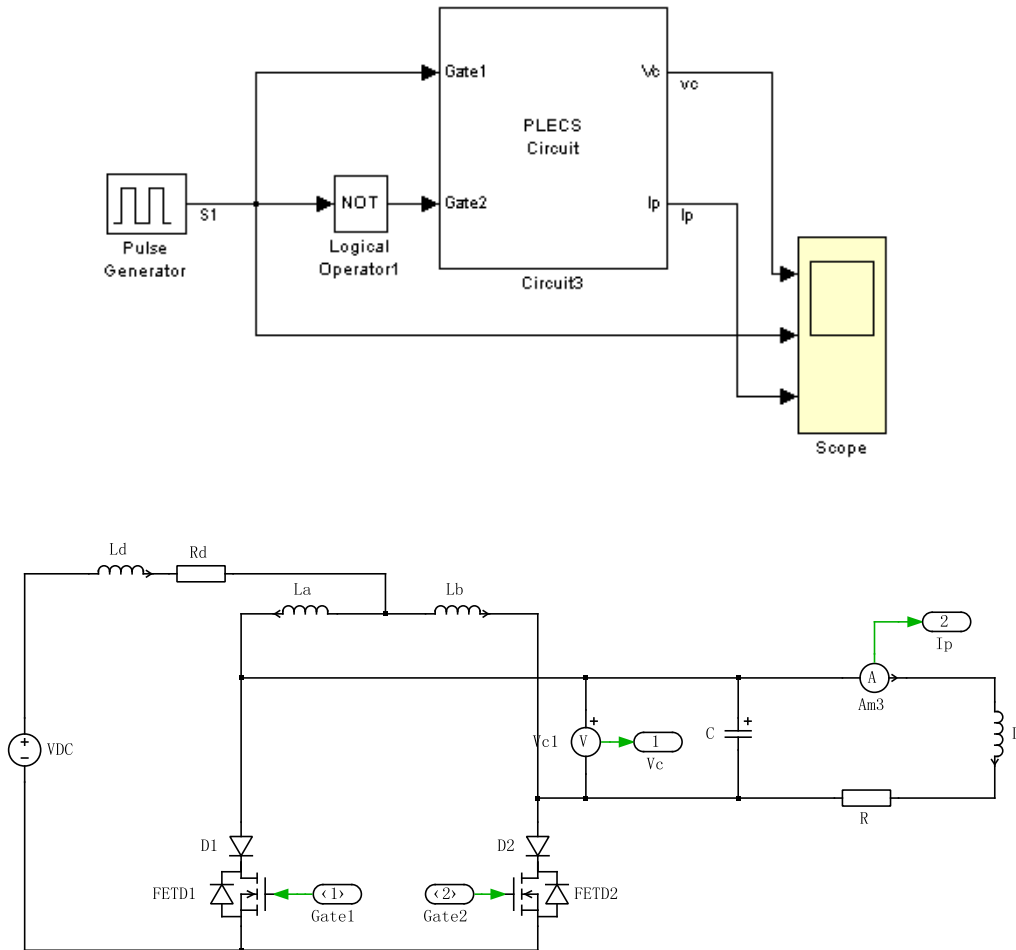
Figure 7-11: PLECS circuit model of the push pull converter in boost operation

The multiple odd ZVS points obtained previously are listed in Table 7-2. The simulation study takes the 3rd and 5th operation points as examples to evaluate the operation and performance. For comparison, simulation at the fundamental ZVS point is also undertaken.

The simulation waveforms of the resonant voltage and the track current are shown in Figure 7-12.

$f_s=f_1$ $f_s=1/3\,f_1$ $f_s=1/5\,f_1$
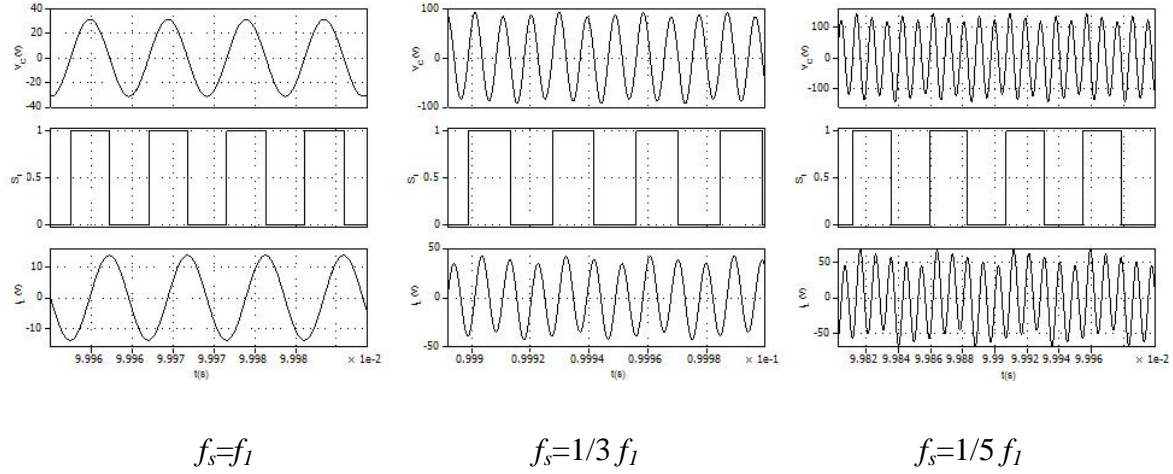
Figure 7-12: Simulation results of the selected odd ZVS points

It can be seen that as expected from earlier analysis the resonant voltage is boosted by about three and five times compared to the fundamental ZVS operation point when operation is at a third or a fifth of the fundamental frequency respectively. The track current is boosted accordingly. But it can also be seen from the simulation result that the boosted current has some ripples, which is mainly caused by the DC offset and the circuit decay. Using the Powergui FFT analysis tool within Matlab/Simulink, FFT analysis of resonant current has been undertaken and results are shown in Figure 7-13 and Figure 7-14 respectively. Although the current amplitude fluctuates, the waveform is smooth and nearly sinusoidal. The overall THD is 0.81% and 0.87% at the 3rd and 5th ZVS operation point respectively. This is sufficiently good for IPT applications, where the average power transfer is the major interest.
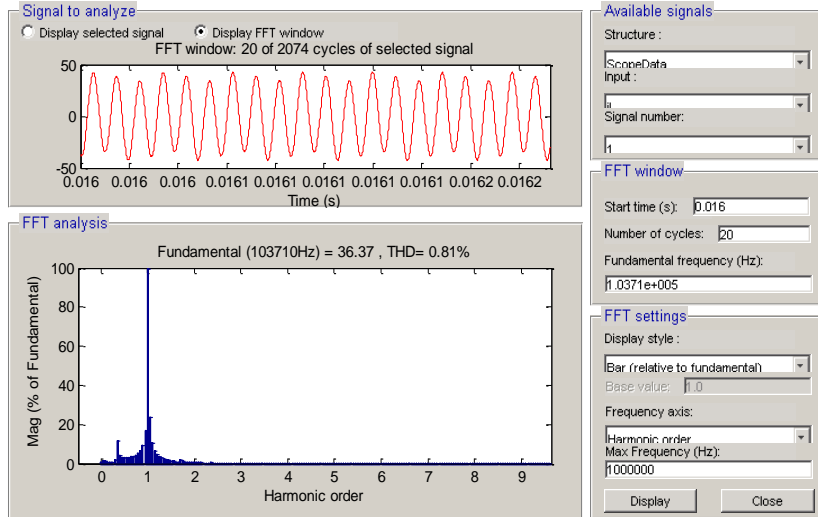
Figure 7-13: FFT analysis of track current at the 3rd ZVS point
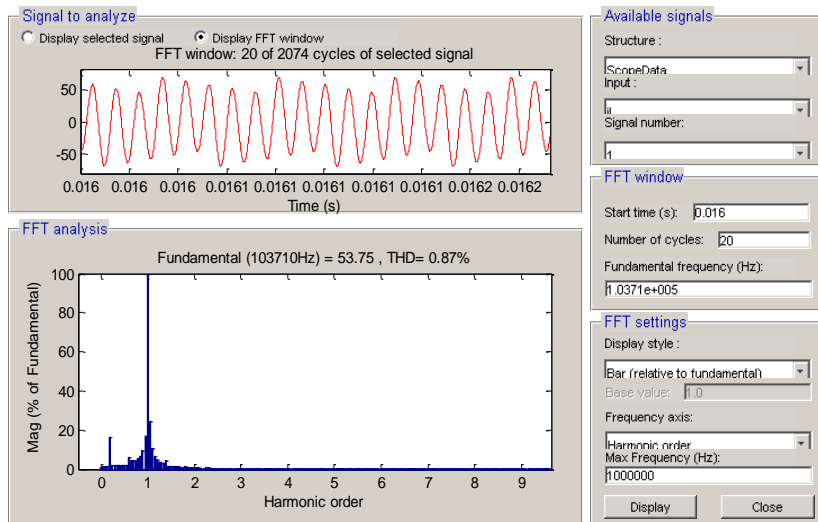
Figure 7-14: FFT analysis of track current at the 5th ZVS point

An experimental system has also been set up using the same circuit as in the simulation study. The Q of the circuit is 36, which is much higher than the theoretical values of 3.98 and 5.23 to ensuring the existence of the 3rd and the 5th ZVS operation points. As shown in the Figure 7-15 to Figure 7-17, the experiment has demonstrated these two points do exist, and the inverter is operated at the fundamental, and the 3rd and 5th ZVS operation periods. The experimental results of the gate drive signal, the resonant voltage, and the resultant track current are also shown. From top to bottom, the waveforms are the resonant voltage of the capacitor (trace 2), the gate signal of S_1 (trace 1), and the track current (trace 3).
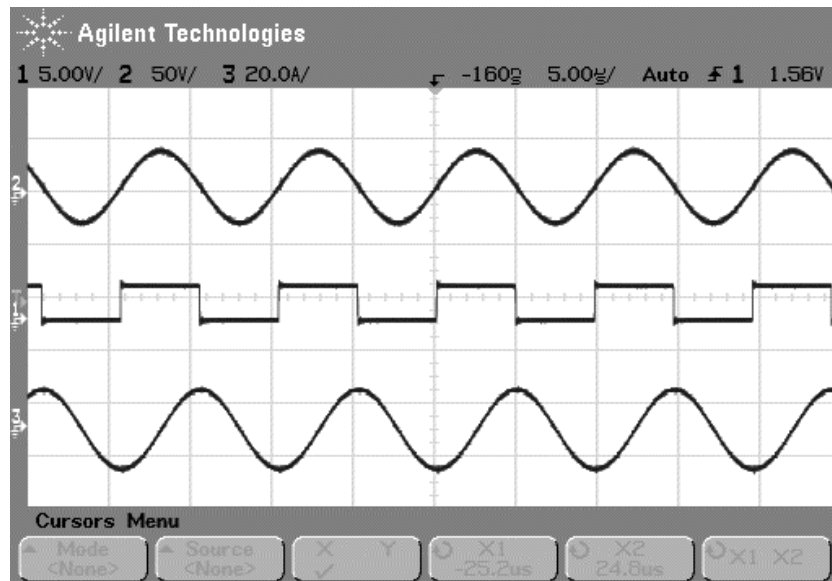
Figure 7-15: Steady state waveforms under 1st ZVS operation point
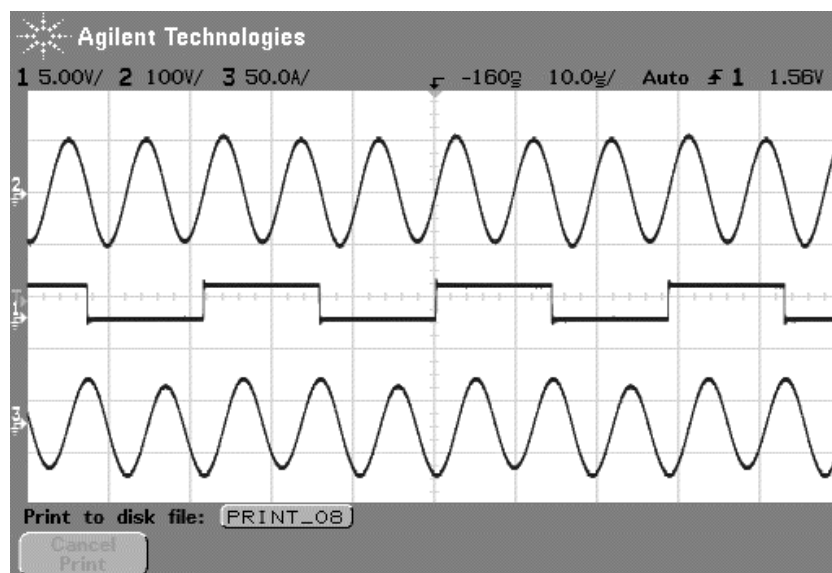
Figure 7-16: Steady state waveforms under the 3rd ZVS operation point
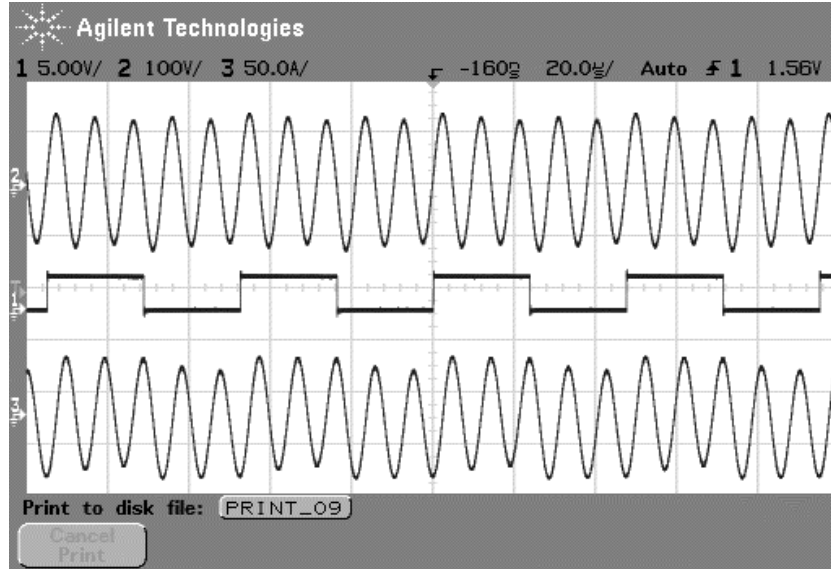
Figure 7-17: Steady state waveforms under the 5th ZVS operation point

It can be observed that the push pull inverter results in different resonant voltages and tracks current when operated at these different ZVS switching frequencies. These experimental results are very close to simulation results shown in Figure 7-12. The peak value of the resonant voltage in Figure 7-16 is about 100V, which is nearly three times over the voltage at the first points shown in Figure 7-15. Accordingly, the voltage in Figure 7-17 is about five times higher. The track current has also been increased by operating at different frequencies, which is also nearly three and five times higher by operating at the 3rd and 5th operation points. As shown, the track current fluctuations are clearly observable when the push pull inverter operates at the boost mode, but the track current waveform obtained is sufficiently good for IPT applications where the key interest is the high frequency magnetic field generation for average energy transfer.

7.6 Summary

In this chapter, a method of operating a traditional push pull inverter in the boost mode has been proposed. The principle of this boost operation was discussed. It has been found that operating over a long period operation leads to a boost in both the resonant voltage and track current of a push pull configuration for IPT systems. To achieve ZVS operation, different zero voltage crossing points have been found using a stroboscopic mapping model. The boost ability and quality of the voltage and current at different ZVS operation frequencies were analyzed. As shown the traditional push pull inverter should be operated

at one of the ZVS operation points to ensure high quality while boosting the resonant voltage and track current.

From a system design point of view, the conditions of the existence of different ZVS points of a push pull inverter were analyzed. The minimum critical *Q* was defined for different ZVS operation points, which is important for designing a push pull inverter with boost operation.

In order to verify the boost operation, a simulation study was undertaken. A practical push pull inverter was built and tested. Both the simulation and practical results demonstrated that push pull inverter can operate under boost mode at lower ZVS frequencies, which offers a good choice of operating a traditional push pull inverter for high power IPT applications.

Chapter 8

Conclusions and Suggestions for Future Work

8.1 General Conclusions
8.2 Contributions of This Thesis Work
8.3 Suggestions for Future Work
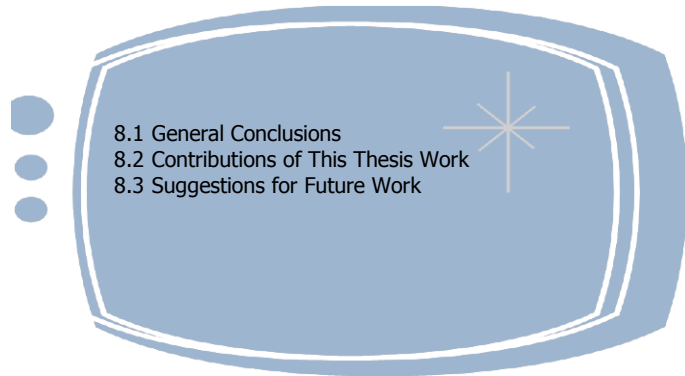
8.1 General Conclusions

A comprehensive study on new resonant converters based on energy injection method for IPT (Inductive Power Transfer) systems was undertaken in this thesis. Attention was paid to the following four main aspects:

- New conversion methods for voltage and current fed converters,
- High frequency current generation and control methods for IPT systems,
- New resonant converters and practical aspects of IPT applications,
- Performance evaluation of multiple high frequency IPT power converters.

A general introduction to contactless power transfer technology was presented in the first chapter of this thesis. It has been shown that although wire connected power transfer technology is mainstream, the need for contactless power transfer; has recently increased significantly, and will continue to increase in the future due to the need to eliminate direct electric connections in many emerging industries. Many different solutions were discussed to achieve this, such as laser, electromagnetic wave, CPT, and IPT. All of these wireless power transfer technologies have advantages and constraints, and thanks to the rapid

advances in modern converter technologies, IPT has proven to be the most feasible technology for most practical applications. Many research groups and commercial companies have shown their interest, and have been involved in the research and development of wireless power transfer technologies. Among various research topics, high frequency current generation on the primary track has been found to be a key aspect in an IPT system. Consequently, high quality power converters which generate the high frequency current are of primary importance for IPT applications.

In Chapter 2, a general overview of the technologies of high frequency power converters for IPT systems was presented. It has been found that resonant converters are the most suitable solution for IPT applications to generate the high frequency currents required with minimal switching losses and electromagnetic interference. Since the inherent track can be used as the inductance in a resonant tank, load resonant converters are preferred in IPT systems. Several types of commonly used DC-AC voltage and current fed high frequency resonant inverters (including their topologies and control strategies) were presented and discussed. In addition, several matrix structures that attempt to provide a direct AC-AC conversion was also overviewed. Although most of the AC-AC matrix converters have been developed for low frequency applications, it is possible to generate a high frequency current using circuit resonance. A fixed frequency PWM switching strategy with switching commutation is normally used for high frequency current generation. But the difficulties involved in the switching commutation and the magnitude regulation of the high frequency output make matrix converters unsuitable for practical IPT applications.

Following the overview of the IPT system and mainstream high frequency converters, a new concept called "energy injection and free oscillation" was introduced. According to this, a new conversion method was proposed based on the high frequency circuit resonance. An extensive study was undertaken into both the simple half bridge and improved full bridge configurations. Circuit modeling and theoretical analysis were conducted to understand the energy injection inverters. In order to achieve soft switching and reduce EMI, a ZCS strategy was proposed to control the full bridge inverter, which is an extension of the half bridge inverter. Simulations were conducted to verify the operation of the full bridge energy injection inverter during the conditions of the startup, steady state, and varying load. Using a FPGA as the core control unit, a practical inverter

was developed to implement the control strategy with a fast and accurate ZCS operation. Experimental and simulation results have demonstrated that the proposed inverter based on energy injection control is able to generate a high frequency output current at a low switching frequency. The inverter can operate at full ZCS conditions offering very good startup and steady state properties, which are predicable.

In chapter 4, a thorough study was conducted on the behavior and properties of the variable frequency controlled energy injection inverter with one or more secondary pickups at a system level. Like other load resonant converters, the frequency variation may also limit the proposed energy injection inverters to applications with light loads. Therefore, a detailed frequency bifurcation phenomenon was discussed including the effect of loading conditions. It was found that the primary inverter can operate at other zero current switching frequencies with the variable frequency control strategy when the load on the pickup increases to a certain level. A theoretical analysis enables the two bifurcation frequencies, and an analytical critical maximum loading condition to be predicted enabling frequency bifurcation to be avoided during operation. In addition, the system frequency stability problem was analyzed for an IPT system with multiple distributed pickups. It was found that the proposed inverter can achieve a better power transfer capability for a multiple pickups system. The maximum boundary condition for a given number of pickup was found, which is helpful for designing a primary inverter without bifurcation.

The effect of coupling between the primary and the secondary pickups on the system frequency stability was also analyzed to find the boundary coupling condition corresponding to bifurcation. The effect of this coupling condition was investigated against the output power. An optimal coupling factor was found which ensures the maximum power transfer capability from the primary inverter to the pickup. Experimental results proved the existence of the optimal coupling. In addition, a circuit sensitivity and worst case analysis was undertaken when bifurcation did not occur. It was shown that the output frequency is most sensitive to variations in the primary side components, and therefore these must be carefully designed.

In chapter 5, a primary side regulation method for closed loop single pickup control was proposed. The proposed method, which is only suitable for one secondary pickup, controls

the power flow to the contactless power pickup by regulating the primary track current. A T transformer model was used to analyze the maximum output voltage capability. A factor Q_m was defined as the ratio of the load R_L and $\omega_0 M$ for the analysis. It was found that under the nominal operation frequency and certain Q_m, the output voltage is higher if the system has a better coupling. A simulation analysis was conducted to verify the proposed power flow regulation method under different loading conditions. The simulation results show that the power flow control method proposed has an excellent dynamic and steady state performance during the startup and load variations. A practical contactless slip ring system was designed and implemented to verify the power flow control method. The validation of this proposed power flow control method was proven experimentally.

In chapter 6, a novel direct AC-AC converter was proposed based on free oscillation and energy injection control. This novel topology with four semi-conductor switches was developed to obtain a flat high frequency track current without any DC energy storage. The direct AC-AC converter was shown to have a simple structure and demonstrated a greater freedom compared to traditional AC-DC-AC converters and traditional matrix converters. A detailed control strategy to achieve a constant amplitude track current was proposed. The variable frequency control enables ZCS operating conditions and very smooth commutations during operation. In addition, the switching transitions are only necessary when the resonant tank requires energy injection. A mathematical model was developed to analyze the converter operation and performance with a focus on the track current for IPT applications. The maximum and the minimum current during the current controlled period were analyzed by considering the worst case scenarios. In addition, the uncontrollable current sag caused by the input ac voltage around each zero crossing point was analyzed using energy and power balance principles. The current fluctuations under both normal and zero crossing conditions are related to the circuit parameters. At a certain operation frequency, a resonant tank with a large Q will contribute to a stable current under all conditions.

To verify the operation and theoretical analysis, simulation and experiment were conducted. Both simulation and experimental results demonstrated that the proposed direct AC-AC converter can generate a high frequency current directly from the low frequency AC input with relatively good waveforms for IPT applications.

In chapter 7, a push pull inverter was investigated for generating a high frequency current with boost operation. This configuration is a reverse transformation of the energy injection concept, which has a lower switching frequency leading to a buck operation for voltage fed converters. The operation principle of the boost operation for a push pull configuration was discussed. A stroboscopic mapping model was used to determine the suitable low frequency ZVS operation points. It was found that a push pull inverter can have multiple low frequency ZVS points. The effects on the steady state waveform of the resonant voltage and the track current of operating at different operational ZVS frequencies were discussed. The result showed that only the odd number ZVS points can boost the resonant voltage and track current with smooth waveforms. As an indication for future design, the existence condition of the multiple ZVS operation frequencies was analyzed. It was found that Q determined the system multiple operation points. The minimum critical Q for ensuring the existence of the required multiple ZVS points was defined.

Both the simulation and experimental results have proven that the voltage and current can be made to increase when the ZVS operation frequency is reduced. It was found that the proposed boost operation offers a simple and cost-effective solution to deliver more power for an IPT system with a given push-push resonant converter.

8.2 Contributions of This Thesis Work

The main contributions of the thesis work include:

Proposing DC-AC inverters based on free oscillation and energy injection control, and experimentally demonstrating that the inverters can generate high frequency current with flexible control and low switching frequency for IPT applications.

Determining the critical loading and coupling conditions corresponding to frequency bifurcation, which is very useful for designing a stable primary energy injection inverter.

Determining an optimal coupling coefficient, corresponding to the maximum power transfer capability of an IPT system.

The proposal and implementation of a power flow control method for an IPT system on the primary side inverter based on energy injection control.

The proposal and development of a direct AC-AC matrix configuration based on circuit oscillation and energy injection. The converter has a simple structure supplying a number of useful features for generating high frequency current without a DC link.

The proposal and investigation of a boost operation method using a traditional push pull inverter. A stroboscopic mapping model method is used to accurately locate the ZVS operation points for this boost operation.

Part of the above contribution has been published in three journal papers [128-130], seven conference papers [131-137]. In addition, one journal paper [138] and one book chapter have been accepted [139]. A provisional patent based on the energy injection controlled power converters has been filed.

8.3 Suggestions for Future Work

The work of this thesis is focused on the development of an alternative high frequency power converter based on energy injection control for IPT systems. Various theoretical analyses, system and component level simulations and experimental tests have been successfully undertaken to achieve and validate the research objectives presented in this thesis. However, there are many more areas which have been opened up for further investigation. Suggestions for future research are given below.

Studies on nonlinear phenomena

The developments of power converters for IPT systems are mainly concerned with switch-mode nonlinear circuits comprising semiconductor switches and passive energy storage components. A switch mode converter acts between different switching transients during operation. Additionally, if pickups are included, the effect of the rectification circuit and additional high order characteristics significantly complicate the circuit behavior and the analysis. There is a need for further fundamental studies on nonlinear circuits that include the practically nonlinearities, transients and high order to help to guide engineering design and promote further practical applications in future.

Multiphase AC-AC converters

As discussed in Chapter 6 of this thesis, a single phase input can cause current sags when the input changes its polarity. In fact, this is caused by insufficient energy injection at the zero crossing points. If multiple phases are used, a more complicated switching network can be built to smooth out the energy injection by shifting between the various phases of the input source. Accordingly current ripples and sags can be reduced. In addition, multiple phase converters can also help to increase the power transfer capability. It opens an important and interesting research area in designing network oscillation, isolation, EMI, and protection of AC-AC high frequency IPT power converters.

Improvement on high frequency operation detection

Detection techniques are critically important to ensure voltage fed energy injection resonant converters to operate under ZCS conditions. Passive current detection methods like current transformers are widely used in IPT applications, but time delays exist in the detection due to the phase delay between the primary and secondary current, as well as the propagation delay due to signal processing. As such, the existing current detection method is more suitable for low frequency IPT systems. To design converters that can operate at MHz level as desired for some low power (100W-1KW) with accurate ZCS operation, the improvement on the zero crossing detection of the resonant current and associated signal processing technology are required.

EMI filter design

Although the concept of circuit resonance and energy injection could be used to develop a high frequency converter for IPT systems, the current pulse generated by a fast switching network could be a practical concern. This is because the current pulse is discrete and determined by loading or coupling conditions. Variations in the operation conditions will cause different switching patterns, and therefore different current pulse sequences. Therefore, the design of the common mode EMI filter design is important and need for the consideration as part of the design of energy injection converters for different IPT applications to meet industrial EMC standards.

References

[1]   G. L. Johnson, "Building the world's largest Tesla coil-history and theory," in *Power Symposium, 1990. Proceedings of the Twenty-Second Annual North American*, 1990, pp. 128-135.

[2]   G. Chowdhary, R. Gadre, and N. Komerath, "Policy issues for retail Beamed Power transmission," in *Science and Innovation Policy, 2009 Atlanta Conference on*, 2009, pp. 1-6.

[3]   G. A. Landis, "Photovoltaic receivers for laser beamed power in space," in *IEEE Photovoltaic Specialists Conference*, 1991, pp. 1494-1502 vol.2.

[4]   J. E. Dagle, "Performance enhancement using power beaming for electric propulsion Earth orbital transporters," *IEEE Aerospace and Electronic Systems Magazine* vol. 6, pp. 17-20, 1991.

[5]   A. W. Guy, "History of biological effects and medical applications of microwave energy," *IEEE Transactions on Microwave Theory and Techniques,* vol. 32, pp. 1182-1200, 1984.

[6]   W. C. Brown, "The History of Power Transmission by Radio Waves," *IEEE Transactions on Microwave Theory and Techniques,* vol. 32, pp. 1230-1242, 1984.

[7]   A. Dolgov, R. Zane, and Z. Popovic, "Power Management System for Online Low Power RF Energy Harvesting Optimization," *IEEE Transactions on Circuits and Systems I: Regular Papers,* vol. 57, pp. 1802-1811, 2010.

[8]   A. P. Hu, C. Liu, and H. L. Li, "A novel contactless battery charging system for soccer playing robot," in *15th International Conference on Mechatronics and Machine Vision in Practice*, 2008, pp. 646-650.

[9]   E. Culurciello and A. G. Andreou, "Capacitive coupling of data and power for 3D silicon-on-insulator VLSI," in *IEEE International Symposium on Circuits and Systems (ISCAS 2005)*, Kobe, Japan, 2005, pp. 4142-4145.

[10]   C. Liu, A. P. Hu, and N. K. C. Nair, "Coupling study of a rotary capacitive power transfer system," in *IEEE International Conference on Industrial Technology, ICIT 2009*, 2009, pp. 1-6.

[11]   J. D. Kraus, *Electromagnetics*, Fourth ed.: McGraw-Hill, 1991.

[12]   Z. Wenqi and M. Hao, "Steady-State Analysis of the Inductively Coupled Power Transfer System," in *IEEE 32nd Annual Conference on Industrial Electronics*, Paris, France, 2006, pp. 2438-2443.

[13]   J. T. Boys, G. A. J. Elliott, and G. A. Covic, "An Appropriate Magnetic Coupling Co-Efficient for the Design and Comparison of ICPT Pickups," *IEEE Transactions on Power Electronics,* vol. 22, pp. 333-335, 2006.

[14]   R. H. Nansen, "Wireless power transmission: the key to solar power satellites," *IEEE Aerospace and Electronic Systems Magazine,* vol. 11, pp. 33-39, 1996.

[15]   J. Benford, "Space Applications of High-Power Microwaves," *IEEE Transactions on Plasma Science,* vol. 36, pp. 569-581, 2008.

[16]   A. P. Hu, "Selected Resonant Converters for IPT Power Supplies," PhD thesis, Department of Electrical and Computer Engineering, University of Auckland, Auckland, 2001.

[17]   A. W. Green and J. T. Boys, "10 kHz inductively coupled power transfer-concept and control," in *5th International Conference on Power Electronics and Variable-Speed Drives*, 1994, pp. 694-699.

[18]   B. V. Dawson, I. G. C. Robertson, W. R. Wilson, L. J. Zwi, J. T. Boys, and A. W. Green, "Evaluation of Potential Health Effects of 10 kHz Magnetic Fields: A Rodent Reproductive Study," 1998.

[19]   T. D. Dissanayake, D. Budgett, H. Patrick, and S. Malpas, "Experimental thermal study of a TET system for implantable biomedical devices," in *IEEE Biomedical Circuits and Systems Conference (BioCAS 2008)*, 2008, pp. 113-116.

[20]   J. U. W. Hsu, A. P. Hu, and A. Swain, "A Wireless Power Pickup Based on Directional Tuning Control of Magnetic Amplifier," *IEEE Transactions on Industrial Electronics,* vol. 56, pp. 2771-2781, 2009.

[21]   J. T. Boys, C. I. Chen, and G. A. Covic, "Controlling Inrush Currents in Inductively Coupled Power Systems," in *7th International Power Engineering Conference*, Singapore, 2005, pp. 1-6.

[22]   T. D. Dissanayake, A. P. Hu, S. Malpas, L. Bennet, A. Taberner, L. Booth, and D. Budgett, "Experimental Study of a TET System for Implantable Biomedical Devices," *IEEE Transactions on Biomedical Circuits and Systems,* vol. 3, pp. 370-378, 2009.

[23]   K. Iwawaki, M. Watada, S. Takatani, and Y. S. Um, "The design of core-type transcutaneous energy transmission systems for artificial heart," in *IEEE 30th Annual Conference of the Industrial Electronics Society (IECON 2003)*, Busan, Korea, 2004, pp. 948-952.

[24]   D. C. White, R. D. Thornton, and C. Kingsley, "Some Problems related to Electric Propulsion," ed, U.S. Dept. of Commerce, November 1966.

[25]   A. Karalis, J. D. Joannopoulos, and M. Soljačić, "Efficient wireless non-radiative mid-range energy transfer," *Annals of Physics,* vol. 323, pp. 34-48, January 2008.

[26]   A. Kurs, A. Karalis, R. Moffatt, J. D. Joannopoulos, P. Fisher, and M. Soljacic, "Wireless Power Transfer via Strongly Coupled Magnetic Resonances," *Science,* vol. 317, pp. 83 - 86, 2007.

[27]   N. A. Keeling, J. T. Boys, and G. A. Covic, "Unity Power Factor Inductive Power Transfer Pick-up for High Power Applications," in *IEEE 34th Annual Conference of Industrial Electronics Society (IECON 2008)*, Orlando, Florida, 2008.

[28]   C.-I. Chen, G. A. Covic, and J. T. Boys, "Regulator Capacitor Selection for Series Compensated IPT Pickups," 2008.

[29]   J. T. Boys, C. Y. Huang, and G. A. Covic, "Single-phase unity power-factor inductive power transfer system," in *IEEE Power Electronics Specialists Conference (PESC 2008)*, Rhodes, 2008, pp. 3701-3706.

[30]   A. P. Hu, G. A. Covic, and J. T. Boys, "Direct ZVS start-up of a current-fed resonant inverter," *IEEE Transactions on Power Electronics,* vol. 21, pp. 809-812, 2006.

[31]   A. P. Hu, J. T. Boys, and G. A. Covic, "ZVS frequency analysis of a current-fed resonant converter," in *7th IEEE International Power Electronics Congress*, Acapulco, Mexico, 2000, pp. 217-221.

[32]   E. L. v. Boheemen, J. T. Boys, and G. Covic, "Dual-tuning IPT systems for low bandwidth communications," in *IEEE Conference on Industrial Electronics and Applications (ICIEA 2007)*, Harbin, China, 2007, pp. 586-591.

[33]   P. Si, A. P. Hu, J. W. Hsu, M. Chiang, Y. Wang, S. Malpas, and D. Budgett, "Wireless power supply for implantable biomedical device based on primary input voltage regulation," in *IEEE Conference on Industrial Electronics and Applications (ICIEA 2007)*, 2007, pp. 235-239.

[34]   G. A. Covic, J. T. Boys, M. L. G. Kissin, and H. G. Lu, "A Three Phase Inductive Power Transfer System for Roadway Powered Vehicles," *IEEE Transactions on Industrial Electronics,* vol. 54, pp. 3370-3378, 2007.

[35]   "IPT technology in practice of power electronics group," ed: University of Auckland, 2010.

[36]   T. Sekitani, M. Takamiya, Y. Noguchi, S. Nakano, Y. Kato, K. Hizu, H. Kawaguchi, T. Sakurai, and T. Someya, "A large-area flexible wireless power transmission sheet using printed plastic MEMS switches and organic field-effect transistors," in *International Electron Devices Meeting*, 2006, pp. 1-4.

[37]   T. Sekitani, M. Takamiya, Y. Noguchi, S. Nakano, Y. Kato, T. Sakurai, and T. Someya, "A large-area wireless power-transmission sheet using printed organic transistors and plastic MEMS switches," *Nature Materials,* vol. 6(6), p. 413～417, 2007.

References

[38]   H. Sakamoto and K. Harada, "A novel converter for non-contact charging with electromagnetic coupling," *IEEE Transactions on Magnetics,* vol. 29, pp. 3228-3230, 1993.

[39]   H. Sakamoto and S. Washimiya, "Magnetic coupled power and data transferring system with a detachable transformer," *IEEE Transactions on Magnetics,* vol. 32, pp. 4983-4985, 1996.

[40]   M. Nishimura, A. Kawamura, G. Kuroda, Z. Chi, and E. K. Sato, "High Efficient Contact-less Power Transmission System for the High Speed Trains," in *IEEE Power Electronics Specialists Conference (PESC 2005)*, 2005, pp. 547-553.

[41]   J. Hirai, K. Tae-Woong, and A. Kawamura, "Study on intelligent battery charging using inductive transmission of power and information," *IEEE Transactions on Power Electronics,* vol. 15, pp. 335-345, 2000.

[42]   J. Hirai, K. Tae-Woong, and A. Kawamura, "Wireless transmission of power and information and information for cableless linear motor drive," *IEEE Transactions on Power Electronics,* vol. 15, pp. 21-27, 2000.

[43]   J. Hirai, K. Tae-Woong, and A. Kawamura, "Study on crosstalk in inductive transmission of power and information," *IEEE Transactions on Industrial Electronics,* vol. 46, pp. 1174-1182, 1999.

[44]   L. Wonseok, N. Jaehyun, C. Byungcho, and A. Taeyoung, "Low-profile contactless battery charger using planar printed circuit board windings as energy transfer device," in *IEEE Power Electronics Specialists Conference (PESC 2002)*, 2002, pp. 579-584 vol.2.

[45]   C. Byungcho, N. Jaehyun, C. Honnyong, A. Taeyoung, and C. Seungwon, "Design and implementation of low-profile contactless battery charger using planar printed circuit board windings as energy transfer device," *IEEE Transactions on Industrial Electronics,* vol. 51, pp. 140-147, 2004.

[46]   S. Y. Hui, S. C. Tang, and C. Henry Shu-Hung, "Optimal operation of coreless PCB transformer-isolated gate drive circuits with wide switching frequency range," *IEEE Transactions on Power Electronics,* vol. 14, pp. 506-514, 1999.

[47]   X. Liu and S. Y. Hui, "Optimal design of a hybrid winding structure for planar contactless battery charging platform," *IEEE Transactions on Power Electronics,* vol. 23, pp. 455-463, 2008.

[48]   X. Liu and S. Y. R. Hui, "Equivalent circuit modeling of a multilayer planar winding array structure for use in a universal contactless battery charging platform," *IEEE Transactions on Power Electronics,* vol. 22, pp. 21-29, 2007.

[49]   S. C. Tang, S. Y. Hui, and C. Henry Shu-Hung, "Coreless planar printed-circuit-board (PCB) transformers-a fundamental concept for signal and energy transfer," *IEEE Transactions on Power Electronics,* vol. 15, pp. 931-941, Sept. 2000.

[50] H. Ma and W. Zhou, "Modeling a current source push-pull resonant converter for loosely coupled power transfer systems," in *IEEE 30th Annual Conference of the Industrial Electronics Society (IECON 2004)*, Busan, Korea, 2004, pp. 1024-1029.

[51] Y. Su, C. Tang, S. Wu, and Y. Sun, "Research of LCL Resonant Inverter in Wireless Power Transfer System," in *International Conference on Power System Technology (PowerCon 2006)*, Chongqing, China, 2006, pp. 1-6.

[52] Y. Su, W. Shuping, T. Chunsen, and S. Yue, "Investigating a High Frequency DC/DC Converter with Soft-Switching Technology," in *International Conference on Power System Technology (PowerCon 2006)*, 2006, pp. 1-5.

[53] S. Yue, L. Yan Ling, D. Xin, S. Yu Gang, and T. Chun Sen, "Study on multiple resonant points control strategy of contactless power transfer system using neural network," in *8th World Congress on Intelligent Control and Automation*, 2010, pp. 4686-4690.

[54] S. Yue, A. P. Hu, D. Xin, and S. Yugang, "Discrete time mapping modeling and bifurcation phenomenon study of a ZVS converter," in *International Conference on Power System Technology (PowerCon 2004)* 2004, pp. 1015-1018 Vol.2.

[55] T. Chun Sen, S. Yue, S. Yu Gang, N. Sing Kiong, and A. P. Hu, "Determining Multiple Steady-State ZCS Operating Points of a Switch-Mode Contactless Power Transfer System," *IEEE Transactions on Power Electronics,* vol. 24, pp. 416-425, 2009.

[56] Conductix-Wampfler. (09/October). Available: http://www.wampfler.com/index.asp?id=10&plid=12&e1=2&lang=E

[57] G. A. Covic, G. Elliott, O. H. Stielau, R. M. Green, and J. T. Boys, "The design of a contact-less energy transfer system for a people mover system," in *Proceedings International Conference on Power System Technology*, Perth, Australia, 2000, pp. 79-84.

[58] Auckland University. *The University of Auckland: Conductix-Wampfler electric people mover at Rotorua, New Zealand*. Available: http://web.ece.auckland.ac.nz/uoa/powerelectronicsresearch

[59] VAHLE. (09/October). *CPS Introduction* Available: http://www.vahle.de/en/index.php?ption=com_content&task=view&id=130&Itemid=376

[60] N. Release. (2008). *Epson Develops Non-Contact Power Transmission Module Capable of Transmitting 2.5 W with a 0.8mm Coil*.

[61] Seiko-Epson. (2008, 09/October). *wireless power transfer module*. Available: http://global.epson.com/newsroom/2008/news_20080922.htm

[62] G. Scheible and R. Disselnkoetter. (2003). *Wireless power in wireless products*.

[63]   ABB. White Paper: Introduction to WISA V2.0, ABB - Introduction to WISA. Available: http://www05.abb.com/global/scot/scot209.nsf/veritydisplay/c81a48ddc34c5125c1 2571f100410e74/$File/White_Paper%20Introduction%20to%20WISA%20V2.pdf

[64]   Energizer. (25/Jan). Available: http://techgadgetx.com/charge-your-iphone-4-wirelessly-with-energizer-gadget-video/

[65]   Witricity. (09/October). Available: http://www.witricity.com/

[66]   Spikecharger. (09/October). Available: http://www.spikecharger.com/

[67]   Powercast. (09/October). Available: http://www.powercastco.com/

[68]   Wipower. (09/October, 2010. Available: www.research.ufl.edu/otl/pdf/startup/WiPower.pdf

[69]   PowerbyProxi. (09/October). *Proxi-Ring*. Available: http://www.powerbyproxi.com/

[70]   3iinnovation. (09/October). Available: http://www.3iinnovation.com/

[71]   Telemetry Research. (09/October). *Charging of Transmitters*. Available: http://www.telemetryresearch.com/index.php?option=com_content&task=view&id =39&Itemid=164

[72]   Wireless Power Consortium. *Qi standard*. Available: http://www.wirelesspowerconsortium.com/news/announcements/low-power-standard-ready.htmlr

[73]   C.-S. Wang, O. H. Stielau, and G. A. Covic, "Design considerations for a contactless electric vehicle battery charger," *IEEE Transactions on Industrial Electronics,* vol. 52, pp. 1308-1314, 2005.

[74]   J. M. Barnard, J. A. Ferreira, and J. D. Van Wyk, "Linear contactless power transmission systems for harsh environments," in *4th IEEE AFRICON*, 1996, pp. 711-714.

[75]   J. Meins, "Linear Inductive Power Transmission," in 14th International Conference on Magnetically Levitated Systems and Linear Drives, Bremen, Germany 1995.

[76]   Y.-H. Chao, J.-J. Shieh, C.-T. Pan, W.-C. Shen, and M.-P. Chen, "A Primary-Side Control Strategy for Series-Parallel Loosely Coupled Inductive Power Transfer Systems," in *IEEE Conference on Industrial Electronics and Applications (ICIEA 2007)*, Harbin, China, 2007, pp. 2322-2327.

[77]   G. A. Kendir, L. Wentai, W. Guoxing, M. Sivaprakasam, R. Bashirullah, M. S. Humayun, and J. D. Weiland, "An optimal design methodology for inductive power link with class-E amplifier," *IEEE Transactions on Circuits and Systems I: Regular Papers,* vol. 52, pp. 857-866, 2005.

[78] H. Ayano, K. Yamamoto, N. Hino, and I. Yamato, "Highly efficient contactless electrical energy transmission system," in *IEEE 28th Annual Conference of Industrial Electronics Society (IECON 2002)*, Sevilla, Spain, 2002, pp. 1364-1369.

[79] H. Abe, H. Sakamoto, and K. Harada, "A noncontact charger using a resonant converter with parallel capacitor of the secondary coil," in *Applied Power Electronics Conference and Exposition* Fukuoka, Japan, 1998, pp. 136-141.

[80] H. H. Wu, A. P. Hu, P. Si, D. Budgett, C. Tung, and S. Malpas, "A push-pull resonant converter with dual coils for Transcutaneous Energy Transfer systems," in *IEEE Conference on Industrial Electronics and Applications (ICIEA 2009)*, 2009, pp. 1051-1056.

[81] X. Cao, W.-J. Chiang, Y.-C. King, and Y.-K. Lee, "Electromagnetic energy harvesting circuit with feedforward and feedback DC-DC PWM boost converter for vibration power generator system," *IEEE Transactions on Power Electronics,* vol. 22, pp. 679-685, 2007.

[82] G. S. N. Raju and S. Doradla, "An LCL resonant converter with PWM control-analysis, simulation, and implementation," *IEEE Transactions on Power Electronics,* vol. 10, pp. 164-174, 1995.

[83] L. QingFeng, W. HuaMin, and L. ZhaoXia, "Discuss on the Application of Multilevel Inverter in High Frequency Induction Heating Power Supply," in *IEEE Region 10 Conference*, 2006, pp. 1-4.

[84] R. L. Steigerwald, "High-frequency resonant transistor DC-DC converters," *IEEE Transactions on Industrial Electronics,* vol. 31, pp. 181-191, May 1984.

[85] A. K. S. Bhat, "A fixed frequency LCL-Type series resonant converter," *IEEE Transactions on Aerospace and Electronic Systems,* vol. 31, pp. 125-137, 1995.

[86] A. N. Belyaev and S. V. Smolovik, "An improvement of AC electrical energy transmission system with series compensation by implementation of controllable shunt reactors," in *IEEE Power Tech Conference Proceedings*, Bologna, 2003, p. 6.

[87] S. Ping, "Wireless Power Supply for Implantable Biomedical Devices," Phd, The University of Auckland, 2006.

[88] M. Borage, S. Tiwari, and S. Kotaiah, "LCL-T Resonant Converter With Clamp Diodes: A Novel Constant-Current Power Supply With Inherent Constant-Voltage Limit," *IEEE Transactions on Industrial Electronics,* vol. 54, pp. 741-746, 2007.

[89] M. Borage, S. Tiwari, and S. Kotaiah, "Analysis and design of an LCL-T resonant converter as a constant-current power supply," *IEEE Transactions on Industrial Electronics,* vol. 52, pp. 1547-1554, 2005.

[90] Y.-H. Chao, J.-J. Shieh, C.-T. Pan, and W.-C. Shen, "A Closed-form Oriented Compensator Analysis for Series-parallel Loosely Coupled Inductive Power

Transfer Systems," in *IEEE Power Electronics Specialists Conference (PESC 2007)*, Orlando, Florida, 2007, pp. 1215-1220.

[91]   C.-S. Wang, G. A. Covic, and O. H. Stielau, "Power transfer capability and bifurcation phenomena of loosely coupled inductive power transfer systems," *IEEE Transactions on Industrial Electronics,* vol. 51, pp. 148-157, 2004.

[92]   W. Guoxing, L. Wentai, R. Bashirullah, M. Sivaprakasam, G. A. Kendir, J. Ying, M. S. Humayun, and J. D. Weiland, "A closed loop transcutaneous power transfer system for implantable devices with enhanced stability," in *IEEE International Symposium on Circuits and Systems (ISCAS 2004)*, Vancouver, Canada, 2004, pp. IV-17-20.

[93]   J. Meins, F. Turki, and R. Czainski, "Phase control of resonant power supply inverters," in *European Conference on Power Electronics and Applications*, 2005, pp. 1-7.

[94]   S. V. Mollov, M. Theodoridis, and A. J. Forsyth, "High frequency voltage-fed inverter with phase-shift control for induction heating," *IEE Proceedings on Electric Power Applications,* vol. 151, pp. 12-18, 2004.

[95]   A. P. Hu and S. Hussmann, "Improved power flow control for contactless moving sensor applications," *IEEE Power Electronics Letters,* vol. 2, pp. 135-138, 2004.

[96]   C.-S. Wang, G. A. Covic, and O. H. Stielau, "Investigating an LCL load resonant inverter for inductive power transfer applications," *IEEE Transactions on Power Electronics,* vol. 19, pp. 995-1002, 2004.

[97]   S. Ping, A. P. Hu, S. Malpas, and D. Budgett, "Switching Frequency Analysis of Dynamically Detuned ICPT Power Pick-ups," in *International Conference on Power System Technology (PowerCon 2006)*, 2006, pp. 1-8.

[98]   J. T. Boys, A. P. Hu, and G. A. Covic, "Critical Q analysis of a current-fed resonant converter for ICPT applications," *Electronics Letters,* vol. 36, pp. 1440-1442, 2000.

[99]   A. Hu, J. T. Boys, and G. A. Covic, "Dynamic ZVS direct on-line start up of current fed resonant converter using initially forced DC current," in *IEEE International Symposium on Industrial Electronics*, Cholula, 2000, pp. 312-317.

[100] W. Zhou and H. Ma, "Design Considerations of Compensation Topologies in ICPT System," in *22nd Annual IEEE Applied Power Electronics Conference*, 2007, pp. 985-990.

[101] M. Z. Youssef, H. Pinheiro, and P. K. Jain, "Self-sustained phase-shift modulated resonant converters: modeling, design, and performance," *IEEE Transactions on Power Electronics* vol. 21, pp. 401-414, 2006.

[102] F. F. A. Van der Pijl, P. Bauer, J. A. Ferreira, and H. Polinder, "Quantum Control for an Experimental Contactless Energy Transfer System for Multiple Users," in *IEEE Power Electronics Specialists Conference (PESC 2007)*, 2007, pp. 343-349.

[103] S. Dieckerhoff, M. J. Ruan, and R. W. De Doncker, "Design of an IGBT-based LCL-resonant inverter for high-frequency induction heating," in *Conference Record of the 1999 IEEE Industry Applications Conference* Phoenix, USA, 1999, pp. 2039-2045.

[104] N. H. Kutkut, "A full bridge LCL resonant battery charger for an EV conductive coupler," in *IEEE 29th Annual Power Electronics Specialists Conference*, Fukuoka, Japan, 1998, pp. 2069-2075.

[105] C.-Y. Huang, "A Low Cost ICPT Power Supply," M.E. thesis, Department of Electrical and Computer Engineering, University of Auckland, Auckland, 2006.

[106] K. W. Klontz, A. Esser, R. R. Bacon, D. M. Divan, D. W. Novotny, and R. D. Lorenz, "An electric vehicle charging system with `universal' inductive interface," in *Proceedings of the Power Conversion Conference*, Yokohama, 1993, pp. 227-232.

[107] J. J. Casanova, L. Zhen Ning, and L. Jenshan, "Design and Optimization of a Class-E Amplifier for a Loosely Coupled Planar Wireless Power System," *IEEE Transactions on Circuits and Systems II: Express Briefs,* vol. 56, pp. 830-834, 2009.

[108] G. Lutteke and H. C. Raets, "High Voltage High Frequency Class-E Converter Suitable for Miniaturization," *IEEE Transactions on Power Electronics,* vol. PE-1, pp. 193-199, 1986.

[109] P. Colantonio, F. Giannini, R. Giofre, M. A. Y. Medina, D. Schreurs, and B. Nauwelaers, "High frequency class E design methodologies," in *European Gallium Arsenide and Other Semiconductor Application Symposium*, 2005, pp. 329-332.

[110] Y. Tianliang, Z. Chunyu, Z. Jinying, and C. Dayue, "Power loss and efficiency of Transcutaneous Energy Transmission System with Class-E power amplifier at any duty ratio," in *International Symposium on Signals, Circuits and Systems (ISSCS 2009)* 2009, pp. 1-4.

[111] W. Guoxing, L. Wentai, M. Sivaprakasam, and G. A. Kendir, "Design and analysis of an adaptive transcutaneous power telemetry for biomedical implants," *IEEE Transactions on Circuits and Systems I: Regular Papers,* vol. 52, pp. 2109-2117, 2005.

[112] N. Mohan, T. Undeland, and W. Robbins, *Power Electronics*, Third ed.: Wiley, 2002.

[113] N. Nguyen-Quang, D. A. Stone, C. M. Bingham, and M. P. Foster, "A three-phase to single-phase matrix converter for high-frequency induction heating," in *European Conference on Power Electronics and Applications*, 2009, pp. 1-10.

[114] L. Wei and T. Houjun, "Analysis of Voltage Source Inductive Coupled Power Transfer Systems Based on Zero Phase Angle Resonant Control Method," in *IEEE Conference on Industrial Electronics and Applications (ICIEA 2007)*, 2007, pp. 1873-1877.

[115] C.-S. Wang, G. A. Covic, and O. H. Stielau, "General stability criterions for zero phase angle controlled loosely coupled inductive power transfer systems," in *IEEE 27th Annual Conference of the Industrial Electronics Society (IECON 2001)*, Denver, USA, 2001, pp. 1049-1054.

[116] C.-S. Wang, O. H. Stielau, and G. A. Covic, "Load models and their application in the design of loosely coupled inductive power transfer systems," in *Proceedings International Conference on Power System Technology*, Perth, Australia, 2000, pp. 1053-1058.

[117] G. A. Covic, J. James, and J. T. Boys, "Analysis of a Series Tuned IPT Pick-Up Using DC Transformer Modeling Methods," in *6th International Power Engineering Conference*, Singapore, 2003.

[118] S. Raabe, J. T. Boys, and G. A. Covic, "A high power coaxial inductive power transfer pickup," in *IEEE Power Electronics Specialists Conference (PESC 2008)*, Rhodes, Greece, 2008, pp. 4320-4325.

[119] J. T. Boys, G. A. Covic, and A. W. Green, "Stability and control of inductively coupled power transfer systems," *IEE Proceedings on Electric Power Applications,* vol. 147, pp. 37-43, 2000.

[120] S. ping, A. P. Hu, S. Malpas, and D. Budgett, "A Frequency Control Method for Regulating Wireless Power to Implantable Devices," *IEEE Transactions on Biomedical Circuits and Systems,* vol. 2, March 2008.

[121] J. Gyu Bum and B. H. Cho, "An energy transmission system for an artificial heart using leakage inductance compensation of transcutaneous transformer," *IEEE Transactions on Power Electronics,* vol. 13, pp. 1013-1022, 1998.

[122] Y. Kaiming and L. Lei, "Full Bridge-full Wave Mode Three-level AC/AC Converter with High Frequency Link," in *IEEE Applied Power Electronics Conference and Exposition (APEC 2009)*, 2009, pp. 696-699.

[123] S. Hisayuki, E. Ahmad Mohamad, K. Soon-Kurl, L. Hyun Woo, E. Hiraki, and N. Mutsuo, "High frequency cyclo-converter using one-chip reverse blocking IGBT based bidirectional power switches," in *Proceedings of the Eighth International Conference on Electrical Machines and Systems*, 2005, pp. 1095-1100 Vol. 2.

[124] H. Sugimura, M. Sang-Pil, K. Soon-Kurl, T. Mishima, and M. Nakaoka, "Direct AC-AC resonant converter using one-chip reverse blocking IGBT-based bidirectional switches for HF induction heaters," in *IEEE International Symposium on Industrial Electronics*, 2008, pp. 406-412.

[125] D. J. Thrimawithana and U. K. Madawala, "Analysis of Split-Capacitor Push-Pull Parallel Resonant Converter in normal mode," in *Power Electronics, Electrical Drives, Automation and Motion, 2008. SPEEDAM 2008. International Symposium on*, 2008, pp. 778-783.

[126] U. K. Madawala and D. J. Thrimawithana, "Mathematical model for split-capacitor push-pull parallel resonant converter in Buck mode," *IET Power Electronics,* vol. 1, pp. 356-367, 2008.

[127] A. W. Green, "Modelling a push-pull parallel resonant convertor using generalised state-space averaging," *IEE Proceedings on Electric Power Applications,* vol. 140, pp. 350-356, 1993.

[128] H. L. Li, A. P. Hu, G. A. Covic, and C. S. Tang, "Optimal coupling condition of IPT system for achieving maximum power transfer," IET *Electronics Letters,* vol. 45, pp. 76-77, 2009.

[129] H. L. Li, A. P. Hu, and G. A. Covic, "Primary Current Generation for a Contactless Power Transfer System Using Free Oscillation and Energy Injection Control," *Journal of Power Electronics,* Vol.11, pp.256-263, 2011.

[130] Y. Sun, C. S. Tang, A. P. Hu, H. L. Li, and S. K. Nguang, "Multiple Soft-Switching Operating Points Based Power Flow Control of Contactless Power Transfer Systems," *IET Power Electronics,* Vol.4, pp.725-731, 2011.

[131] H. L. Li, A. P. Hu, and G. A. Covic, "Development of a discrete energy injection inverter for contactless power transfer," in *IEEE Conference on Industrial Electronics and Applications (ICIEA 2008)*, Singapore, 2008, pp. 1757-1761.

[132] A. P. Hu and H. L. Li, "A new high frequency current generation method for inductive power transfer applications," in *IEEE Power Electronics Specialists Conference (PESC 2006)*, Jeju, Korea, 2006, pp. 1-6.

[133] H. L. Li, A. P. Hu, and G. A. Covic, "A power flow control method on primary side for a CPT system," in *International Power Electronics Conference (ECCE-Asia)*, 2010, pp. 1050-1055.

[134] H. L. Li, A. P. Hu, G. A. Covic, and T. ChunSen, "A new primary power regulation method for contactless power transfer," in *IEEE International Conference on Industrial Technology (ICIT 2009)*, 2009, pp. 1-5.

[135] H. L. Li, A. P. Hu, G. Jinfeng, and D. Xin, "Development of a Direct AC-AC Converter Based on a DSPACE Platform," in *International Conference on Power System Technology (PowerCon 2006)*, 2006, pp. 1-6.

[136] H. L. Li, A. P. Hu, and G. A. Covic, "Current fluctuation analysis of a quantum ac-ac resonant converter for contactless power transfer," in *IEEE Energy Conversion Congress and Exposition (ECCE 2010)*, 2010, pp. 1838-1843.

[137] H. L. Li, A. P. Hu, and G. A. Covic, "FPGA controlled high frequency resonant converter for contactless power transfer," in *IEEE Power Electronics Specialists Conference (PESC 2008)*, Rhodes, 2008, pp. 3642-3647.

[138] H. L. Li, A. P. Hu, and G. A. Covic, "A Direct AC-AC Converter for Inductive Power Transfer Systems," *IEEE Transactions on Power Electronics,* Nov 2010.

[139] H. L. Li, A. P. Hu, and G. A. Covic, "A High Frequency Energy Injection Converter for Inductive Power Transfer (IPT) Applications," Wireless Energy Transfer based on Electromagnetic Resonance: Principle and Engineering Explorations, ISBN 979-953-307-152-6, INTECH.

Appendices

Code of Stroboscopic Mapping Model for Detecting ZVS Frequencies of a Push Pull Inverter

```
% initial circuit parameters
Ld=1000*10^(-6);
La=1000*10^(-6);
Lb=1000*10^(-6);
Rd=0.1;
C=(0.67)*10^(-6);
Lp=3.45*10^(-6);
R=0.072;
w=1/sqrt(Lp*C);
U=10;

% State matrix
DETa=Lb*(Ldc+La)+La*Ldc;

DETb=La*(Ldc+Lb)+Lb*Ldc;

A1=[-Rdc*Lb/DETa, -(Rdc*Lb)/DETa, -Ldc/DETa, 0;
    -Rdc*La/DETa, -Rdc*La/DETa, (Ldc+La)/DETa, 0;
     0, -1/C, 0, -1/C;
     0, 0, 1/Lp, -R/Lp];
B1=[Lb/DETa;
    La/DETa;
    0;
    0];

A2=[-Rdc*Lb/DETb, -Rdc*Lb/DETb, -(Ldc+Lb)/DETb, 0;
    -Rdc*La/DETa, -Rdc*La/DETa, Ldc/DETb, 0;
     1/C, 0, 0, -1/C;
     0, 0, 1/Lp, -R/Lp];

B2=[Lb/DETb;
    La/DETb;
    0;
    0];
```

```matlab
%Selection matrix
Y=[0 0 1 0];
Z=[0 0 0 1];

%ZVS frequencies detecting
t=0.01e-6:0.02e-6:8e-4;
k=1;
for i=1:length(t)

ph1=expm(A1*t(i)*0.5);

ph2=expm(A2*t(i)*0.5);

X0=inv(eye(4)-ph2*ph1)*(ph2*inv(A1)*(ph1-eye(4))+inv(A2)*(ph2-
eye(4)))*B1*U;

Vc(i)=Y*X0;

IL(i)=Z*X0;

if i>1&&Vc(i)*Vc(i-1)<=0
    Tz(k)=t(i);
    k=k+1;
end
end

Tz

fz=1./Tz
```